DarcyTools, Version 2.1
Verification and validation

Urban Svensson,
Computer-aided Fluid Engineering AB, Sweden

March 2004

SKB

DarcyTools, Version 2.1
Verification and validation

Urban Svensson,
Computer-aided Fluid Engineering AB, Sweden

March 2004

Table of Contents

1   Introduction

DarcyTools is a computer code for simulation of flow and transport in porous and/or fractured media. The fractured media in mind is a fractured rock and the porous media the soil cover on the top of the rock; it is hence groundwater flows, which is the class of flows in mind.

A number of novel methods and features form the present version of DarcyTools. In the verification studies, these methods are evaluated by comparisons with analytical solutions for idealized situations. The five verification groups (see Table 3-1 below), thus reflect the main areas of recent developments.

The present report will focus on the Verification and Validation of DarcyTools. Two accompanying reports cover other aspects:

- Concepts, Methods, Equations and Demo Simulations, Svensson et al. (2004) (Hereafter Report 1).

- User's Guide, Svensson and Ferry (2004) (Hereafter Report 2).

The objective of this report is to compile all verification and validation studies that have been carried out so far. After some brief introductory sections, all cases will be reported in Appendix A (verification cases) and Appendix B (validation cases).

2 Confidence building

During the last twenty years CFD (Computational Fluid Dynamics) has become a standard simulation tool in most engineering problems, dealing with groundwater flow and transport. This development has been driven by readily available software packages and the significant increase in affordable computer speed and memory capacity. CFD is however not a simple technique to use; generally speaking a basic understanding of several subjects like fluid mechanics, numerical analysis and computer software programming is required. For groundwater modelling an understanding of geohydrology is of course also needed. In an ongoing project, ERCOFTAC (Casey and Wintergerste, 2000), guidelines for CFD simulations are discussed and summarised. Partly based on this report, the following main sources of errors and uncertainties in groundwater simulations can be identified:

- Mathematical model. The mathematical model does not describe the real flow exactly. For example, in textbooks the approximations inherent in the Darcy equation are often analysed and listed. Another often used approximation is that the water is incompressible.

- Discretisation. Numerical solutions are performed on a grid in space and time. The difference between the solution on this grid and the exact solution of the modelled equations is called the discretisation error.

- Convergence and round-off errors. Typically a CFD simulation involves iterative procedures. Convergence errors occur because these iterations are stopped by a certain criteria before they are completed. Round-off errors are due to the limited number of digits when a number is stored in the computer memory.

- Application uncertainties. This includes uncertainties about the geometry of the domain (for example a fracture network), boundary conditions, fluid properties, etc.

- Code errors. It is difficult to get software "bug-free".

- User errors. These are the errors that result from misstakes or carelessness by the user.

More points could have been listed (errors in postprocessing, interpretation of results, etc) but the list given probably gives the most important ones. In this context it may be of interest to refer to the following definitions (from ERCOFTAC):

Error: A recognisable deficiency that is not due to lack of knowledge.

Uncertainty: A potential deficiency that is due to lack of knowledge.

As DarcyTools deals with flow and transport in a fractured rock, one should view the points given from this perspective. The significance of the different points may still vary depending on the modelling approach chosen and the problem studied. Here we concern ourselves with a fracture network, as represented in a continuum model. All of the above discussed errors and uncertainties may still be relevant to consider and it is not easy, in the author's view, to neglect (or set priority to) any of the points. For the modelling approach chosen it is however

expected that the "quality" of a simulation is strongly dependent on how well the fracture network is represented in the continuum model. The fracture network is however only partly known (geometry, properties, etc) and we therefore need to consider the uncertainty introduced.

The question whether a computer code is credible or not and methods to answer this question are given in a recent issue of the AIAA journal (AIAA, 1998). Based on the papers presented, Table 2-1 has been created. The table is an attempt to illustrate the actions involved in the confidence building process. A few comments to the table:

- The order (from top to bottom) is essential. It is not possible to achieve certification without having demonstrated verification and validation.

- There is a consensus in the literature about the definitions of verification and validation. Additional steps and actions in the confidence building are still open to discussion.

- Some authors emphasise that it is important to distinguish between confidence building in a computer code and in a specific application. Related to this issue is the concept "fitness for purpose". It is for example of little value to have a very accurate numerical solution if the algorithm is so slow that the code is impractical for its intended use.

Table 2-1. Processes and actions involved in confidence building.

C O N F I D E N C E B U I L D I N G		Process	Definition	Action
		Verification	**Demonstrate that the equations are solved correctly.**	**Comparison with analytical solutions and other models.**
		Validation	**Demonstrate that the right equations are solved.**	**Comparison with measurements (laboratory and field data).**
		Certification	**Assess whether the right things are done and whether they are done right.**	**Evaluate software construction and working procedures.**
		More (QA-systems, wide range of applications, publications in international journals, etc)		

3　Verification

The verification cases performed can be found in Appendix A and are summarised in Table 3-1.

All cases tested show "good result", i.e. the comparison with the corresponding analytical solution, or another model study, is satisfactory; the reader is referred to the cases to study the details.

A few words may however be needed to explain the objectives when selecting the test cases and the way the comparisons have been carried out.

- The test cases should include one, two and three dimensional, steady and transient cases.

- A wide range of relevant physical processes should be included, i.e. density stratification, unsaturated zones, storativity effects, etc.

- The representation of fractures in a continuum model is a key feature of DarcyTools and should be well covered by the test cases.

Some verification studies described in the literature are focused on grid refinement studies. Here the listed objectives have however been considered to be more important with the "fitness for purpose" argument in mind.

Table 3-1. Compilation of verification cases.

Group	Case	Comment
A. Numerical methods	A1. One dimensional transient diffusion A2. One dimensional steady advection/diffusion A3. Flow through a complex channel A4. Tests of grids A5. Test of pressure-salinity coupling	This group of cases intends to show that the numerical methods work as expected
B. Porous media	B1. Regional groundwater circulation B2. Steady ground-water table B3. Theis problem B4. Transient pressure in a borehole B5. Specific yield, Neuman (1975) B6. Horizontal well problem	This group considers some classical geohydrological testcases
C. Fractured media	C1. Three fractures in a two dimensional domain C2. Intersecting fracture zones C3. Single fracture in a box C4. Many fractures in a box C5. Percolation theory C6. Diffusion in a dead-end fracture C7. Matrix-fracture temperature problem	This group of cases deals with the representation of fractures in a continuum model
D. Transport and dispersion	D1. Taylor dispersion D2. Break-through-curve, PARTRACK D3. Break-through-curve, adv/diff egn D4. Seven fractures in a 2D domain, PARTRACK D5. Three fractures in a 2D domain, PARTRACK D6. Single fracture in a box, PARTRACK	This group considers transport, retention, dispersion and particle tracking cases.
E. Buoyancy effects	E1. Henry's problem E2. The salt dome E3. Coupled temperature-salinity fields E4. Upconing E5. The floating island E6. Two fluid problem	This group considers comparisons where density stratification, due to salinity and temperature gradients, is a key factor.

4 Validation

As validation should be concerned with comparisons with measurements and this report describes version 2.1 of DarcyTools, it is not surprising that very few such comparisons can be reported at this stage. However, as discussed in Report 1, it is relevant to include cases that were carried out with PHOENICS as the equation solver, as it has been carefully evaluated that the two solvers give very similar solutions. Note that the descriptions of the fracture network (GEHYCO) and other descriptions of physical processes are in most respects the same in the PHOENICS cases to be discussed, as in the present version of DarcyTools.

For simulations of flow and transport in a fractured rock, it is difficult to separate the steps "validation" and "calibration". To discuss this we first need to define "calibration" (following AIAA, 1998):

- **Calibration** is the process of tuning a code, in order to improve its prediction of global quantities, for realistic geometries, of design interest.

If we require that validation studies should be concerned with comparisons with field measurements, we also need to accept that these measurements are obtained in conditions that are to a large extent unknown. We do not know the fracture network (its geometry, fracture properties, boundary conditions, etc). In the author's view, we therefore have to accept the following tentative definition of validation:

- For the flow and transport in a fractured rock, validation of a simulation can be claimed if calibration can be performed with all adjustable parameters within realistic limits.

This definition immediately raises the question "what is realistic limits?". For major fracture zones we may be able to define bounds for properties (thickness, transmissivity, porosity, etc) and these bounds then define the "realistic limits". However, for most applications properties and boundary conditions can not be given with error bounds and we have to accept the admittedly weak definition given.

Validation cases are described in Appendix B and summarised in Table 4-1. As can be seen the validation cases are taken from calibration studies in various projects. We thus follow the definition of validation given above.

Table 4-1. Compilation of validation cases.

Case	Project (Reference)	Comments
A site scale validation (Case V1)	Impact of the tunnel construction on the groundwater system at Äspö. Task #5 Svensson et al. (2002).	Calibration focuses on: - Groundwater table - Pressure in boreholes - Kinematic porosity - Water composition Code: PHOENICS
A laboratory scale validation (Case V2)	A laboratory scale analysis of flow and salinity distribution in the Äspö area, Svensson (1999).	Calibration focuses on: - Fracture transmissivities - Pressure in boreholes - Conductivity distributions Code: PHOENICS
A repository scale validation (Case V3)	Prototype Repository Groundwater flow, pressure and salinity distributions around the Prototype Repository. Continuum model No1, Svensson (2001).	Calibration focuses on: - Tunnel inflows (skin) - Pressure in boreholes - Conductivity distributions Code: DarcyTools
An experimental scale validation (Case V4)	Simulation of tracer transport considering both experimental and natural, i.e. long, time scales, Svensson (2003).	Calibration focuses on - PARTRACK - Sorbing and non-sorbing tracer retention. Code: DarcyTools

5 Concluding remarks

It is clear from Section 2 that the process of confidence building is complex and involves many aspects. The bottom line is if a particular simulation is credible or not. The computer code, and its verification and validation, is of course a key factor when credibility is judged, but the user of the code is also important. CFD simulations are still far from routine calculations and the modeller normally takes a number of decisions when formulating the problem conceptually and mathematically. The "credibility of the modeller" is hence also a factor to consider.

The number and range of verification and validation cases presented is, in the author's view, a good indication of the qualities of DarcyTools. More cases are not urgently needed; real world applications would however contribute to the confidence building. As DarcyTools is one of the codes used for the SKB Site Investigations, such applications will soon be available.

6   References

AIAA Journal. 1998. Special issue, Vol. 36, No. 5, May 1998.

Barten, W. 1996. Linear response concept combining advection and limited rock matrix diffusion in a fracture network transport model. Water Resources Research, Vol. 32, No. 11, Pages 3285-3296.

Bour O., Davy P., 1998. On the connectivity of three-dimensional fault networks. Water Resources Res. 34 (10), 2611-2622.

Casey M., Wintergerste T. 2000. Best practice guidelines. ERCOFTAC Special Interest Group on "Quality and Trust in Industrial CFD".

Charlaix E., Guyon E., Rivier N., 1984. A criterion for percolation threshold in a random array of plates. Solid State Communications 50 (11), 999-1002.

Claesson J., Hellström G. and Probert T. 1992. Buoyancy flow in fractured rock with a salt gradient in the groundwater. A second study of coupled salt and thermal buoyancy. SKB Technical Report TR92-41.

Cvetkovic, V., Selroos, J.O., Cheng, H. 1999. Transport of reactive tracers in rock fractures. J. Fluid Mech. Vol. 378, pp. 335-356.

Domenico P. A. and Schwartz F. W., 1990. Physical and Chemical Hydrogeology. John Wiley& Sons, New York, USA.

Elert, M., Svensson, H. 1999. Äspö Hard Rock Laboratory. Deconvolution of breakthrough curves from TRUE-1 tracer tests (STT-1 and STT-1b) with sorbing tracers. Äspö Task Force, Task 4E. SKB, IPR-99-35.

Fetter C. W., 1994. Applied Hydrogeology. Third edition. Prentice Hall, Englewood Cliffs, NJ 07632.

Follin S., Hermansson J., 1996. A discrete fracture network model of the Äspö TBM tunnel rock mass. SKB Report AR D-97-001.

Forsmark T and Rhén I., 1999. Prototype Repository. Hydrogeology interference test campaign 1 after drill campaign 3. SKB International Progress Report IPR-00-07.

Forsmark T., Rhén I., Andersson C., 2001. Prototype Repository. Hydrology-deposition- and lead-through boreholes: Inflow measurements, hydraulic responses and hydraulic tests. SKB IPR-00-33.

Gurban I, Laaksoharju M, Andersson C. 1998. Influences of the tunnel construction on the groundwater chemistry at Äspö. SKB Technical note:TN-98-16g.

Haggerty R., McKenna S. A. and Meigs C., 2000. On the late-time behavior of tracer breakthrough curves. Water Resour. Res., Vol. 36, No.12, pp 3467-3479.

Hellsröm G., Tsang C-F and Claesson J. 1988. Buoyancy flow at a two-fluid interface in a porous medium: Analytical studies. Water Resources Research, Vol. 24, No. 4, Pages 493-506.

Hydrocoin. 1988. The international hydrocoin project. OECD, Paris 1988.

La Pointe P. R., 1994. Evaluation of stationary and non-stationary geostatistical models for inferring hydraulic conductivity values at Äspö. SKB Technical Report TR-94-22.

Neretnieks, I. 2002. A stochastic multi-channel model for solute transport - analysis of tracer tests in fractured rock. Journal of Contaminant Hydrology 55(3-4): 175-211.

Neuman, S. P. 1975. Analysis of pumping tests data from anisotropic unconfined aquifers considering delayed gravity response. Water Resour Res. 11(2), 329-342.

Painter S., 1999. Long-range spatial dependence in fractured rock. Empirical evidence and implications for tracer transport. SKB

Probert T. and Claesson J. 1997. Heat as a tracer in fractured rock. SKB Progress Report HRL-97-29.

Rhén I. (ed), Gustafson G., Stanfors R., Wikberg P., 1997. Äspö HRL -Geoscientific evaluation 1997/5. Models based on site characterization 1986-1995. SKB Technical Report TR-97-06.

Rhén I. and Forsmark T., 2000. Äspö Hard Rock Laboratory. High-permability features (HPF). SKB International Progress Report IPR-00-02.

Robinson P.C., 1984. Numerical calculations of critical densities for lines and planes. J.Phys. A:Math. Gen. 17, 2823-2830.

Sahimi M., 1995. Flow and transport in porous media and fractured rock. VCH Verlagsgesellschaft mbH, Weinheim.

Segol G., 1994. Classic Groundwater Simulations. PTR Prentice Hall, New Jersey, USA.

Spalding D.B., 1981. "A general purpose computer program for multi-dimensional one- and two-phase flow". Math. Comp. Sim., 8, 267-276. See also: http://www.cham.co.uk.

Stigsson M., Outters N., Hermanson J., 2000. Prototype Repository. Hydraulic DFN model no.2, -Final draft-. Draft report.

Svensson U., 1999b. A laboratory scale analysis of groundwater flow and salinity distribution in the Äspö area. SKB Technical Report TR-99-24.

Svensson U., Laaksoharju M. and Gurban Ioana., 2002. Impact of the tunnel construction on the groundwater system at Äspö. Task 5, Äspö Task Force on groundwater flow and transport of solutes. SKB Report in print.

Svensson U., Kuylenstierna H-O., Ferry M. 2004. DarcyTools, Version 2.1 - Concepts, Methods, Equations and Demo Simulations. SKB report in progress.

Svensson U. and Ferry M. 2004. DarcyTools, Version 2.1 – User's Guide. SKB report in progress.

Tóth, J. A. 1963. A theoretical analysis of ground-water flow in small drainage basins. Journal of Geophysical Research 68, no. 16:4795-4811.

Versteeg H.K., Malalasekera W., 1995. An introduction to computational fluid dynamics. The finite volume method. Longman Group Ltd.

Zhan H. and Zlotnik V. A. 2002. Groundwater flow to a horizontal or slanted well in an unconfined aquifer. Water Resources Research, Vol. 38, No. 7, 10.1029/2001WR000401.

APPENDIX A   Verification cases

ONE-DIMENSIONAL TRANSIENT DIFFUSION (Case A1)

1 Introduction

The simplest possible test case is perhaps the one-dimensional transient diffusion problem. In order to relate this problem to fractured rocks, we will chose diffusion coefficients and dimension that describe "diffusive exchange with a dead-end fracture". However, the chosen simulation parameters are of course of no significance for the test problem, i.e. we may equally well study the non-dimensional problem.

The situation considered is outline in Figure A1:1. Initially the concentration in the 1D domain is 1.0. At time = 0.0 the concentration at the left boundary is suddenly reduced to 0.0, while the right boundary is of the zero flux type.

The analytical solution to this problem can be found in Versteeg and Malalasekera (1995):

$$C(x,t) = C_0 \frac{4}{\pi} \sum_{n=1}^{\infty} \frac{(-1)^{n+1}}{2n-1} \exp\left(-\alpha \lambda_n^2 t\right) \cos\left(\lambda_n x\right) \tag{A1:1}$$

where $\lambda_n = \frac{(2n-1)}{2L}\pi$ and α denotes diffusion coefficient, t time and C_0 initial concentration.

The objective of the test case is to verify that DarcyTools can predict one-dimensional transient diffusion correctly.
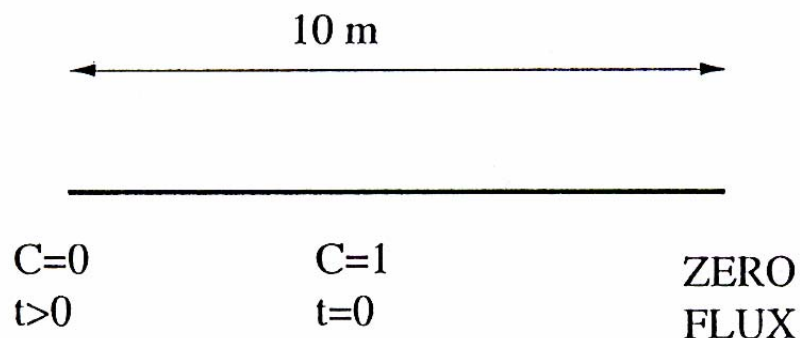

Figure A1:1. *One-dimensional transient diffusion. Outline of situation studied.*

2 Numerical simulation

Three different diffusion coefficients will be evaluated. With the coefficients and dimensions chosen, see Table A1:1, the time scale of the problem will be about 10^4 years.

Simulation parameters are summarised in Table A1:1.

Table A1:1. Simulation parameters.

Domain	1D, 10 metres
Initial condition	c = 1.0
Boundary conditions	$c = 0$ at $x = 0$, $\partial c / \partial x = 0$ at $x = L$, for $t > 0$
Diffusion coefficients	Varied: 0.5, 1.0 and 2.0×10^{-10} m²/s
Grid	Space: NX = 200 uniform Time: $\Delta t = 5$ years, uniform

3 Results / Discussion

The concentration at $x = L$ was used for the comparison with the analytical solution, see Figure A1:2. A near perfect agreement is found.

4 Conclusion

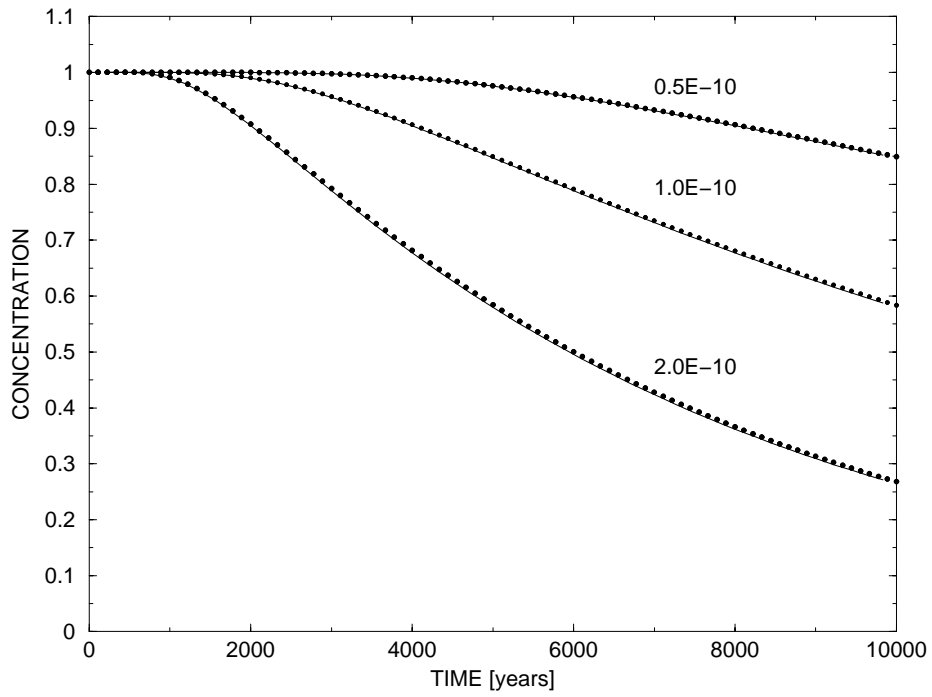DarcyTools can calculate one-dimensional transient diffusion, with high accuracy.

Figure A1:2. *One-dimensional transient diffusion. Comparison of the concentration at* *x = L as given by the analytical solution (* ——— *) and DarcyTools (* ● ● ● *).*

ONE-DIMENSIONAL STEADY ADVECTION / DIFFUSION (Case A2)

1 Introduction

The situation studied is outlined in Figure A2:1. A steady flow, with a velocity of 2 m/s along the *x*-axis, is convecting a property ϕ. The property ϕ is subject to sources and sinks and is also diffused along the *x*-axis. The steady state distribution of ϕ is the solution of interest. This distribution is given by the following equation:

$$\frac{\partial}{\partial x}(\rho u \phi) = \frac{\partial}{\partial x}\left(\Gamma \frac{\partial \phi}{\partial x}\right) + s \qquad (A2:1)$$

where *u* denotes velocity, Γ diffusion coefficient and *s* sources and sinks.

This test case has been presented in the book by Versteg and Malalasekera (1995), where also an analytical solution is given. An attempt was made to calculate the ϕ-distribution from the analytical solution. This was however not successful; one possible reason for this is that there may be a printing error in the equations presented. The analytical solution was therefore taken from the graphical presentation, given by Versteg and Malalasekera (1995).

The objective of the test case is to see how well DarcyTools predicts the ϕ distribution when both convection and diffusion are significant in the flow direction.
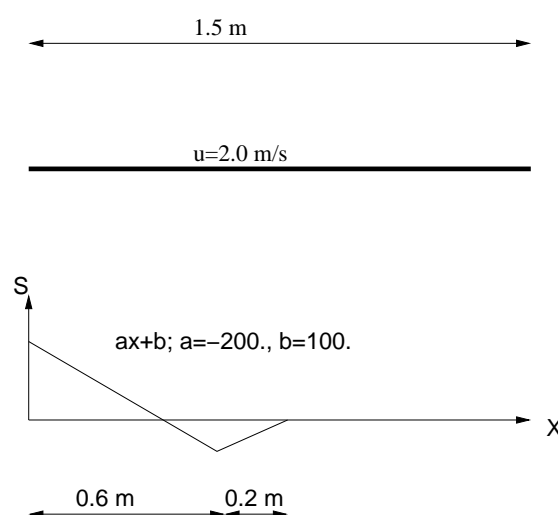

Figure A2:1. *The situation considered.*

2 Numerical simulations

Some of data specifying the problem are given in Figure A2:1; a complete account is given in Table A2:1.

Three grid sizes will be tested in order to evaluate if a gridindependent solution can be obtained.

Table A2:1. Simulation parameters.

Domain	1D, Lenght = 1.5 metres
Velocity	2.0 m/s, uniform
Boundary Conditions	$\phi = 0$ at $x = 0$, $d\phi / dx = 0$ at $x = L$
Source/Sink	$a = -200$, $b = 100$ (see Figure A2:1)
Properties	$\Gamma = 0.03$ kg/m/s, $\rho = 1$ kg/m^3
Grid	Varied: NX = 100, 200 and 300, uniform

3 Results / Discussion

A comparison with the analytical solution and a grid independence test can be found in Figure A2:2.

Starting with the comparison with the analytical solution, it is seen that a close agreement is achieved. As mentioned above, the analytical solution was taken from a figure given by Versteg and Malalasekera (1995) and there is course some uncertainty involved in that procedure. The agreement is thus concluded to be acceptable.

The grid independence test shows that NX = 100 is not enough to generate a grid independent solution. Solutions for NX = 200 and 300 are however very close. The reason for the fairly fine discretisation needed is probably the use of a hybrid difference scheme. This scheme has been chosen for its many favourable properties (conservative, stable, etc) but it is a first-order scheme in terms of the Taylor series truncation error. In practical groundwater simulations it is however not expected that "diffusion in the flow direction" is a significant process and there is hence no strong reason to abandon the hybrid scheme, based on the results from the present test case.

4 Conclusion

DarcyTools predicts a correct steady state distribution of a scalar, subject to the combined effects of convection and diffusion. A fairly large number of grid cells is however needed to obtain a grid independent solution.
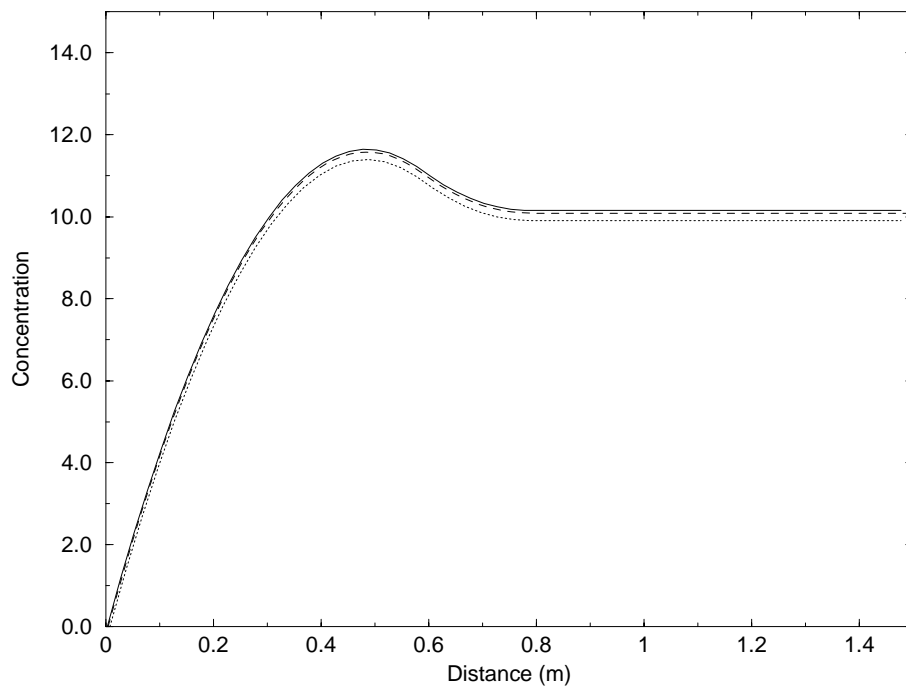
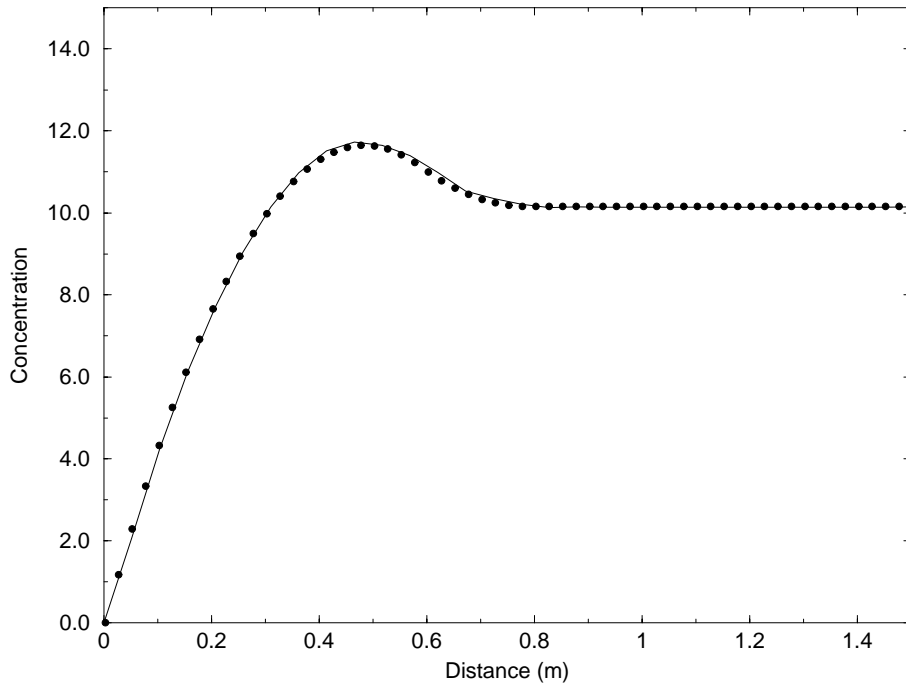***Figure A2:2.*** *Comparison with analytical solution (top) and grid independence test.*
Symbols top: Analytical solution
                            ● ● ● ● Numerical solution
           bottom: ———— Numerical solution NX = 300
                  – – – – – Numerical solution NX = 200
                  ············ Numerical solution NX = 100

A8

TWO-DIMENSIONAL PRESSURE PROBLEM (Case A3)

1 Introduction

In this test the pressure solver in DarcyTools will be used to predict the flow through a channel that has a complex pattern, see Figure A3:1. The channel will be given a much higher conductivity than the background and the flow through the domain will hence be restricted to the channel. A pressure drop from the lower left corner to the upper right is prescribed through the boundary conditions. In the channel a linear pressure drop is the correct solution.

The objective of the test case is to verify that DarcyTools predicts a correct flow and pressure distribution for the situation described.
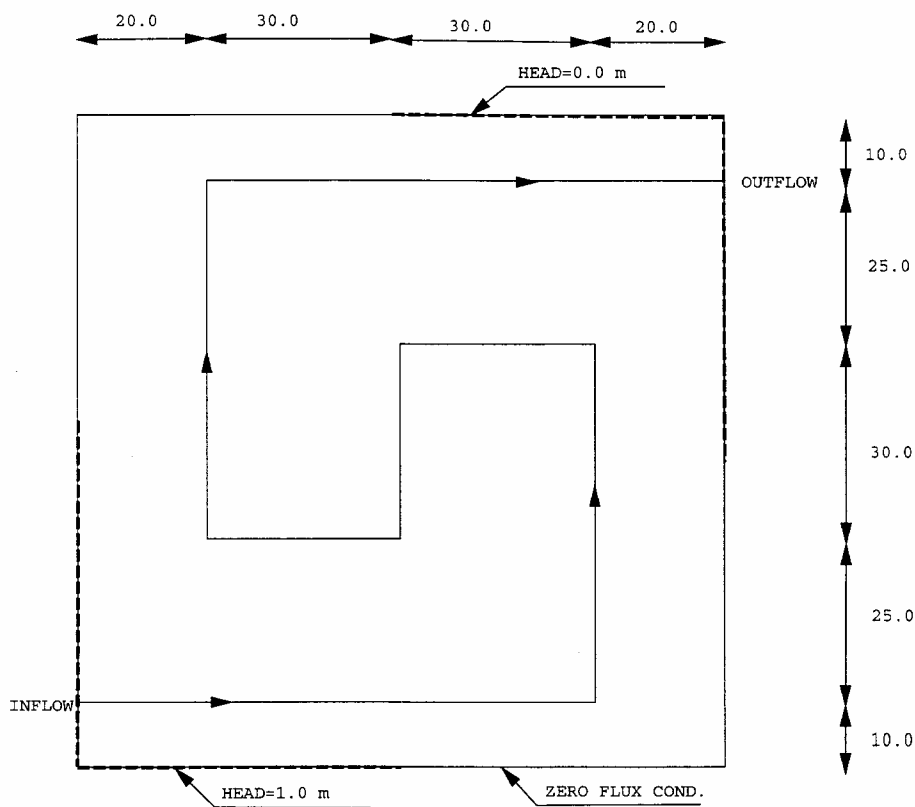

Figure A3:1. *Flow through a complex channel. Outline of situation studied and coordinates for the centre line of the channel.*

2 Numerical simulation

The channel will be implemented by simply specifying the relevant cell wall conductivities. The general method in DarcyTools for describing a fracture in a continuum model (GEHYCO) will hence not be used here; a number of other test cases are devoted to GEHYCO.

As we follow the gridsystem, the length of the channel will not be exactly the same as shown in Figure A3:1 (360 metres in the figure as compared to 359 in the numerical representation). This will be taken into account when calculating the through-flow analytically, Q_a.

Most of the test case specification is given in Figure A3:1; same additional data are given in Table A3:1.

Table A3:1. Simulation parameters.

Domain	100 x 100 x 1 metres
Conductivity (channel)	10^{-5} m/s
Grid	$\Delta = 1.0$ m, uniform

3 Results / Discussion

The through-flow was predicted with an accuracy of 5 correct digits ($Q_a / Q_{calc} = 1.00001$, where Q_{calc} is the predicted flow).

The calculated pressure distribution is shown in Figure A3:2. As can be seen a complex pattern is obtained, but the pressure drop along the channel is linear, as expected.

4 Conclusion

It is concluded that the flow through a channel that runs along the coordinate directions can be calculated with high accuracy.
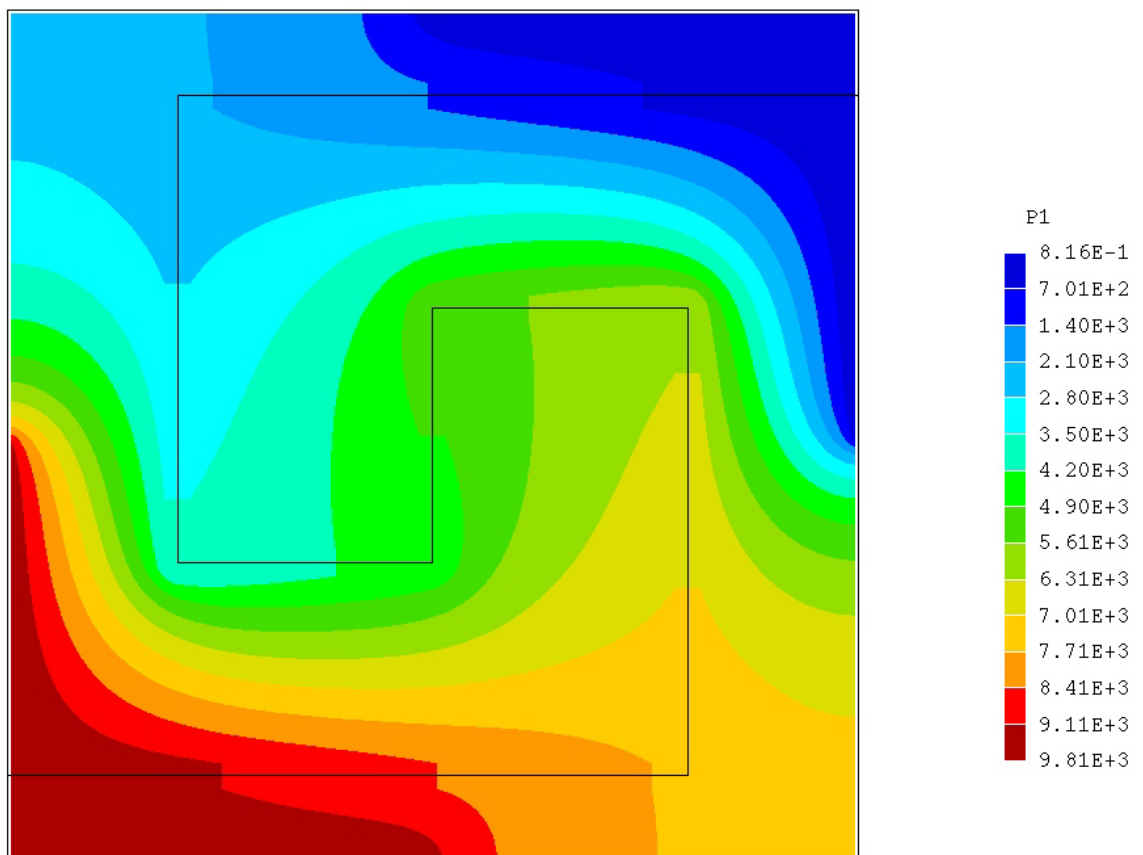

Figure A3:2. *A channel in a 2D domain. Pressure distribution. The solid line indicates the centreline of the fracture.*

TESTS OF GRIDS
(Case A4)

1 Introduction

In this test case various grid options in DarcyTools will be evaluated. For a common situation, see Figure A4-1, different grids will be used and the results compared. It is thus an intercomparison between model results, as no analytical solution is available for the situation considered.

The situation outlined in Figure A4-1, is an idealised case of an island in a salt water sea. The salinity at the vertical boundaries is prescribed to vary from 1.0% at the top boundary to 3.0% at the bottom. At the top boundary the salinity is 1% except for the square where a fixed inflow of fresh water (0% salinity) is prescribed. This will give a fresh water lens below the "island".

The objective of the test case is to demonstrate that similar solutions are obtained for a range of different grid arrangements.
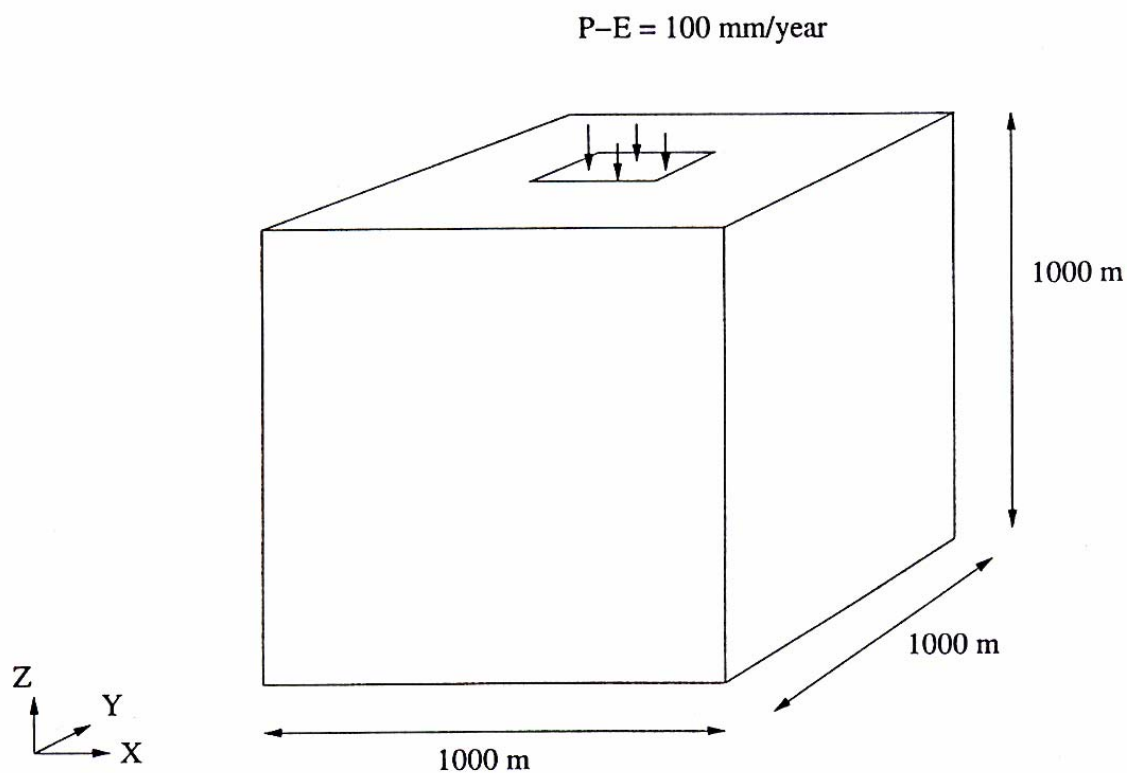

Figure A4-1. *Outline of situation studied.*

2 Numerical simulations

The input data are given in Table A4:1, see also Figure A4-1. The following grid types will be tested:

- Cartesian, with constant Δ

- BFC:s, i.e. simplified, or floating, BFC grid

- BFC

- Cartesian with embedded grid

The grids will be plotted together with the simulation results.

Table A4:1. Simulation parameters.

Domain	$1 \times 1 \times 1 \text{ km}^3$
Boundary conditions	Top: Prescribed pressure and salinity below "sea" (1%), prescribed mass flow $\left(P - E = 100 \text{ mm/year}\right)$ with zero salinity below "island".
	Vertical and bottom: Prescribed salinity and pressure. Salinity 1% at ground level and 3% at bottom
Properties	Conductivity = 10^{-7} m/s Diffusivity = 0.0
Grid	NX = NY = NZ = 50 m Δ varied, see result section

3 Results / Discussion

We will study the salinity distribution in a *xz*-plane through the island (*y* = 500 m), see Figure A4-1.

The salinity distribution as calculated in the Cartesian grid is shown in Figure A4-2. This simulation will be regarded as a reference, to be compared with solution obtained on other grids. For this purpose we will select the isolines 0.1 and 2.0% salinity; this reference figure is also shown in Figure A4-2.

The first comparison concerns the BFC:s grid, see Figure A4-3. The grid is distorted in the interior, but in agreement with the Cartesian grid at the boundaries. It is concluded that the BFC:s grid gives the same salinity distribution as the Cartesian grid.

Next we study the BFC grid solution, see Figure A4-4. Now both the vertical and horizontal grid lines are distorted in the interior. The solution is however in good agreement with the Cartesian one.

Finally an embedded grid case is tested, see Figure A4-5. As can be seen both the parent and embedded grid are of the Cartesian type. Once again we find a good agreement with the reference solution.

Many more grid types and combinations of embedded grids can be handled in DarcyTools, for example a Cartesian grid with non-uniform Δ or an embedded grid which is of different type from the parent grid. More tests can, and perhaps should, hence be done.

4 Conclusion

For the grids tested a consistency in the predicted results has been demonstrated. More cases may be needed to test all grid options in DarcyTools.
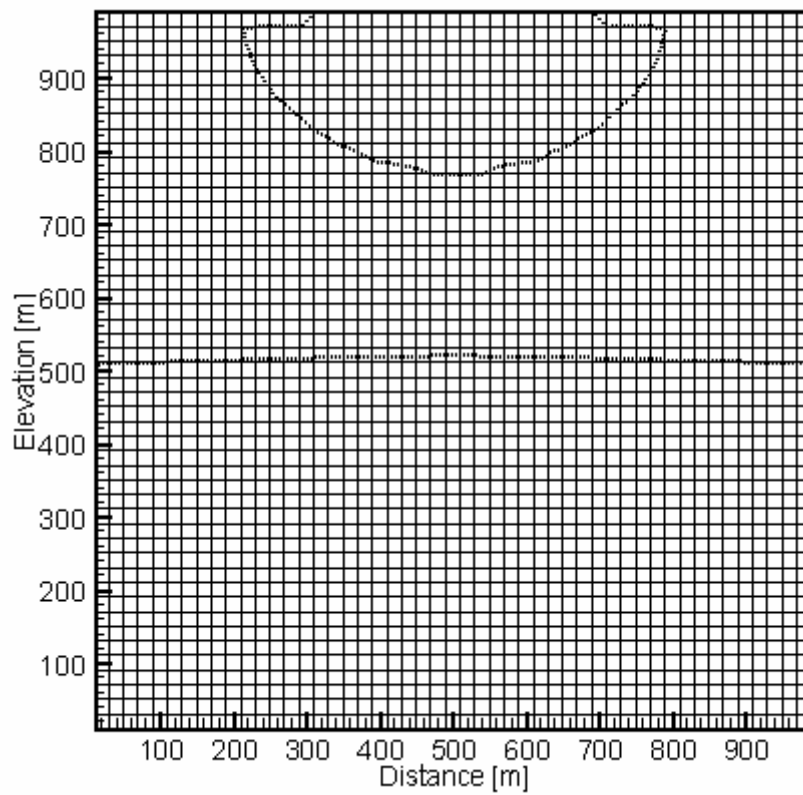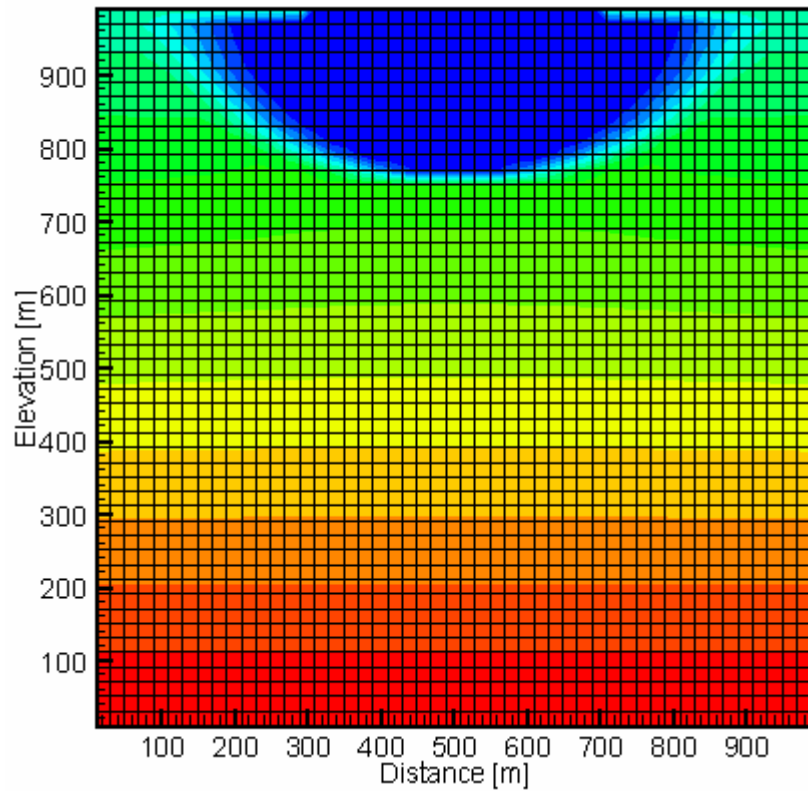
Figure A4-2. *Cartesian grid. Salinity distribution (top) and reference figure.*
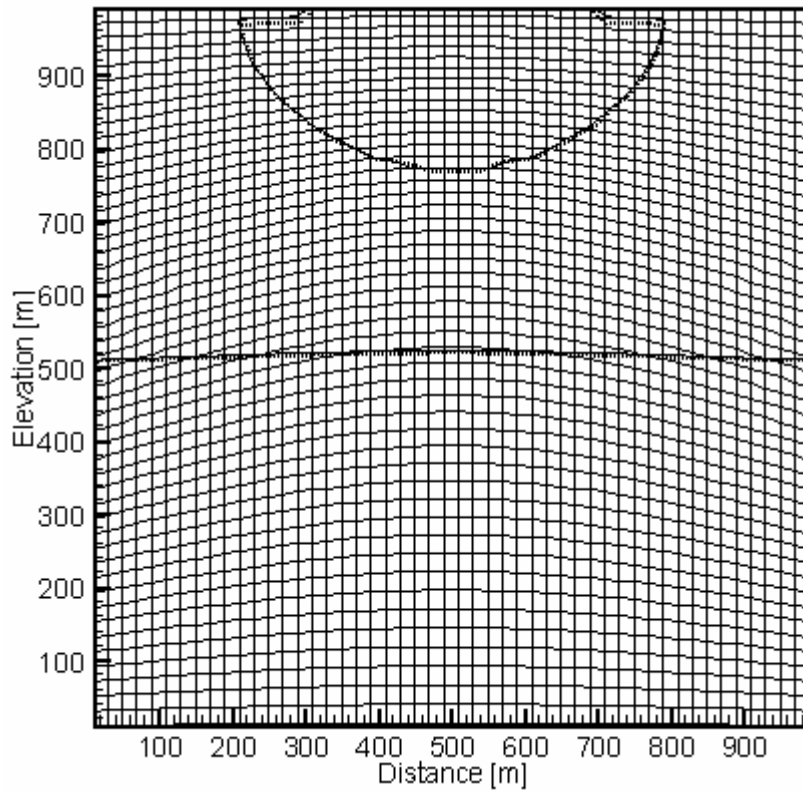
Figure A4-3. BFC:s grid. Dotted lines represent the solution on the Cartesian grid, solid line the BFC:s solution.
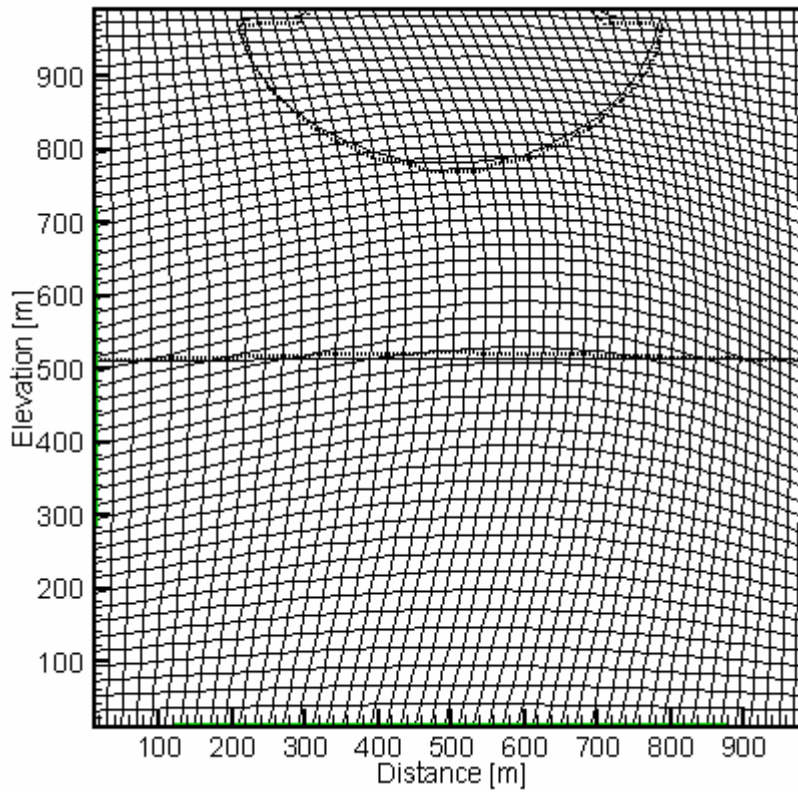

Figure A4-4. BFC grid. Dotted lines represent the solution on the Cartesian grid, solid the line the BFC solution.
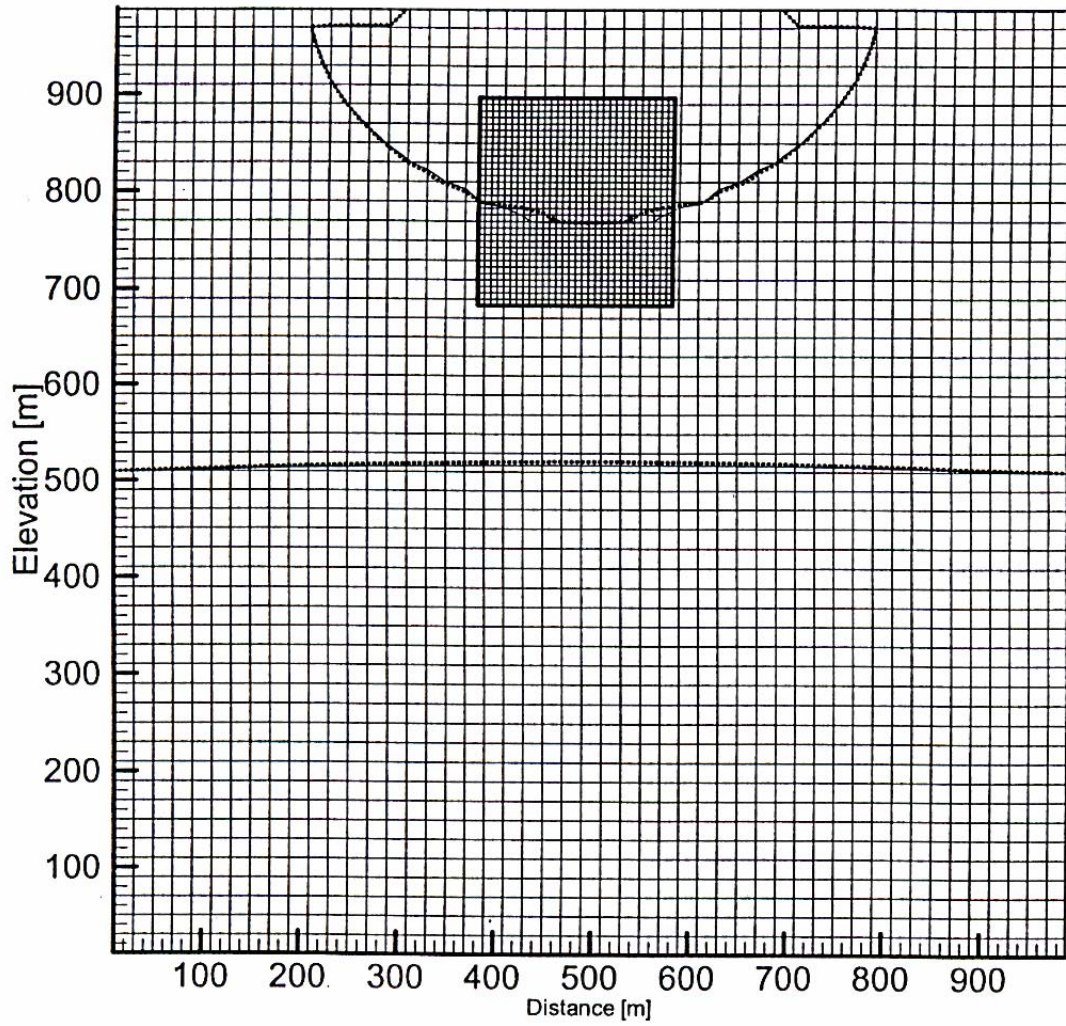
Figure A4-5. *Embedded grid. Dotted lines represent the solution on the Cartesian grid, solid line the embedded grid solution.*

TEST OF PRESSURE-SALINITY COUPLING (Case A5)

1 Introduction

The situation considered in Case A4, will in this test be used to study some properties of the coupled pressure-salinity option available in DarcyTools. For a Cartesian and a BFC:s grid the solution and convergence properties will be compared with the uncoupled solution.

The objective of the test is to evaluate if the two solution techniques give the same results and to compare execution times.

2 Numerical simulation

All data were introduced in Case A4 and will not be repeated here.

Four cases will be run and the development of the pressure and salinity in a monitoring point will be analysed. The monitoring point is chosen at $x = y = 500$ metres, at a depth of about 250 metres; this is right below the fresh water lens.

3 Results / Discussion

The development of pressure and salinity in the monitoring point can be studied in Figure A5-1 (Cartesian grid) and A5-2 (BFC:s grid). The horizontal line in the figures indicates the fully converged solution; as can be seen the uncoupled solution for salinity did not reach this value in 250 sweeps. In order to demonstrate that the same solution is eventually reached by the two solution methods, the uncoupled solution was continued till the value in the monitoring point was within $\pm 1\%$ of the final value. The number of sweeps needed to reach this convergence criterion can be studied in Table A5-1. As can be seen more than 500 sweeps were needed for the uncoupled solution method.

The first impression of these tests is that the coupled solution is superior to the uncoupled one. However, one should note that the coupled solution requires roughly three times longer execution time per sweep. If this is taken into account we find that the coupled solution is about twice as fast as the uncoupled one.

This test is far from complete and should only be considered as a first indication. If more tests are to be done the following aspects should be evaluated:

- MIGAL provides a number of settings that influence the convergence speed. A range of these needs to be evaluated.

- Other situations (for example Henry's problem) should be included, to see if the convergence statistics are general.

4 Conclusion

For the problem considered, including two grid types, the coupled solution was found to be roughly twice as fast as the uncoupled one.

Table A5-1. Convergence statistics. Number of sweeps needed to reach an error limit of ±1% of the converged value in a monitoring point.

Case	Uncoupled		Coupled	
	Pressure	**Salinity**	**Pressure**	**Salinity**
Cartesian	138	432	27	104
BFC:s	109	600	21	144

Figure A5-1. *Convergence history in a monitoring point, for Cartesian grid. Salinity (top) and pressure head. (- - - -) Uncoupled solution, (——) Coupled solution.*
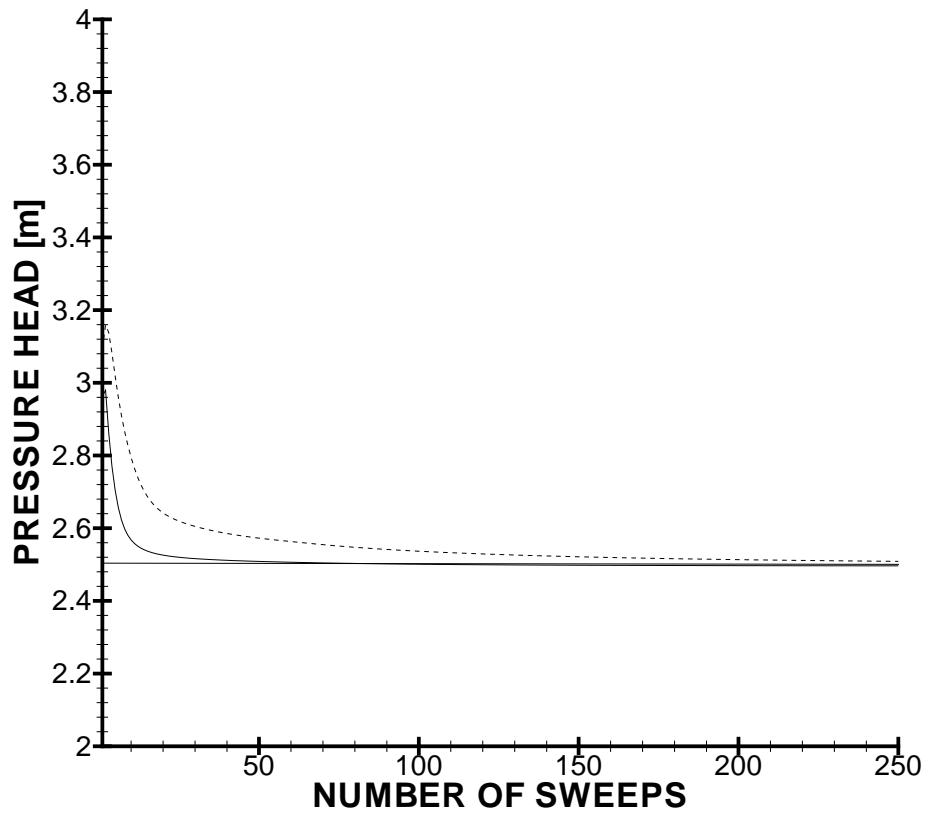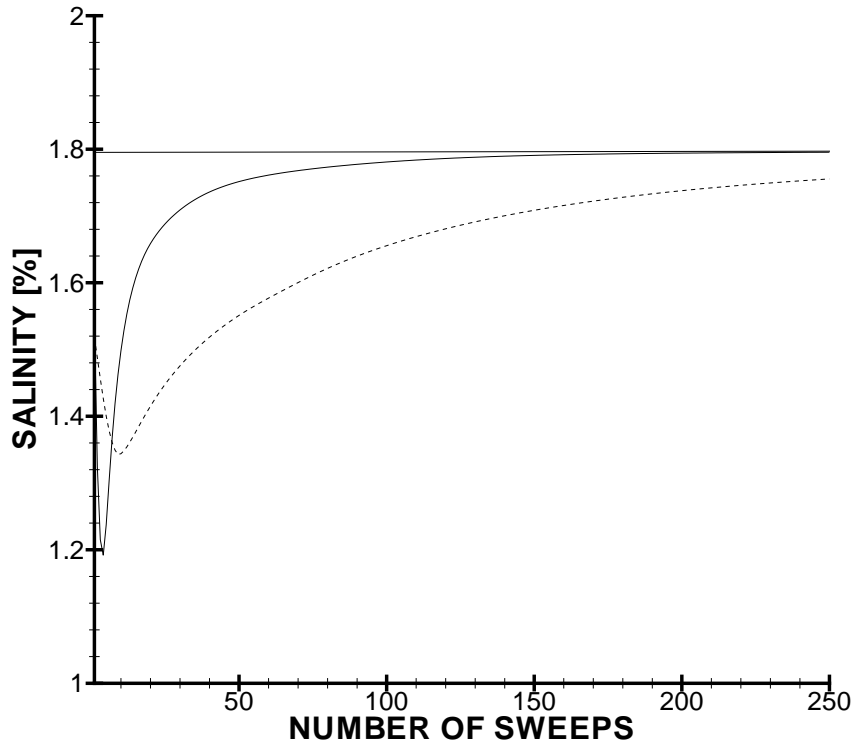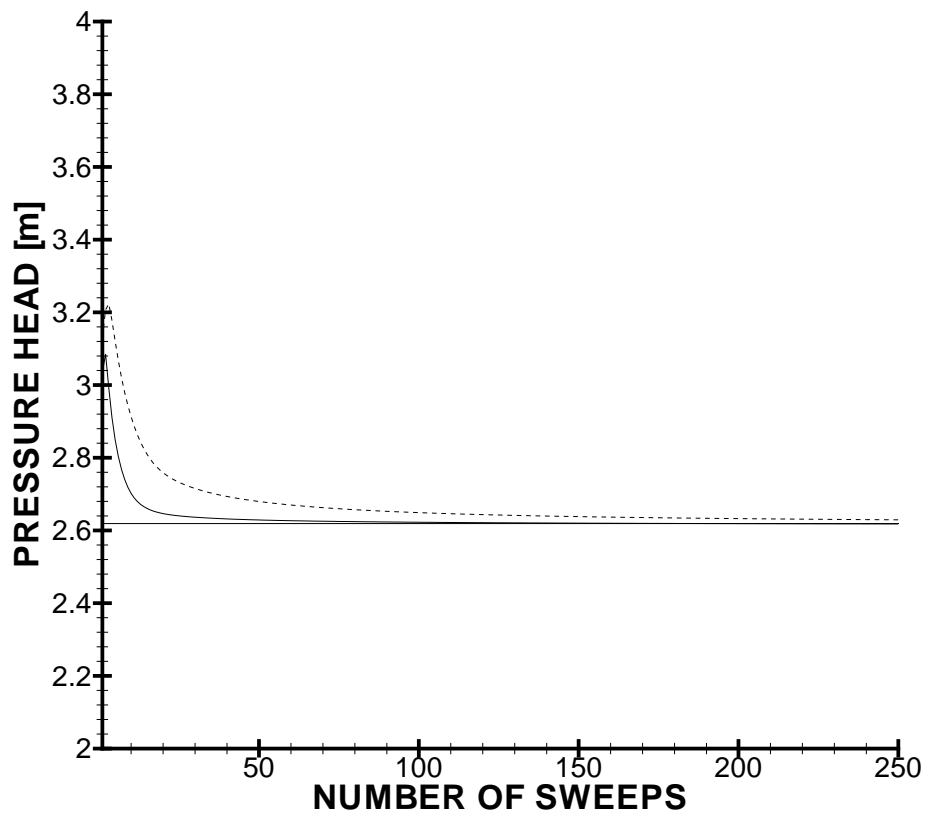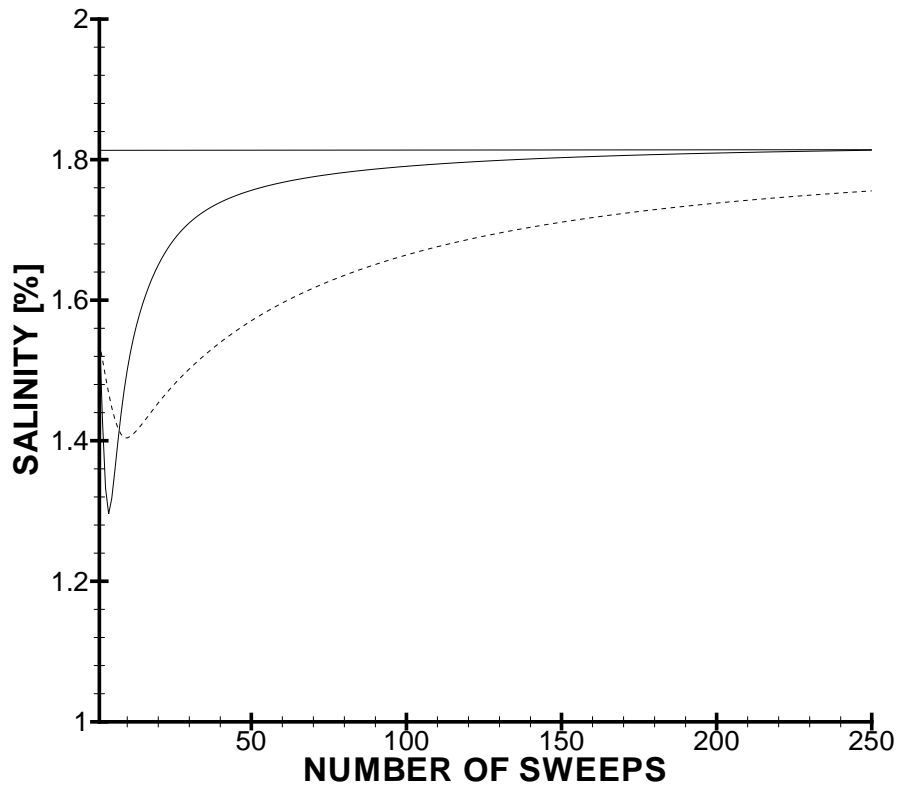
Figure A5-2. *Convergence history in a monitoring point, for BFC:s grid. Salinity (top) and pressure head. (----) Uncoupled solution, (———) Coupled solution.*

REGIONAL GROUNDWATER CIRCULATION, TOTH (1963) (Case B1)

1 Introduction

The natural ground water table often follows the topography. If one assumes that the ground water table coincides with the topography it is possible, under some further assumptions, to predict the ground water circulation.

Toth (1963) (as described in Fetter (1994)) provides an analytical solution for the case of a linear slope with an over-laying undulating sin-wave shaped upper boundary. This solution is illustrated in Figure B1:1.

The objective of this testcase is to compare the numerical solution by the analytical solution, as given in Figure B1. The comparison will only be qualitative.
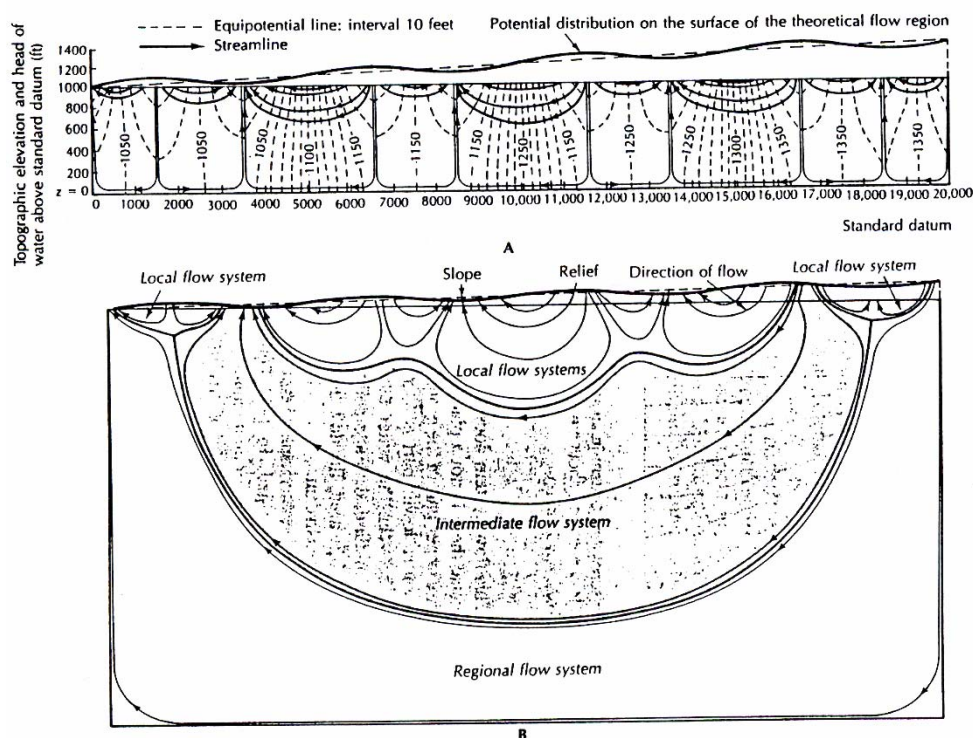
Figure B1-1. *The effect of increased basin depth is shown on these two figures. In Part A, the basin depth/length ratio is 1:20; in Part B, it is 1:2. The shallow basin has only local flow systems, whereas the deep basin has local, intermediate, and regional flow systems. The water-table configuration is the same for both basins. From Fetter (1994).*

2 Numerical simulation

A computational domain of length 20 km and depth 10 km is specified, i.e. a two-dimensional situation is studied.

The linear part of the slope has a total elevation of 400 metres, while the undulating part has an amplitude of 50 metres.

Further details are given in Table B1:1.

Table B1:1. Simulation parameters

Domain	2D, $20 \times 10 \left[km^2 \right]$
Boundary Conditions	Zero flux on all boundaries except for the top boundary where a fixed pressure, according to the topography, is prescribed.
Properties	Permeability $= 2 \times 10^{-16} \left[m^2 \right]$ Porosity $= 10^{-3}$ Viscosity $= 2 \times 10^{-3} \left[kg / ms \right]$ Density $= 1\,000 \, [kg/km^3]$
Grid	Uniform, $NX = 200$, $NZ = 100$

3 Results / Discussion

The predicted ground water circulation is shown in Figure B1:2, which can be compared with the lower figure in Figure B1:1. A close agreement is found.

4 Conclusion

A qualitative agreement with the solution by Toth (1963) has been demonstrated.
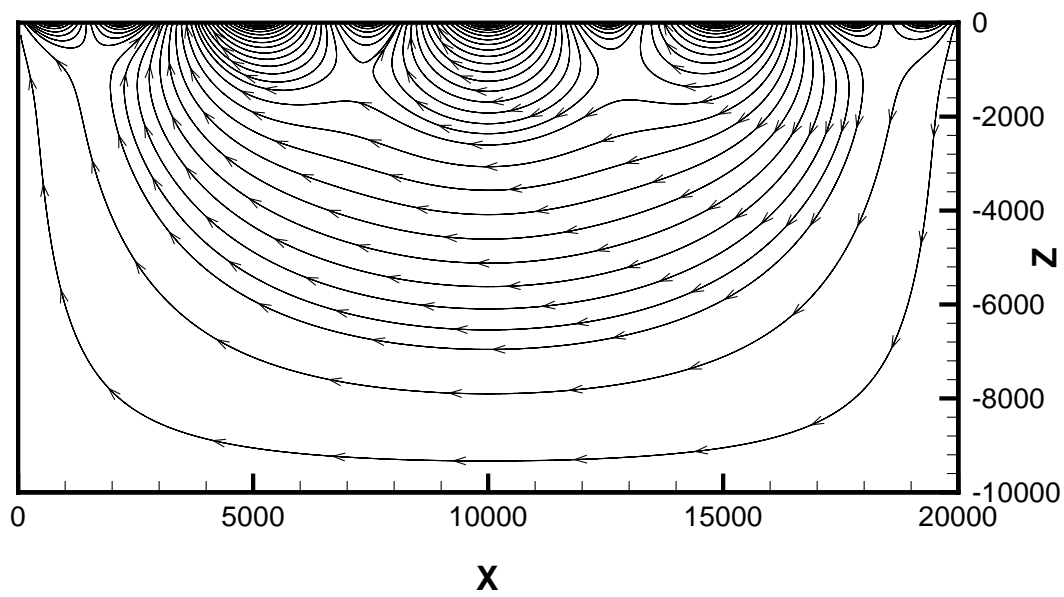
Figure B1:2. *Simulated groundwater circulation below an undulating topography.*

STEADY GROUND-WATER TABLE
(Case B2)

1 Introduction

The problem addressed is illustrated in Figure B2:1. In a two-dimensional vertical section the ground water elevation is sought. The groundwater flow may be forced by a pressure difference between the boundaries $(h_1 - h_2)$ or a vertical inflow at the top boundary, or both simultaneously. Only the steady state solution is to be considered.

The groundwater level, h, at distance, x, is given by (from Fetter, 1994):

$$h = \sqrt{h_1^2 - \frac{\left(h_1^2 - h_2^2\right)x}{L} + \frac{w}{K}(L - x)x} \qquad\qquad \text{(B2:1)}$$

where K is conductivity and other notation as given in Figure B2:1.

The objective of the test case is to verify that the algorithm used in DarcyTools (GRWT) predicts a groundwater table that is in agreement with the analytical solution.
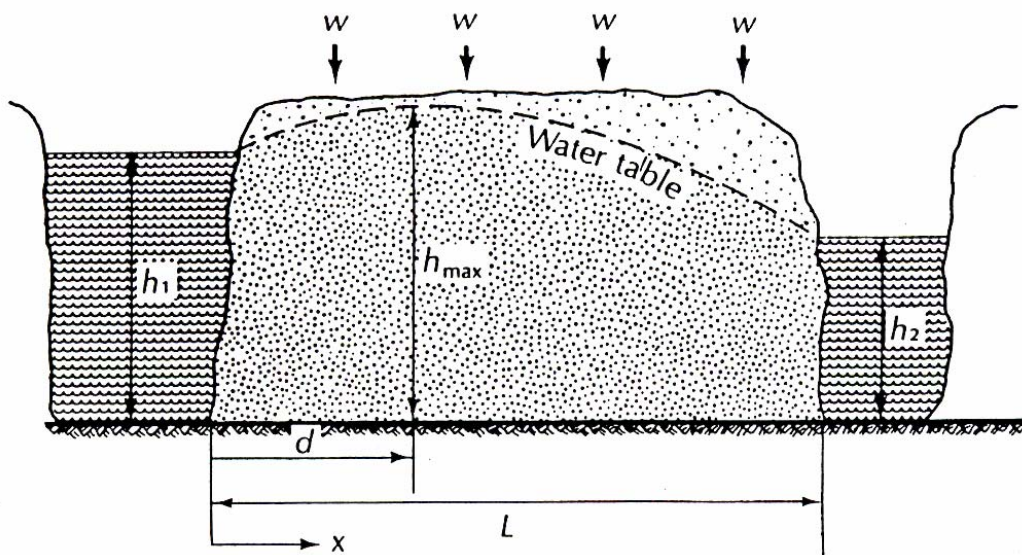
Figure B2:1. *The groundwater table problem. Illustration of the situation and notation used.*

2 Numerical simulation

The analytical solution is based on the Dupuit assumptions; a fact that needs to be considered in the numerical model set-up. One way to simulate the Dupuit assumptions is to introduce a higher conductivity in the vertical direction (as compared to the horizontal ones). This will make the vertical pressure distribution close to the hydrostatic one. A few test calculations revealed that increasing the vertical conductivity by a factor of 100 would "do the trick".

Predicting the groundwater table is of interest when the model domain includes the ground, i.e. the topography of the domain. For this reason we will try two grid types; cartesian and BFC:s.

Further details of the test case are given in Table B2:1.

Table B2:1. Simulation parameters.

Domain	100 (horizontal) x 50 (vertical) metres
Conductivity	10^{-8} (horizontal), 10^{-6} (vertical) m/s
Boundary Conditions	Bottom: zero flux Top: prescribed flux (base case 100 mm/year or 3.2×10^{-9} m/s) Left: hydrostatic pressure, $h_1 = 30$ m Right: hydrostatic pressure, $h_2 = 20$ m
Grid	$\Delta = 1$ m, uniform for cartesian grid, stretched for BFC:s.

3 Results / Discussion

The comparison with the analytical solution is shown in Figure B2:2. The agreement is very close and needs no further comments.

Figure B2:3 shows the results for the two grid types. The vertical coordinates were stretched with up to 10 metres (at the top boundary and $x = 50$ metres) using a sin-function in the x-direction and a linear expansion in the z-direction. The flow pattern and the level of the groundwater table are however the same for both grids, as expected.

4 Conclusion

The steady state groundwater table, as predicted by DarcyTools, is in good agreement with the corresponding analytical solution.
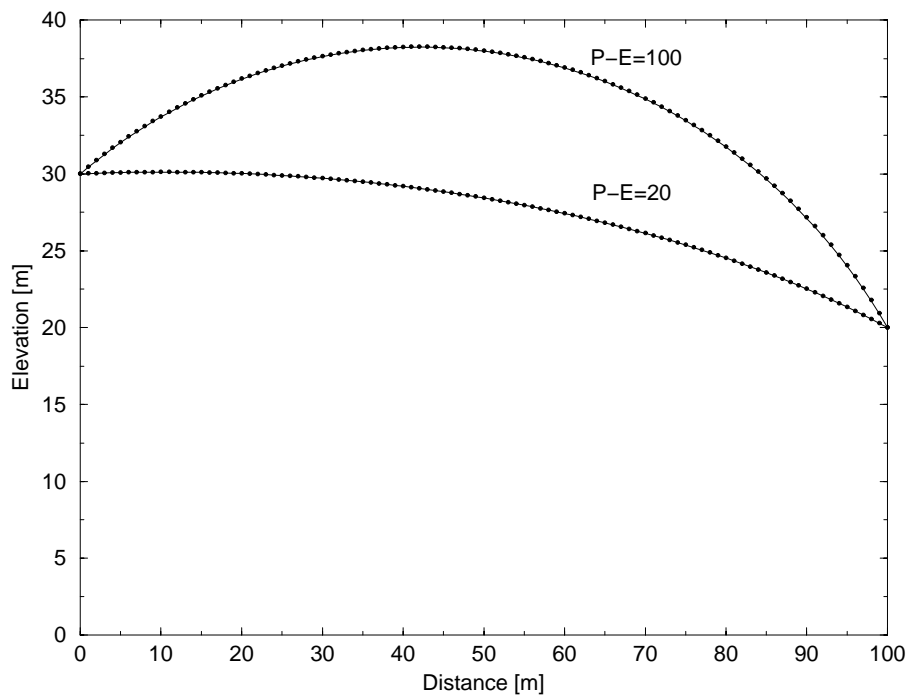
Figure B2:2. *Comparison between analytically (———) and numerically (• • •) calculated groundwater table for two P-E values.*
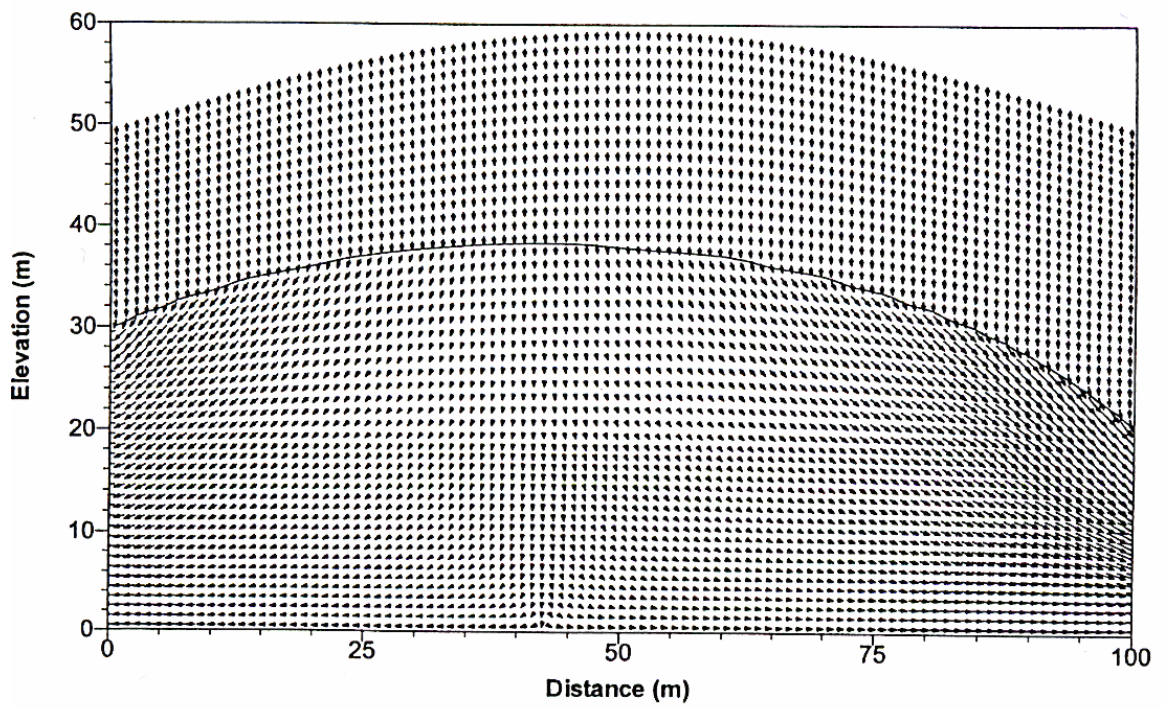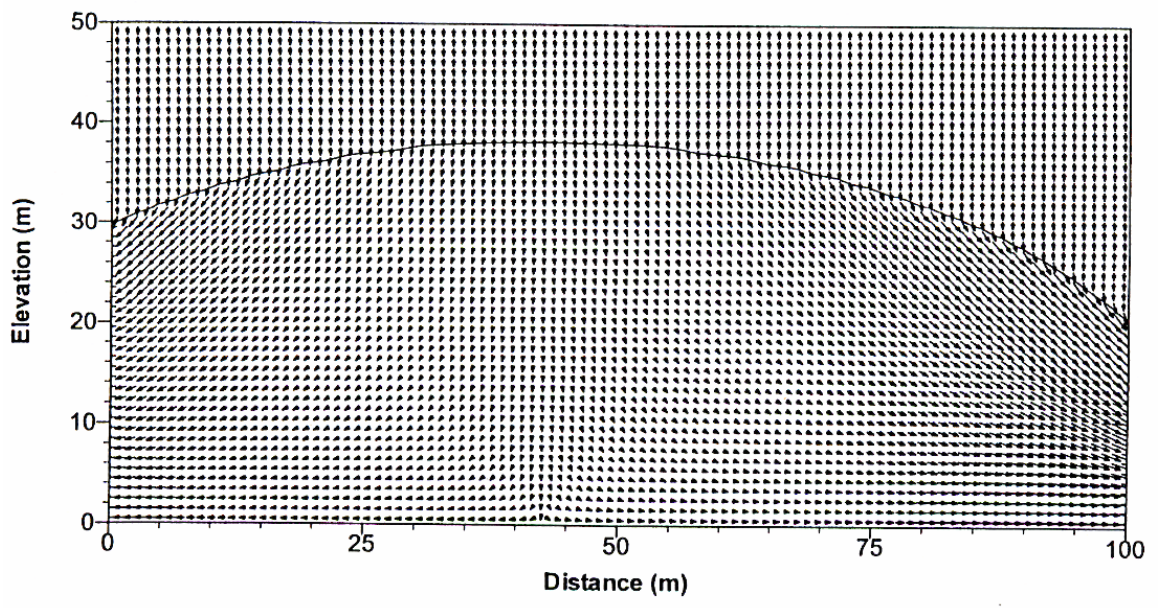
Figure B2:3. *Predicted flow and groundwater table for a cartesian (top) and a BFC:s grid.*

THEIS PROBLEM
(Case B3)

1 Introduction

Theis problem deals with the transient drawdown due to a well that is discharging at a constant rate, Q, from an areally extensive confined aquifer. The situation considered is outlined in Figure B1:1. Some further specification:

- The potentiometric surface is initially horizontal.

- There is no source of recharge to the aquifer.

- The aquifer is compressible and water is released instantaneously from the aquifer, as the head is lowered.

The analytical solution to this problem is given by the following relations (as presented in Fetter, 1994):

$$h_0 - h = \frac{Q}{4\pi T} \int_u^\infty \frac{e^{-u}}{u}\, du \qquad\qquad (B3:1)$$

The integral in Equation B1:1 can be replaced with an infinite series so that the Theis equation becomes:
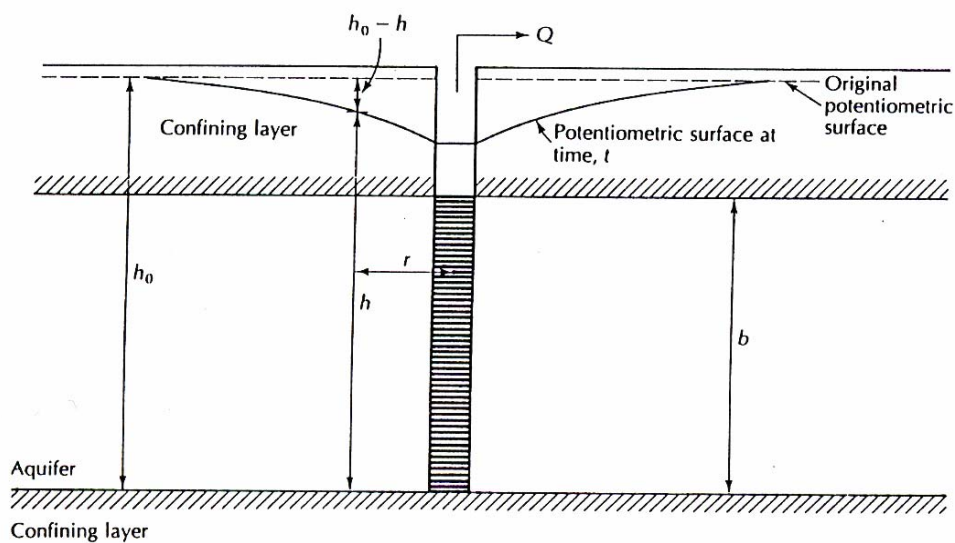
Figure B3:1. *Fully penetrating well pumping from a confined aquifer (from Fetter, 1994).*

$$h_0 - h = \frac{Q}{4\pi T}\left[-0.5772 - \ln u + u - \frac{u^2}{2\times 2!} + \frac{u^3}{3\times 3!} - \frac{u^4}{4\times 4!} + \cdots\right] \qquad \text{(B3:2)}$$

The argument u is given as

$$u = \frac{r^2 S}{4Tt} \qquad \text{(B3:3)}$$

where h is hydraulic head, T transmissivity, b the aquifer thickness, r radial distance and S aquifer storativity (product of the specific storativity and aquifer thickness).

In DarcyTools the relation between the porosity, ϕ, and pressure, p, is expressed as a state law (see main report). It can be shown that the two ways of expressing the storativity effect are related as follows:

$$\sigma_0 = S/(b\theta_0) \qquad \text{(B3:4)}$$

where σ_0 is the coefficient in the state law and θ_0 the porosity before pumping starts.

The objective of the testcase is to demonstrate that the storativity effect, as expressed in DarcyTools, is in accordance with Theis analytical solution.

2 Numerical simulations

The flow towards the well will be radial and the problem is hence best handled in polar coordinates. This system is however not provided in DarcyTools and we thus need to simulate the problem as a 2D problem (it is 1D in polar coordinates) in cartesian coordinates. Due to symmetry conditions we need however only to consider one quater of the domain and the "pumped cell" is hence placed in the lower left corner of the domain.

Further details of the simulations are given in Table B3:1.

Table B3:1. Simulation parameters.

Domain	2D, 1000 x 1000 x 10 metres
Transmissivity	10^{-3} m^2/s
Pumping rate	2.5×10^{-3} m^3/s
Storativity	Varied: 0.005, 0.01 and 0.02
Boundary conditions	Zero flux condition on all boundaries
Grid	Expanding in x and y directions, one cell in z-direction (NX = 100, NY = 100, NZ = 1). First cell in expansion 1.0 metre, the last one 15 metres. Time direction: Ten days of integration time, subdivided into 1000 steps.

3 Result / Discussion

The comparison between the analytical and numerical solution, for three storativity values, is shown in Figure B3:2. A point at a radius of 100 metres from the well was chosen for the comparison. It is clear from the figure that a near perfect agreement is achieved (the error is always less than 1%).

4 Conclusion

It has been shown that DarcyTools is in good agreement with the analytical solution of Thies problem.
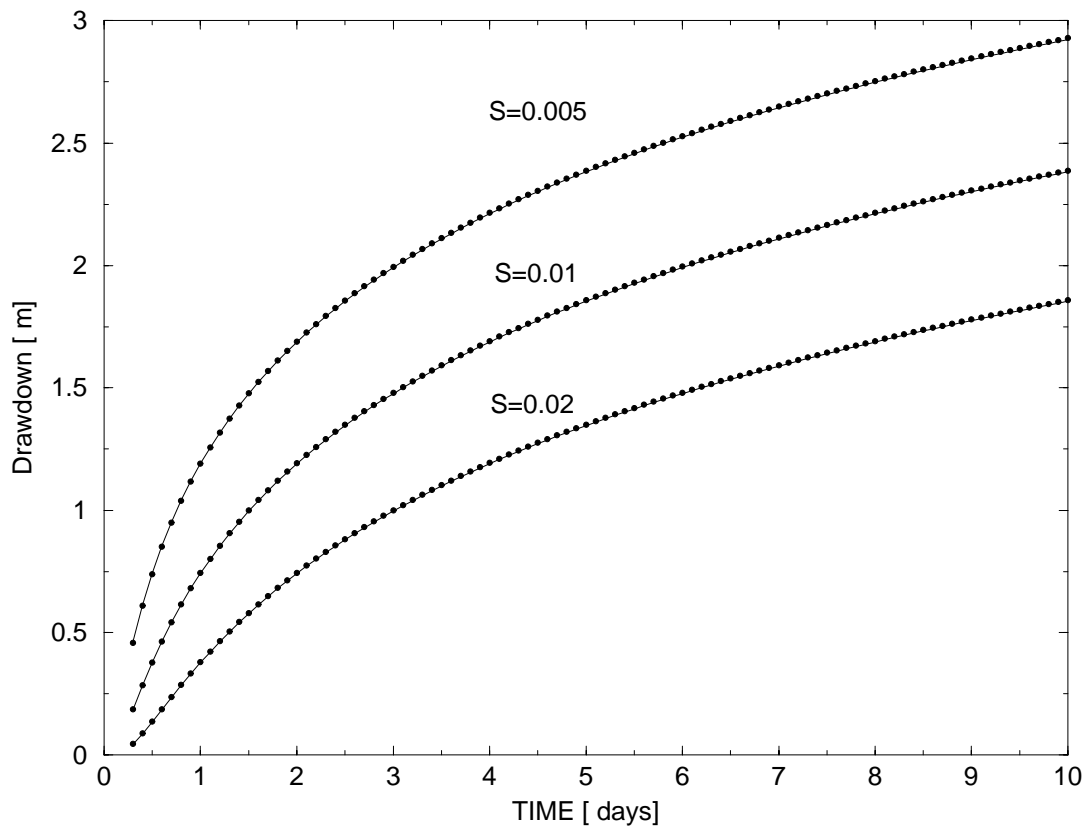

Figure B3:2. *Comparison between analytically (——) and numerically (•••) calculated drawdown at a radius of 100 metres from a well.*

TRANSIENT PRESSURE IN A BOREHOLE
(Case B4)

1 Introduction

This is Case 1 in the Hydrocoin series of test cases. From the Hydrocoin report we quote:

> Background
>
> This case concerns the transient flow of water from a borehole which penetrates a confined aquifer consisting of a homogeneous, isotropic permeable medium which is underlain by a single horizontal fracture. The case is shown schematically in Figure B4:1. The purpose of this test case is to verify the ability of codes to model transient tests in boreholes. Such tests are used to extract information about the hydraulic properties of a rock mass, namely the permeability of the rock matrix and the transmissivities of fractures.
>
> Thus a problem has been formulated involving unsteady flow from a finite-radius borehole in a finite cylindrical region of permeable rock with a single fissure. Also, the piezometric head in the borehole is assumed to change continuously from its initial to its final value. It should be borne in mind that this problem, as well as the other Level 1 cases, is explicitly designed to test numerical codes rather than to model a realistic experimental situation.
>
> Conceptual model
>
> A vertical borehole is assumed to penetrate a saturated permeable layer of rock which is underlain by horizontal fracture and confined between impermeable horizontal boundaries (see Figure B4:1). From symmetry considerations, this is seen to be equivalent to the case where a horizontal fracture bisects a permeable medium.
>
> A prescribed time dependent head relative to a fixed head at a radial distance b is maintained in the borehole. The pressure field induced in the matrix and fracture could in principle be monitored using piezometers.
>
> Assumptions
>
> It is assumed that flow in both the rock matrix and the fracture can be described by Darcy's law. The matrix is taken to be homogeneous and isotropic and characterised by hydraulic conductivity and a specific storage. The fracture is characterised by a transmissivity and a storage coefficient. It is further assumed that there is no vertical hydraulic gradient in the fracture.
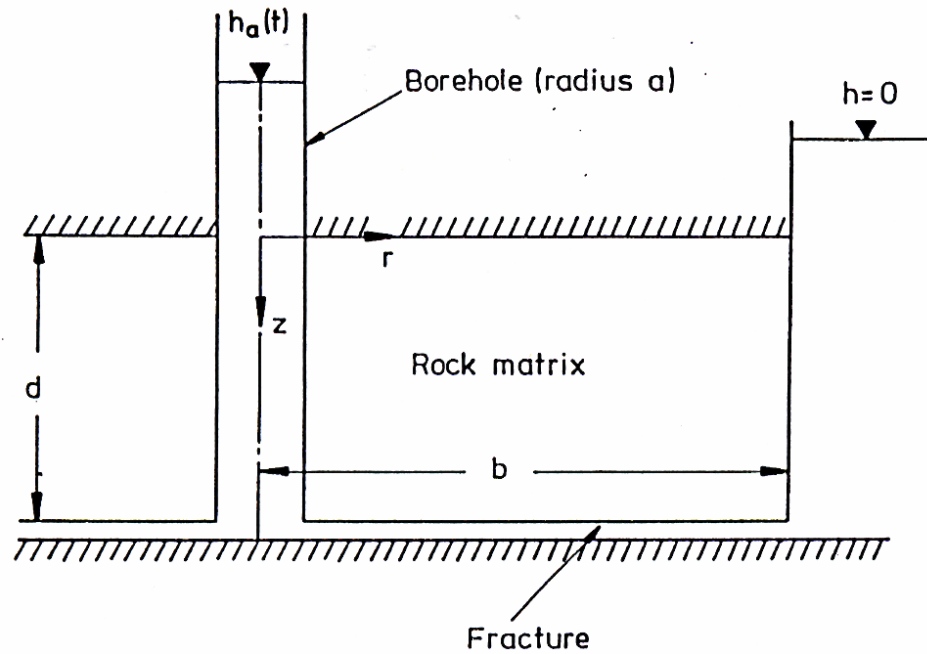
Figure B4:1. *Schematic diagram of the test problem (from the Hydrocoin report).*

2 Numerical simulation

The problem is best described in cylindrical coordinates; a coordinate system which however is not provided in DarcyTools. An approximate description of a cylindrical grid can be obtained with the BFC:s option, see Figure B4:2. This is the coordinate system to be used.

Simulation parameters are summarized in Table B4:1.

Table B4:1. Simulation parameters

Domain	Borehole radius = 0.1 m, $b = 10.0$, $d = 5.0$ m, with notation from Figure B4:1.
Boundary Conditions	Transient head = $1.0 \left(1 - e^{-t/0.1}\right)$ [m] zero flux at $y = 0$ and $y = y_{max}$ Head = 0.0 at $x = 0$
Properties	<u>Matrix</u> Conductivity = 10^{-9} m/s Specific storage coeff = 10^{-7} m^{-1} <u>Fracture</u> Conductivity = 10^{-6} m/s Specific storage coeff = 10^{-7} m^{-1}
Grid	NX = 105, Ny = 56, NZ = 2 see Figure B4:2. The timestep was 0.01 s, initially and gradually increased to 1.0 s

3 Results/Discussion

The transient build up of the head in two selected points is shown in Figure B4:3. Considering that the grid is an approximation of a grid in cylindrical coordinates, the solution is considered to be in good agreement with the analytical solution.

As specified in Table B4:1, two cell layers were used in the z-direction. This is not required from the problem specification, but was found to be necessary for the numerical solution. This point and the sensitivity to the conductivity between the two layers, should be clarified.

Figure B4:2. *The computational domain.*
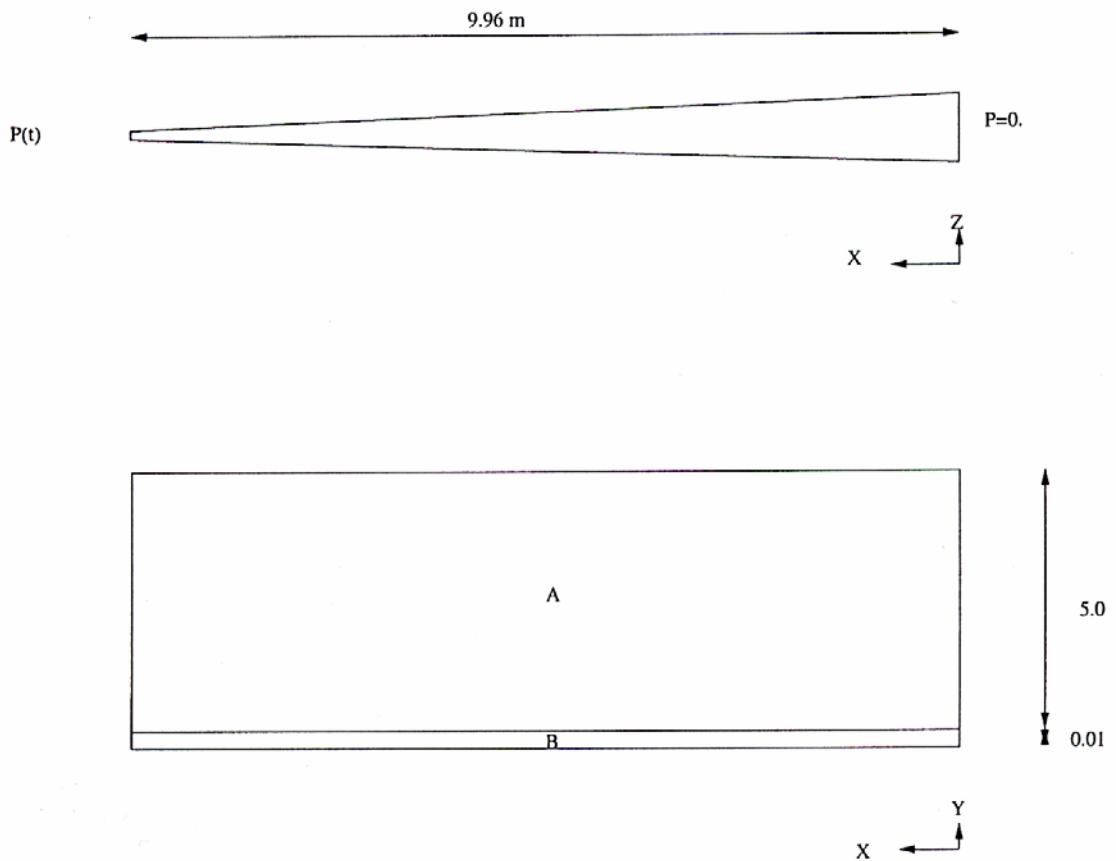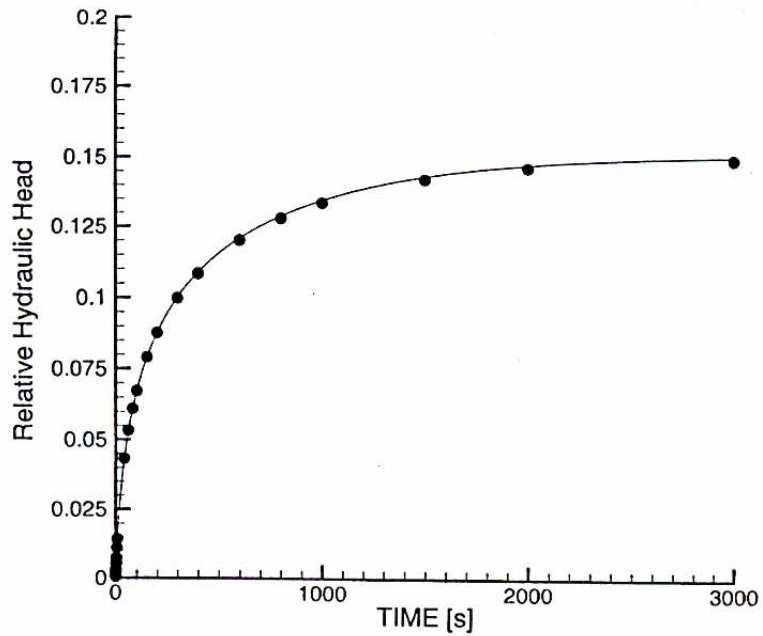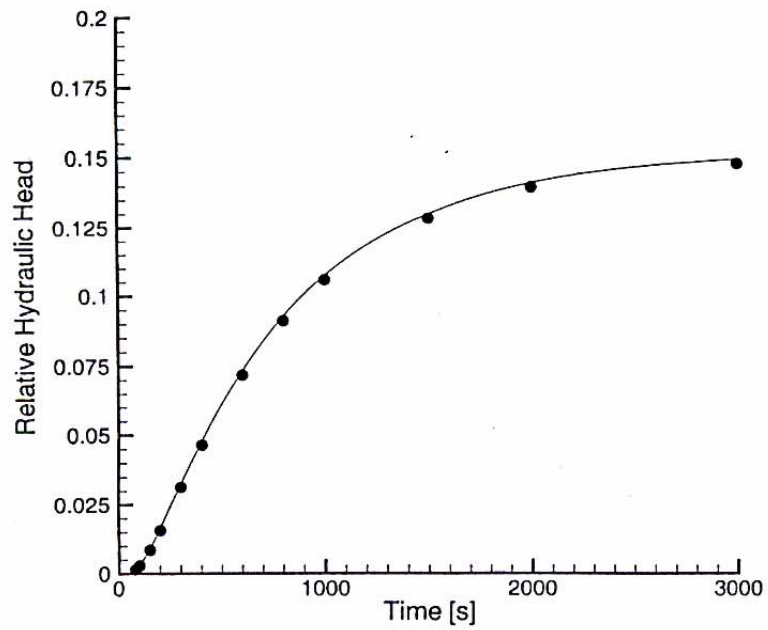
Figure B4:3. *Comparison between simulated (————) and analytically determined*

(• • •) head build up in two points. Top figure gives point A (see Figure B4:2) and bottom one point B.

4 Conclusion

A good agreement between the simulated and analytically determined head built up has been demonstrated.

Some aspects of the simulation remain to be clarified.

SPECIFIC YIELD, NEUMAN (1975) (Case B5)

1 Introduction

The pumping of an unconfined aquifer generates a characteristic time-drawdown curve in a near borehole piezometer; first a steep part, then an almost flat part and finally a relatively steep late-time segment. The flat part is attributed to "delayed yield", which is the gravitational drainage of the unsaturated zone.

Neuman (1975) gives an analytical solution which covers all three parts. The assumptions of this solution are different to the ones in the numerical technique embodied in DarcyTools (see Part A). In particular, Neuman (1975) assumes that the water table remains at its original position, while the numerical model considers a moving ground water table.

The objective of this case is to compare the first two parts of the drawdown curve and in particular the levels of the flat part. For longer pumping (and larger drawdowns) the two solutions may not be comparable, but this point will not be investigated here.

2 Numerical simulation

The problem will be specified as a three dimensional one in cartesian coordinates, although a two dimensional solution in cylindrical coordinates would have been more appropriate. An outline is given in Figure B5:1; we are hence only studying one quarter of the complete domain (due to symmetry conditions).

Input data are given in Figure B5:1 and Table B5:1.
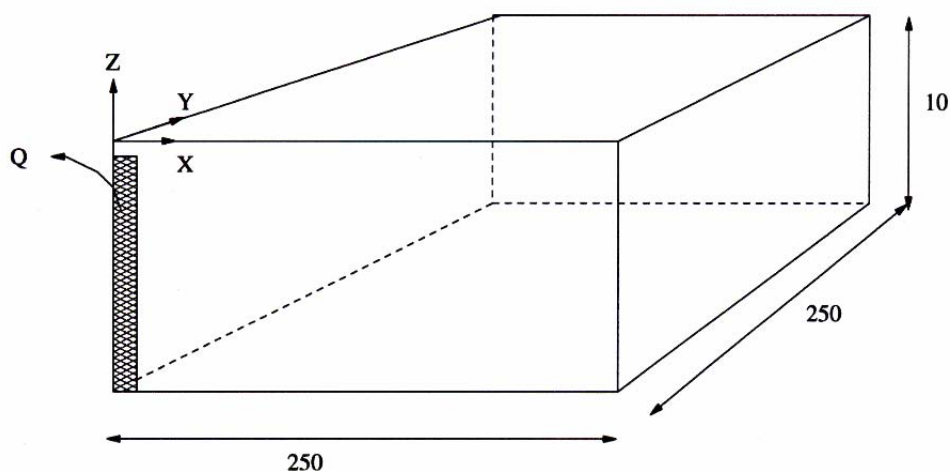
Figure B5-1. *Outline of situation studied.*

Table B5:1. Simulation parameters

Domain	$250 \times 250 \times 10 \left[\text{m}^3 \right]$
Boundary Conditions	Zero flux
Sink due to pumping	$5 \times 10^{-3} \left[\text{m}^3/\text{s} \right]$
Properties	Permeability = $2 \times 10^{-11} \left[\text{m}^2 \right]$ Porosity = 10^{-2} Density = 1 000 [kg/km^3] Spec. storativity = 2×10^{-5} Delay time = 50 s Specific yield = 0.2
Grid	x and y: Uniform for 20 metres with cell size 0.5 m, then expanding up to 250 metres, using 60 cells. z: Uniform. NZ = 16.

3 Results / Discussion

The simulated time-drawdown curves in three points (at different distances from the well) are shown in Figure B5:2. The levels of the flat part, as given by the analytical solution, is also given in the figure. As can be seen a surprisingly close agreement, considering the different basic assumptions, is found.

4 Conclusion

It is found that the flat part of the time-drawdown curve is in agreement with the analytical solution by Neuman (1975).
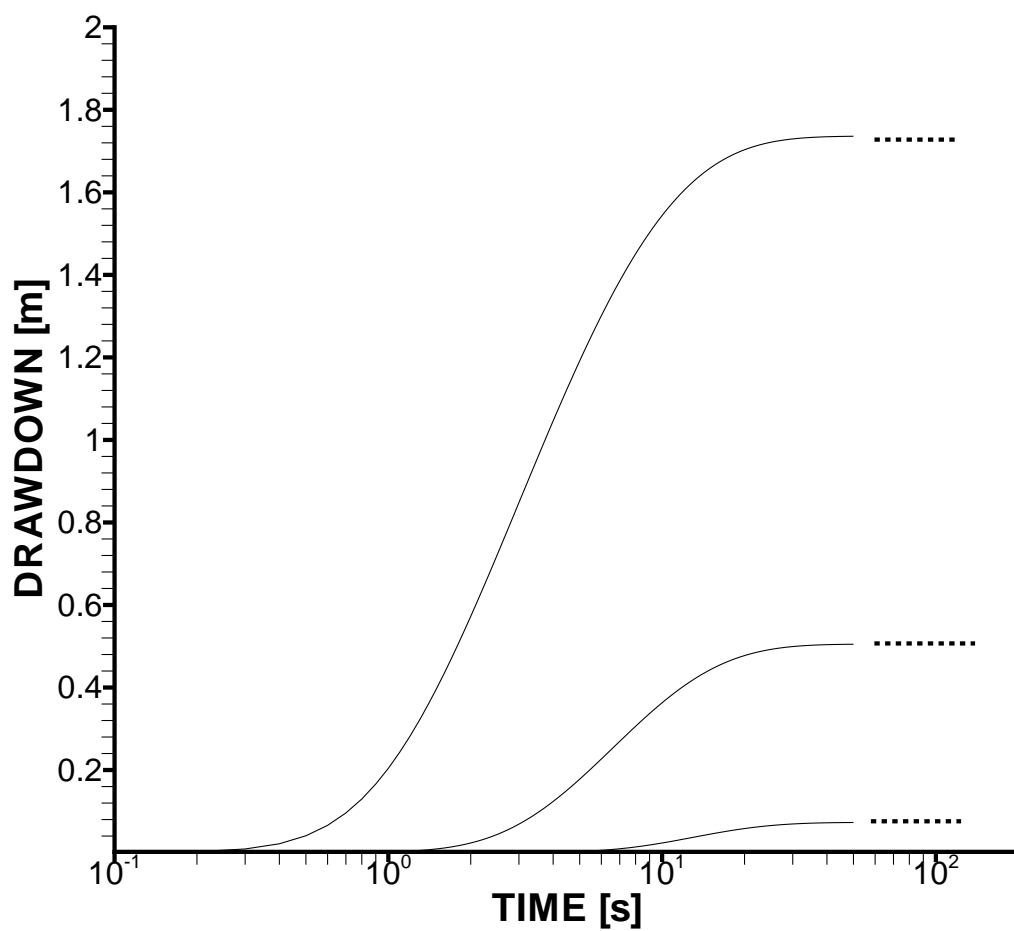
Figure B5:2. *Time-drawdown at distances 4.5 (top), 10 (middle) and 20 (bottom) metres from the well. Dotted lines give the corresponding analytical solutions for the flat part.*

HORIZONTAL WELL PROBLEM
(Case B6)

1 Introduction

Analytical solutions of the drawdown in an unconfined aquifer, due to a horizontal well, are presented by Zhan and Zlotnik (2002).

The situation studied is outlined in Figure B6:1. The drawdown in four different piezometer locations is studied, as a function of time. A uniform sink strength, in space and time, is assumed.

The analytical solution assumes that the change in the water table is much smaller than the depth of the aquifer. Further, a delayed drainage can be specified by what is called a "delay index", $1/\alpha_1$, with dimension time. The numerical solution handles a moving ground water table and the top boundary condition is thus not similar to the one in the analytical solution. A similar time constant for the delayed drainage is however also present in the numerical method.

The objective of the testcase is to compare the time-drawdown curves in the four piezometer locations and to evaluate the significance of the delay index.
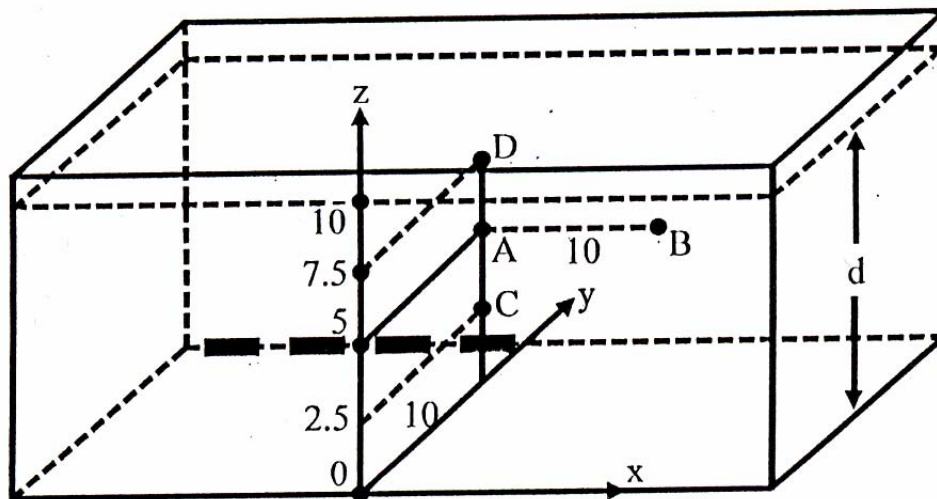
Figure B6:1. *Outline of situation studied. Locations of piezometers at point A (0, 10 m, 5 m), B (10 m, 10 m, 5 m), C (0, 10 m, 2.5 m), and D (0, 10 m, 7.5 m). Figure from Zhan and Zlotnik (2002).*

2 Numerical simulation

The coordinates for the four points are given in Figure B6:1. Other input data are summarised in Table B6:1.

Due to symmetry conditions only one quarter of the domain needs to be considered.

Table B6:1. Simulation parameters

Domain	$200 \times 200 \times 10 \left[\text{m}^3 \right]$
Boundary Conditions	Zero flux
Sink due to pumping	$5 \times 10^{-3} \left[\text{m}^3/\text{s} \right]$
Properties	Permeability $= 2 \times 10^{-11} \left[\text{m}^2 \right]$ Porosity $= 10^{-2}$ Density $= 1\ 000\ [\text{kg/km}^3]$ Spec. storativity $= 2 \times 10^{-5}$ Delay time $= 100$ s Specific yield $= 0.2$
Grid	x and y: Uniform for 10 metres with cell size 0.25, then expanding up to 200 metres, using 60 cells. z: Uniform. $NZ = 40$.

3 Results / Discussion

It was not possible to get a close agreement with the analytical solution for the drawdown in the four points. The reason for this is not clear but the different top boundary conditions is one possibility.

This expectation is supported by the fact that a slightly modified vertical conductivity, increasing K_z from 10^{-4} to 1.7×10^{-4} m/s, brings the numerical solution into fair agreement with the analytical one.

In Figure B6:2 the two solutions for the four points are compared. All curves have been made dimensionless in the same way (for details, see Zhan and Zlotnik (2002)) and are hence directly comparable. A fair agreement is found.

Next the influence of the time scale for the drainage is evaluated, see Figure B6:3. If the delay time, given in Table B6:1, is 100 s or smaller the drainage can be regarded as instantaneous and a smaller value will not change the result. Also Zhan and Zlotnik found that the influence of their α_1, which is the inverted time, had a limit of about 0.01; a larger value did not produce any change. In the numerical simulation it was not possible to increase the delay time to any big number as the ground water table would then be lowered down to the horizontal well. A value of 1 000 s was however acceptable, see Figure B6:2. The analytical solution postulates that the ground water table movement is small and one may hence question if the analytical solutions are realistic for small α_1 - values.
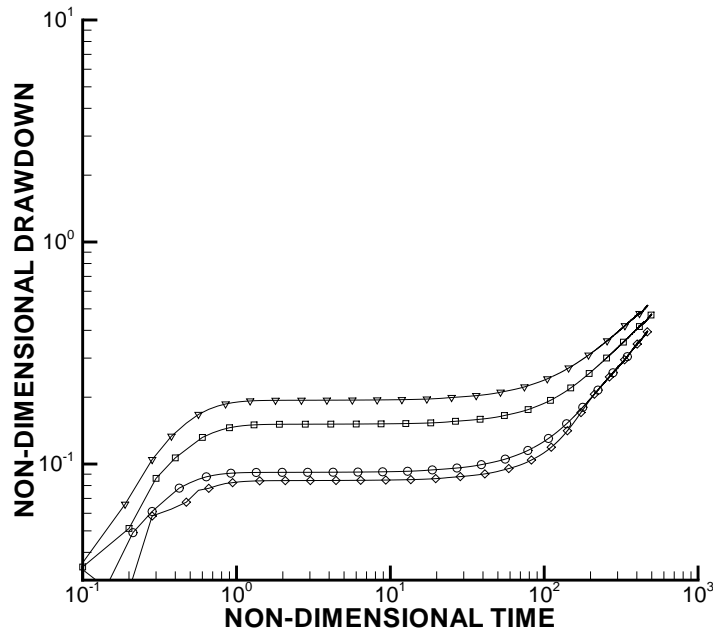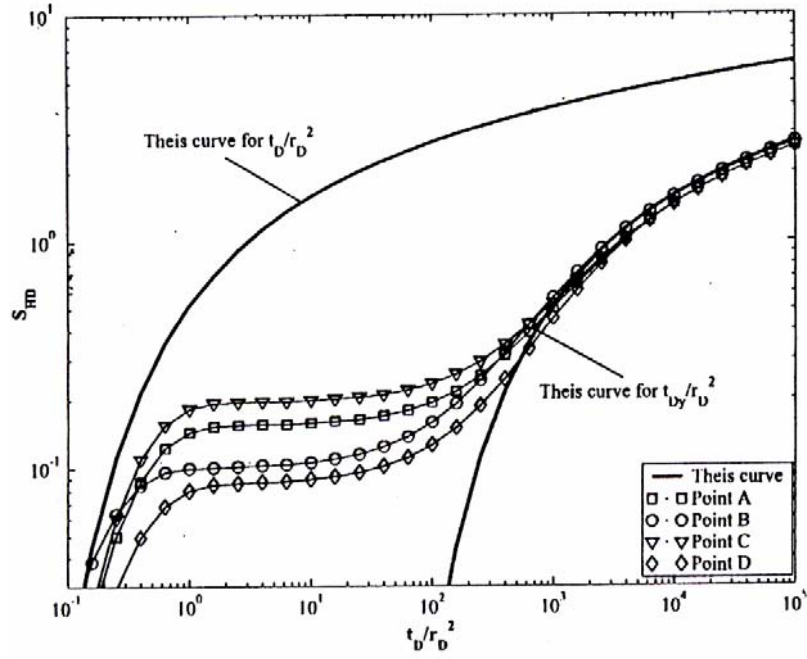
Figure B6:2. *Non-dimensional drawdown versus non-dimensional time for four piezometer locations. Analytical (top) and numerical solutions.*
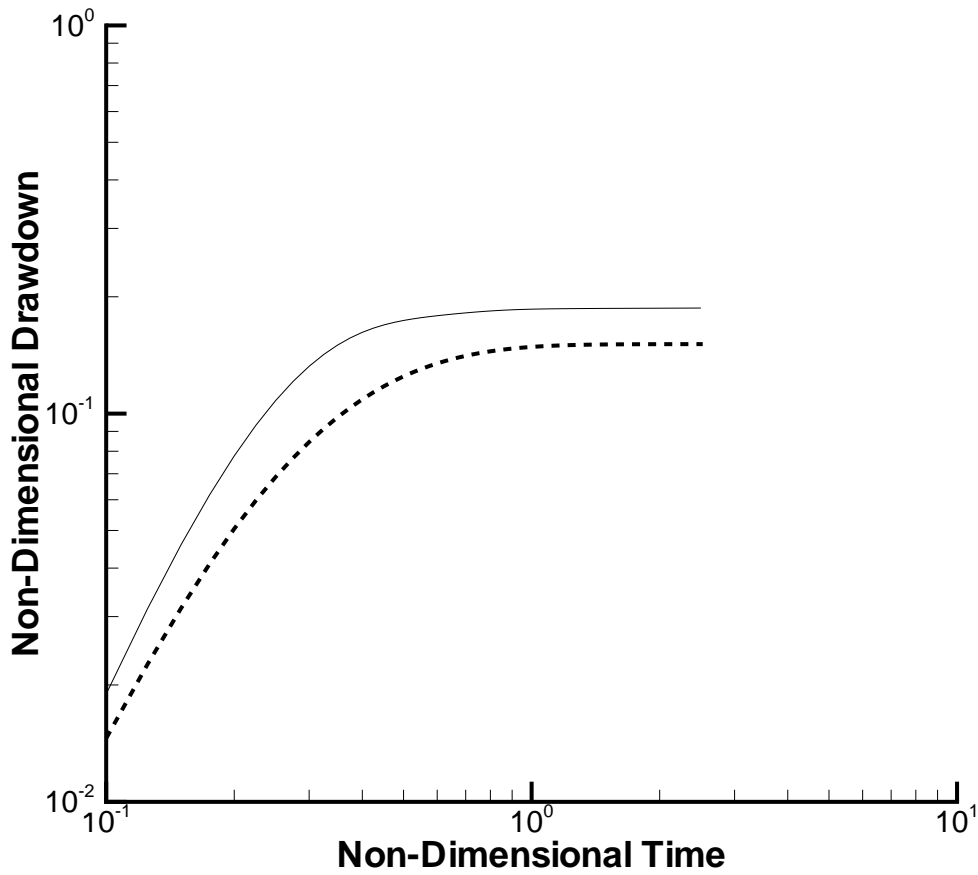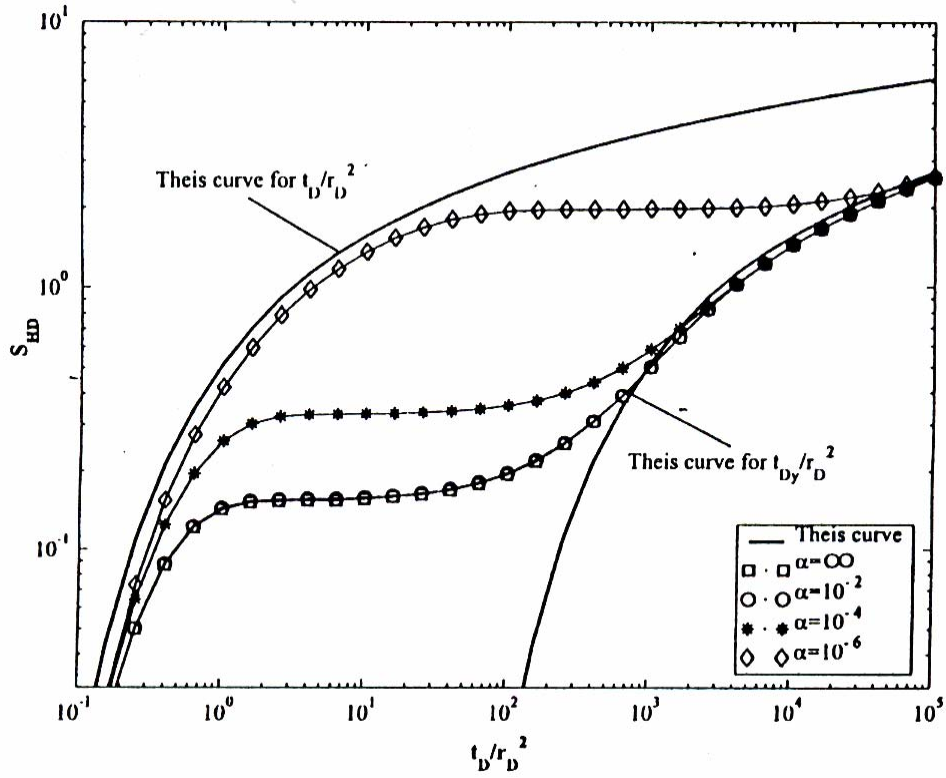
Figure B6:3. *Sensitivity to delay index in point A. Analytical (top) and numerical solutions. In the numerical solution the delay times shown are 100 s (dotted line) and 1 000 s.*

4 Conclusion

A fair agreement with the analytical solution for the case considered could be achieved by a slight modification of the vertical conductivity (multiplied with a factor of 1.7). The reason for this is not clear but could be due to the different top boundary conditions in the two solutions.

THREE FRACTURES IN A 2D DOMAIN (Case C1)

1 Introduction

This case considers the steady flow through three crossing fractures in a 2D domain, see Figure C1:1. Pressure is prescribed on the left and right boundaries, while the top and bottom boundaries are of zero flux type.

It is possible to determine the flow in all individual parts of the network analytically, as well as the pressure in the fracture crossings; these data will be used for verification of the numerical results. It is of special interest to study the accuracy of the numerical solution as a function of the fracture thickness, b, in relation to the cell size, Δ.

The objective of the test case is to verify that DarcyTools is in agreement with the analytical solution for the case considered.
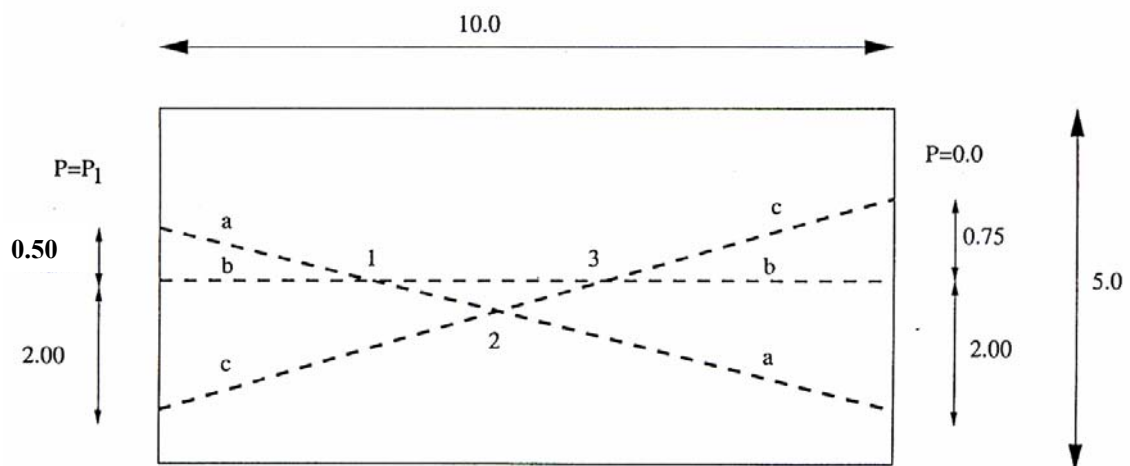
Figure C1:1. *Flow in a two-dimensional fracture system. Outline of situation considered.*

2 Numerical simulation

The computational domain is specified in Figure C1:1 and some further details are given in Table C1:1. The pressure difference ($(P_1 - 0)$ and the fracture conductivity are of no importance, as we will normalize all results with the data from the analytical solution. The number of grid cells is held constant and the ratio b/Δ is hence varied by varying the fracture thickness b.

A test with a fracture network, where all the fractures do not directly connect the two sides with prescribed pressure, will also be carried out. In this test part of fracture c (from inlet to point ②) and part of fracture b (from point ③ to outlet) will be removed.

Table C1:1. Simulation parameters

Domain	2D 10 x 5 metres
P_1	9810 Pa
Fracture Conductivity	5×10^{-5} m/s
Fracture thickness	b/Δ varied: 0.1, 0.5, 1.0 and 2.0
Grid	400 x 200 cells, $\Delta = 0.025$ m

3 Results / Discussion

All results are summarised in Table C1:2. Both the total flux through the domain, Q, and the pressures in points 1, 2 and 3 have been normalised with the corresponding values from the analytical solution. The general picture is that the numerical solution is in close agreement with the analytical one, it should however be noted that calculated flow decreases, in relation to the analytically calculated, with a decreasing ratio b/Δ.

Table C1:2. Flow and pressure in a fracture network. Values calculated with DarcyTools have been normalised with the corresponding values from the analytical solution.

Parameter	Fracture thickness normalised with Δ (b/Δ).				
	0.1	0.5	1.0	2.0	1.0, fractures removed
Q	0.960	0.987	0.997	1.001	0.998
P_1	1.000	1.001	1.001	1.001	0.998
P_2	0.998	0.999	0.999	1.000	1.005
P_3	0.998	1.000	1.000	1.000	0.982

4 Conclusion

Flow and pressure in three crossing fractures in a 2D domain can be accurately calculated by DarcyTools.

INTERSECTING FRACTURE ZONES
(Case C2)

1 Introduction

The case is described in the Hydrocoin report, from where we quote:

Background

This test case concerns steady-state flow in a two-dimensional vertical slice of a fractured rock. The region contains two inclined fracture zones which have a higher permeability than the surrounding rock. The fracture zones intersect one another depth.

The purpose of this problem is to test capabilities of different codes to treat large permeability contrasts. In view of the complicated geometry, no attempt was made to find an analytical solution for this problem. Thus, the accuracy of the solutions is judged by examining the convergence with respect to spatial discretisation.

It is recognised that the flow in crystalline rock systems is generally poorly described by two-dimensional models. However, a two-dimensional problem was chosen since it was deemed tractable by the majority of the participants, especially since convergence tests for three-dimensional problem would have been extremely expensive and time consuming. The main point of this case, namely the solution convergence of a problem with large permeability contrasts, can still be appropriately tested in two dimensions.

Conceptual model

A two-dimensional cross-section of a fractured rock mass is intersected by two fracture zones as shown in Figure C2:1. The zones, which have different widths and inclinations, intersect at depth within the modelled region.

The topography has been made simple so that it consists of two valleys located where the fracture zones meet the surface. To simplify the problem definition, the shape of the surface is described by straight lines. It should be noticed that in order to define the horizontal derivative unambiguously at the top corners, the surface is taken to be horizontal for the first ten metres. Although the surface topography is symmetric, the flow is influenced by the asymmetry of the fracture zones.

Assumptions

It is assumed that Darcy's law is applicable to both the fracture zones and the rock matrix. Moreover, both units are assumed to be homogeneous and isotropic media with hydraulic conductivities K_f and K_m respectively.

The rainfall is assumed to be sufficient to cause the water table to be coincident with the surface. The remaining boundaries are assumed to be impermeable to water flow.

2 Numerical simulations

The original Hydrocoin case was focused on grid refinement. Here only a very fine grid will be used (it is expected that the solution on the grid represents the grid independent solution).

The details of the simulation are summarized in Table C2:1.

Table C2:1. Simulation parameters.

Domain	See Figure C2:1.
Boundary Conditions	Prescribed pressure at top: zero flux on all other boundaries.
Properties	Conductivity fractures = 10^{-6} m/s Conductivity background = 10^{-8} m/s
Grid	160 (horizontal) x 110 (vertical) cells, stretched to follow the upper boundary.

3 Results/Discussion

The distribution of hydraulic heads at the levels of -200 m and −800 m are shown in Figures C2:2 and C2:3, respectively. The top diagrams in these figures represent the Hydrocoin results and the bottom ones the present predictions. A fair agreement is found.

The flow and pressure distributions are illustrated in Figure C2:3. This figure is included to provide a more complete view of the present simulation and is not used for comparisons with the Hydrocoin results.

4 Conclusion

A fair agreement with the head distributions provided by the Hydrocoin simulations has been demonstrated.
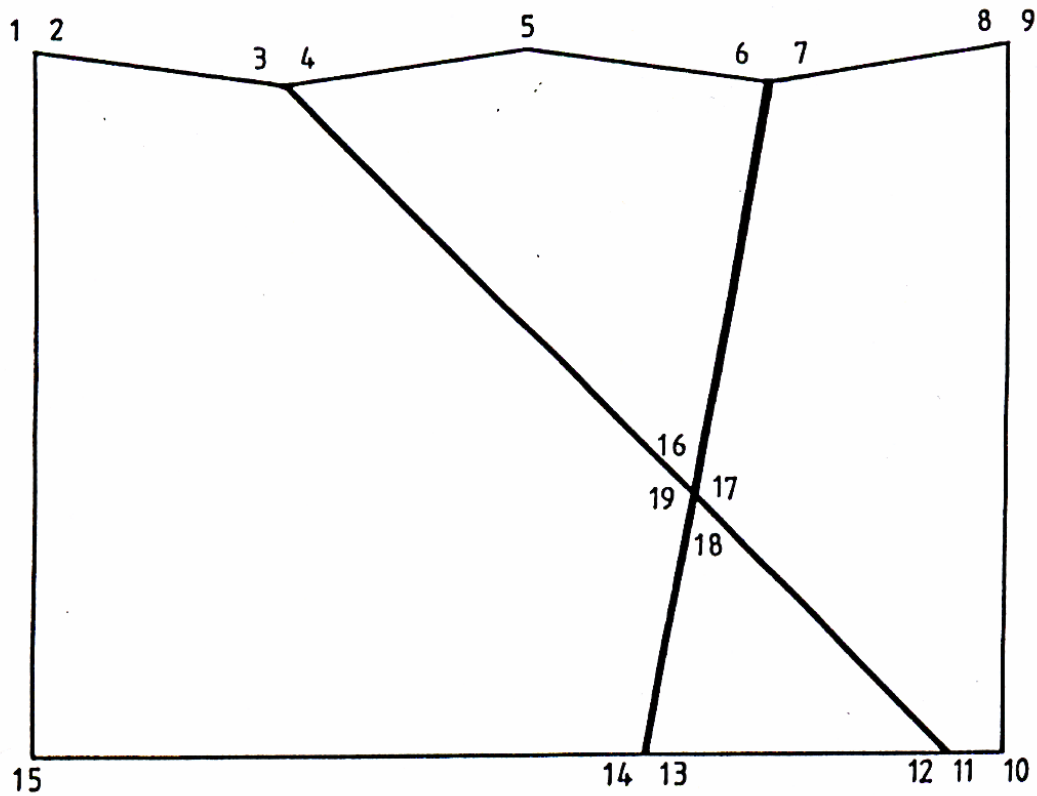
Co-ordinates of numbered points in the modelled domain

Point no.	x (m)	z (m)
1	0.0	150.0
2	10.0	150.0
3	395.0	100.0
4	405.0	100.0
5	800.0	150.0
6	1192.5	100.0
7	1207.5	100.0
8	1590.0	150.0
9	1600.0	150.0
10	1600.0	-1000.0
11	1505.0	-1000.0
12	1495.0	-1000.0
13	1007.5	-1000.0
14	992.5	-1000.0
15	0.0	-1000.0
16	1071.35	-566.35
17	1084.04	-579.04
18	1082.5	-587.5
19	1069.81	-574.81

Figure C2:1. Geometry of the modelled domain.

A51
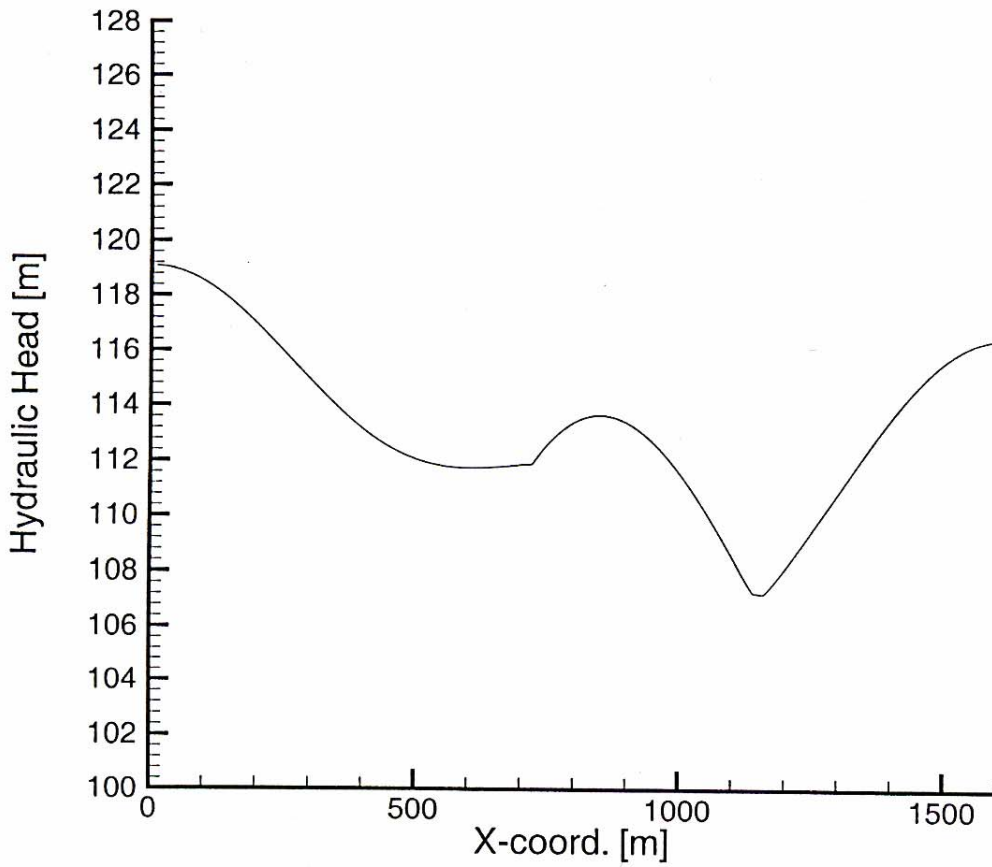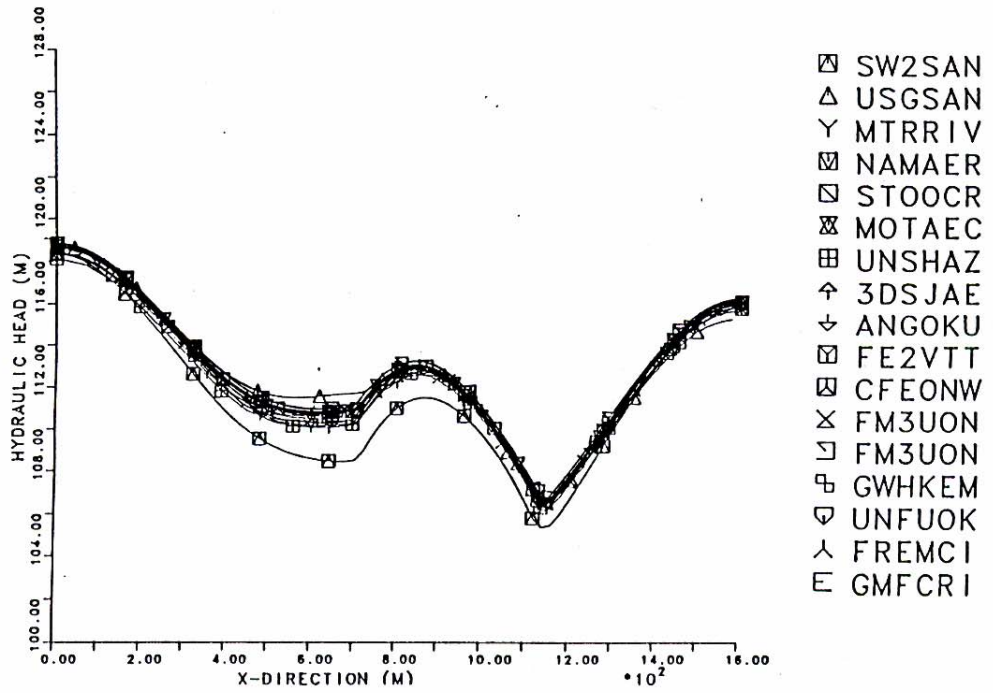
Figure C2:2. *Distribution of hydraulic head at a level of –200 m. Hydrocoin results (top) and present prediction.*

Legend (top chart):
- ⊠ SW2SAN
- △ USGSAN
- Y MTRRIV
- ⊠ NAMAER
- ⊠ STOOCR
- ⊠ MOTAEC
- ⊞ UNSHAZ
- ⇧ 3DSJAE
- ⇩ ANGOKU
- ⊠ FE2VTT
- ⊠ CFEONW
- ✕ FM3UON
- ⅃ FM3UON
- ⅁ GWHKEM
- ▽ UNFUOK
- ⅄ FREMCI
- E GMFCRI
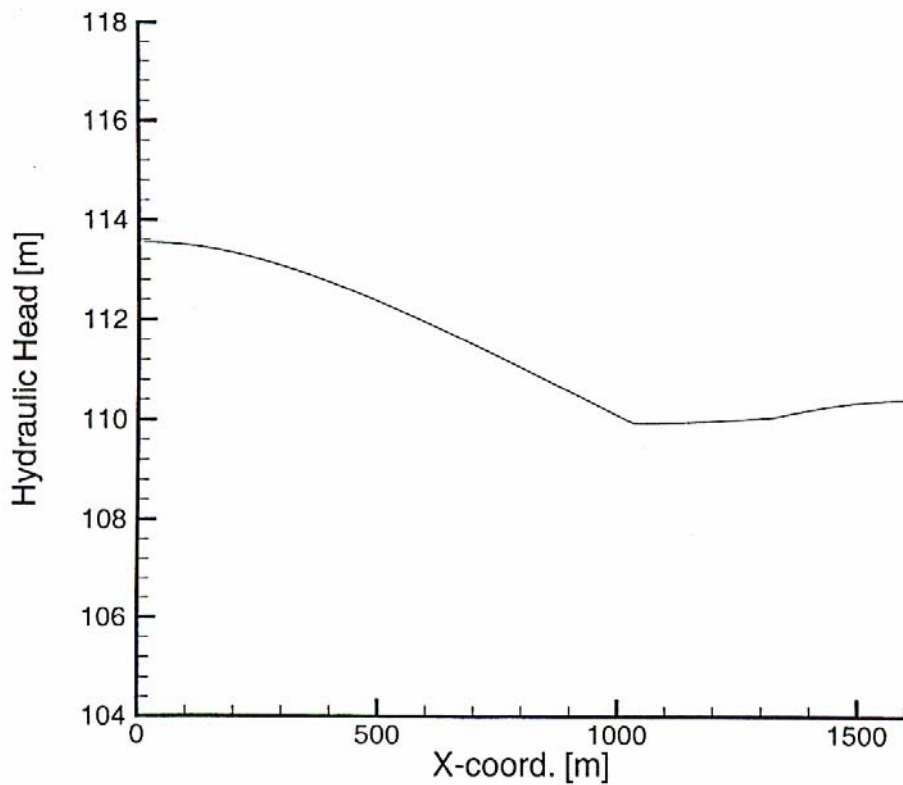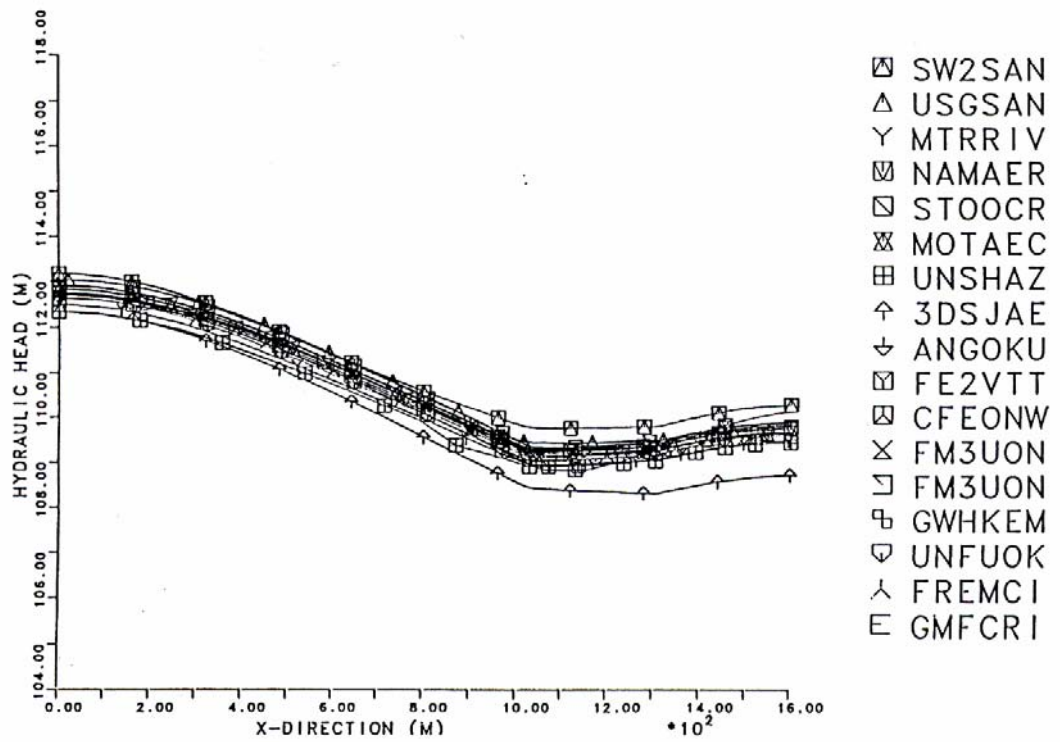
Figure C2:3. *Distribution of hydraulic head at a level of –800 m. Hydrocoin results (top) and present prediction.*
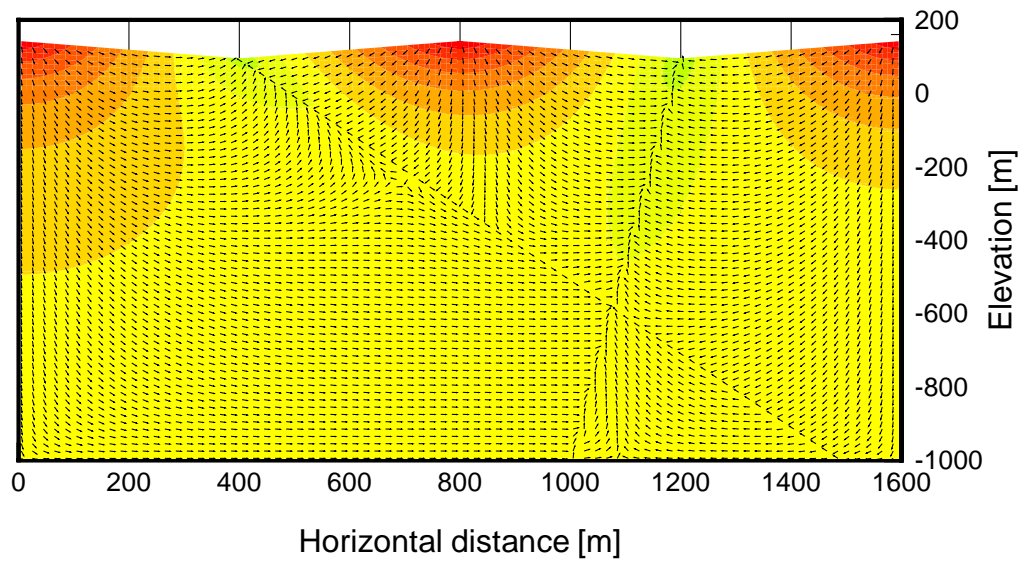
Figure C2:4. Predicted flow and pressure. Uniform length on velocity vectors.

SINGLE FRACTURE IN A BOX
(Case C3)

1 Introduction

It was noted in the main part of the report that the accuracy of the representation of a fracture depends on the angles the fracture forms with the coordinate directions and the thickness of the fracture (in relation to the cell size Δ). The purpose of this test case is to establish the magnitude of the errors that can be expected due to these effects.

The situation studied is outlined in Figure C3:1. The pressure is held constant on two opposite faces ($y = 0.0$ m and $y = 100.0$ m) and a zero flux condition is used on all other boundaries. At the inflow boundary the position of the fracture is fixed, with centreline coordinates (10.0, 0.0, 10.0). The fracture position at the downstream boundary is varied in order to test a wide range of angles to the coordinate directions. Also a range of thicknesses was tested, but the height of the fracture, H, was kept constant at 5 metres.
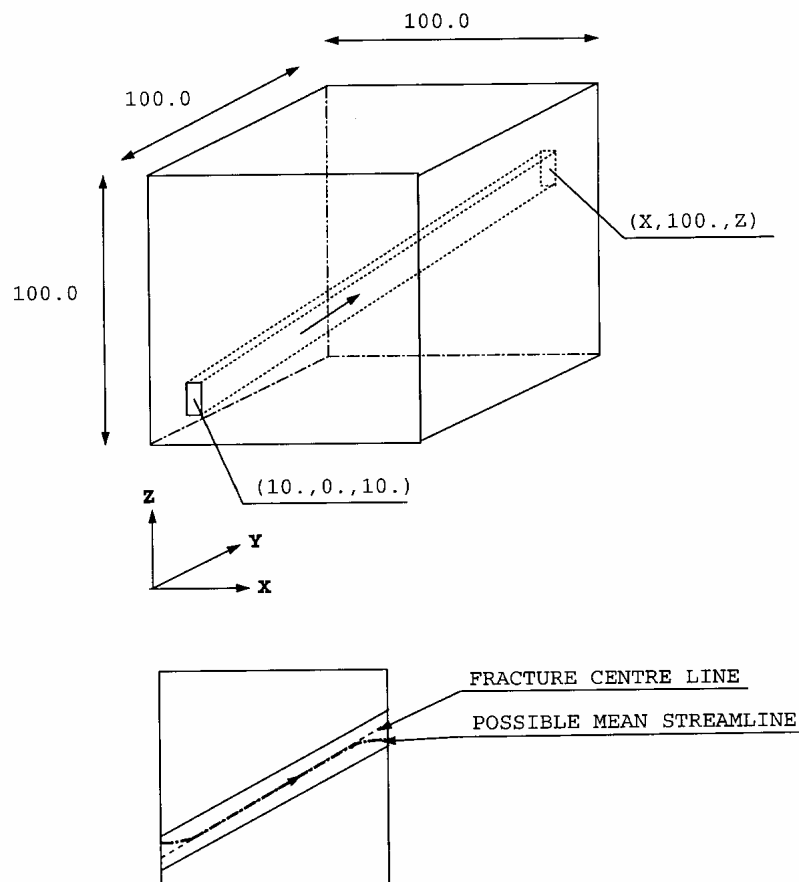
Figure C3:1. *A single fracture in a 3D domain. Outline of situation studied (top) and illustration of fracture centre line and mean streamline. All distances in metres.*

2 Numerical simulations

Most of the simulations parameters are introduced in Figure C3:1, some further details are summarised in Table C3:1.

A systematic variation of the fracture thickness and the downstream position will be in focus in the simulations.

Table C3:1. Simulation parameters

Domain	100 x 100 x 100 metres
Boundary conditions	Fixed pressure difference (= 1 metre head) between two opposite faces. Zero flux on other faces
Fracture dimensions	Height = 5 metres, thickness varied (see Result section)
Fracture position	Fixed at inflow boundary (see Figure C3:1), varied at outflow boundary (see Result section)
Fracture conductivity	10^{-4} m/s
Grid	$\Delta = 1$ metre, uniform

3 Results / Discussion

Results are presented in Table C3:2. Five downstream fracture positions and five fracture thicknesses were tested. The five downstream fracture positions will give a fracture that, for the first position, is parallel to the y- coordinate while the last position gives a fracture that almost follows a diagonal in the box. Note also that the x and z coordinates for the downstream positions are different; this ensures that the fracture will have different angles to all three coordinate directions (except for the first position). The grid representation of the transmissivity, T, is obtained from the calculated flow rate, Q_c, the head difference, dh, between the inlet and outlet planes, the fracture height, H, and the centre line length of the fracture, L.

$$T = \frac{Q_c}{H} \frac{L}{dh} \tag{C3:1}$$

In Table C3:2 the ratio T / T_0, where T_0 is the true, prescribed, transmissivity, is given for the five downstream positions and fracture thicknesses, b. For the first position, i.e. the fracture that is parallel to the y-coordinate, the transmissivity is represented exactly

in the grid. For other angles it is found, as expected, that the error generally increases with decreasing b/Δ. In Table C3:2 also the average T/T_0 as a function of b/Δ can be found. The average ratio for all 25 tested situations is 0.984.

A comment may be needed to the value 1.007 ($x = 90$, $z = 70$, $b/\Delta = 2.0$) in Table C3:2. It is expected that the method gives $T/T_0 \leq 1.0$ for all thicknesses and all angles the fracture forms with the coordinate directions. The explanation for values larger than 1.0 is that the mean streamline may be shorter than the centreline of the fracture, see Figure C3:1. The *T*-values in Table C3:2 were all calculated using the centreline of the fracture as the distance between the inlet and outlet plane and may hence overestimate the length somewhat.

Table C3:2. Single fracture in a 3D domain. The transmissivity as represented in the computational grid, *T*, normalised with the true transmissivity, *T₀*, for various fracture thicknesses and orientations.

| Fracture coordinates at downstream boundary [m] | Transmissivity ratio, *T/T₀* | | | | |
| | Fracture thicknesses, *b/Δ* | | | | |
	2.0	1.0	0.5	0.25	0.125
x = 10.0, z = 10.0	1.000	1.000	1.000	1.000	1.000
x = 30.0, z = 25.0	0.997	0.993	0.981	0.953	0.949
x = 50.0, z = 40.0	0.997	0.989	0.970	0.947	0.926
x = 70.0, z = 55.0	1.001	0.995	0.983	0.969	0.966
x = 90.0, z = 70.0	1.007	1.002	0.996	0.993	0.989
Average	1.000	0.996	0.986	0.972	0.966

4 Conclusion

It is concluded that the flow through a single fracture, with arbitrary orientation to the coordinate directions, can be expected to be accurately predicted (maximum error about 1%) provided that $b/\Delta > 1.0$. If $b/\Delta = 0.125$ the average error is about 3%, but for some fracture orientations an error of 5% can result.

MANY FRACTURES IN A BOX
(Case C4)

1 Introduction

This case is based on the same computational domain as case C2 (see Figure C2:1). It is thus a box with dimensions 100 x 100 x 100 metres, which is discretized using a cell size , Δ, of 1 metre. A range of thicknesses, b, will be considered, but the height, H, of the fractures will be held constant and equal to 5 metres. 25 fractures will be generated with start and end positions randomly distributed on the squares $10.0 < x < 90.0$, $10.0 < z < 90.0$. The total flow rate, Q_t, will be equal to the sum of the flow in each fracture:

$$Q_t = \sum Q = \sum HT \frac{dh}{L} = HTdh \sum \frac{1}{L} \qquad \text{(C4:1)}$$

where dh is the applied head difference, T the fracture transmissivity and L the length of a fracture.

The objective of the test case is to evaluate how well we can represent the transmissivity of several, randomly oriented, crossing fractures.

2 Numerical simulation

In order to calculate the average fracture transmissivity as represented in the grid, T, we need to know the total flow rate and the sum of L^{-1}, where L is the fracture length. These lengths are calculated and stored during the generation of the fractures. The generated fracture system, consisting of 25 fractures, is shown in Figure C4:1. As can be seen a complex system of crossing fractures is generated. Simulations were carried out for a range of fracture thicknesses and the average fracture transmissivity, T, was estimated from Equation C4:1.

The simulation parameters are summarised in Table C4:1.

3 Results / Discussion

Results from simulations are found in Table C4:2. As for the previous test cases we find that the error increases with decreasing fracture thickness. For $b / \Delta = 2.0$ the ratio $T / T_0 > 1$; this is probably due to the estimate of the mean streamline length, discussed in the previous test cases.

4 Conclusion

It is concluded that the flow rate through a simple fracture network in 3D is calculated correctly by DarcyTools, provided the fracture thickness (b/Δ) is not to small.

Table C4:1 Simulation parameters

Domain	100 x 100 x100 metres
Boundary Conditions	Fixed pressure on two opposite faces (y =0.0 and 100 metres)
Fracture thickness	Varied; b/Δ = 0.125, 0.25, 0.5, 1.0 and 2.0
Fracture transmissivity	$b \times 10^{-4}$ m^2/s
Grid	$\Delta = 1$ metre, uniform
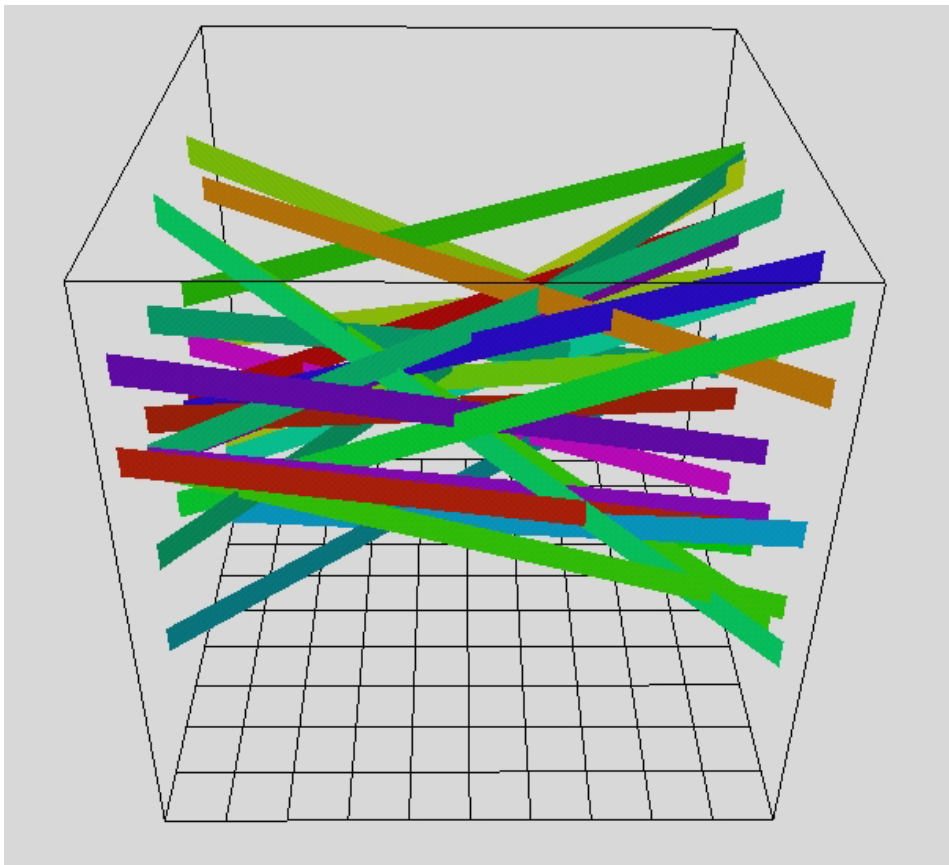
Figure C4:1. *25 fractures in a 3D domain. Illustration of the fracture system. The bottom of the box has been marked with a grid. Colours do not indicate any varying property.*

Table C4:2. Many fractures in a 3D domain. The average transmissivity as represented in the computational grid, *T*, normalised with the true transmissivity, T_0, for a range of fracture thicknesses.

Fracture thickness/Δ	Average transmissivity
2.0	1.011
1.0	1.000
0.5	0.990
0.25	0.971
0.125	0.960

PERCOLATION THEORY
(Case C5)

1 Introduction

Percolation theory deals with the question whether two, or more, faces of a box are connected through a fracture network. Below a certain fracture density, d, (number of fractures per unit volume) the box faces are not connected, while they are connected above this value. The critical density, d_c, is called the percolation threshold. Estimates of d_c for various fracture networks can be found in the percolation literature and we want to ensure that our fracture network connects the box faces at the correct fracture density.

In a numerical simulation only finite size systems can be considered, while theoretical estimates of d_c often assume infinite systems. Many studies are also restricted to orthogonal fracture sets; a recent example is Bour and Davy (1998). Fewer results are available for the situation we have in mind. However, in Robinson (1984) randomly oriented square planes in a finite volume are studied and a critical density is given. The percolation criterion was that all six faces should be connected by one single cluster. The critical density given by Robinson for a box of 20 x 20 x 20 m^3 filled with thin squares of side length one metre is 1.231 planes per unit volume; this value will be used as a reference.

A fracture network, at the critical fracture density, is shown in Figure C5:1. The fractures have random positions and orientations and a side length of 10 metres; all isolated fractures and fracture clusters have been removed.

The objective of the case is to show that a fracture network at the percolation threshold results in connected flow channels, when the network has been represented as grid cell conductivities.
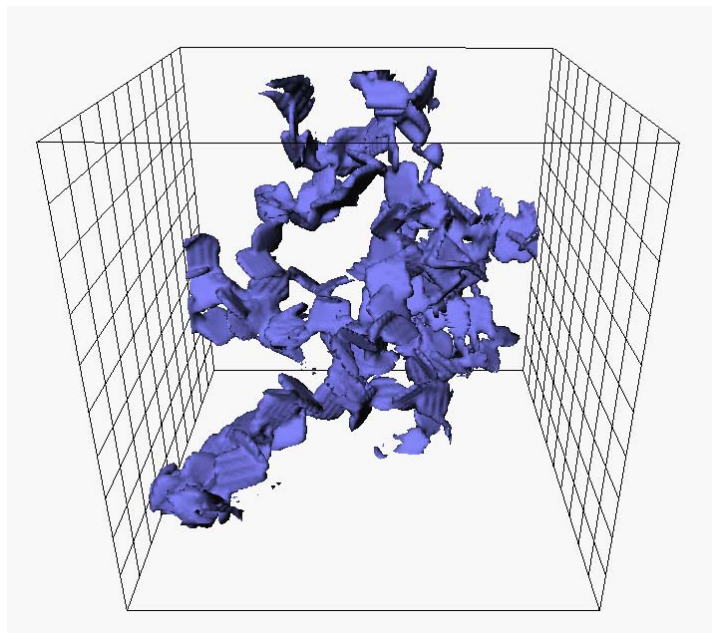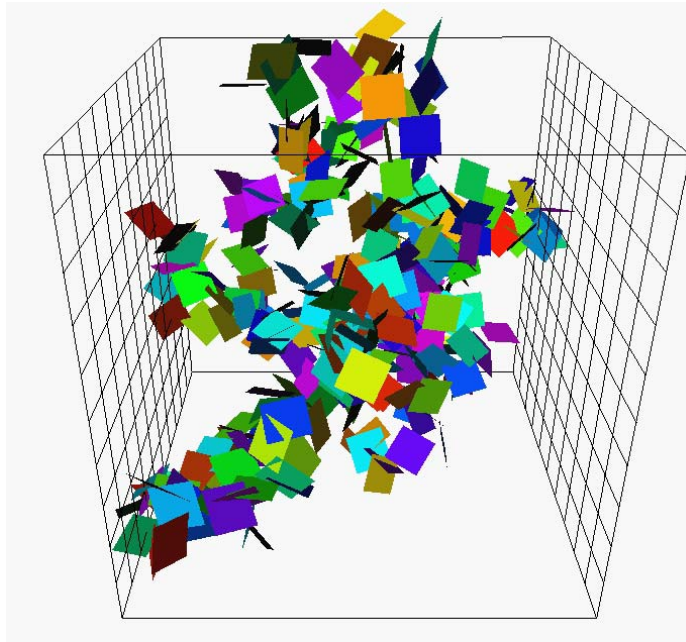
Figure C5:1. *A fracture network that connects two opposite faces of the box (top) and the corresponding flow channels. Fracture density at the percolation threshold. Fracture size is 10 metres. The two connected sides of the box have been marked with grids.*

2 Numerical simulations

Thin (thickness = 0.1 m) squares (10 x 10 m) will be distributed randomly in a box with dimensions 100 x 100 x 100 metres. Also the orientation of the fractures will be random.

A range of fracture densities will be tested and for each a flow calculation will be carried out. The relation between the flow rate, Q, and the fracture density is sought.

The simulation parameters are summarised in Table C5:1.

Table C5:1 Simulation parameters

Domain	100 x 100 x100 metres
Boundary Conditions	Fixed pressure on two opposite faces (y =0.0 and 100 metres)
Fracture size	10 x 10 x 0.1 metres
Fracture transmissivity	10^{-4} m^2/s
Fracture density	Varied: $0.8 \times 10^{-3} \rightarrow 1.5 \times 10^{-3}$ m^{-3}.
Grid	$\Delta = 1$ metre, uniform

3 Results / Discussion

The main result is given in Figure C5:2, where the flow rate versus the fracture density is shown. The two vertical lines give the estimated critical density as given by Robinson (1984) (discussed above) and Charlaix et al. (1984):

$$p = d \times \text{ (average area of the fractures) } \times \text{ (average half perimeter)} \qquad \text{(C5:1)}$$

Charlaix et al. (1984) proposed that the dimensionless number p must lie between 1.5 and 3 at the percolation threshold. The line in Figure C5:2 was based on a $p = 2.25$, which is in the middle of the range given.

The results are regarded as evidence that fracture connectivity is maintained when a network is represented as grid cell conductivities. As we are using networks at the percolation threshold, the network represents the weakest possible connection between the two box faces; still flow channels are generated.

An important aspect of the problem considered is the probabilistic nature of d_c (both position and orientation are random variables). It is hence not possible to estimate d_c from a single realisation of the network. An analysis that considers this aspect, and also analyses a network with fractures of a side length 5 metres, is given in Svensson (2001).

4 Conclusion

It has been shown that, a fracture network at the percolation threshold, represented as grid cell conductivities, results in a connected flow system.
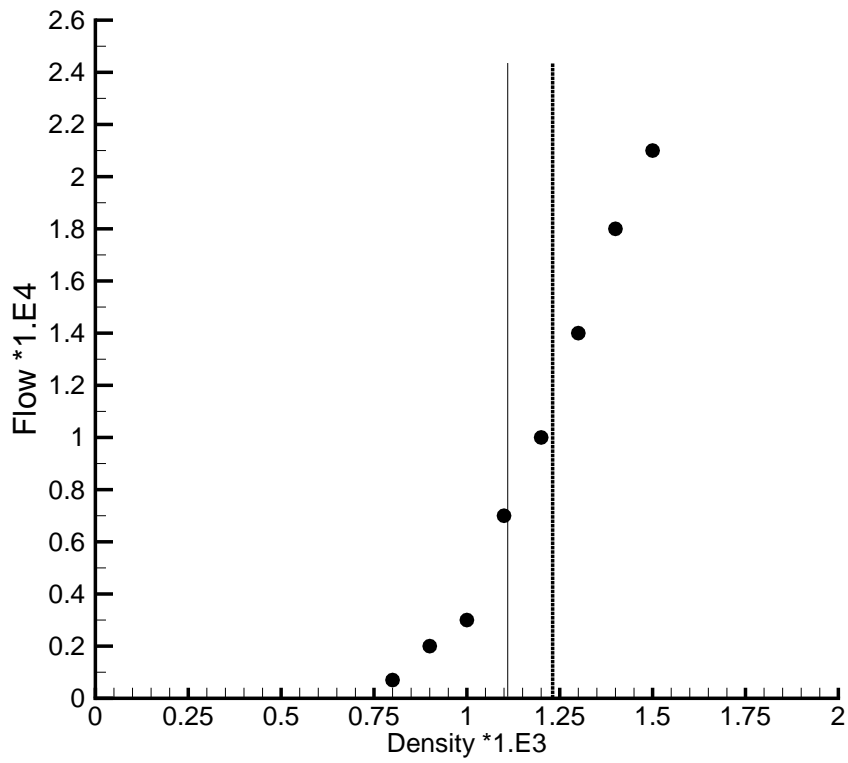
Figure C5:2. *Predicted (●●●) relation between fracture density and flow through the domain. Lines represent estimates of d_c from the literature; (———) Charlaix et al. (1984), (------) Robinson (1984)*

DIFFUSION IN A DEAD-END FRACTURE
(Case C6)

1 Introduction

This test case, see Figure C6:1, has previously been used to verify that a correct flow rate through a single fracture is calculated and also that a correct transport time is obtained (Svensson, 2001). Now, it is the diffusive transport that is in focus. Initially the fracture has a concentration (of some substance) of 1.0. A zero flux boundary condition is prescribed at $y = 10$ metres and a concentration of 0.0 is prescribed for $y = 0$ metres. The fracture position at the downstream boundary is varied in order to test a wide range of angles to the coordinate directions. Also a range of thicknesses was tested, but the height of the fracture was kept constant at 0.5 metres.

This problem has an analytical solution, for example presented by Versteeg and Malalasekera (1995), which reads:

$$c\left(x^1, t\right) = \frac{4}{\pi} \sum_{n=1}^{\infty} \frac{(-1)^{n+1}}{2n-1} \exp\left(-D_a \lambda_n^2 t\right) \cos\left(\lambda_n x^1\right) \qquad (C6:1)$$

where $\lambda_n = \dfrac{(2n-1)\pi}{2L}$, and t is time, L total length of the fracture, x^1 coordinate starting from the zero flux boundary and following the fracture and D_a the diffusion coefficient.

The objective of the test case is to verify that the numerical solution is in agreement with the analytical one.
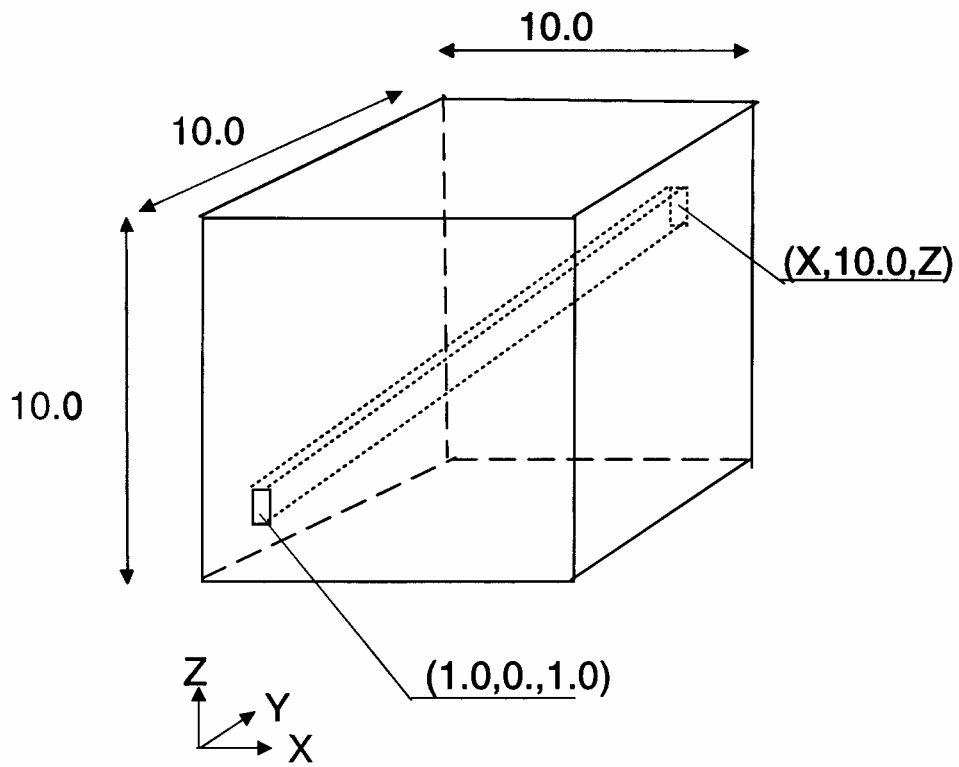
Figure C6:1. *Diffusion in a dead-end fracture. Outline of situation studied. All distances in metres.*

2 Numerical simulation

The time scale of the problem can be estimated as L^2 / D_a. As we are interested in "long time storage of water" we choose $D_a = 10^{-10}$ m²/s, which gives a time scale of the order of $10^{12} s$. The integration time will be 10 000 years, which is equal to $3 \times 10^{11} s$.

The simulation parameters are summarised in Table C6:1, see also Figure C6:1.

Table C6:1. Simulation parameters

Domain	10 x 10 x 10 metres
Initial and Boundary conditions	$c = 1, t = 0$ $c = 0, t > 0$ at $y = 0$ $\partial c / \partial y = 0$ at $y = 10$
Fracture dimension	Height = 0.5 metres, thickness varied (see Result section)
Fracture position	Fixed at $y = 0$ metres boundary (see Figure C6:1), varied at $y = 10$ metres (see Result section)
Diffusion coefficient	10^{-10} m²/s
Grid	$\Delta = 0.1$ metre, uniform.

3 Results / Discussion

Results are presented in Table C6:2. Five downstream fracture positions and four fracture thicknesses were tested. The five downstream fracture positions will give a fracture that, for the first position, is parallel to the *y*- coordinate while the last position gives a fracture that almost follows a diagonal in the box. Note also that the *x* and *z* coordinates for the zero flux boundary are different; this ensures that the fracture will have different angles to all three coordinate directions (except for the first position). The concentration at the zero flux end of the fracture is normalised with the analytically determined concentration, c_a, all after 10^4 years.

Table C6:2. Diffusion in a dead-end fracture. Concentration as represented in the grid, c, normalised with the true concentration, c_a, for various fracture thicknesses and orientations. All for a time of 10 000 years and at the zero flux boundary.

Fracture coordinates at zero flux boundary [m]	Analytically determined concentration, c_a	Concentration (c/c_a)			
		Fracture thickness (b/Δ)			
		0.1	0.5	1.0	2.0
X = 1.0, Z = 1.0	0.588	1.0	1.00	1.00	1.00
X = 3.0, Z = 2.5	0.612	1.05	1.02	1.01	1.01
X = 5.0, Z = 4.0	0.685	1.05	1.02	1.01	1.00
X = 7.0, Z = 5.5	0.772	1.02	1.01	1.01	1.00
X = 9.0, Z = 7.0	0.852	1.00	1.00	1.00	1.00
	Average	1.02	1.01	1.01	1.00

From Table C6:2 one may conclude that accurate concentrations are calculated provided b/Δ is not to small; if b/Δ is larger than 0.5 the error is less than 2%. In Svensson (1999a), it was found that the flow rate through a single fracture in a 3D domain was under-predicted with a few percent. The error in the concentrations has the same origin, as the diffusive flux is represented in the grid by a procedure that is analogous to that of the Darcy flux.

The concentration at the zero flux boundary as a function of time is given in Figure C6:2. As can be seen, the numerical solution is in fair agreement with the analytical one also for the development in time.

4 Conclusion

Accurate diffusive transport is calculated for a single fracture of varying thickness and orientation in a 3D domain, provided the fracture thickness in relation to the grid size is not to small. If $b/\Delta > 0.5$, the maximum error in the calculated concentrations is found to be less than 2%.
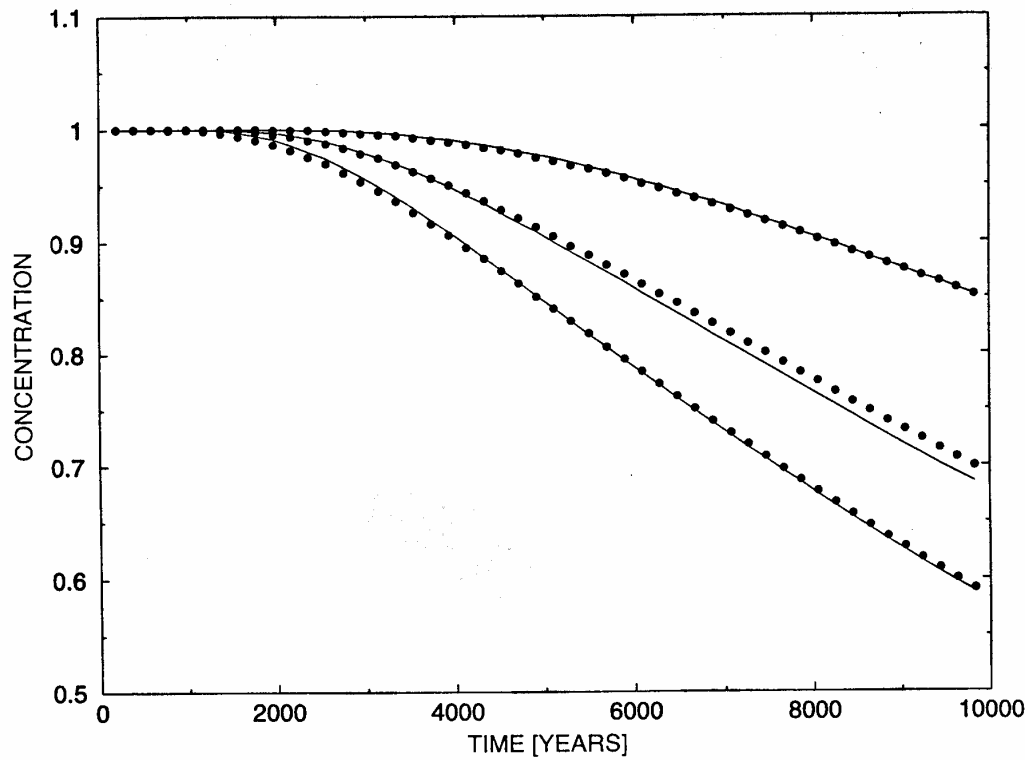
Figure C6:2. *Diffusion in a dead-end fracture. Concentration at the zero flux boundary for three positions of the fracture*
(x = 9.0, z = 7.0 (top) x = 5.0, z = 4.0 (middle) and
x = z = 1.0 (bottom)). Solid line gives the analytical solution.

MATRIX-FRACTURE TEMPERATURE PROBLEM (Case C7)

1 Introduction

This study concerns the convective-conductive processes in a fracture plane and the surrounding rock matrix, see Figure C7:1. A point heat source is located at (7.875, 0.125, 0.125) (cell centre coordinates) and the steady state temperature distribution in the fracture and the rock is sought.

An analytical solution for this case is given by Probert and Claesson (1997). They found that the temperature distribution is governed by a dimensionless parameter, p:

$$p = \frac{\rho_w c_w q_{wc}}{2\lambda} \qquad (C7:1)$$

where,

ρ_w = water density $\left[\text{kg} / \text{m}^3 \right]$

c_w = water heat capacity $\left[J / \text{m}^3 \, {}^\circ C \right]$

q_{wc} = water flow in fracture $\left[\text{m}^3 / \text{ms} \right]$

λ = heat conductivity of the rock $\left[\text{W} / \text{m}^\circ C \right]$

For further details see Probert and Claesson (1997). The objective of this testcase is to compare the numerical and the analytical solution. Two different p-values will be considered.
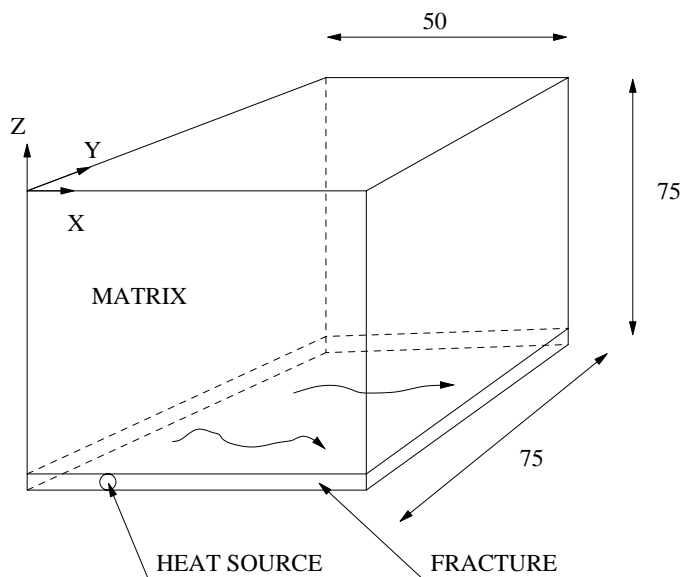
Figure C7:1. *Outline of the situation studied.*

2 Numerical simulation

The general outline of the computational domain is given by Figure C7:1. Additional input data are summarized in Table C7:1. The prescribed pressures at the $x = 0$ and $x = 50$ boundaries will give a uniform flow q_{wc}, in the x- direction.

Note that due to symmetry conditions only one quarter of the domain is specified in the numerical solution.

Table C7:1. Simulation parameters

Domain	$50 \times 75 \times 75 \ \left[m^3 \right]$
Boundary Conditions	$P_{x=0} = 2.93 \times 10^5 \ \left[Pa \right]$ $P_{x=50} = 0.$ Zero flux on other boundaries. Temperature put to zero at $z = z_{max}$, $y = y_{max}$ and at fracture inlet.
Heat source	$600/4 = 150$ [W].
Properties	Viscosity $= 1.78 \times 10^{-3} \ \left[kg / ms \right]$ Fluid heat capacity $= 4200 \ \left[J / m^3 \ {}^\circ C \right]$ Density $= 1 \ 000 \ \left[kg / m^3 \right]$ Porosity $= 0.01$ Permeability $= 10^{-12} \ [m^2]$ Thermal conductivity $= 3.5 \ \left[W / m^\circ C \right]$ Rock thermal capacity $= 2 \times 10^6 \ \left[J / m^3 \ {}^\circ C \right]$
Grid	$NX = 120$, $NY = 100$, $NZ = 100$, expanding from the heat source.

3 Results / Discussion

The numerical solution is compared with the corresponding analytical solution for $p = 1$, Figure C7:2, and $p = 5$, Figure C7:3. As can be seen, a good agreement is obtained for both p values.

The numerical solution was found to be sensitive to the boundary conditions at $z = z_{max}$ and $y = y_{max}$. It was hence necessary to increase the domain size in these directions until the near source temperature fields were unaffected by the boundary conditions. This explains the large domain size in these directions.

4 Conclusion

The temperature distribution in a fracture-matrix system is studied. A good agreement between the numerical and analytical solutions has been demonstrated.
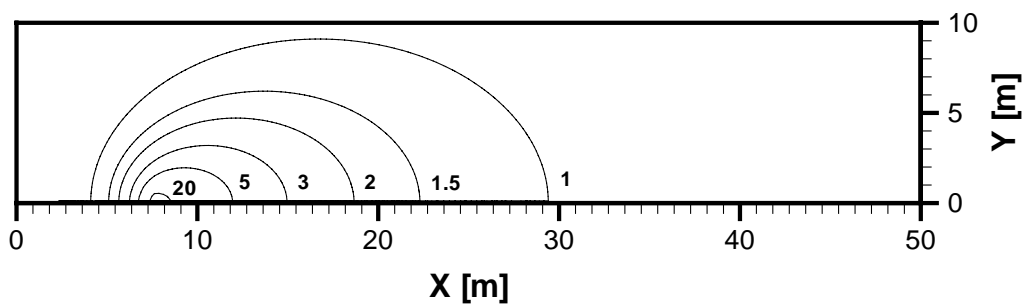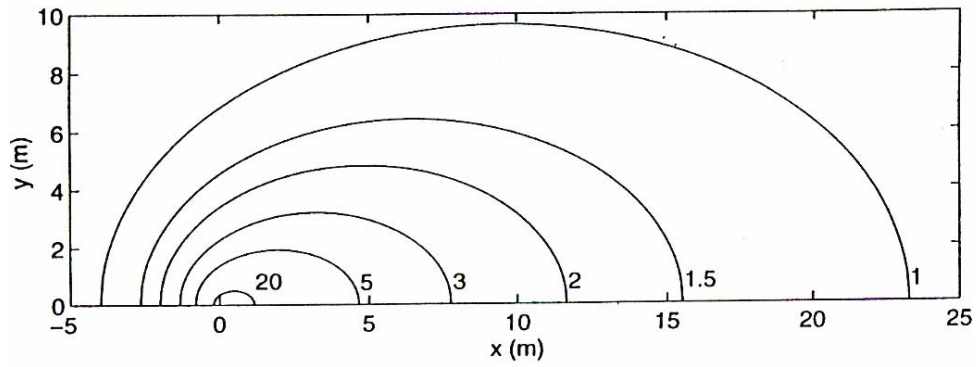
Figure C7:2. *Temperature distribution in the fracture plane for p = 1. Analytical (top) and numerical solution. Note that the origo in the x-direction is different in the two figures.*
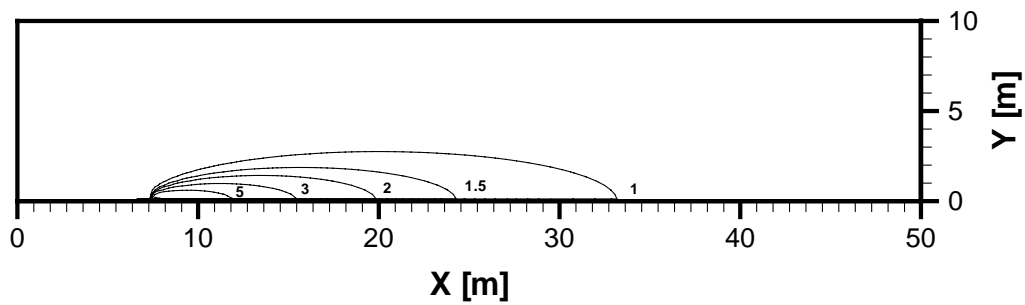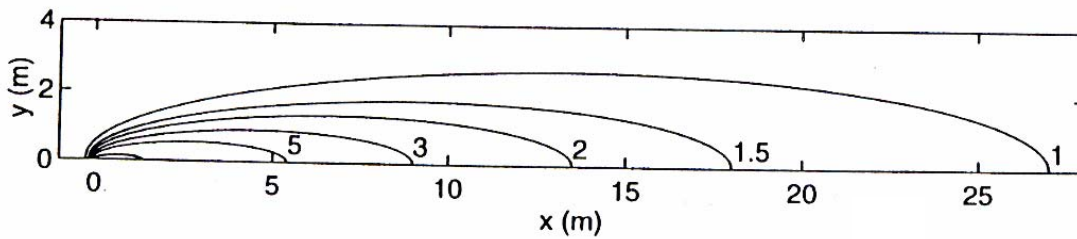
Figure C7:3. *Temperature distribution in the fracture plane for p = 5. Analytical (top) and numerical solution. Note that the origo in the x-direction is different in the two figures.*

TAYLOR DISPERSION,PARTRACK (CASE D1)

1 Introduction

If a cloud of particles is introduced in a fully developed flow between two parallel walls, the particles will be dispersed longitudinally at a rate given by (Sahimi, 1995):

$$D_L = \frac{2}{105}\frac{h^2 u^2}{D_m} \qquad\qquad (D1:1)$$

where D_L is the longitudinal dispersion coefficient, h half the aperture, u the mean velocity and D_m the molecular diffusion coefficient of the solute the particles represent. When we use PARTRACK to simulate Taylor dispersion we subdivide the space between the two walls into a number of layers.
The objective of this testcase is to verify that PARTRACK predicts Taylor dispersion correctly.

2 Numerical simulations

Input data are summarised in Table D1:1.

Table d1:1. Simulation parameters

Domain	$10 \times 0.1 \times 5 \times 10^{-4} \; \left[m^3 \right]$
Boundary Conditions	At $x = 0$ a fixed flux is prescribed, at x 0 10 the pressure is fixed to zero 10 000 particles were injected as a Dirac pulse ay $x = 0$
Properties	The fixed flux conditions gives a velocity of 10^{-4} m/s, other properties are of no significance. Molecular diffusion coefficient D_m is varied
Grid	$NX = 100$, $NY = NZ = 1$

3 Result / Discussion

Three runs, with D_m equal to 10^{-9}, 10^{-10} and 10^{-11} m²/s respectively, were carried out in order to compare the simulated dispersion with Equation D1:1. The result can be studied in Figure D1:1. From the breakthrough curves the mean arrival time and the standard deviation, σ, was calculated. The standard deviation is then related to the longitudinal dispersion coefficient, D_L ($s = \sqrt{2D_L t}$, where t is the mean transport time). As can be seen a perfect agreement between the analytically determined and simulated dispersion is obtained. The breakthrough curves, also shown in Figure D1:1, show that the Taylor dispersion effect is small for $D_m = 10^{-9}$ m²/s, while a significant spread is obtained for $D_m = 10^{-11}$ m²/s. This result is of course related to the parameters and geometry used in this testcase.
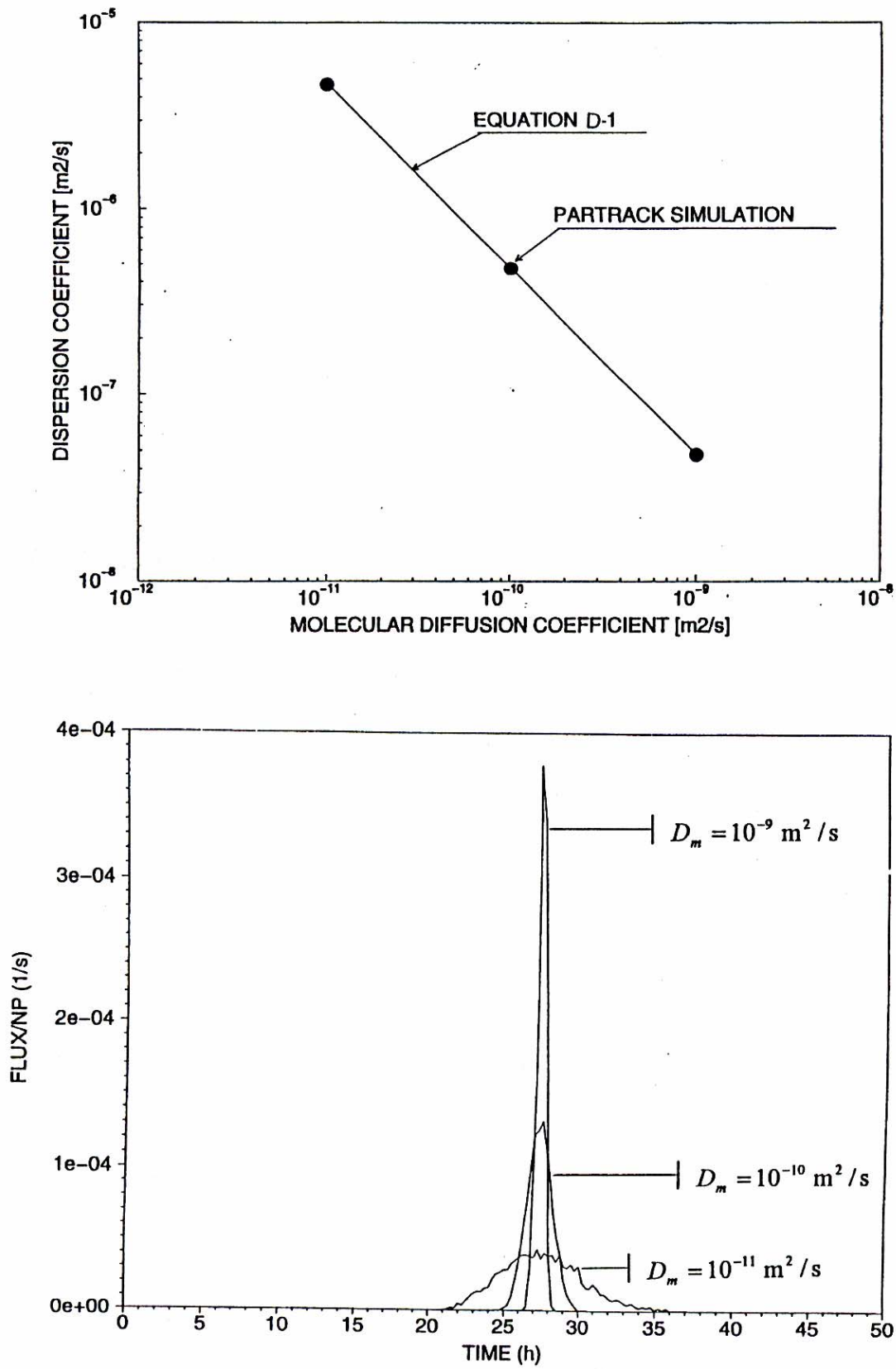
Figure D1:1. *Taylor dispersion in a single fracture. Comparison with Equation D1:1 (top) and breakthrough curves.*

4 Conclusion

The results presented show that PARTRACK predicts Taylor dispersion in perfect agreement with the analytical solution.

BREAK-THROUGH-CURVE, PARTRACK (CASE D2)

1 Introduction

The objective of this study is to compare the solutions given by DarcyTools with the analytical solutions for single rate diffusion. The multi-rate diffusion model in DarcyTools is hence "degenerated" to a single rate model; this is done by specifying the late time slope, k, to -3/2.

The situation studied is outlined in Figure D2:1. A channel with constant width and aperture is bounded by an infinite matrix. A Dirac pulse injection is prescribed and the BTC at the outlet is studied.

The analytical solution of the equation describing this case is given by, for example, Barten (1996), Cvetkovic et al. (1999) and Neretnieks (2002). It can be written as:

$$m = \Theta(t-\alpha)\frac{\gamma}{2\sqrt{\Pi}}(t-\alpha)^{-3/2}\exp\left(-\frac{\gamma^2}{4(t-\alpha)}\right) \qquad (D2:1)$$

where m is mass flux at the outlet, $\Theta(t)$ Heaviside step function and t time. The two parameters α and γ are defined as:

$$\alpha = R_m\theta_m L / q, \qquad (D2:2)$$

$$\gamma = L\delta_f\theta_{im}\sqrt{D_w R_{im}} / q \qquad (D2:3)$$

with definitions of parameters as given in Table D2:1, below.

Figure D2:1. *Outline of situation studied.*

2 Numerical simulations

A reference case is given by the values specified in Table D2:1. The two parameters $\alpha_{\min}$ and $\alpha_{\max}$ are chosen to give a large enough range of capa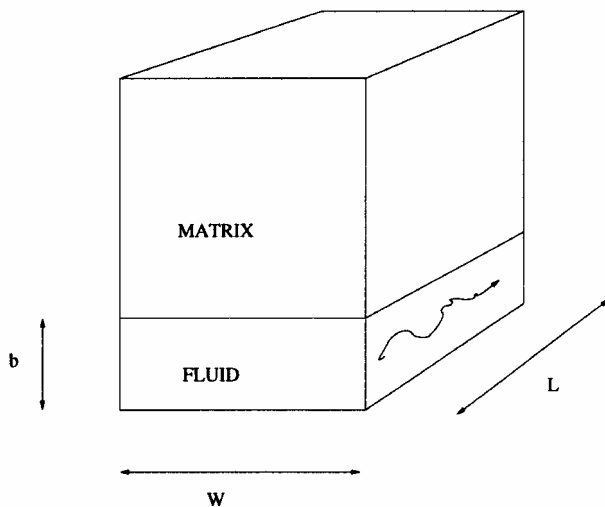city boxes. The specification of these does however influence the setting of β_n, the volume ratio for a non sorbing tracer. The analytical solution is for an infinite matrix, while a specification of $\alpha_{\min}$ implies a limitation. The method to calculate β_n for such a case is described in Part A.

Table D2:1. Simulation parameters.

Domain	$L = 10.0, W = 0.1, b = 0.5 \times 10^{-3}$
	Surface to volume ratio: $\delta_f = 1/b$
Properties	Porosity mobile zone: $\theta_m = 1.0$
	Porosity immobile zone: $\theta_{im} = 0.05$
	Retention mobile zone: $R_m = 1.0$
	Retention immobile zone: $R_{im} = 1.0$
	Diffusivity: $D_w = 10^{-10}$
	Volume ratio: β_n = 20.85
Transport	Flow velocity: $q = 10^{-5}$
	Injection: Dirac pulse
	$\alpha_{\min} = 10^{-9} / R_{im}$
	$\alpha_{\max} = 5 \times 10^{-2} / R_{im}$

3 Result / Discussion

For the reference data a perfect agreement with the analytical solution is obtained, see Figure D2:2. For the cases to follow β was evaluated as: $\beta = \dfrac{R_{im}V_{im}}{R_m V_m} = \dfrac{R_{im}}{R_m} \times \beta_n$.

In Figure D2:3 the effect of changing R_m and R_{im} by a factor of five can be studied. The change from the reference case is calculated correctly.

Figure D2:4 shows consistency checks, which are based on the parameters α and γ, given by (D2:2) and (D2:3) respectively. In the first case (Figure D2:4, top), R_m, q and θ_{im} were all increased by a factor of 2.0. As both α and γ remain the same, the BTC should be unaffected. This is also found. Similarly we may increase θ_{im} with a factor of two and decrease D_w with a factor of four and still get the same BTC, which is also the case (Figure D2:4, bottom).

4 Conclusion

It is clear that the numerical solutions, based on a particle tracking technique, is in good agreement with the analytical solution of the governing advection/diffusion equation.

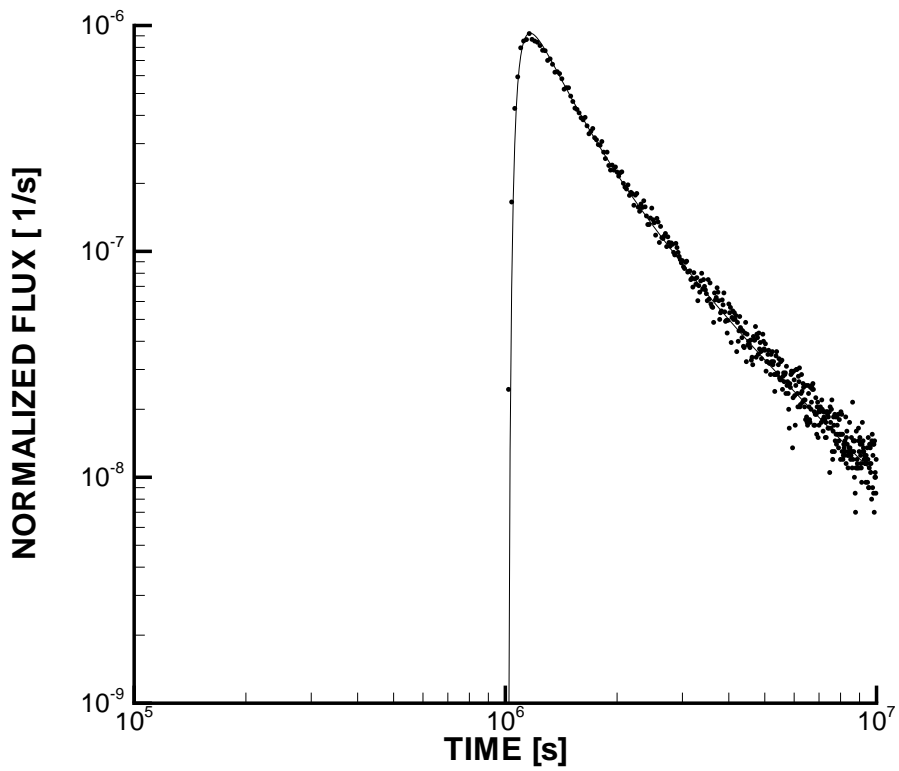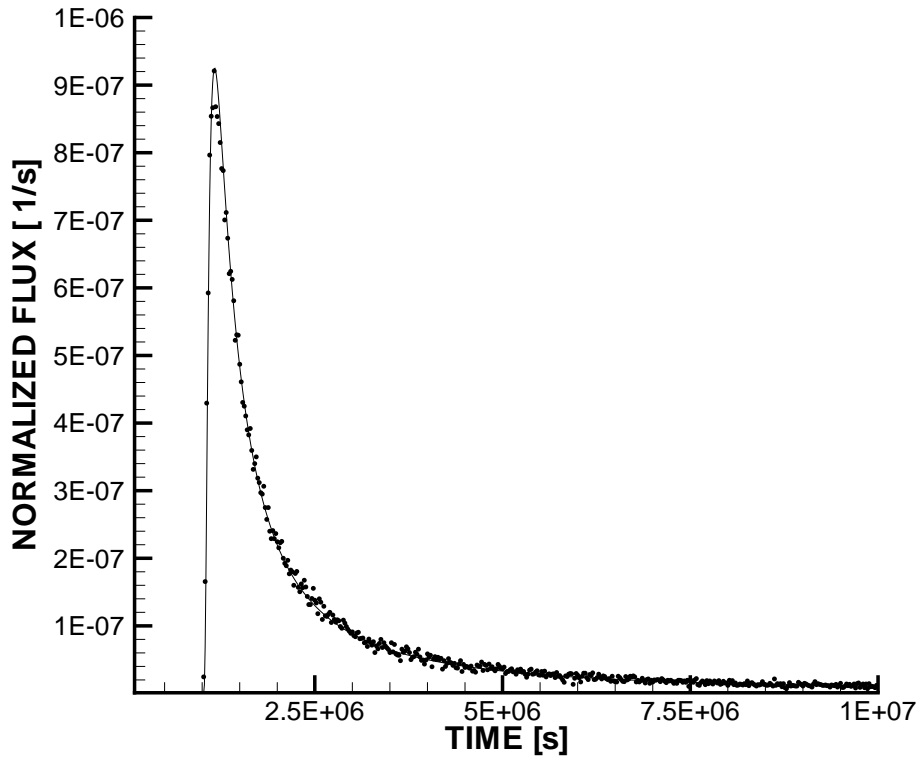**Figure D2:2.** *Comparison with the analytical solution for the reference parameters. Linear scale (top) and log-log scale. Solid line gives analytical solution.*
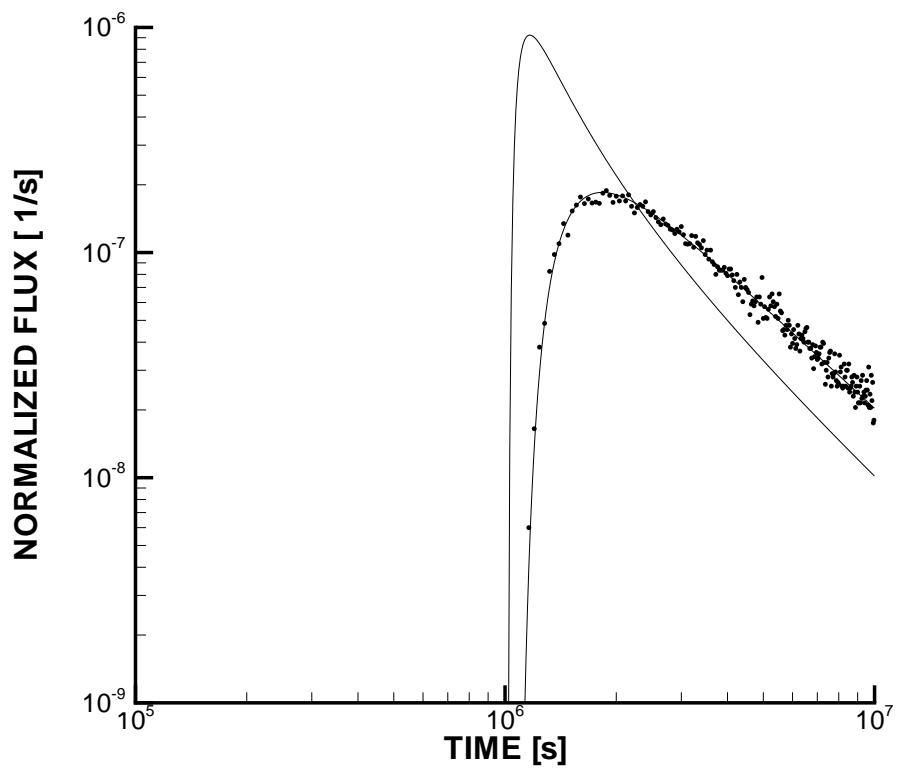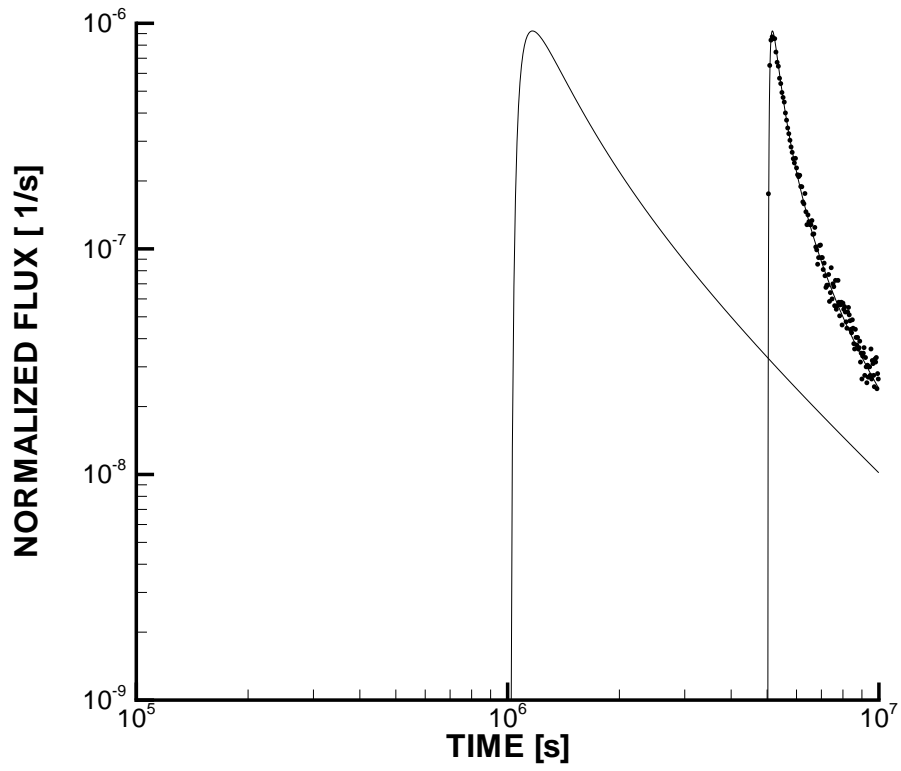
Figure D2:3. *Effect of changing* R_m *(top) and* R_{im} *by a factor of five. Solid line gives analytical solution.*
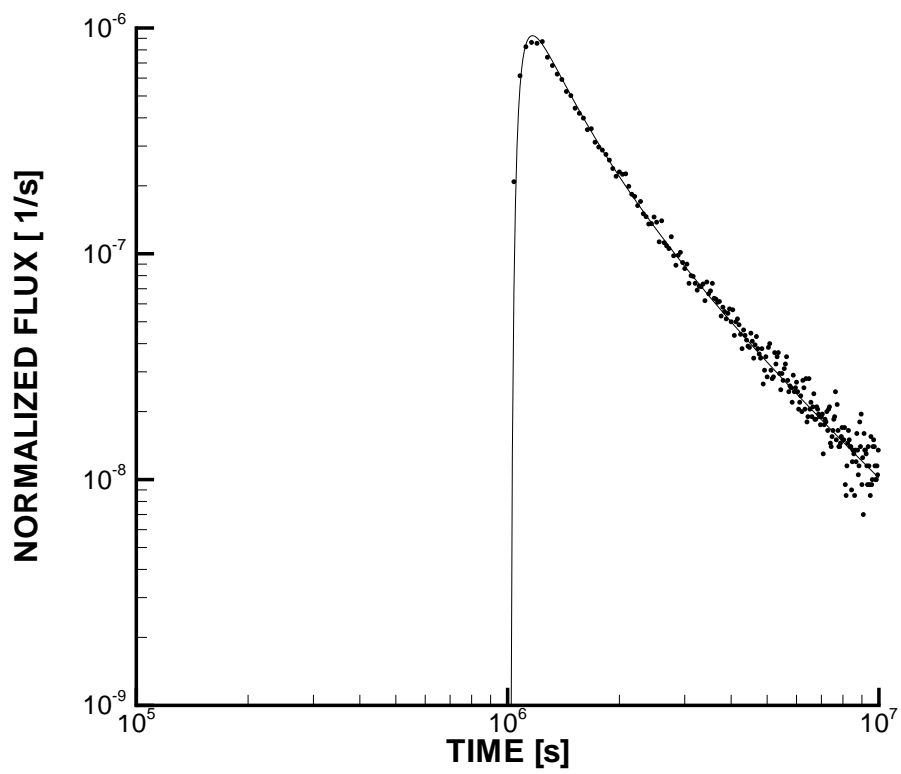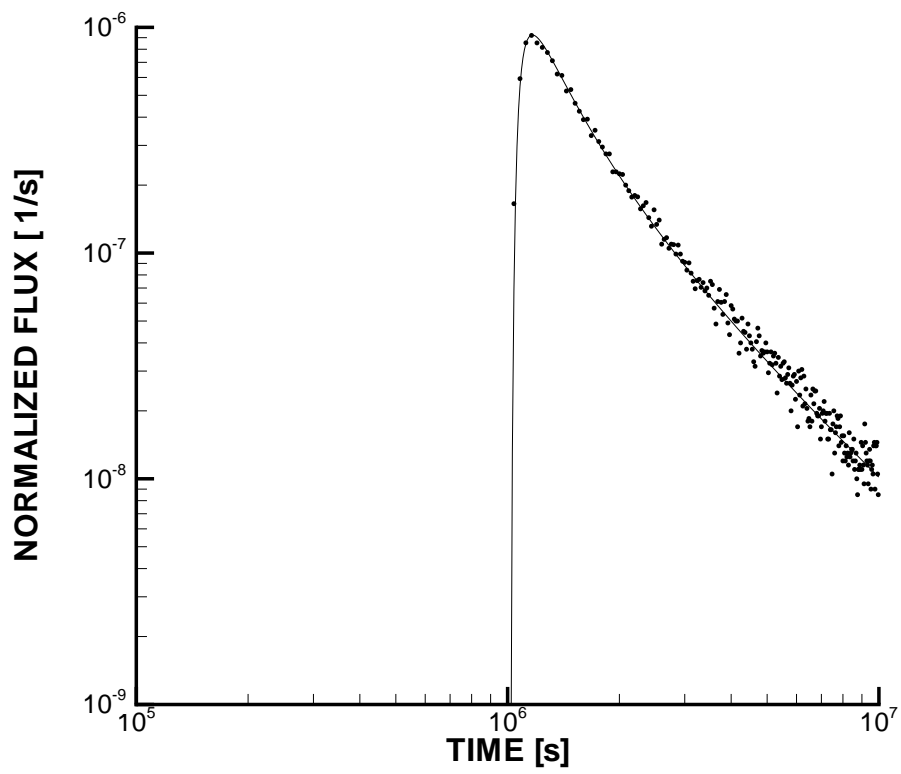
Figure D2:4. *Consistency checks. R_m, q and θ_{im} increased (top), θ_{im} increased and D_w decrease*

BREAK-THROUGH-CURVE, ADV/DIFF EGN (CASE D3)

1 Introduction

The objective of this study is to compare the solutions given by DarcyTools with the analytical solutions for single rate diffusion. The multi-rate diffusion model in DarcyTools is hence "degenerated" to a single rate model; this is done by specifying the late time slope, *k*, to -3/2.

The situation studied is outlined in Figure D3:1. A channel with constant width and aperture is bounded by an infinite matrix. A Dirac pulse injection is prescribed and the BTC at the outlet is studied.

The analytical solution of the equation describing this case is given by, for example, Barten (1996), Cvetkovic et al. (1999) and Neretnieks (2002). It can be written as:

$$m = \Theta(t - \alpha)\frac{\gamma}{2\sqrt{\Pi}}(t - \alpha)^{-3/2}\exp\left(-\frac{\gamma^2}{4(t - \alpha)}\right) \qquad (D3:1)$$

where *m* is mass flux at the outlet, $\Theta(t)$ Heaviside step function and *t* time. The two parameters α and γ are defined as:

$$\alpha = R_m\theta_m L / q, \qquad (D3:2)$$

$$\gamma = L\delta_f\theta_{im}\sqrt{D_wR_{im}} / q \qquad (D3:3)$$

with definitions of parameters as given in Table D3:1, below.
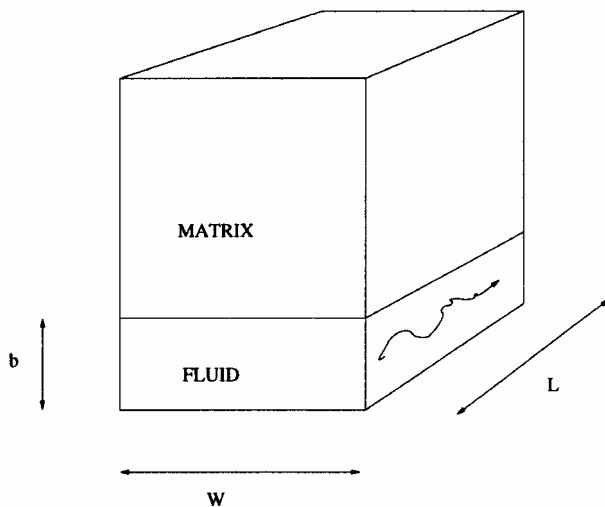
Figure D3:1. *Outline of situation studied.*

2 Numerical simulations

The case is given by the values specified in Table A1. The two parameters $\alpha_{\min}$ and $\alpha_{\max}$ are chosen to give a large enough range of capacity boxes. The specification of these does however influence the setting of β_n, the volume ratio for a non sorbing tracer. The analytical solution is for an infinite matrix, while a specification of $\alpha_{\min}$ implies a limitation. The method to calculate β_n for such a case is described in Part A.

Table D3:1. Simulation parameters.

Domain	$L = 10.0, W = 0.1, b = 0.5 \times 10^{-3}$
	Surface to volume ratio: $\delta_f = 1/b$
Properties	Porosity mobile zone: $\theta_m = 1.0$
	Porosity immobile zone: $\theta_{im} = 0.05$
	Retention mobile zone: $R_m = 1.0$
	Retention immobile zone: $R_{im} = 1.0$
	Diffusivity: $D_w = 10^{-10}$
	Volume ratio: β_n = 20.85
Transport	Flow velocity: $q = 10^{-5}$
	Injection: Dirac pulse
	$\alpha_{\min} = 10^{-9} / R_{im}$
	$\alpha_{\max} = 5 \times 10^{-2} / R_{im}$

3 Result / Discussion

As the numerical solution is based on the advection/diffusion equation it is expected that numerical diffusion will influence the predicted break-through-curve. This is also seen in Figure D3:2, where predicted BTC is compared with the analytical one. A fair agreement is however found.

4 Conclusion

The numerical solutions, based on an advection/diffusion equation, is in fair agreement with the analytical solution of the governing equation.
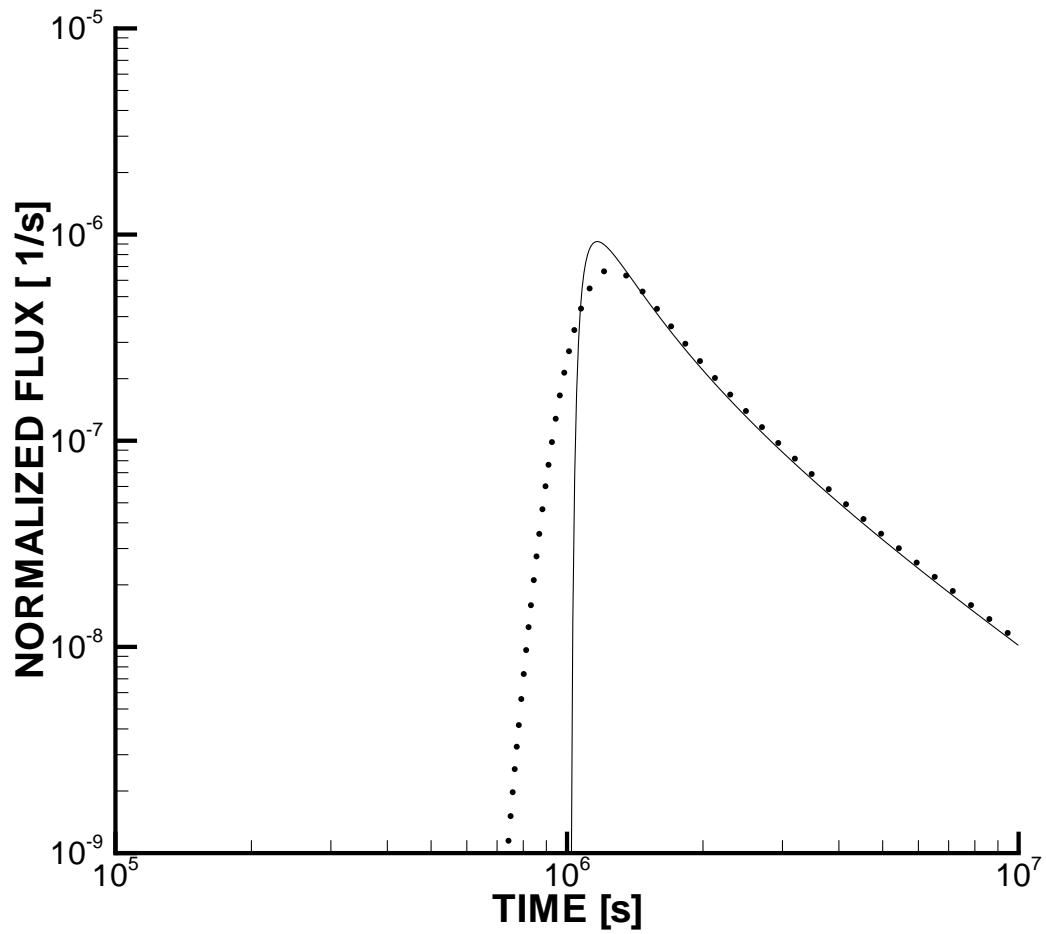
Figure D3:2. *Comparison with analytical solution (solid line).*

SEVEN FRACTURES IN A 2D DOMAIN, PARTRACK (CASE D4)

1 Introduction

The two dimensional fracture network considered is shown in Figure D4:1. A pressure gradient is applied, to give a flow from left to right with a pore velocity of about 10^{-4} m/s.

This case is of interest for the following reasons:

- It is possible to determine the flow in each part of the fracture network analytically.

- If we assume complete mixing in fracture intersections, one can determine analytically how a cloud of particles, injected at the upstream side, will leave through the outlets.

The analytical solution gives the flow-rates in each of the fracture sections. If we inject a cloud of particles in fracture A-A, it will split up in fracture intersections in proportion to the flow rates (assuming complete mixing in fracture intersections). The fractions at the outlet plane are given in Figure D4:1, assuming that all fractures have the same transmissivity.

The objective is to verify that the numerical solution is in agreement with the analytical one. In particular it is of interest to see how a particle cloud is split up at intersections.
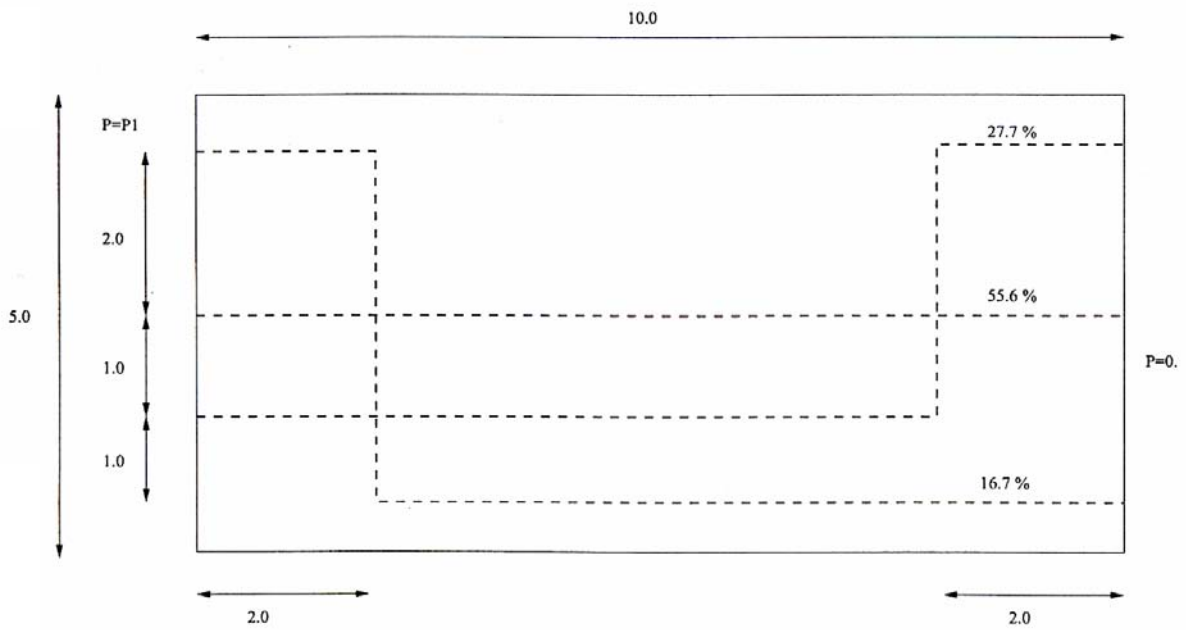
Figure D4-1. *A fracture network. Outline of situation studied. The %-figures give the proportions for the split-up of a tracer cloud at the outlet boundary (assuming complete mixing).*

2 Numerical simulations

The size of and fracture system in the domain is given in Figure D4:1. Additional input data are summarised in Table D4:1.

Table D4-1. Simulation parameters

Domain	$2D, 10 \times 5 \left[m^2 \right]$
Boundary Conditions	$p_{x=0} = 9810 \left[Pa \right]$ $P_{x=10} = 0$ zero flux on other boundaries.
Properties	Density = 1 000 [kg/m^3] Viscosity = 2.0×10^{-3} [kg/ms] Permeability = 2.0×10^{-12} [m^2]
Grid	$NX = 400$, $NY = 200$, uniform

3 Result / Discussion

First a steady flow calculation is performed then 100 000 particles are injected in Fracture A-A at $x = 0$. From the analytical solution we know the flow in each part of the channel system and it is hence possible to calculate how a cloud of particles will split up at a fracture intersection. The underlying assumptions is that the cloud will be split up in proportions to the outgoing flows at the intersection, i.e. the "fully mixed assumption".
The result is summarised in Table D4:2. An almost perfect agreement is found.

Table D4-2. Distribution of particles at the boundary $x = 10$.

Solution	Outlet		
	top	middle (A-A)	bottom
Analytical	27.7%	55.6%	16.7%
Numerical	27.8%	55.6%	16.6%

4 Conclusion

It has been shown that the "well mixed assumption at fracture intersections" is correctly implemented in the numerical algorithms.

THREE FRACTURES IN A 2D DOMAIN
(Case D5)

1 Introduction

The two dimensional fracture network considered next is shown in Figure D5:1. A pressure gradient is applied, to give a flow from left to right with a pore velocity of about 10^{-4} m/s.

This case is of interest for the following reasons:

- It is possible to determine the flow in each part of the fracture network analytically.

- The transport time for a particle is known, whatever path it takes.

- If we assume complete mixing in fracture intersections, one can determine analytically how a cloud of particles, injected at the upstream side, will leave through the outlets.

The analytical solution gives the flow-rates in each of the fracture sections. If we inject a cloud of particles in fracture B-B, it will split up in fracture intersections in proportion to the flow rates (assuming complete mixing in fracture intersections). These fractions are given in Figure D5:1, assuming that all fractures have the same transmissivity. From the analytical solution we can thus get both the arrival time and size of each breakthrough pulse. In the numerical solution of the flow field we assume that the kinematic porosity of the fractures is equal to 0.05. The fracture thickness, b, will be varied in order to test a range of ratios b/Δ, where Δ is the grid size (equal to 0.1 metre). In all simulations 10^5 particles were injected in fracture B-B.

The main objective is to verify that the numerical solution is in agreement with the analytical one. It is a part of this objective to evaluate the sensitivity to the ratio b/Δ.

2 Numerical simulations

Input data are summarized in Table D5:1.

Table D5:1. Simulation parameters.

Domain	2D 10 x 5 metres
P_1	9810 *Pa*
Fracture Conductivity	5×10^{-5} m/s
Fracture thickness	b/Δ varied: 0.1, 0.5, 1.0 and 2.0
Grid	400 x 200 cells, $\Delta = 0.025$ m

3 Result / Discussion

We first calculate the flow and porosity fields by the flow model. A cloud of particles, injected in fracture B-B, is then tracked by PARTRACK. The result can be studied in Figure D5:2. In order to understand the result one may first note that the transport time in fracture B-B is 27.8 hours and that all other pathways have longer transport times. The size of the pulses is explained by noting that 100% enters in fracture B-B, about 50% go each way in each crossing. The first pulse that leaves fracture B-B will thus contain about 25% of the injected pulse. It will however not be exactly 25% as the flow rates in the fracture sections are not exactly the same. As seen in Figure D5:2, the numerical solution is in good agreement with the analytical solution. One may question why we do not get an exact agreement. The answer is probably that we do not get the assumed split up of the particle cloud in fracture intersections. In the analytical solution we assumed that the cloud will split up in proportion to the outflows. In the numerical solution, we solve for the flow and transport in the intersection. The effect can be noted in the intersection between fractures A-A and C-C. The particles arrive in fracture A-A and should split up in about equal fractions in the two outlets. From Figure D5:2 it is seen that the numerical solution gives fewer particles in fracture A-A, as compared to the analytical solution. This is probably due to the local flow pattern in the fracture intersection. In the literature, see for example Park and Lee (1999), two concepts for solute transport in a fracture intersection are used; "complete mixing" and "streamline routing". The effect described is due to streamline routing in the fracture intersection.

The results given in Figure D5:2 are based on a fracture thickness, b, of 0.05 m $(b/\Delta = 0.5)$. The sensitivity to the fracture width is presented in Table D5:2, where results for $b/\Delta = 0.1,\ 0.5,\ 1.0$ and 2.0 are given. It is seen that the transport time does not vary strongly with b/Δ, while the size of the breakthrough pulse depends strongly on b/Δ (see for example fracture A-A). As discussed above, this is due to the two dimensional representation of the fracture intersection.

4 Conclusion

The transport times for a simple two dimensional fracture network are in agreement with the analytical solution. The simulated partitioning of a particle cloud in a fracture intersection is close to complete mixing for small fracture thicknesses, while the streamline routing effect is important when $b > \Delta$.
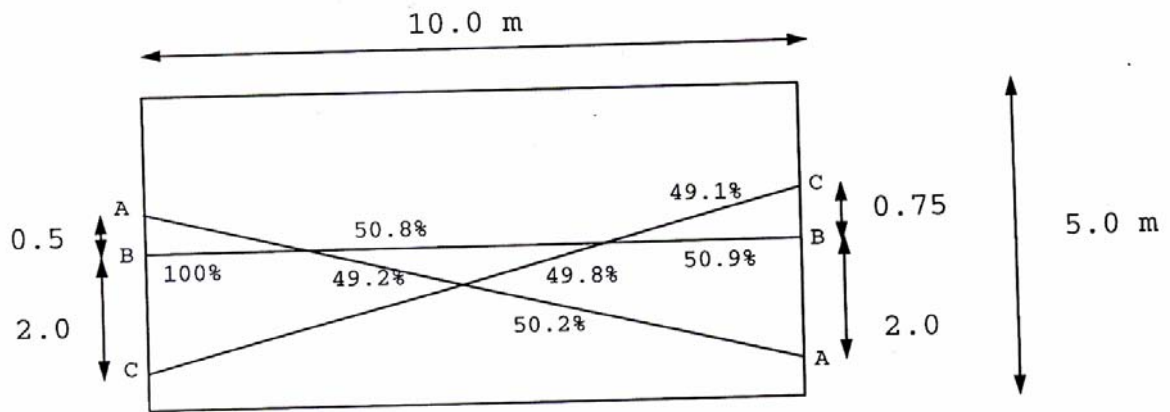
Figure D5:1. *A fracture network. Outline of situation studied. The %-figures give the proportions for the split-up of a tracer cloud at the three fracture intersections (assuming complete mixing).*
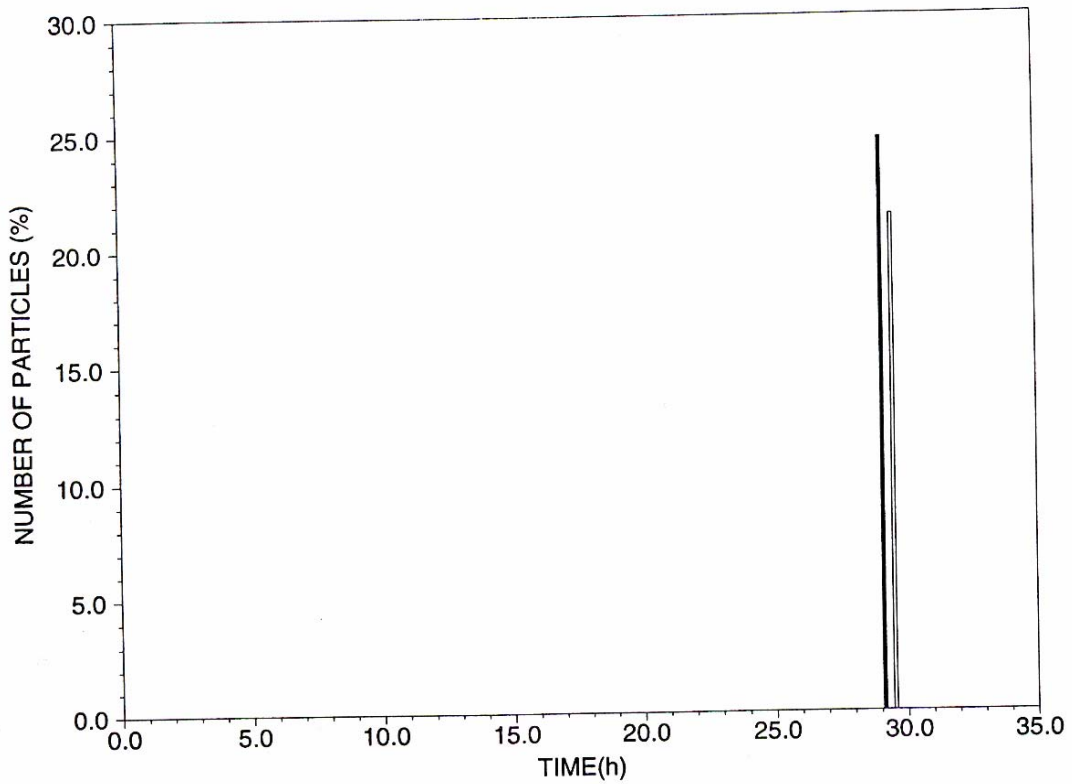
Figure D5:2. *A fracture network. Breakthrough curve in fracture A-A. Solid bar gives the analytical solution.*
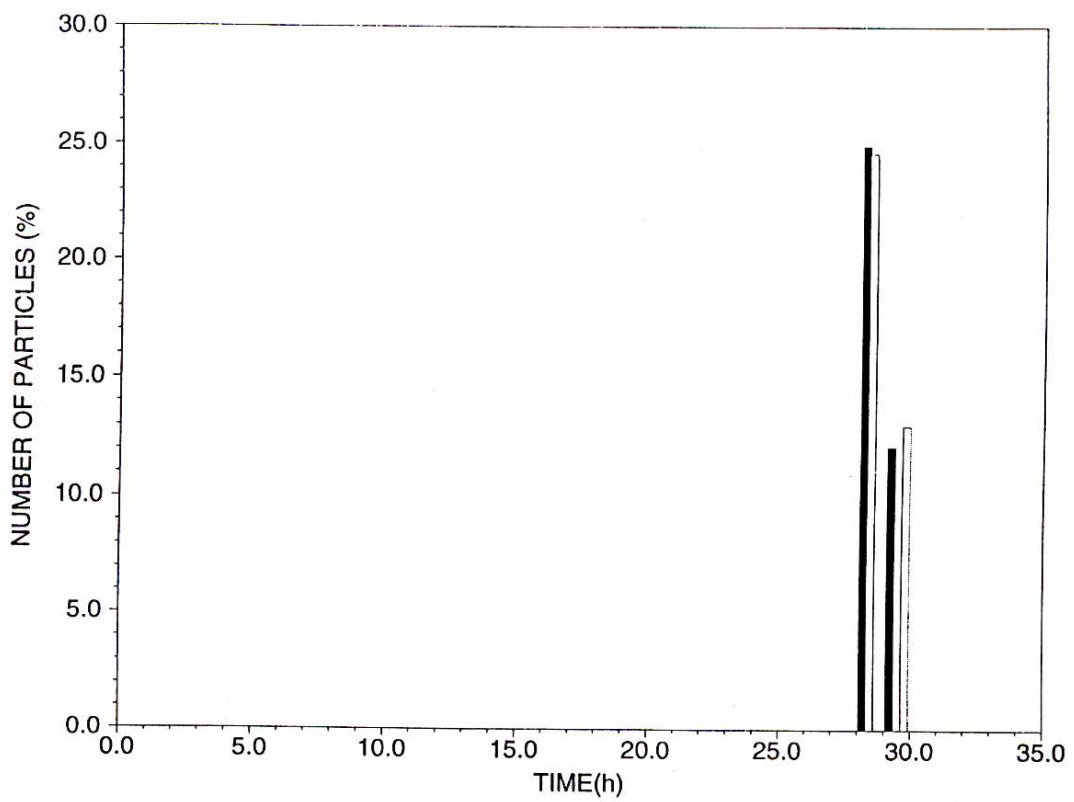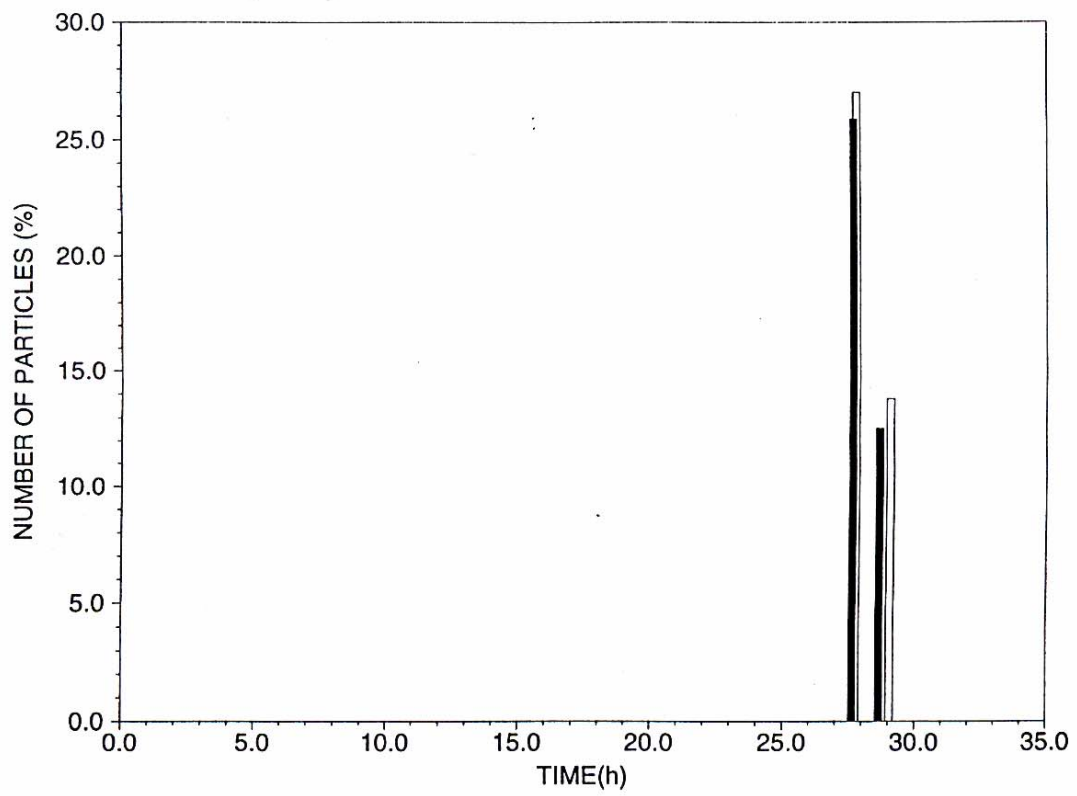
Figure D5:2. Cont. *Breakthrough curves in fractures B-B (top) and C-C.*

Table D5:2. A fracture network. Breakthrough curves (time, *t*, and fraction, *f*) in various fracture outlets as a function of normalised fracture thickness (*b/Δ*).

Breakthrough curve in fracture	Analytical solution		Fracture thickness normalised with Δ (*b/Δ*).							
			0.1		0.5		1.0		2.0	
	$t_a(h)$	$f_a(\%)$	t/t_a	f/f_a	t/t_a	f/f_a	t/t_a	f/f_a	t/t_a	f/f_a
A-A	29.2	24.7	1.02	0.94	1.02	0.95	1.00	0.75	1.00	0.50
B-B	27.7	25.8	1.00	1.02	1.00	1.02	1.00	1.01	0.99	0.90
B-B	28.8	12.5	1.01	1.06	1.01	1.05	0.98	1.20	0.95	1.87
C-C	28.3	24.9	1.01	1.00	1.00	1.00	1.00	1.09	1.00	1.00
C-C	29.4	12.1	1.02	0.99	1.02	0.99	1.01	1.09	1.00	1.31

SINGLE FRACTURE IN A BOX, PARTRACK (Case D6)

1 Introduction

This test case is the same as used in Case C3, to evaluate how the flow rate through a single fracture varied with the orientation and thickness of the fracture. The situation studied is outlined in Figure D6:1. The pressure is held constant on two opposite faces ($y = 0.0$ m and $y = 10.0$ m) and a zero flux condition is used on all other boundaries. At the inflow boundary the position of the fracture is fixed, with centreline coordinates (1.0, 0.0, 1.0). The fracture position at the downstream boundary is varied in order to test a wide range of angles to the coordinate directions. Also a range of thicknesses were tested, but the height of the fracture was kept constant at 0.5 metres.

For each of the situations studied, a steady state flow calculation is first performed. PARTRACK is then used to calculate the transport time from the inlet to the outlet.

The objective is to verify that PARTRACK gives correct transport times for fractures of different thicknesses and orientations. As the flow and porosity is calculated in the flow model, the test case also evaluates the integrated performance of the flow and transport model.

Figure D6:1. *Outline of situation studied. A single fracture in a 3D domain. Outline of situation studied. All distances in metres.*

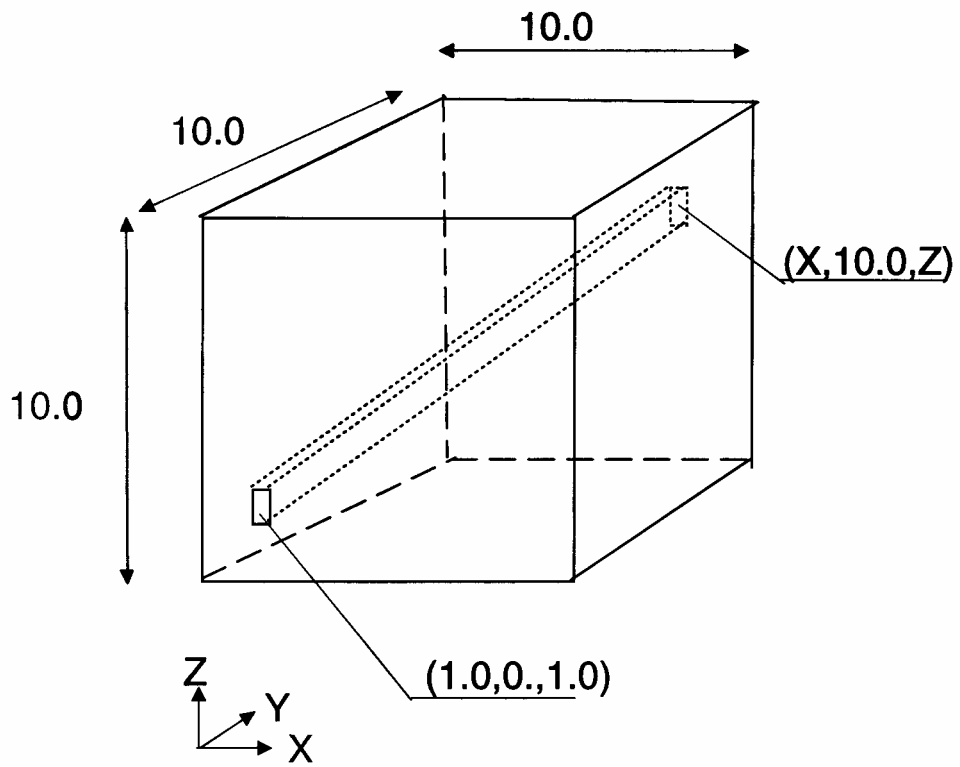# 2 Numerical simulations

Most of the simulations parameters are introduced in Figure D6:1, some further details are summarised in Table D6:1.

A systematic variation of the fracture thickness and the downstream position will be in focus in the simulations.

Table D6:1. Simulation parameters.

Domain	$10 \times 10 \times 10$ [m^3]
Boundary conditions	Fixed pressure difference (= 1 metre head) between two opposite faces. Zero flux on other faces
Fracture dimensions	Height = 0.5 metres, thickness varied (see Result section)
Fracture position	Fixed at inflow boundary (see Figure D6:1), varied at outflow boundary (see Result section)
Fracture conductivity	10^{-4} m/s
Grid	$\Delta = 0.1$ metre, uniform

3 Result / Discussion

Results are presented in Table D6:2. Five downstream fracture positions and four fracture thicknesses were tested. The five downstream fracture positions will give a fracture that, for the first position, is parallel to the y- coordinate while the last position gives a fracture that almost follows a diagonal in the box. Note also that the x and z coordinates for the downstream positions are different; this ensures that the fracture will have different angles to all three coordinate directions (except for the first position). The transport times are normalised with the analytically determined transport time, t_a, which is easily obtained from the specified pressure gradient, kinematic porosity and fracture length.

From Table D6:2, one may conclude that accurate transport times are calculated provided b/Δ is not too small; if b/Δ is larger than 0.5 the error is less than 3%. In Case C3 it was found that the flow rate through a single fracture in a 3D domain was underpredicted with a few percent. The error in the transport times is thus mainly due to the error in the flow rates, which can be concluded from a comparison with Table 4-2 in Case C3.

It is also of interest to note that the spread of the breakthrough curve in all simulations was small. Ideally all particles should arrive at the same time, but some numerical dispersion is present as particles will have different flow paths. The standard deviation of the breakthrough curve was however always less than 2% of the transport time and the numerical dispersion effect is hence small (as compared to other effects to be discussed).

4 Conclusion

Accurate transport times are calculated for a single fracture of varying thickness and orientation in a 3D domain, provided the fracture thickness in relation to the grid size is not too small. If $b/\Delta > 0.5$, the maximum error in the calculated transport time is found to be less than 3%.

Table D6:2. A single fracture in a 3D domain. Transport time as represented in the grid, t, normalised with the true transport time, t_a, for various fracture thicknesses and orientations.

Fracture coordinates at downstream boundary [m]	Analytically determined transport time, t_a [h]	Transport time (t/t_a)			
		Fracture thickness (b/Δ)			
		0.1	0.5	1.0	2.0
X = 1.0, Z = 1.0	27.50	1.00	1.00	1.00	1.00
X = 3.0, Z = 2.5	29.02	1.06	1.02	1.01	1.00
X = 5.0, Z = 4.0	34.37	1.08	1.03	1.01	1.00
X = 7.0, Z = 5.5	42.97	1.04	1.02	1.01	1.00
X = 9.0, Z = 7.0	54.98	1.02	1.01	1.00	1.00
	Average	1.04	1.02	1.01	1.00

HENRY'S PROBLEM
(Case E1)

1 Introduction

Henry's problem is the most widely used, classic, test case for density stratified simulations. The basic situation in mind is that of sea water intrusion into a fresh water aquifer, see Figure E1:1. At the left boundary, the inland boundary, a fixed fresh water inflow is specified while the right side boundary has a prescribed hydrostatic pressure distribution based on a given salinity. The top and bottom boundaries are of zero mass flux type.

Henry's problem is discussed in detail in Ségol (1994), where also Henry's analytical solution and a number of numerical solutions are presented and discussed. The present study will be based on, and make reference to, the review of Henry's problem as given in Ségol (1994).

The objective of the test case is to simulate Henry's problem and compare the result with Henry's analytical solution and results from other model (all as presented in Ségol, 1994).
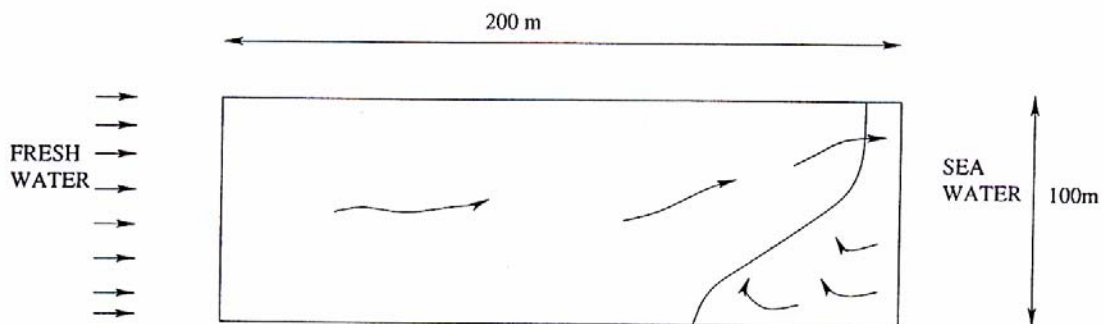

Figure E1:1. *Illustration of Henry's, or the seawater intrusion, problem.*

2 Numerical simulations

The numerical simulation will be based on the parameters and boundary conditions specified in Table E1:1, see also Figure E1:1. We are seeking the steady state solution and the initial conditions are hence of no importance. The data within brackets in Table E1:1 are the values specified in Ségol (1994); here SI units are used throughout.

Table E1:1. Parameters for Henry's problem.

Domain	Rectangular section with a length of 200 m and a depth of 100 m
Hydraulic Conductivity	1.157×10^{-5} m/s (= 1m/day)
Density difference	25 kg/m^3
Porosity	0.35
Dispersion coefficient	7.639×10^{-7} m^2/s (= 0.066 m^2/day)
Fresh water inflow	7.639×10^{-8} m^3/m^2, s
Grid	Coarse: $\Delta = 4$m (NX = 50, NZ = 25), uniform Fine: $\Delta = 2$m (NX = 100, NZ = 50), uniform

3 Result / Discussion

Henry's analytical solution, and a number of numerical simulations, are shown in Figure E1:2. The sharp interface solution is the solution obtained if no mixing occurs between the salt and fresh water; this solution is included only as a reference. It is seen that Henry's solution gives a penetration length of about 90 metres, while the numerical models, shown in the same figure, give a penetration length of about 80 metres. DarcyTools is found to give a penetration length of about 85 metres.

This is a grid independent solution as can be seen in Figure E1:3; reducing the cell size with a factor of two does not change the penetration length.

One may question why the numerical models are not closer to the analytical solution. One possibility is the type of boundary conditions used at the "seaward side". Some model studies fixed the depth of the mixed water outflow region, while others let the model decide the depth of the division point between inflow and outflow. In the present study a hydrostatic assumption based on a fixed density difference was used for the whole vertical. Further discussions about possible causes of deviations between numerical and analytical solutions can be found in Ségol (1994).

4 Conclusion

It has been demonstrated that a grid independent solutions of Henry's problem, by DarcyTools, is in fair agreement with the analytical solution.
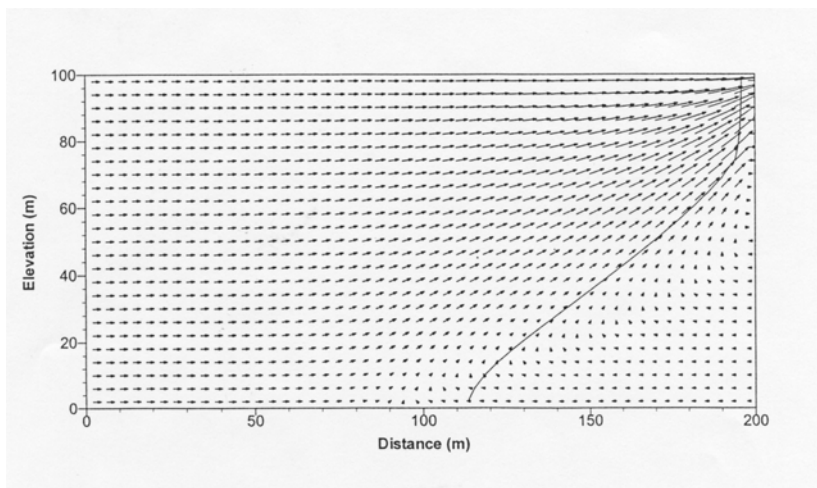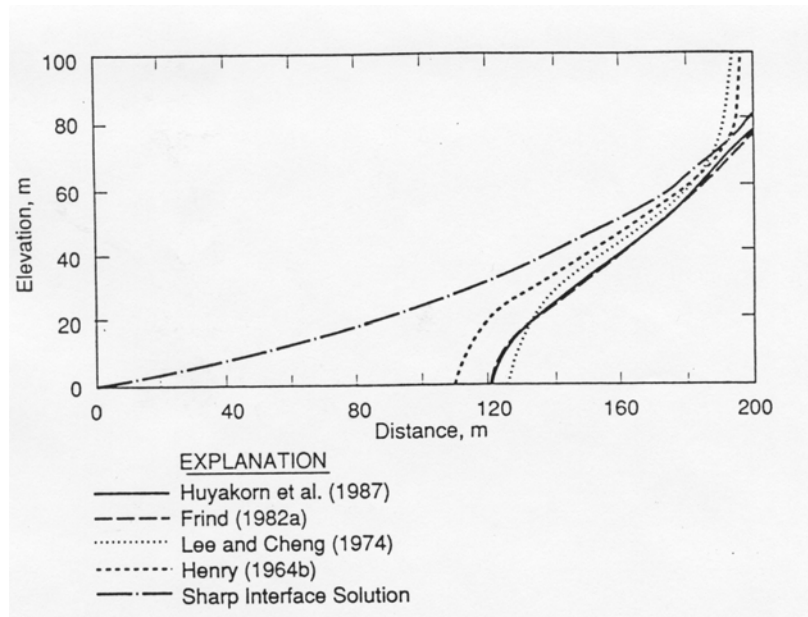
Figure E1:2. *Comparison between Henry's solution and a number of numerical models (top), figure from Ségol (1994). Result from DarcyTools (bottom).*
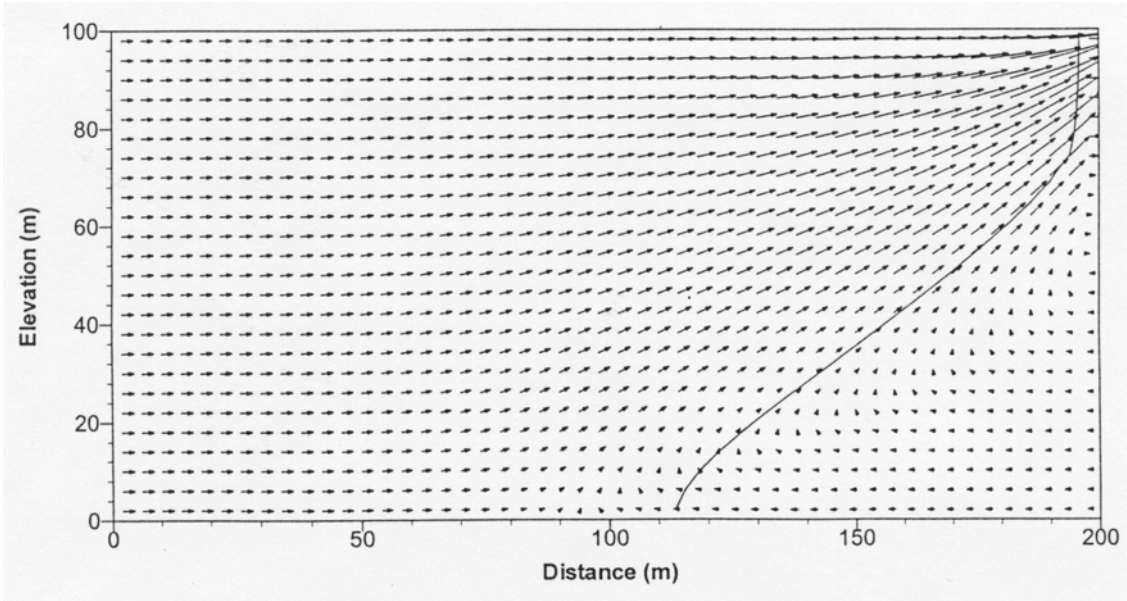*The isochlor s = 0.5 s_{max} is chosen to illustrate the salt-water wedge.*
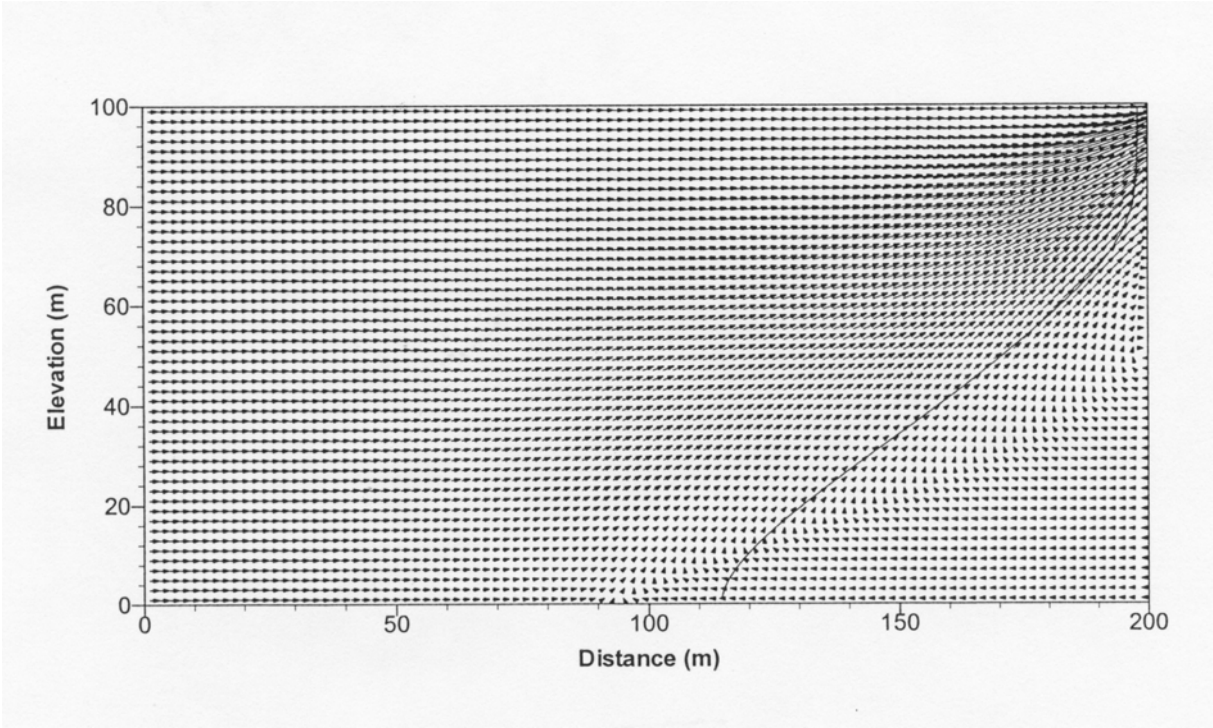
Figure E1:3. *Grid independence test. Solution with cell size 4 metres (top) and 2 metres.*

THE SALT DOME
(Case E2)

1 Introduction

This case is described in the Hydrocoin report, from where we quote:

Background

There are number of important situations where groundwater flow is influenced by density and viscosity variations due to the presence of dissolved salt. The most notable of these situations concerns flow in regions surrounding salt domes or bedded salt deposits which may be used for the disposal of radioactive waste. However, such considerations are also important for repositories at coastal sites.

The particular problem considered here is an idealisation of the situation found in the rocks overlaying the Gorleben salt domain in Germany. The uppermost Quaternary aquifer at this site contains fresh water, but at a depth of 300 m the groundwater is saturated with salt.

The geophysical measurements in boreholes demonstrate that the interface between fresh and salt water usually is sharp. The interface is a result of the hydrogeological situation and of diffusive/dispersive processes. Site specific mathematical models containing these processes could possibly be validated by making use of the measured salt water distribution.

Conceptual model

In the present idealised example the porous sedimentary rock is assumed to have homogeneous and isotropic rock properties. Since this is a verification exercise rather than a site-specific simulation, it is sufficient to consider a two-dimensional vertical cross-section.

Assumptions

The flow is assumed to be isothermal and governed by Darcy's law using an appropriately mass-averaged velocity. The permeability is assumed to be homogeneous and isotropic. The assumptions and equations underlying the flow of concentrated salt solutions are discussed in some recent reports by HYDROCOIN participants. In the interests of simplicity the viscosity is assumed to be independent of the brine concentration.

2 Numerical simulation

The computational domain is a two-dimensional rectangular vertical slice, see Figure E2:1.

The application of DarcyTools to this case uses two simplifications, as compared to the problem formulation in the Hydrocoin report:

- The density-salinity relation is based directly on mixing proportions in the specification, while DarcyTools uses a linear relation. The linear relation is an approximation that introduces a small error.

- The salinity equation should be solved subject to the dispersion tensor

$$E_{ij} = \alpha_T U \delta_{ij} + \left(\alpha_L - \alpha_T\right) U_i U_j / U$$

where U is velocity, δ_{ij} Kronechers delta, α_T transverse dispersion length and α_L longitudinal dispersion length. DarcyTools only considers dispersion in the coordinate directions and the off-diagonal components are hence neglected.

The simulation parameters are summarized in Table E2:1.

Table E2:1. Simulation parameters.

Domain	900 x 300 m
Boundary Conditions	Top: $p = 10^5 \left(1 - x / 900\right)$ $\qquad s = 0$ Bottom: p, zero flux $\qquad s = s_{max}$ between points 5 and 4 $\qquad$ (Figure E2:1) Vertical walls: zero flux
Properties	$K = 1.05 \times 10^{-8}$ m/s $E_{xx} = \alpha_T \times \left\vert U \right\vert + \left(\alpha_L - \alpha_T\right) U_x^2 / \left\vert U \right\vert$ $E_{zz} = \alpha_T \times \left\vert U \right\vert + \left(\alpha_L - \alpha_T\right) U_z^2 / \left\vert U \right\vert$ $\alpha_T = 2, \alpha_L = 20$ S_{max} gives a $\rho_{max} = 1200$ kg/m^3 $n = 0.2$
Grid	$180 \times 60, \ \Delta = 5$ m, uniform
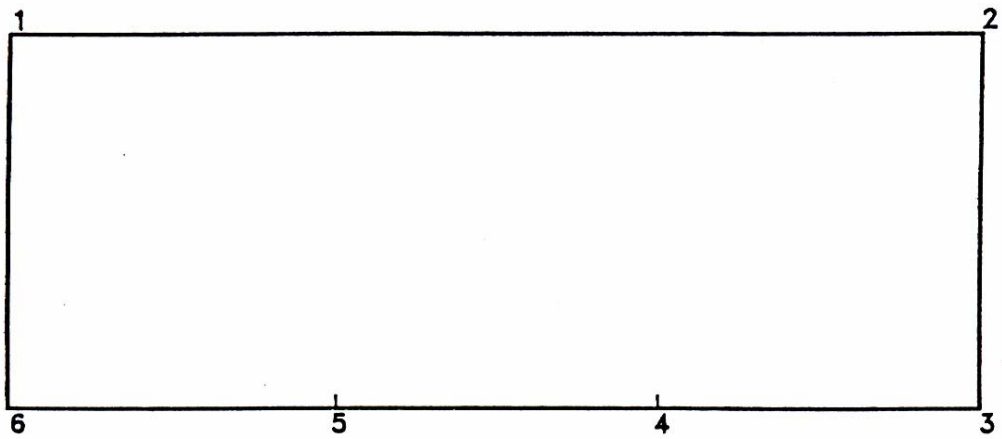
Point no.	x (m)	z (m)
1	0	0
2	900	0
3	900	-300
4	600	-300
5	300	-300
6	0	-300

Figure E2:1. Computational domain.

3 Results/Discussion

The concentration distributions are best visualised from contour plots. Two contour plots, which were considered to be accurate by the Hydrocoin project team, are shown in Figure E2:2 together with the DarcyTools simulation. As can be seen a good agreement is found.

It was the experience of the Hydrocoin exercise that this case was very difficult to handle numerically (new methods had to be developed). No special arrangements were needed in DarcyTools, but several thousand timesteps were needed to get a steady state solution. Due to lack of time, the advanced options in MIGAL for handling coupled equations were not evaluated. This should be done.

4 Conclusion

A good agreement with the Hydrocoin simulations, that were regarded to be the most accurate, was obtained.
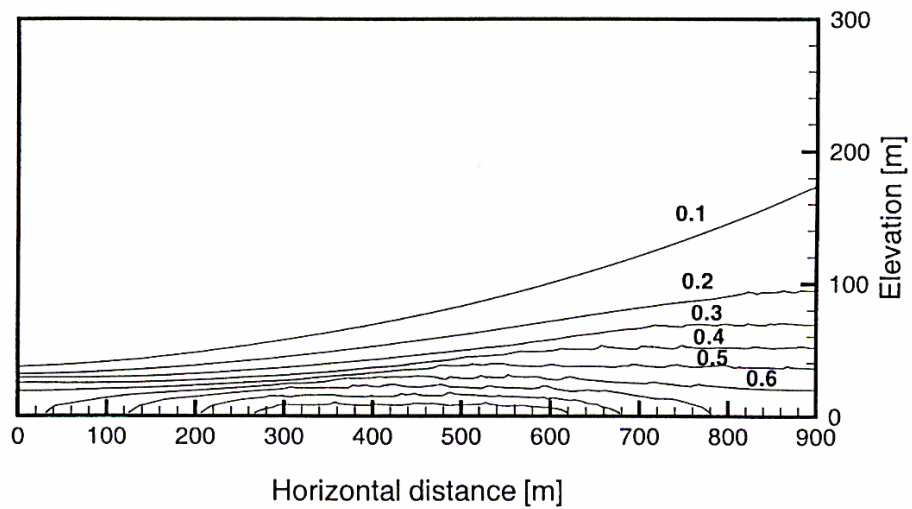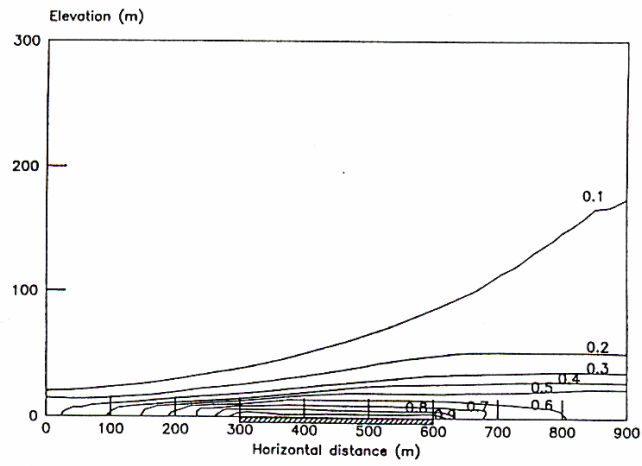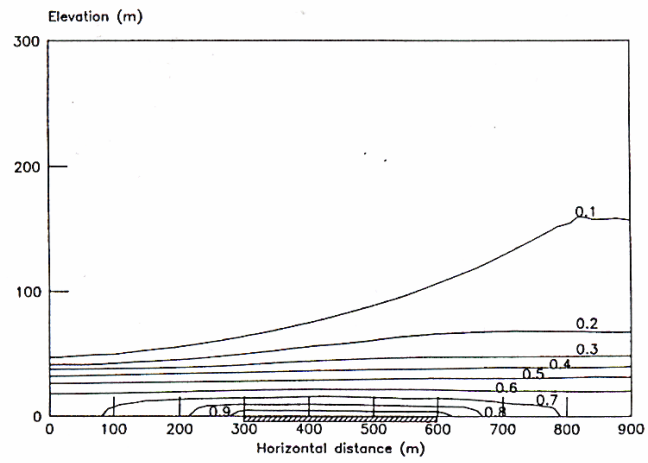
Figure E2:2. *Contour plots by NAMAER (top), SUTRA (middle) and DarcyTools.*

COUPLED TEMPERATURE AND SALINITY FIELDS (CASE E3)

1 Introduction

This case considers the coupled buoyancy effect due to temperature and salinity fields. If a point heat source is placed in a stable salinity field an upward movement will result. This movement will eventually be halted by the stable salinity gradient. The task is to calculate the maximum vertical displacement.

An analytical estimate of this displacement is given in Claesson et al. (1992). In a porous media the maximum vertical displacement due to an instantaneous point heat source is:

$$Z_{max} = \sqrt[4]{\frac{\overline{\alpha} E_0}{2\pi}}$$

(E3:1)

where

$E_0 =$ heat source $\left[J \right]$

$\overline{\alpha} = \dfrac{\alpha_T}{\alpha_c C_z^0 C} =$ buoyancy parameter $\left[m^4 / J \right]$

$\alpha_T =$ thermal expansion coefficient $\left[1/^\circ C \right]$

$\alpha_c =$ salt expansion coefficient $\left[1/\% \right]$

$C_z^0 =$ initial salinity gradient $\left[\% / m \right]$

$C =$ aquifer volumetric heat capacity, rock $\left[J / m^3 \; ^\circ C \right]$

The objective of this test case is to compare estimates by the above formula with the corresponding results from the numerical solution.

2 Numerical simulations

The heat source is placed in the middle of a box with dimensions 100 x 100 100 m^3, see Table E3:1 for additional data.

Note that not all of the parameters in Table E3:1 influence the simulation results to be presented here.

Table E3:1. Simulation parameters

Domain	$100 \times 100 \times 100 \left[m^3 \right]$
Boundary Conditions	Zero flux on all boundaries.
Heat source	Variable
Property data	Porosity = 0.01 Density = 1 000 $\left[kg / m^3 \right]$ Viscosity = 2.0×10^{-3} $\left[kg / ms \right]$ Permeability = 2.0×10^{-12} $\left[m^2 \right]$ Heat capacity, fluid = 4 200 $\left[J / m^3 \ ^\circ C \right]$ Heat capacity aquifer = 2.0×10^6 $\left[J / m^3 \ ^\circ C \right]$ Thermal conductivity = 10^{-7} $\left[W / m ^\circ C \right]$ Thermal expansion coefficient = 10^{-4} $\left[1 / \ ^\circ C \right]$ Salinity expansion coefficient = 10^{-2} $\left[1 / \ \% \right]$
Initial salinity gradient	$0.01 \left[\% / m \right]$
Grid	Uniform $NX = NY = NZ = 50$

3 Result / Discussion

The simulated maximum vertical displacement is in Figure E3:1 compared with the estimate from the analytical solution. The word "estimate" is used as Claesson et al. (1992) consider the formula as "an upper limit on the displacement" and that the formula is "normally more correct for large displacements, while it overestimates the small displacements". The agreement found in Figure E3:1 is hence regarded as acceptable.

An illustration of the disturbed salinity field, in a vertical section through the position of the heat source, can be found in Figure E3:2. This snapshot is at a rather late stage, i.e. long after the maximum displacement has been established.

4 Conclusion

The maximum displacement in a coupled temperature-salinity problem has been simulated and the results have been compared with an analytical solution. An acceptable agreement has been demonstrated.
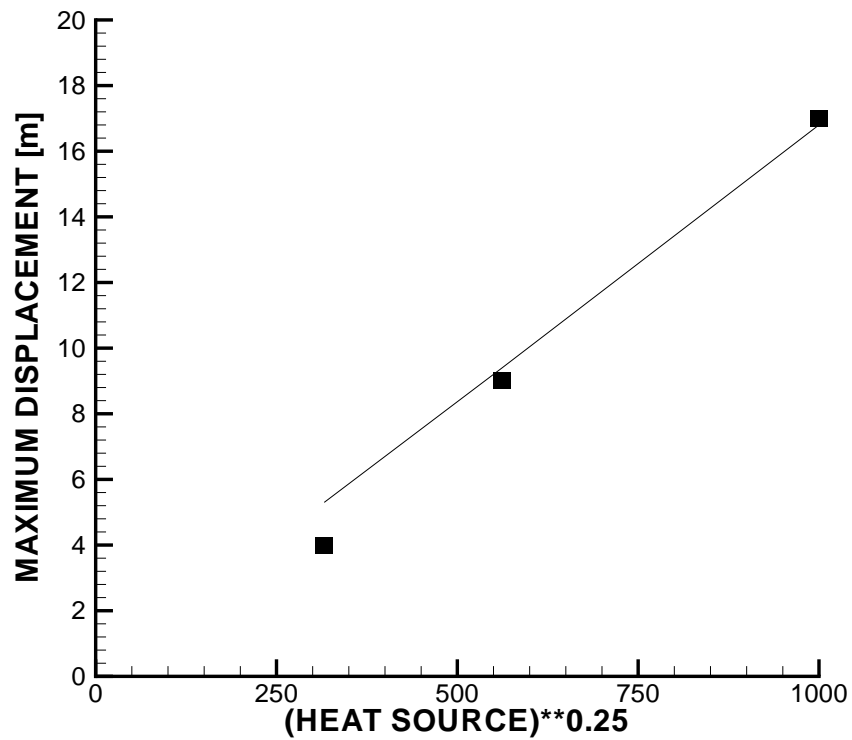
Figure E3:1. *Maximum displacement as a function of the strength of the heat source. Solid line represents the analytical solution and the symbols the numerical solution.*
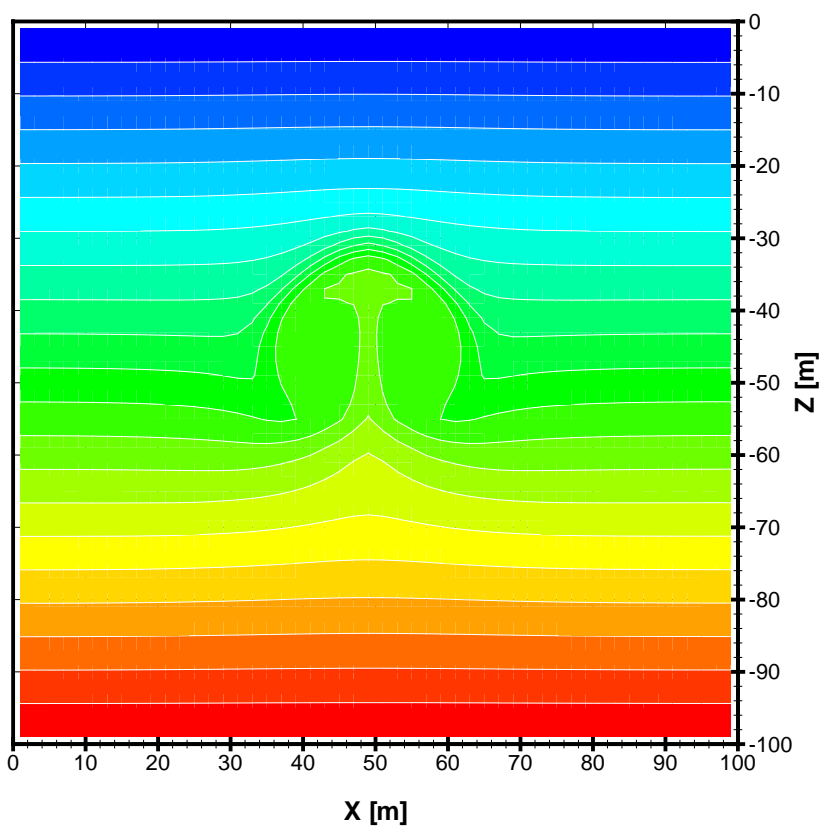
Figure E3:2. *Illustration of the disturbed salinity field. Vertical section through the position of the heat source.*

UPCONING
(Case E4)

1 Introduction

If a well is placed in a two-layered aquifer, with a freshwater layer above a saltwater layer, a phenomenon known as upconing may take place, see Figure E4:1. It is of course the pressure drop due to the pumping that causes the rice of the interface.

An approximate solution, for small rises, is discussed in Domenico and Schwartz (1990). They also discuss a critical elevation at which the interface is no longer stable and saltwater flows to the well. In order to avoid this, the pumping rate, Q, should not exceed Q_{max}, given by:

$$Q_{max} = 0.6\pi d^2 K \left(\frac{\rho_s - \rho_f}{p_f} \right)$$
(E4:1)

where d is the distance from the well to the original interface, K conductivity, ρ_s density of saltwater and ρ_f the freshwater density.
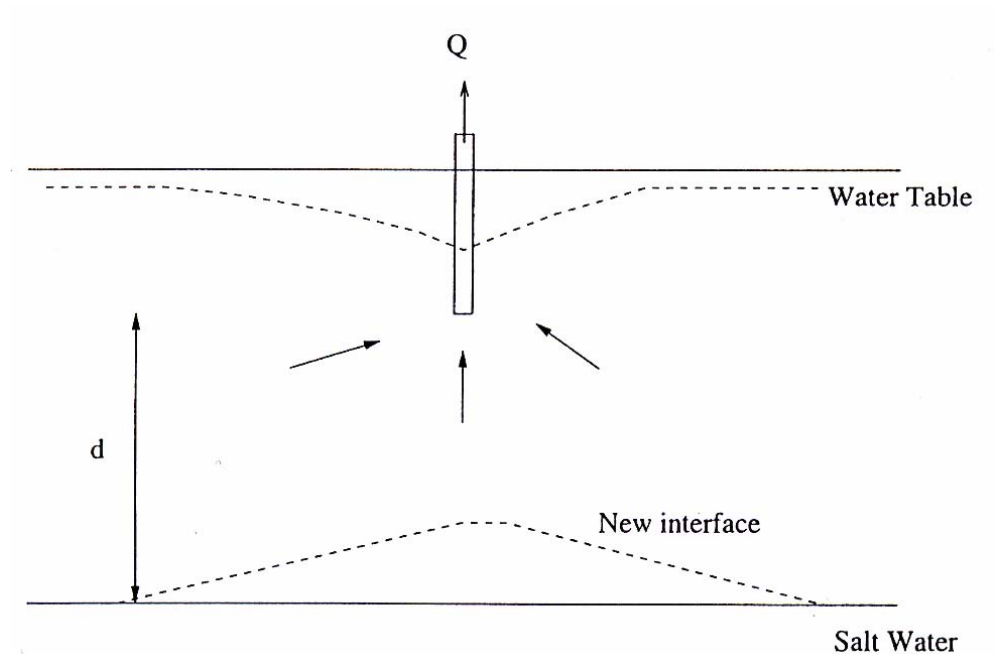
Figure E4:1. *The upconing phenomenon.*

The objective test case is to make a qualitative comparison between results obtained by DarcyTools and Equation (E4:1). The comparison can only be qualitative as Equation (E4:1) is based on relations only valid for small interface rises.

2 Numerical simulations

In polar coordinates the problem is two-dimensional but here it will be treated as a 3D problem, as DarcyTools does not provide polar coordinates. Due to symmetry conditions we only need to consider one quarter of the domain. A summary of the simulation parameters is given in Table E4:1.

Table E4:1. Simulation parameters.

Domain	500 x 500 x 110 metres (x, y, z)
Boundary Conditions.	Prescribed pressure at x_{max} and y_{max}. Zero flux condition on other boundaries. Salinity prescribed at bottom of domain.
Pumping rate	Varied
Distance d (Figure E4:1)	50 metres
Conductivity	10^{-5} m/s
Diffusivity (salt)	10^{-9} m^2/s
Salinity below interface	1 % ($\Delta\rho = 7.8$ kg/m^3)
Grid	Expanding in x and y directions, starting with $\Delta = 2$ metres. Uniform with $\Delta = 2$ m in the vertical direction.

3 Results / Discussion

The predicted relation between the pumping rate and the salinity at the bottom of the well is shown in Figure E4:2. In this figure also the critical pumping rate, as

given by Equation (E4:1), is indicated. As already mentioned we can not evaluate the result more than in a qualitative way; both DarcyTools and Equation (E4:1) do however predict a Q_{max} of the same magnitude.

4 Conclusion

A qualitative agreement with the analytically predicted critical pumping rate, for saltwater intrusion into a well, has been demonstrated.
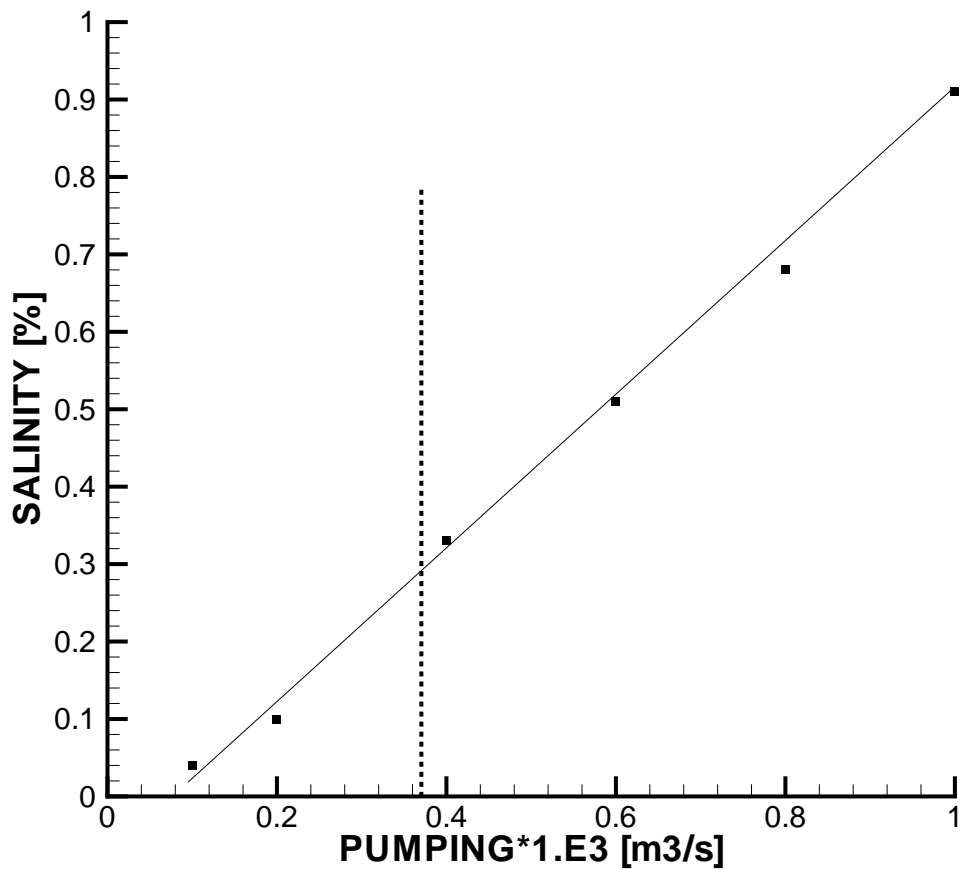
Figure E4:2. *Relation between salinity at the bottom of the well and the pumping rate, as predicted by DarcyTools. Vertical line indicates the critical pumping rate according to Equation (E4:1).*

THE FLOATING ISLAND
(Case E5)

1 Introduction

This case is of special interest as it has some resemblance to the situation at the island of Äspö (location of the SKB Hard Rock Laboratory). The situation considered is outlined in Figure E5:1. A fresh water lens is formed below the island, due to the precipitation. As the surrounding seawater is more dense, due to its salinity, one may think of the freshwater as floating in the saltier seawater.

An analytical solution to this problem can be found in Fetter (1994); the groundwater height, h, as a function of distance from the shore, x, is given by:

$$h^2 = \frac{w\left(a^2 - (a-x)^2\right)}{K(1+G)} \qquad \text{(E5:1)}$$

where w is the recharge on the island, a half-length of the island, K conductivity and $G = \rho_f / (\rho_s - \rho_f)$ (ρ_s and ρ_f are seawater and freshwater densities, respectively).

The objective of this test case is to compare the groundwater tables as predicted by DarcyTools and as given by Equation E5:1.
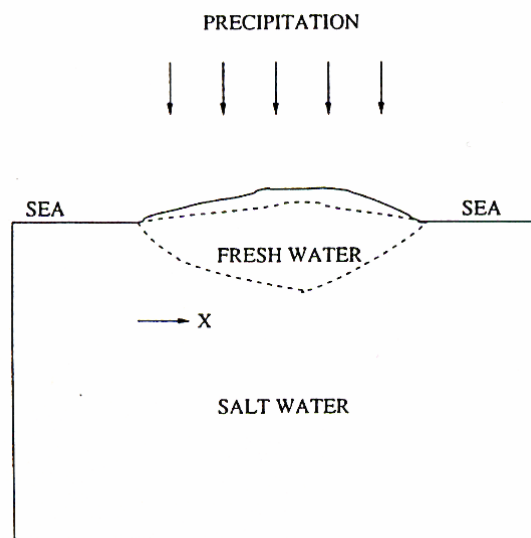
Figure E5:1. Illustration of the floating island problem.

2 Numerical simulations

The simulation parameters for this case are given in Table E5:1, see also Figure E5:1. Some comments.

- The vertical conductivity is increased in order to simulate the Dupuit assumption (as discussed in Case B2).

- As the salinity is fixed to 1.0 below sea and at the bottom boundary, the salinity will be uniform except for the region close to fresh water lens.

- The grid is generated as follows: First a cartesian grid is set up with $\Delta = 10$ metres, except for the top 4 cell layers which have $\Delta_z = 1$, 2, 3 and 4 metres respectively. The top 100 hundred meters of the grid is then stretched/compressed to follow the topography (-10 metres av $x = 0$ and 10 metres at $x = 500$ metres).

Table E5:1. Simulation parameters.

Domain	2D, 1000 x 500 metres. Upper boundary follows a sin-curve.
Conductivity	10^{-7} m/s (horizontal)
	10^{-5} m/s (vertical)
Diffusivity (salt)	10^{-9} m²/s
Boundary Conditions	Bottom: zero mass flux, salinity fixed to 1.0 Top: prescribed mass flux on island, prescribed pressure below sea level. Zero salinity on island, fixed salinity (= 1.0) below sea level.
Grid	NX = 100, NZ = 53, BFC:s

3 Results / Discussion

The comparison with the analytical solution is given in Figure E5:2; as can be seen a near perfect agreement is obtained. The flow and salinity distribution can be studied in Figure E5:3. For a recharge of 50 mm/year it is seen that the freshwater lens reaches a depth of about 200 metres. It may further be noted that the fresh water is discharged into the sea in a very narrow region close to the shore-line.

4 Conclusion

The predicted groundwater table on the floating island is in very good agreement with the corresponding analytical solution.
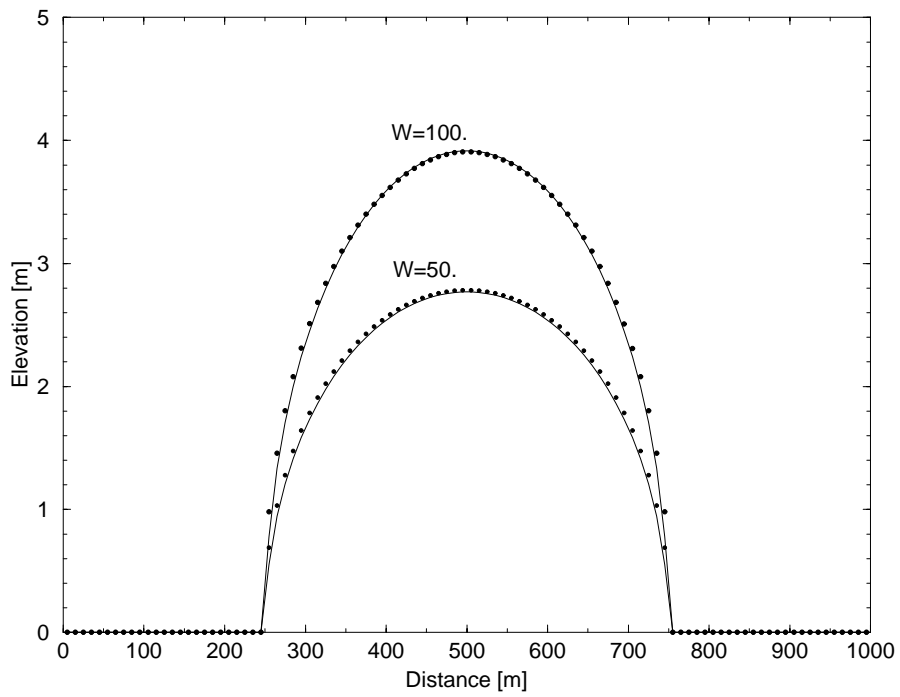
Figure E5:2. *Numerically (●●●) and analytically (———) predicted groundwater table for two recharges.*
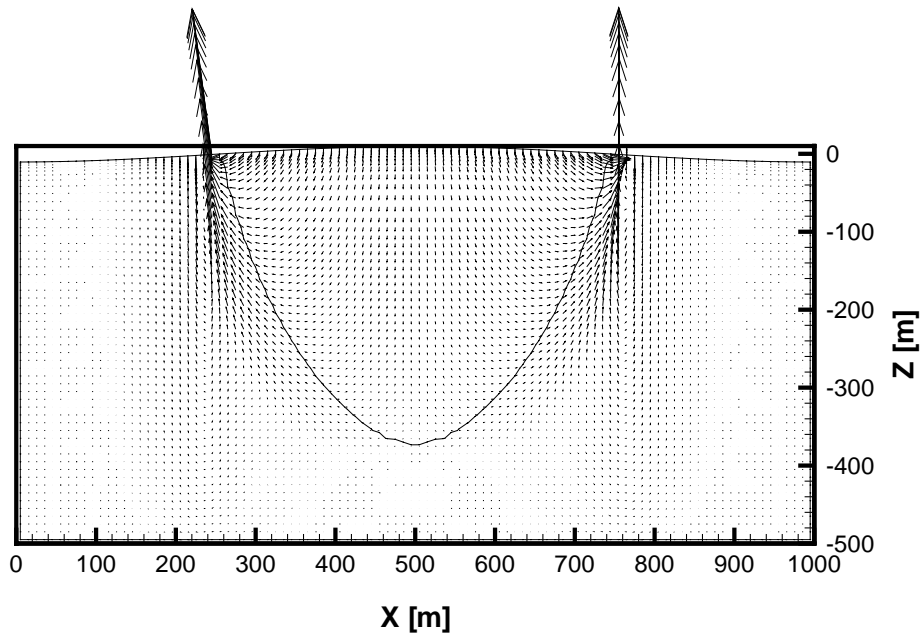
Figure E5:3. *Flow and salinity distributions. The line shows the extent of the fresh water lens.*

TWO-FLUID PROBLEM (CASE E6)

1 Introduction

The motion of an interface between two fluids with different densities and viscosities is studied, see Figure E6:1. The buoyancy flow induced by the density difference will cause the two-fluid interface to tilt.

An analytical solution of this problem is found in Hellström et al. (1988). They found that the horizontal velocity at the interface is given by

$$q(z) = \kappa q_0 \frac{1}{\pi} \ln \left[\frac{1 + \sin\left(\dfrac{\pi z}{H}\right)}{1 - \sin\left(\dfrac{\pi z}{H}\right)} \right] \qquad \text{(E6:1)}$$

where

$$q_0 = \frac{k \Delta \rho g}{\mu_1 + \mu_2} = \text{ a characteristic velocity}$$

and

$\Delta\rho$ = density difference

g = gravitational constant

k = permeability

μ = viscosity

κ = anisotropy factor (= 1 for isotropic permeability)

The objective of this testcase is to compare the numerical and analytical solution for a common situation.
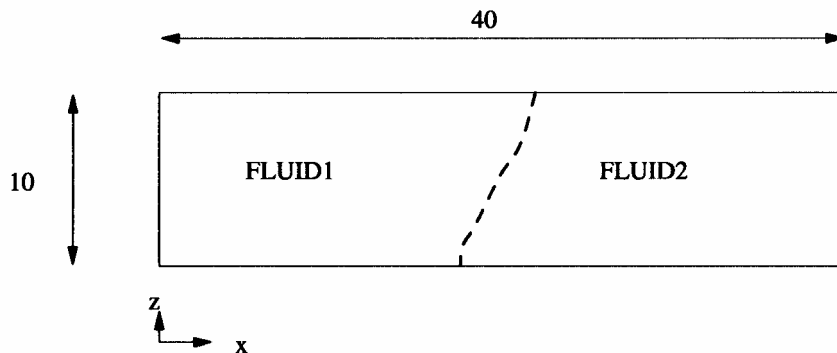
Figure E6:1. *Outline of the situation studied.*

2 Numerical simulations

The domain is outlined in Figure E6:1. A summary of input data is given in Table E6:1. It should be noted that not all of the parameters specified influence the simulations to be discussed. It should further be pointed out that the parameters are not representing any real fluid; they are only chosen to suit the present comparison.

Table E6:1. Simulation parameters

Domain	$2D,\ 40 \times 10 \ \left[\text{m}^2 \right]$
Boundary Conditions	Zero flux on all boundaries.
Property data	$T_1 = 10^{\circ}C,\ T_2 = 20^{\circ}C$ $\rho_1 = 1000,\ \rho_2 = 950 \ \left[\text{kg} / \text{m}^3 \right]$ $\mu_1 = 2 \times 10^{-3},\ \mu_2 = 6 \times 10^{-3} \ \left[\text{kg} / \text{ms} \right]$ Permeability $= 10^{-12} \ \left[\text{m}^2 \right]$ Porosity $= 1.0$ Heat capacity aquifer $=\ 2.0 \times 10^6 \ \left[J / \text{m}^3 \ ^{\circ}C \right]$ Heat capacity fluid $= 4\ 200 \ \left[J / \text{m}^3 \ ^{\circ}C \right]$ Thermal conductivity $= 10^{-10} \ \left[\text{W} / \text{m}^{\circ}C \right]$
Grid	$NX = 160,\ NZ = 40$, uniform

3 Result / Discussion

The main result of this study is the comparison of velocity profiles, shown in Figure E6:2. The agreement is very good indeed and requires no further comments.

An illustration of the velocity field is given in Figure E6:3. From this figure one can conclude that the vertical boundaries are placed sufficiently remote from the interface.

4 Conclusion

The tilting of a vertical interface between two fluids with different densities and viscosities has been studied. It is concluded that the numerical result agrees very well with the analytical solution.

Figure E6:2. *Comparison between numerical (■) and analytical (─) solution.*

Figure E6:3. *Illustration of the velocity field close to the interface.*

APPENDIX B   Validation cases

Case V1   A site scale validation

Introduction

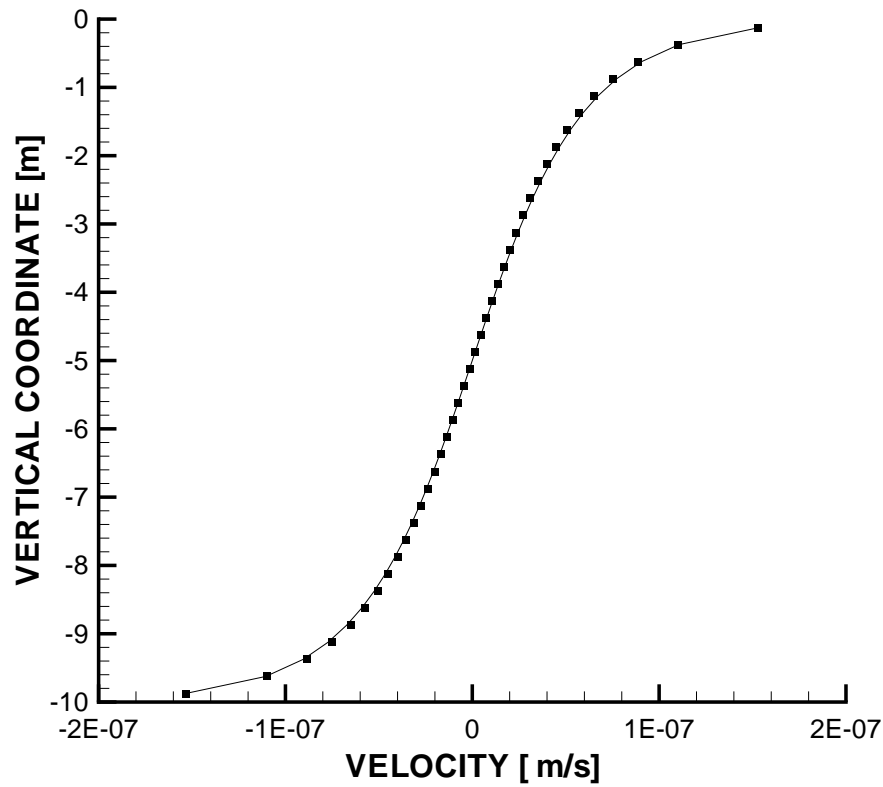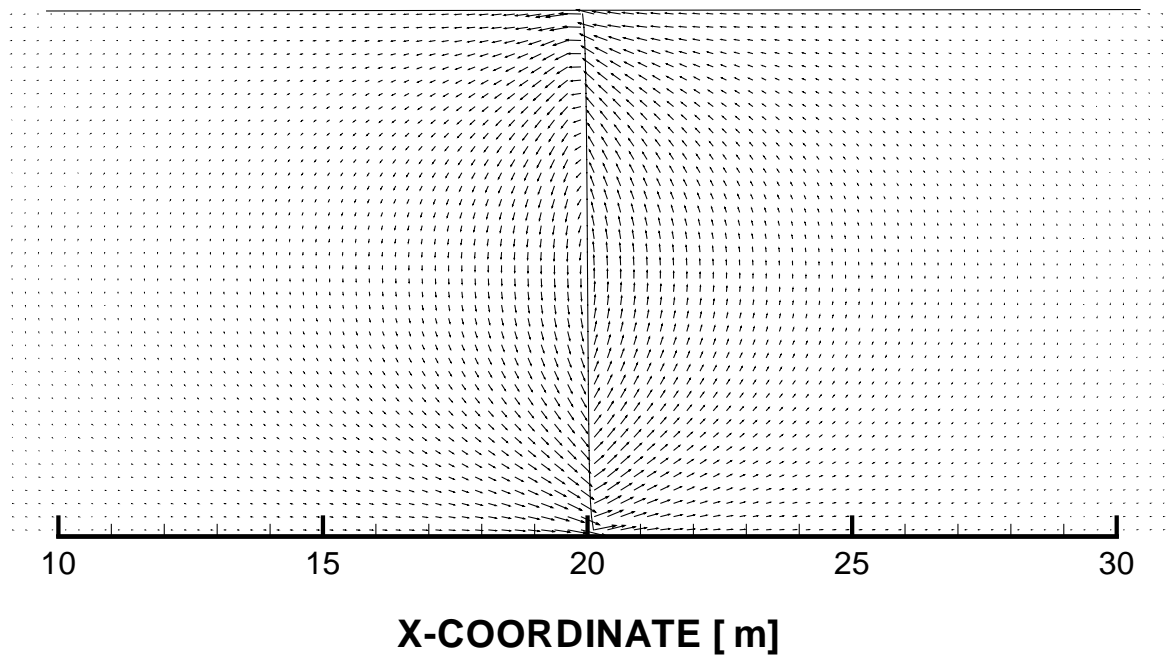This validation study is taken from the report "Impact of the tunnel construction on the groundwater system at Äspö. Task 5 Äspö task force on groundwater flow and transport of solutes; Svensson et al. (2002).

The hydrochemical field data at Äspö HRL has been presented as distributions of four basic water types: Meteoric, Baltic, Glacial and Äspö Brine. The Meteoric water has recently been in contact with the atmosphere and originates from precipitation, while Baltic water has its origin from the Baltic Sea. The Glacial water is believed to come from the meltwater of the last inland ice about 12 000 (or more) years ago. The Äspö Brine water is characterised by its high salinity and its age; it is estimated that it has not been in contact with the atmosphere for at least 1 million years. The Äspö Brine fraction increases with depth and may be the dominating fraction below a depth of, say, 800 metres in the Äspö area.

The numerical model should be able to determine the composition, expressed as the four water types mentioned, of the water leaking into the tunnel. Two problems, which call for basic conceptual assumptions, can be identified when formulating such a model:

- Order of magnitude calculations show that water from outside the computational domain will contribute to the inflow to the tunnel already after a few years after the start of the construction of the tunnel. We thus need an assumption about the water composition outside the domain.

- The hydrochemical data show that large fractions of Glacial water are present already at a depth of a few hundred meters. As there is no source of Glacial water one would expect that this water should have been replaced by younger water during the last 12 000 years. As mentioned, the inflow to the tunnel will replace the water in the computational domain with water from outside the domain in a few years time. So, even if we specify a large fraction of Glacial water as an initial condition we would soon "run out" of this water type.

Boundary conditions

To deal with these problems we need to introduce some assumptions about the water composition at the boundaries of the computational domain. The following concepts and assumptions are introduced.

- Vertical boundaries:

- If s (Salinity) $\leq 0.1\%$ we assume that the water is of Meteoric origin.

- If $0.1 < s \leq 1.2\%$ we call this water type "Mixed Water High" (MWH).

- If s $>1.2\%$ we call this water type "Mixed Water Low" (MWL).

The reason for introducing MWB, MWH and MWL is that we can base an assumption about the composition of these waters on field data. There is also a reason for choosing the salinity value 1.2% as the division between MWH and MWL. When the inland ice had its frontline above Äspö one can expect that Glacial water penetrated very deep into the rock. At about 800 to 1 000 metres, the Äspö Brine provided a lower limit for the circulation. Presumably a mixture of Glacial and Äspö Brine waters resulted in the transition region between the two water types. At about 8 000 years ago the Litorina Sea, with a maximum salinity of about

1.2%, replaced most of the water due to its high density. The maximum penetration depth is however given by the salinity 1.2% and we can therefore assume that MWL is composed mainly of Glacial and Äspö Brine water. Based on these arguments, we assume the following for MWH and MWL:

- MWH. Composition based on field data from borehole KLX01 10% Baltic, 35% Meteoric, 45% Glacial and 10% Äspö Brine.

- MWL. 10% Baltic, 10% Meteoric, 40% Glacial and 40% Äspö Brine. This is to some degree supported by measurements in KLX02, at a depth with a salinity of 1.5%.

For the water entering through the bottom of the domain, MWB, it will be assumed that the composition is the same as for MWL.

Calibration

The model is calibrated both with respect to the hydrogeological and hydrochemical information available.

Above conceptual assumptions were discussed; it was stated that the water composition at the bottom and vertical boundaries of the domain were tentative and should be considered again in the calibration process. Three water types, MWH, MWL and MWB, were introduced, with tentative compositions from borehole measurements.

The focus of the calibration process for water composition is thus on the composition of MWH, MWL and MWB.

In the Task #5 description it was suggested that the calibration should be based on measured water composition in boreholes, with the tunnel front at position 2 900 metres. A review of the field data on water composition shows that more data are available for position 3 170 metres (April -94) and the calibration will therefore be based on conditions prevailing at that time.

Calibration criteria

In the calibration we will try to fulfil the following criteria:

- **Groundwater table for natural conditions.** The distribution can be found in Rhén et al. (1997). One can expect that a certain variation of the groundwater table is found, between seasons and years, and a fair agreement is hence sought.

- **Pressure response in boreholes.** During the construction of the Äspö HRL, the pressure was monitored in a number of borehole sections. The drawdowns at tunnel front position 2875 metres can be found in Rhén et al. (1997); these data will be compared with simulated drawdowns.

- **Kinematic porosity.** The kinematic porosity field is based on the estimated flow aperture of each fracture or zone in the network. In the calibration process this basic distribution will be kept, but each value will be multiplied by a constant, that is to be determined. The time history of the upconing, i.e. the salinity variation in time, will be utilized for this purpose.

- **Water composition for natural conditions.** The water composition in the Äspö area was measured prior to the construction of the Äspö HRL. We will run the model for this

situation, assuming steady state conditions, and compare the result with field data. In the steady state the water composition in the domain is completely determined by the boundary conditions and should thus be sensitive to the assumed compositions of MWH, MWL and MWB. A general agreement between measured and simulated distributions is the criteria set.

- **Water composition for tunnel front at 3 170 metres.** The water composition in 19 boreholes was measured at this tunnel front position. We want to ensure as close agreement as possible with these data.

- **Water composition at time 1996-05.** The measured composition in eight borehole sections, after the completion of the tunnel, will be compared to simulated values. As close agreement as possible is the objective of part of the calibration.

Calibration process

It was decided to perform the calibration in three steps. First the hydrological model was calibrated (the first two criteria above). This involved determining the conductivity for the top five layers of the model and adjusting the transmissivity of some deterministic fracture zones. It was the ambition to keep these adjustments as small as possible. Next the kinematic porosity factor was determined from the measured upcoing dynamics and finally the water composition was considered. Adjustments of the compositions of MWH, MWL and MWB were evaluated, with the ambition to get as close agreement with field data as possible.

Results

The groundwater table for natural conditions is compared to measurements in Figure V1-1 and the drawdowns in borehole sections, for a tunnel front position of 2875 metres, are given in Table V1-1. Starting with the groundwater table, it is seen that the predicted maximum ground water level is about 4 metres. A general agreement with the measured levels (given in Rhén et al. (1997)) is also found. The calculated drawdowns in borehole sections in the domain were compared with measured ones, all for tunnelfront position 2875 metres. It was anticipated that the drawdowns should be sensitive to various realisations of the background fracture network. In order to study this five realisations of the network were generated and the drawdown for each borehole section and each realisation was calculated. The result can be studied in Table V1-1, the location of boreholes can be found in Figure 1-3 (Report 1). It is seen that different realisations are best for different boreholes. Realisation two has only two borehole sections with an error larger than 10 metres and is for this reason considered to be the best one. In the following, it is this realisation of the conductivity field that will be used, if not otherwise stated.

It was found that an increase of the kinematic porosity, based on the flow aperture, with a factor of five gives a realistic description of the upcoing process, see Figure V1-2. We do not know the exact position of the upcoing front and therefore both the predicted maximum salinity at a depth of 370 metres and the predicted salinity at the tunnel position 2 800 metres are given in Figure V1-2. The measurements are from boreholes SA2783 and SA2880. This calibration result is considered to be important, as it focuses on the transport velocity of a fluid property.

These results were obtained by prescribing certain conductivities to the top five layers, see Table V1-2, and by making small adjustments to the transmissivities of the major fracture zones. A small background conductivity, with a lognormal distribution, was also added to all

cells. This conductivity had a value of 10^{-10} m/s north of the line $y = 7050$ metres (in the Äspö coordinate system) and a value of 10^{-9} m/s south of this line. The standard deviation of $Log_{10}(K)$ was 0.8 for the whole domain.

The compositions of MWH and MWL given above were found to give results in fair agreement with field data, both for initial conditions and for the tunnel front at position 3 170 metres. The composition of MWB has no significant influence on these comparisons, but is important when water from the bottom boundary reach the tunnel level. The salinity at the bottom boundary, generated by the regional model, will reach 5-6% when the tunnel is completed. Borehole KLX02, at 1 500 metres, has a salinity of 7-8% and Äspö Brine fraction of 90%. Based on these data and the comparison of measured and simulated water composition at time 1996-05, the following composition for MWB was considered to be more accurate: 5% Meteoric, 5% Baltic, 10% Glacial and 80% Äspö Brine. This is the composition of MWB to be adopted. A small adjustment of the composition of MWL (giving 12% Meteoric, 12% Baltic, 45% Glacial and 31% Äspö Brine) was found to give a minor improvement of the results. With these modifications good agreement was also obtained for the comparison at time 1996-05. Some results that confirm these statements will now be given.

The calculated initial distributions are given in Figure V1-3. The sections are through the centre of the spiral part of the tunnel. The distributions are in general agreement with field data, see Gurban et al. (1998). Of particular significance is the band of glacial water occupying about 50% of the pore volume at a depth of about 600 metres. Point by point comparisons with field data can be found in Table V1-3. It should be mentioned that measurements are available also for depths above 300 metres. These were however not included in the table as the model predicts 100% Meteoric water for depths smaller than 200 to 300 metres. In order to be able to compare the average values for the composition, it was decided to exclude these data.

Next we consider the simulated water composition for tunnel front position 3170 metres. Point comparisons with field data can be found in Table V1-4; the comparison in Table V1-4 is also shown as a graph in Figure V1-4. A certain agreement in proportions of different water types, as well as trends along the tunnel, can be found. It is not easy to anticipate the degree of agreement one can expect in a simulation like this. Distributions for tunnel front position 3 170 metres are shown in Figure V1-5. This figure is included as an illustration of how the tunnel affects the distributions and is not directly used in the calibration process.

Finally, the comparison for 1996-05 is shown in Table V1-5. Also in this comparison both the trends and the average compositions are in fair agreement with field data.

Conclusions

From the comparisons presented, the following conclusions are formulated:

- The hydrogeological simulations are in fair agreement with field measurements.

- The simulations of water compositions are harder to evaluate. A certain agreement in trends can however be claimed.
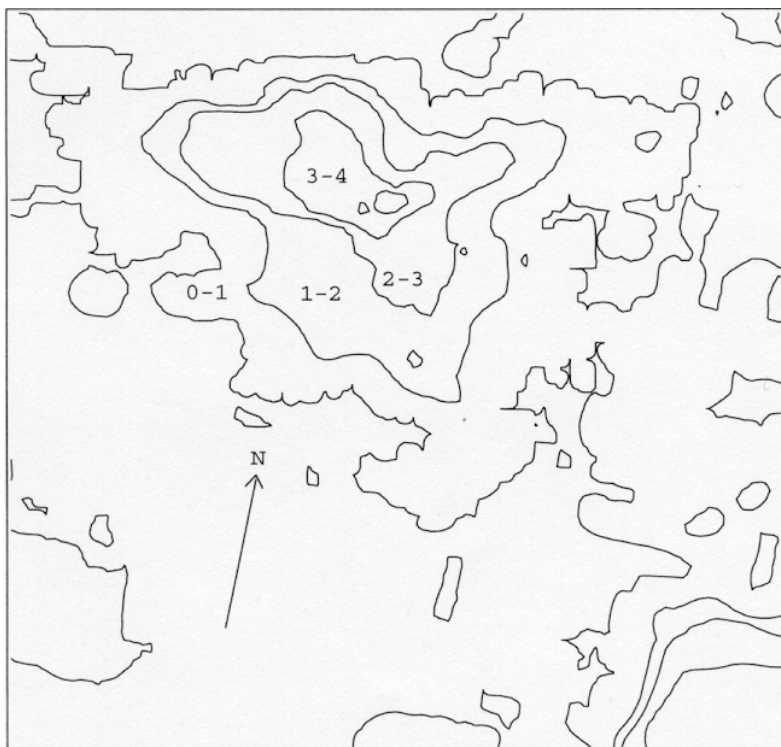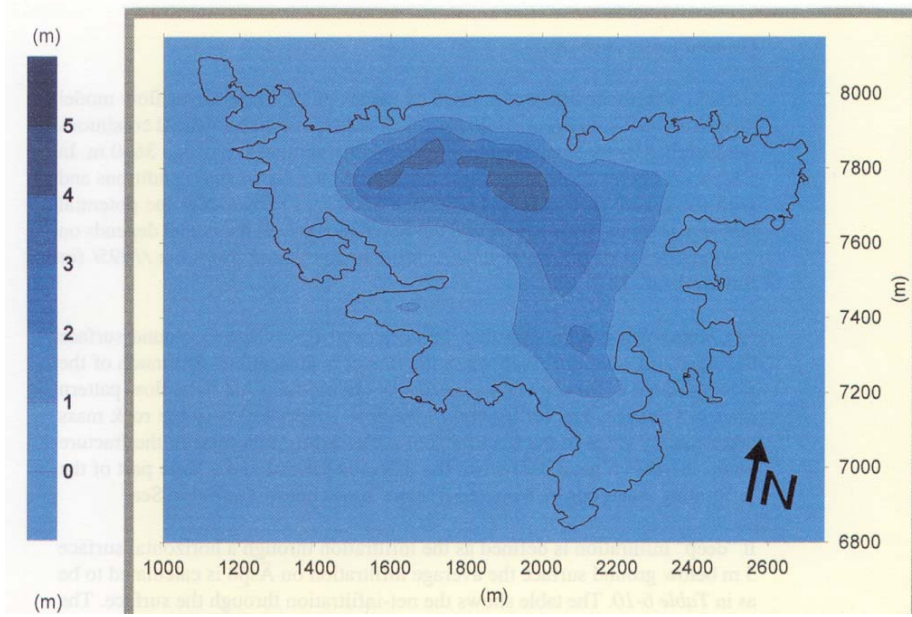
Figure V1-1. *Measured (top) and calculated water table for natural conditions.*

Table V1-1. Errors in calculated drawdown (calculated- measured) for tunnel front at 2875 metres, using five realisations of the conductivity field.

Borehole section	Depth m b s l	Realisation 1	2	3	4	5
K02-B5	-190.00	5.37	7.84	8.53	15.56	0.72
K02-B4	-310.00	- 9.58	-9.81	-11.36	-10.02	-10.31
K02-V3	-530.00	3.63	5.75	4.09	5.60	4.83
K02-V2	-830.00	- 5.84	-5.50	- 5.69	- 5.43	- 5.54
K02-V1	-870.00	- 5.43	-5.21	- 5.34	- 5.16	- 5.24
	-210.00	6.64	5.85	8.11	7.02	5.46
K03-C5	-350.00	0.80	0.62	1.74	0.13	0.33
	-510.00	1.78	1.20	2.28	2.51	1.57
K03-C4	-610.00	1.47	0.98	1.64	1.78	1.67
K03-C3	-670.00	0.54	0.22	0.38	0.28	0.78
K03-C2						
K03-C1	-270.00	2.65	5.59	1.19	5.81	0.26
	-310.00	- 8.85	- 4.45	- 1.91	0.47	-0.15
K05-E4	-430.00	- 9.44	- 7.11	- 5.93	- 5.35	-5.54
K05-E3	-450.00	- 7.46	- 4.83	- 4.51	- 4.23	-3.68
K05-E2						
K05-E1	-90.07	9.30	9.55	6.95	9.27	8.94
	-250.00	- 2.15	- 2.92	- 4.17	- 5.22	- 1.47
K06-F6	-290.00	11.45	16.49	15.17	14.71	13.24
K06-F4	-330.00	- 2.94	0.55	- 3.38	- 1.26	- 2.63
K06-F3	-370.00	- 4.48	- 0.01	- 6.55	- 2.89	- 5.32
K06-F2						
KO6-F1	-110.00	-34.67	-27.76	-31.98	-28.15	-29.55
	-210.00	-10.42	- 6.42	- 4.28	- 5.17	- 8.83
K07-J5	-290.00	- 4.48	- 1.00	- 2.94	- 6.21	- 1.21
K07-J4	-370.00	2.50	3.47	2.52	3.05	2.88
K07-J3	-470.00	- 5.41	- 4.65	- 5.26	- 4.75	- 5.07
K07-J2						
K07-J1	-150.00	2.37	7.08	- 4.10	2.76	1.04
	-310.00	7.42	9.63	3.98	9.38	7.67
K08-M3	-450.00	- 6.20	- 5.50	- 5.74	- 5.38	-5.69
K08-M2						
K08-M1	-90.07	0.49	1.64	0.80	1.55	0.97
	-110.00	0.37	4.73	1.39	8.17	1.90
K09-AE	-150.00	- 1.20	6.17	- 0.08	5.39	7.31
K09-AD	-210.00	1.89	4.88	6.47	6.34	11.75
K09-AC	-350.00	- 2.32	- 2.25	- 2.23	- 2.64	- 2.61
K09-AB						
K09-AA	-50.35	- 2.41	- 2.38	- 2.76	- 2.41	-2.19
K10-BA	- 30.48	- 5.99	- 6.09	- 6.45	- 5.58	-5.90
	- 50.35	- 6.02	- 6.20	- 6.49	- 5.50	-6.01
K11-CF	- 90.07	- 1.41	- 1.05	- 1.51	- 1.39	-1.33
K11-CE	-130.00	- 2.42	- 2.11	- 2.49	- 2.11	-2.25
K11-CD	-170.00	2.79	3.03	2.81	3.21	3.04
K11-CC	-210.00	- 2.07	- 1.61	- 1.95	- 1.57	-1.72
K11-CB						
K11-CA	- 90.07	- 3.02	- 4.97	- 6.58	- 1.89	0.44
	-110.00	- 1.45	- 4.02	- 4.50	- 3.52	1.44
K12-DE	-230.00	2.17	4.68	- 1.97	3.25	1.83
K12-DD	-270.00	4.67	9.84	- 0.26	4.56	6.94
K12-DC	-350.00	2.91	6.49	- 1.03	3.47	3.22
K12-DB						
K12-DA	-7 0.21	- 1.03	- 0.43	- 0.69	- 0.48	-0.43
	-110.00	2.08	2.61	0.55	1.59	1.35
K14-FE	-130.00	2.88	3.56	3.04	4.65	3.02
K14-FD	-130.00	1.66	1.94	1.23	3.83	1.79
K14-FC	-170.00	2.74	0.86	2.20	5.28	2.95
K14-FB						
K14-FA	-110.00	0.36	0.52	- 3.14	0.52	1.54
	-230.00	- 8.69	- 6.93	-10.48	- 8.82	-8.90
	-410.00	- 5.67	- 5.12	- 5.32	- 5.00	-5.25
K16-?D	-490.00	- 4.16	- 3.76	- 4.35	- 3.64	-4.88
K16-?C						
K16-?B	-50.35	1.97	- 1.22	1.48	0.71	2.45
K16-?A	-70.21	12.71	6.36	6.47	9.41	10.62
	-90.07	10.72	7.10	8.08	9.74	9.88
KV2-B6	-130.00	6.22	5.94	6.19	5.74	5.78
KV2-B5						
KV2-B4						
KV2-V3						
Mean error (m)		**- 0.99**	**0.21**	**- 1.20**	**0.39**	**- 0.07**

Table V1-2. Conductivities for the top five cell layers, as given by the calibration process.

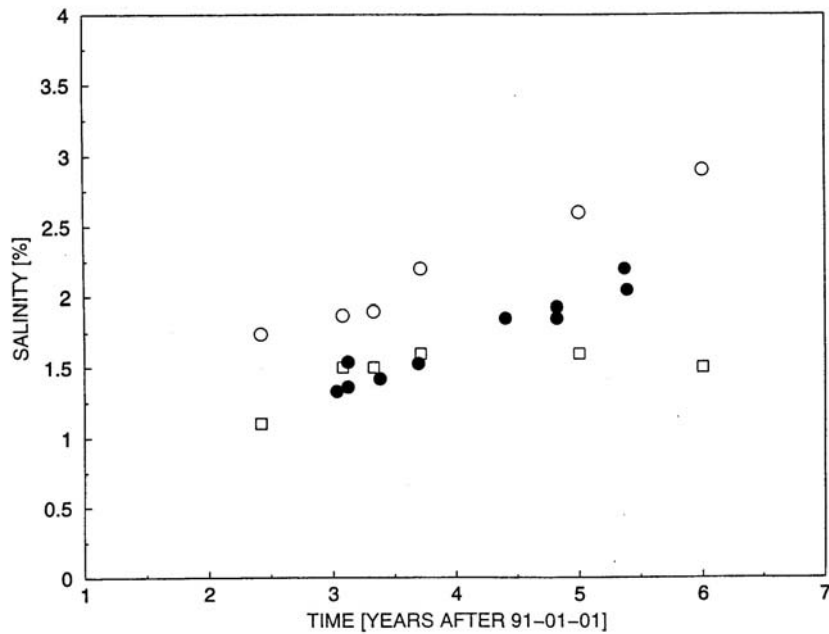| Layer (m)	Conductivity m/s
0-0.5	10^{-4}
0.5-1.5	10^{-4}
1.5-3.0	4×10^{-5}
3.0-5.0	10^{-6}
5.0-10.0	10^{-7}

Figure V1-2. *The upconing process. Salinity as a function of time at a depth of 370 metres.*
• *Field data (SA2783 and SA2880)*
○ *Simulated maximum salinity.*
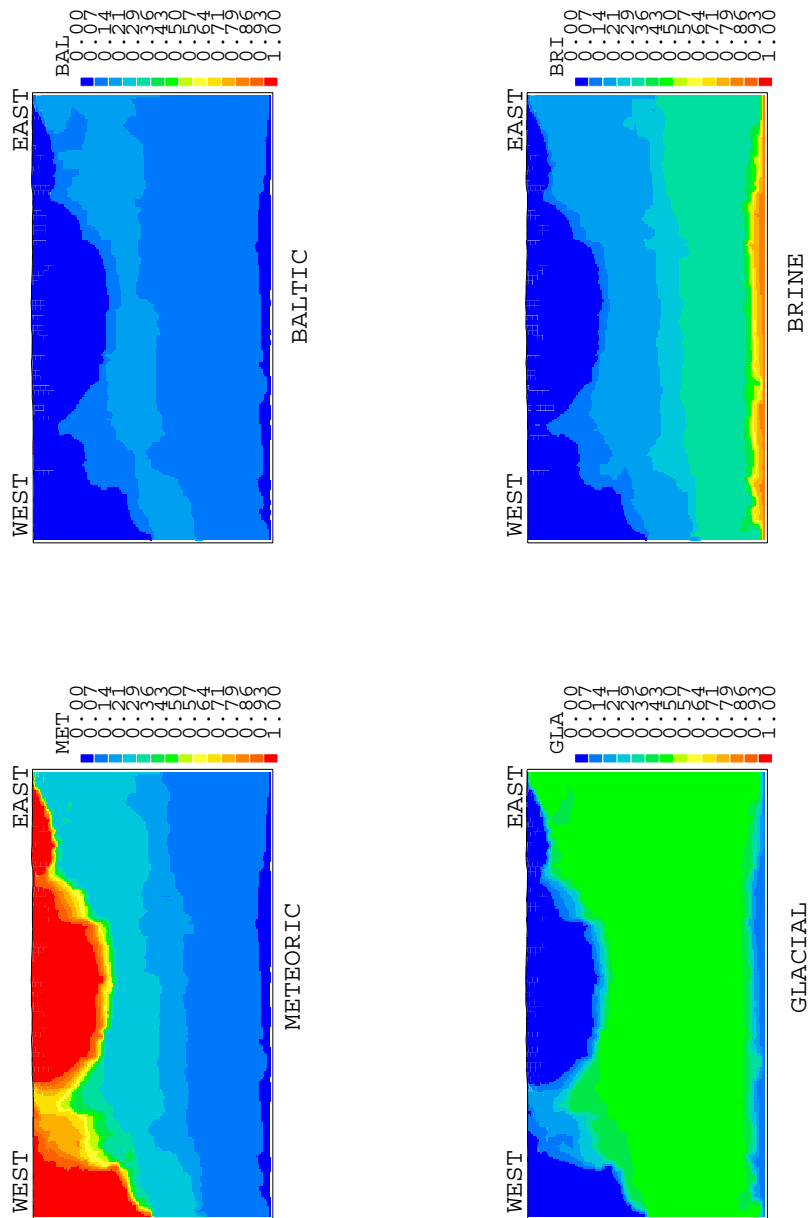□ *Simulated salinity at tunnel coordinate 2 800 metres.*

Figure V1-3. *Vertical sections through the centre of the spiral part of the tunnel, showing the simulated initial distributions of various water types.*
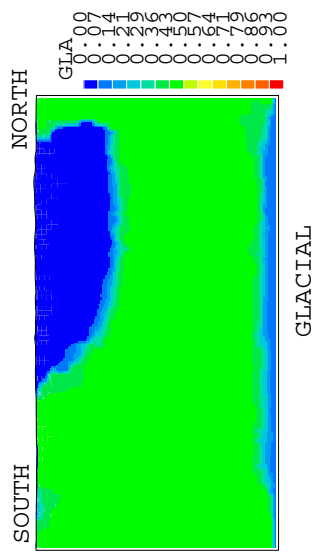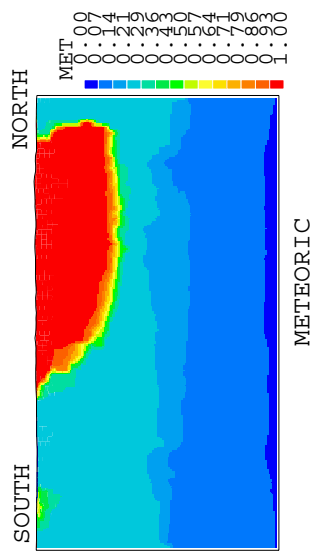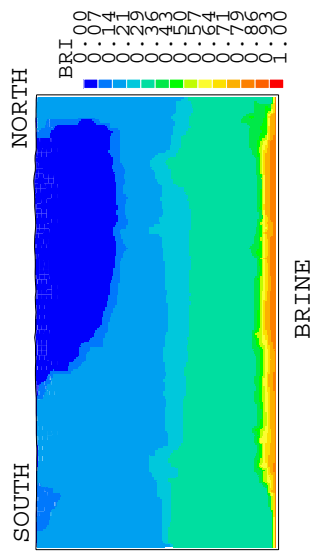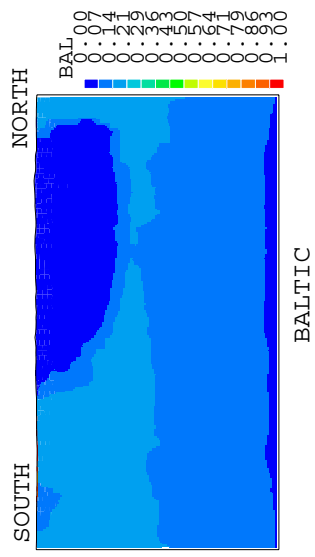
Figure V1-3. Cont.

Table V1-3. Comparison between measured and simulated water compositions in borehole sections prior to tunnel construction.

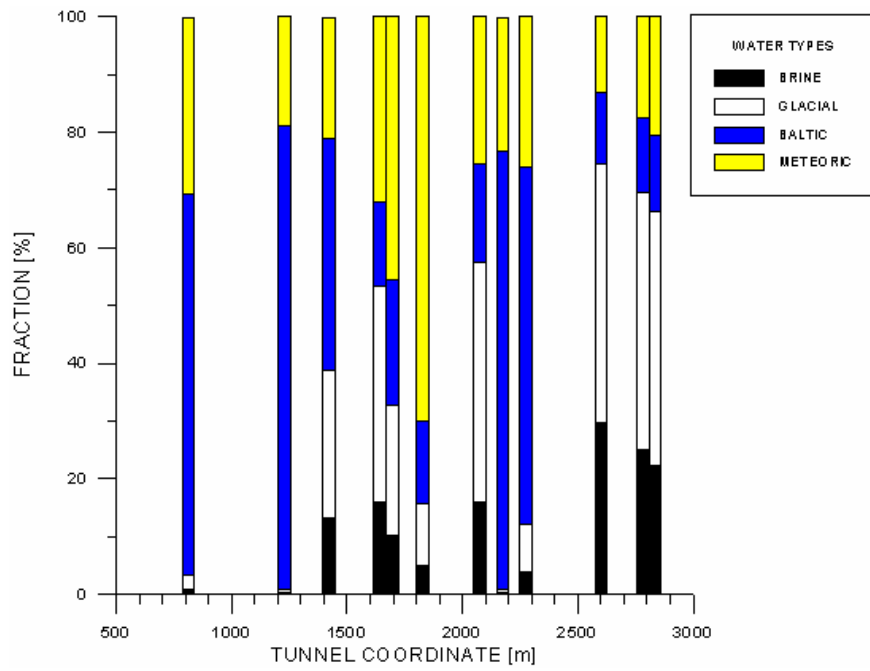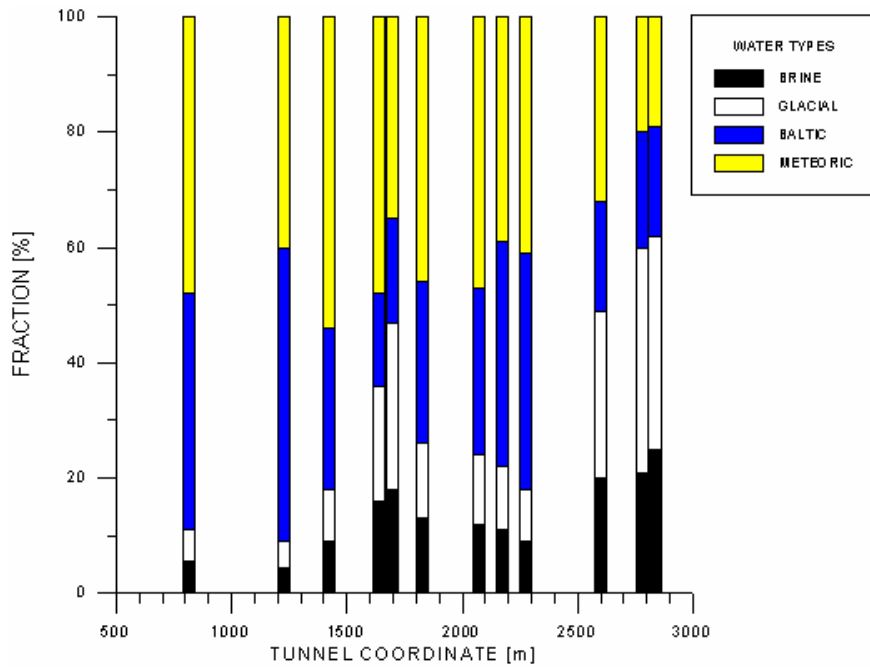| Borehole depth [m]	Measured (top) and simulated water composition			
	Meteoric	Baltic	Glacial	Äspö Brine
KAS02C 300 m	30.1	14.8	40.4	14.8
	66.3	6.5	19.9	7.3
KAS02D 440 m	26.9	15.0	43.0	15.0
	21.7	14.2	45.0	19.1
KAS02E 520 m	17.9	17.9	44.7	19.6
	20.4	13.9	45.0	20.6
KAS02F 840 m	13.6	13.6	45.4	27.4
	12.0	12.0	45.0	31.0
KAS02G 880 m	12.3	12.3	46.8	28.7
	11.9	11.9	44.8	31.3
KAS03D 340 m	20.2	14.7	50.3	14.7
	26.7	14.6	43.9	14.8
KAS03E 440 m	22.6	12.8	51.7	12.8
	24.5	14.9	45.0	15.7
KAS03F 600 m	16.0	16.0	50.9	17.1
	15.5	12.8	45.0	26.7
KAS03G 820 m	14.4	14.4	47.2	24.0
	12.0	12.0	45.0	31.0
KAS03H 900 m	11.1	11.1	44.5	33.4
	11.9	11.8	44.5	31.8
KAS04C 360 m	24.9	17.3	40.5	17.3
	28.8	13.8	42.1	15.4
KAS06C 320 m	34.5	35.4	15.1	15.1
	33.8	12.6	38.9	14.7
KAS06D 420m	33.7	31.3	17.6	17.6
	22.3	14.4	45.0	18.3
Average	21.4	17.4	41.4	19.8
	23.7	12.7	42.2	21.4

Figure V1-4. *Comparison between measured (top) and simulated water composition distribution for tunnel front at 3 170 metres.*

B13

Table V1-4. Comparison between measured and simulated water composition in boreholes. Tunnelfront: 3 170 m.

| Borehole depth [m]	Measured (top) and simulated water composition			
	Meteoric	**Baltic**	**Glacial**	**Äspö Brine**
KAS09	35.0	57.0	4.0	4.0
100 m	17.9	82.0	0.1	0.0
KAS14	32.0	64.0	2.0	2.0
100 m	21.7	77.3	0.8	0.3
SA0813	48.0	41.0	5.5	5.5
100 m	30.6	66.0	2.5	0.8
SA1229	40.0	51.0	4.5	4.5
160 m	18.9	80.2	0.7	0.2
SA1420	54.0	28.0	9.0	9.0
200 m	21.2	40.1	25.6	13.2
KAS07	60.0	32.0	4.0	4.0
200 m	18.2	81.2	0.4	0.2
SA1641	48.0	16.0	20.0	16.0
220 m	32.1	14.6	37.3	16.0
SA1696	35.0	18.0	29.0	18.0
220m	45.5	21.8	22.6	10.0
SA1828	46.0	28.0	13.0	13.0
240 m	70.1	14.4	10.7	4.9
SA2074	47.0	29.0	12.0	12.0
280 m	25.4	17.0	41.6	16.0
SA2175	39.0	39.0	11.0	11.0
280 m	23.3	75.8	0.6	0.2
SA2273	41.0	41.0	9.0	9.0
300 m	26.2	61.9	8.2	3.8
SA2600	32.0	19.0	29.0	30.0
340 m	13.1	12.3	45.0	29.7
SA2783	20.0	20.0	39.0	21.0
360 m	17.7	12.9	44.4	25.1
SA2834	19.0	19.0	37.0	25.0
360 m	20.5	13.2	44.0	22.4
KAS08	37.0	29.0	17.0	17.0
440 m	25.6	20.4	36.8	17.2
KAS07	27.0	18.0	37.0	18.0
460 m	15.8	12.9	45.0	26.3
KAS05	16.0	16.0	45.0	23.0
480 m	13.0	12.2	45.0	29.7
KAS03	25.0	23.0	49.0	13.0
560 m	23.5	14.6	44.9	16.9
Average	36.9	30.9	19.8	12.9
	25.3	38.5	24.0	12.3
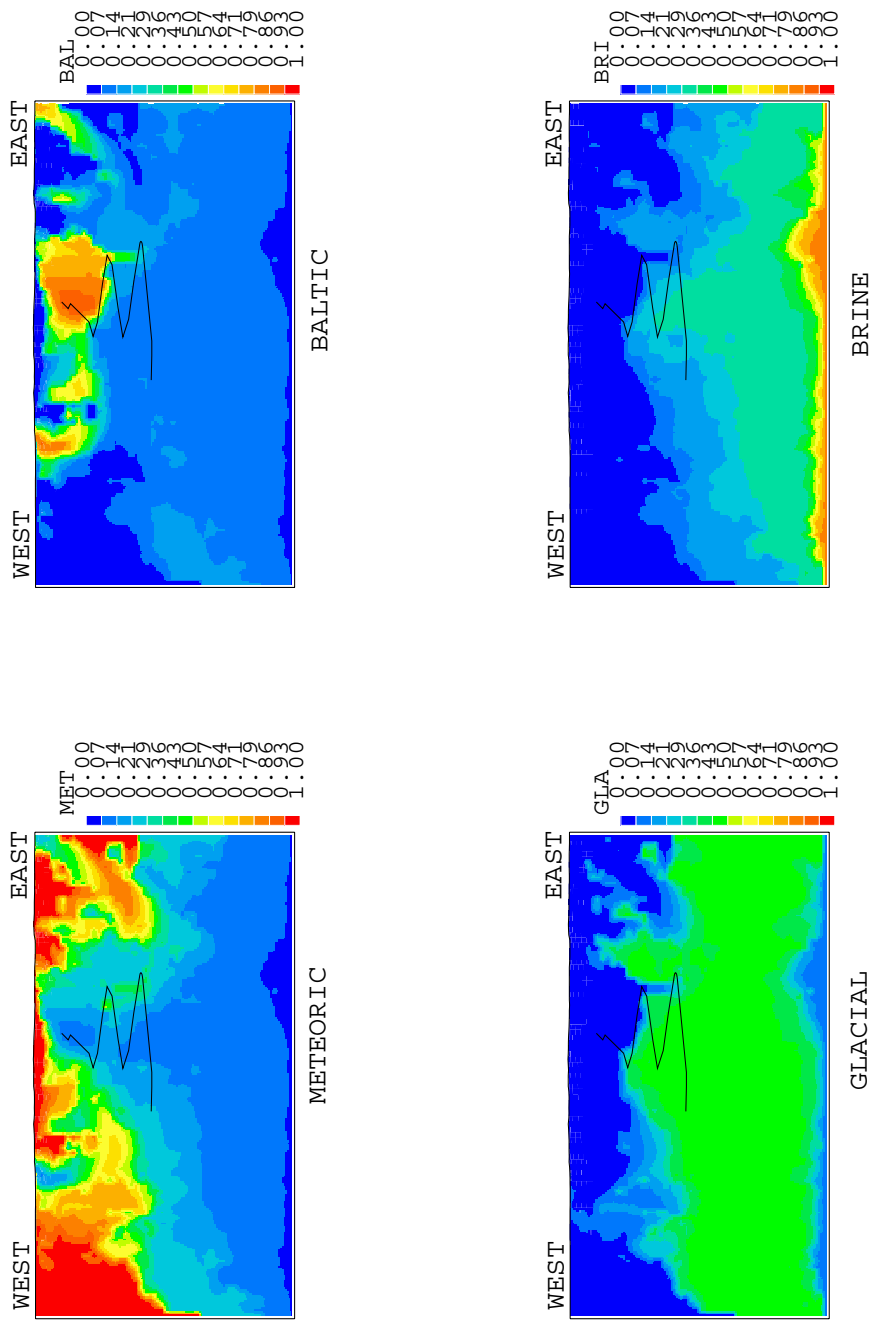
Figure V1-5. *Vertical sections through the centre of the spiral part of the tunnel, showing the simulated distributions of various water types. Tunnel front position: 3 170 metres.*
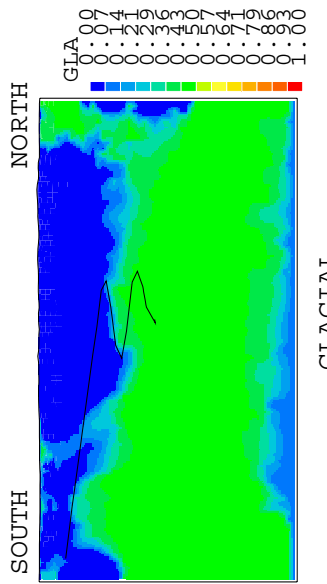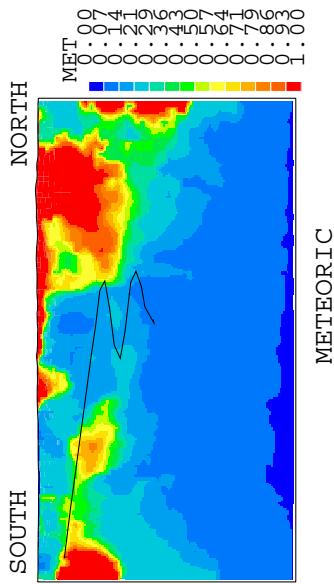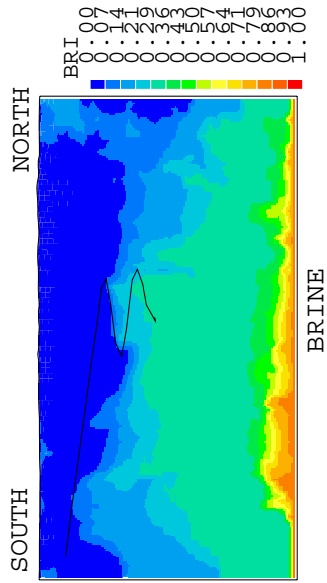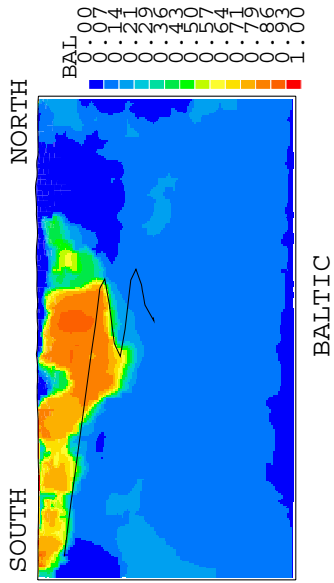
Figure V1-5. *Cont.*

B16

Table V1-5. Comparison between measured and simulated water composition in boreholes at time 1996-05.

Borehole depth [m]	Measured (top) and simulated water composition			
	Meteoric	Baltic	Glacial	Äspö Brine
SA2273 300m	46.0 30.6	38.0 64.7	8.0 3.1	8.0 1.6
Sa2600 340m	48.0 16.5	20.0 12.4	16.0 38.2	16.0 32.8
SA2783 360m	17.0 35.2	17.0 13.2	37.0 32.2	29.0 19.4
SA2880 380m	18.0 35.5	18.0 18.4	34.0 31.1	31.0 14.9
KA3005 400m	54.0 34.9	21.0 13.0	13.0 30.8	13.0 21.2
SA3067 400m	18.0 60.2	18.0 25.3	43.0 10.8	21.0 3.7
KA3110 400m	47.0 46.7	37.0 35.7	8.0 12.4	8.0 5.2
KA3385 440m	38.0 18.4	18.0 13.0	25.0 42.2	18.0 26.5
Average	35.8 34.8	23.4 24.5	23.0 25.1	18.0 15.7

Case V2   A laboratory scale validation

Introduction

The laboratory scale model (Svensson, 1999) was the first application of the GEHYCO approach to calculate the conductivity field. Very little information about the properties of the background fracture network was available and an important part of the calibration process was to find a tentative expression for the transmissivity of the background fractures.

The boundary conditions are generated from a site scale model. For consistency, also the tunnel inflow distribution is taken from the site scale model. The transmissivities of the major fracture zones were calibrated in the site scale model and will not be the subject of calibration here. These conditions and assumptions will strongly determine the flow, pressure and salinity distributions in the present model. It is thus clear that the calibration process is quite constrained and in practice limited to the influence of the background fracture network.

The objective of the calibration is to demonstrate that the conductivity fields generated by the suggested method can be calibrated to match field data from the Äspö HRL.

Calibration criteria

The following calibration criteria were formulated:

- In a recent study, see Rhén and Forsmark (2000), the frequency of "High Permeability Features" (HPF) at the Äspö HRL was studied. It was concluded that fracture zones with a transmissivity $\geq 10^{-5}$ m^2/s are found with an arithmetic mean distance of 75-105 metres. This includes also the deterministic fracture zones, which were found to contribute with about 48% to the total number of fractures found. The arithmetic mean distance between fractures with $T \geq 10^{-6}$ m^2/s was found to be in the range 35-55 metres. We will evaluate the mean arithmetic distances for fractures with $T \geq 10^{-6}$ and $T \geq 10^{-5}$ m^2/s, in the fracture network generated.

- During the construction of the Äspö HRL, the pressure was monitored in a number of borehole sections. The drawdowns at tunnel front position 2875 metres (i.e. when the tunnel was excavated to a length of 2875 metres) can be found in Rhén et al. (1997); these data will be compared with simulated drawdowns.

- The conductivity distribution for a test scale of 3 metres has been extensively studied at Äspö, (La Pointe, 1994, Rhén et al., 1997). The corresponding distribution of cell conductivities, with $\Delta = 3$ m, will be calculated and compared with field data.

Other criteria could have been formulated, but it is believed that the above criteria will constrain the background fracture network in a useful manner. Main arguments for the criteria are:

- The frequency of HPF:s will determine the transmissivity of large background fractures.

- It is essential that the model predicts the correct pressure drops in the borehole sections in the domain, as the drawdown distribution reflects the mean conductivity of the rock.

- By studying the conductivity distribution on the 3 metre scale, we can focus on the distribution of low conductivity cells. This may be essential for transport simulations.

Calibration process

The difficult step in the calibration process is to find a strategy for how the calibration criteria can be met. The more linked the criteria are the more difficult the task is. Fortunately, the criteria above are not strongly linked and the strong influence of boundary conditions and inflows to the tunnel also make the task easier. A few trial calculations indicated that the following strategy would work:

- First determine the transmissivity distribution for the background fractures.

- The comparison of conductivity distributions on a 3 metres scale indicated that the addition of a background conductivity improved the comparison with the measured distribution (details below). The added conductivity is however of the order 10^{-10} m/s. This small added conductivity was found to have a negligible influence on the agreement for other criteria. We can thus perform this operation independently.

- The pressure drops in borehole sections are to a large extent determined by the deterministic fracture zones, which have been calibrated in earlier studies. We thus expect the drawdowns to be of the right magnitude independently of other adjustments.

Results

The main outcome of the calibration is a formula for the transmissivity of the background fractures:

$$T = \begin{cases} 10^{-5}(L/100)^2 & \left[\text{m}^2/\text{s}\right] \text{ for } L \leq 100 \text{ metres} \\ 10^{-5} & \left[\text{m}^2/\text{s}\right] \text{ for } L > 100 \text{ metres} \end{cases} \tag{V2-1}$$

The frequency of High Permeability Features (HPF) was the most important criterion when establishing this relation, but of course it also ensured that the other criteria were fulfilled. Some properties of this relation include: the maximum transmissivity is of the same order as that for the deterministic zones and the transmissivity for $L = 5$ metres is 2.5×10^{-8} m^2/s, which ought to ensure that the smallest fractures do not make a significant contribution to the conductivity field.

As mentioned, the test on a 3 metres scale required the addition of a small background conductivity. It was found that a lognormally distributed conductivity, with $mean\left(\log_{10}(K)\right) = -10.0$ and $std.\ dev\left(\log_{10}(K)\right) = 0.8$, gives good agreement with field data.

Results will now be presented, which demonstrate that the calibration criteria have been adequately fulfilled.

High Permeability Features. In Figure V2-1 illustrations of conductivity fields based on fractures with $T \geq 10^{-5}$ m^2/s and $T \geq 10^{-6}$ m^2/s are found. The arithmetic mean distances were calculated by drawing a number of lines in the east-west direction and count the number of crossings. It was found that the mean distance for $T \geq 10^{-5}$ m^2/s (which includes deterministic zones) is about 80 metres and that the distance decreases to 57 metres if all fractures with $T \geq 10^{-6}$ m^2/s are counted. The corresponding values from the field
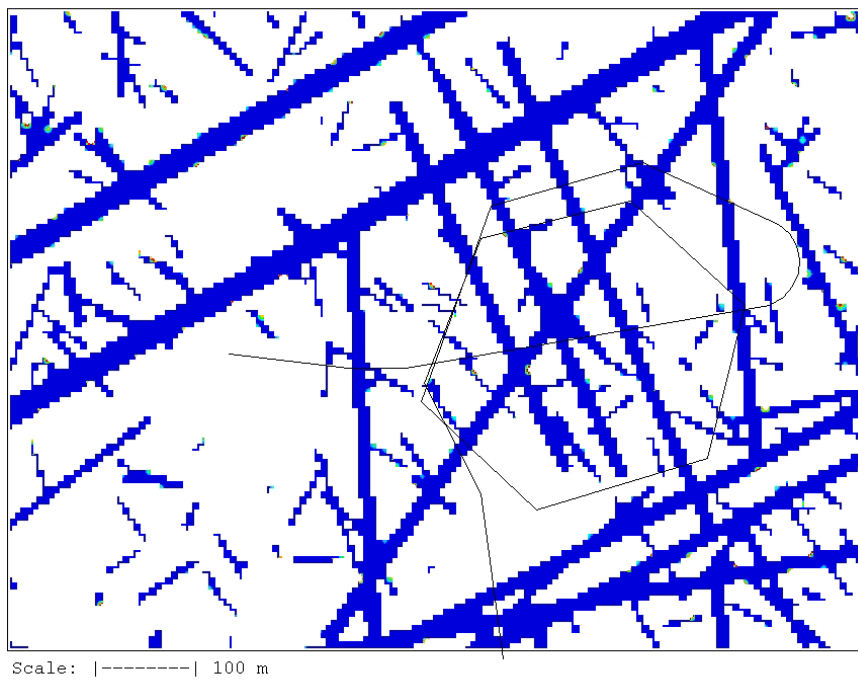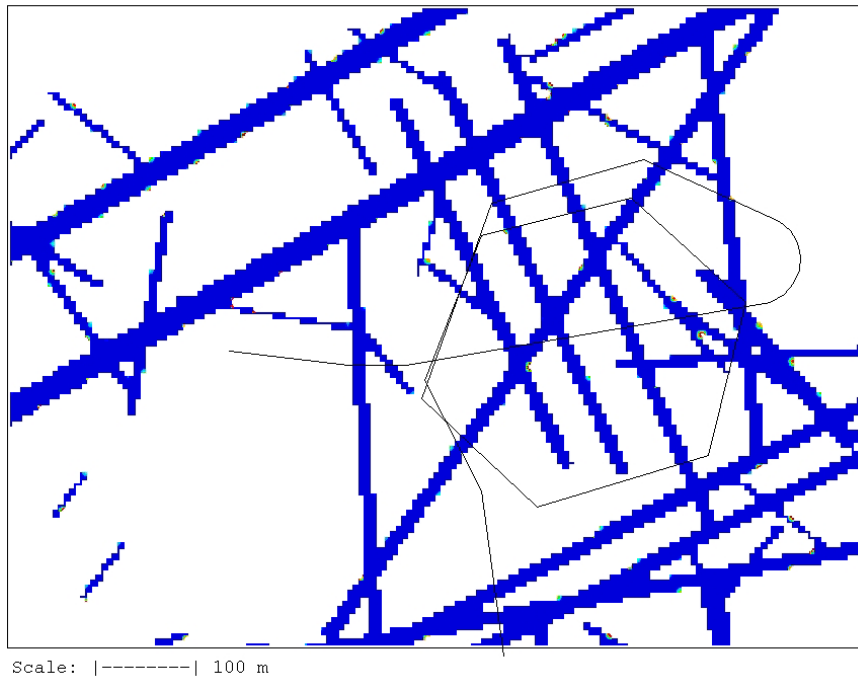
Scale: |--------| 100 m

Scale: |--------| 100 m

Figure V2-1. *Illustrations of calculated High Permeability Features.* $T \geq 10^{-5}$ *m^2/s (top) and* $T \geq 10^{-6}$ *m^2/s, all for a depth of 450 metres.*

B21

measurements are 75-105 metres and 35-55 metres, respectively. It should be noted that the two fields shown in Figure V2-1 are from different realisations; it is hence only the deterministic fracture zones that are the same in the two figures.

Drawdowns. The calculated drawdowns in borehole sections in the domain were compared with measured ones, all for the time when the tunnel was excavated to a length of 2875 metres. It was anticipated that the drawdowns should be sensitive to various realisations of the background fractures. In order to study this eight realisations of the background fractures were generated and the drawdown for each borehole section and each realisation was calculated. The result can be studied in Table V2-1; the location of boreholes can be found in Figure 1-3 (Report 1). It is seen that different realisations are best for different boreholes. Recognising this pattern, it is tempting to try to optimise the comparison by using what can be called the "Method of local realisations". We thus enclose a borehole in a volume and use fractures from the best realisation in this volume. The fracture centre is used to determine if a fracture belongs to the enclosing volume. This means that a large fracture with its centre outside the volume may still dominate the volume, which shows that there is no guarantee that the method improves the comparison in every borehole. In the vertical the volumes extended from the top to the bottom of the domain. In Table V2-1 results including local realisations can be found. When using this method one has to decide which realisation should be used outside the volumes enclosing the boreholes. This realisation is called the base realisation in Table V2-1. It is found that the locally optimised fields improve the agreement with measured drawdowns. Two measures of the agreement between measured and simulated drawdowns are given in Table V2-1, the arithmetic mean error and the goodness of fit value, defined as

$$\sqrt{\frac{\sum (a - \bar{a})^2}{n - 1}}$$, where a is the error, $\bar{a}$ the mean error and n the number of comparisons.

Two examples of the resulting conductivity fields are given in Figure V2-2. Two base realisations are shown, but the realisations around the boreholes are in both cases from the optimum realisation. The rectangles in Figure V2-2 indicate the enclosing volumes. By studying the same rectangle in both figures, one can see that small fractures inside the two rectangles are the same. It should be underlined that this first step towards a conditioning of the background fracture network with local realisations is not an integral part of the method suggested. It is included only to demonstrate that conditioning to field data is possible.

Conductivity on a 3 metres scale. In order to collect statistics for the 3 metres scale a smaller computational domain was used. The depth interval chosen was 200 to 500 metres. The block is thus 300 x 300 x 300 m^3 and with $\Delta = 3$ metres we get 10^6 cells in the grid. Isolated fractures were not removed for this case, as this was considered to be closer to the experimental conditions. Fractures down to a size of 2.5 metres were generated. The reason for this is that the smallest fracture size generated should be comparable to the cell size.

Comparisons with field data are given in Figure V2-3, where it can be seen that the cell conductivity distribution based on this fracture network has 36% of the cells with a conductivity of less than 10^{-11} m/s. A minimum conductivity of 10^{-12} m/s was prescribed to all cells. The calculated distribution is not in agreement with the field data. However, adding a lognormally distributed conductivity with $mean\left(\log_{10}(K)\right) = -10.0$ and $std.\ dev\left(\log_{10}(K)\right) = 0.8$ to all cells gives a much better agreement with field data. The argument for adding a background conductivity is that it represents fractures below the cut-off length in the network. It should be noted that adding this conductivity field does not strongly

Table V2-1. Measured and calculated drawdowns in borehole sections for various background fracture networks. Tunnel front at position 2875 metres.

| Borehole section	Contact with major fracture zone	Measured drawdown (m)	Error (Calculated - Measured drawdown) (in m) for various realizations of the background fracture network									With local realizations	
			Realization number									Base realization	
			1	2	3	4	5	6	7	8	Best	1	4
K02-B4	no	51.50	-10.57	-9.79	-8.48	-9.85	-11.64	-10.89	-11.01	-9.92	3	-10.11	-9.38
K02-V3	yes	16.90	9.13	9.16	9.20	9.28	9.11	9.02	8.92	9.22		9.17	9.26
K05-E4	no	40.40	4.40	5.15	6.48	4.66	5.10	6.95	10.59	2.28	8	3.69	1.99
K05-E3	no	39.90	-2.22	-0.51	0.73	-0.74	0.71	1.83	-0.37	0.93		-0.56	0.41
K05-E2	no	32.50	-3.40	-2.14	-4.84	-3.61	-4.55	-4.64	-4.77	-3.13		-2.90	-3.44
K05-E1	yes	29.20	-1.41	-0.96	-3.36	-1.59	-2.56	-2.99	-3.09	-1.88		-1.58	-2.20
K06-F4	no	33.80	-2.42	-1.60	-0.68	-0.81	-0.24	-0.34	-0.95	-2.10	4	-1.11	-0.78
K06-F3	no	13.90	15.84	17.64	18.12	15.24	19.81	17.30	16.21	18.38		14.57	15.99
K06-F2	no	29.10	-1.70	0.35	-0.78	-1.44	-1.29	0.83	-1.46	-2.13		-2.82	-1.41
K06-F1	yes	30.00	-4.26	-1.13	-2.97	-2.82	-3.76	-1.20	-3.42	-2.91		-4.30	-3.35
K07-J4	no	37.50	-1.23	-0.51	-0.01	-2.07	-0.23	-5.97	0.08	0.72	8	0.68	1.09
K07-J3	no	25.20	1.78	-0.55	-0.59	-1.75	-1.42	4.04	3.86	0.20		0.65	0.83
K07-J2	yes	11.70	4.79	4.45	4.41	4.08	4.33	5.39	4.02	3.80		3.93	3.81
K08-M2	no	16.60	9.59	7.75	8.04	9.25	6.08	9.61	9.27	9.31	5	7.44	6.80
K08-M1	yes	19.50	-5.55	-5.69	-5.58	-5.59	-5.56	-5.47	-5.50	-5.60		-5.40	-5.45
K12-DC	no	25.40	3.44	2.39	3.04	3.05	3.45	2.97	2.98	1.89	1	3.52	3.47
K12-DB	no	25.30	2.31	3.39	3.17	3.26	3.63	3.97	2.62	5.09		2.61	2.30
K12-DA	yes	24.90	2.38	4.09	3.63	3.10	3.86	4.07	3.43	4.48		3.10	2.85
K16-3	no	28.00	-6.61	-6.68	-6.50	-7.72	-6.56	-5.73	-8.28	-7.04	6	-5.97	-5.77
K16-2	yes	18.60	-6.43	-6.48	-6.28	-6.51	-6.45	-6.28	-6.40	-6.48		-6.39	-6.41
K16-1	no	16.70	-5.59	-6.09	-4.79	-5.70	-4.87	-5.01	-5.04	-5.36		-5.59	-5.28
	Mean error		0.11	0.58	0.57	0.08	0.33	0.83	0.56	0.46		0.12	0.25
	Goodness of fit		6.32	6.29	6.40	6.20	6.76	6.75	6.80	6.54		5.86	5.84

Scale: |--------| 100 m
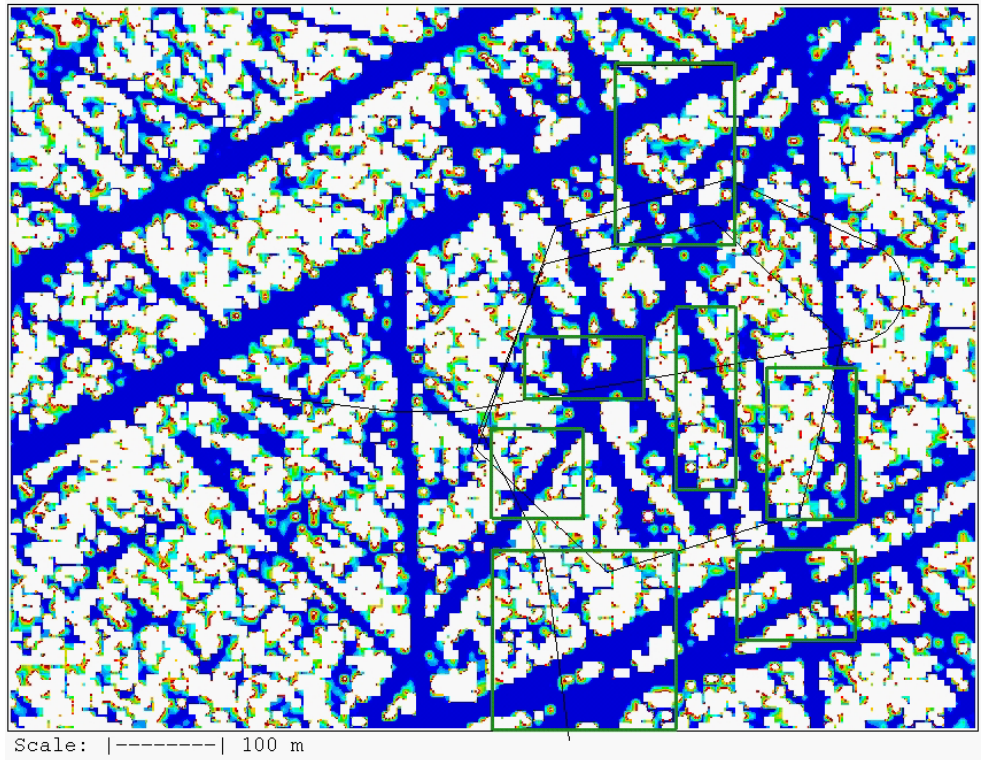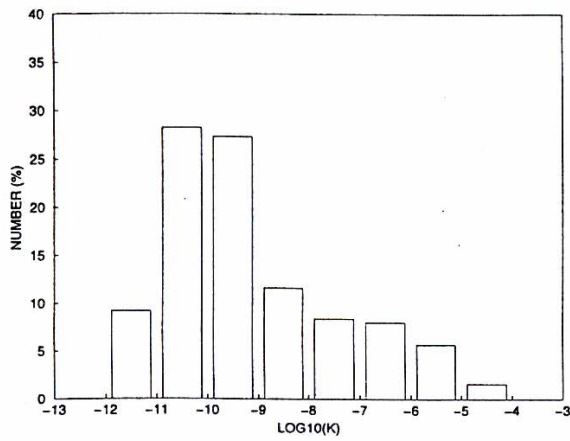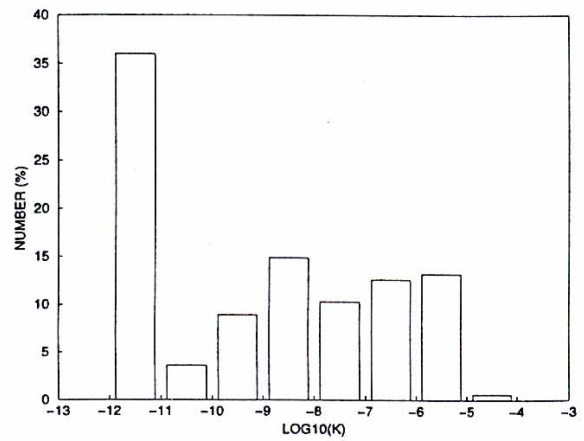

Scale: |--------| 100 m
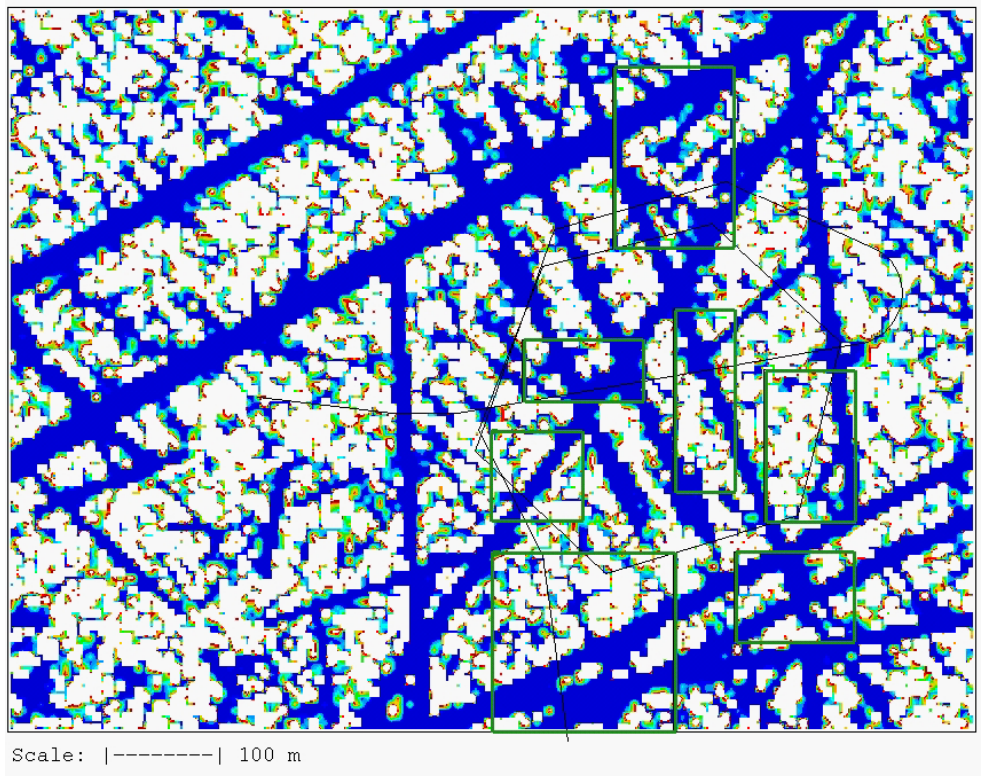
Figure V2-2. *Conductivity fields for base realisations 4 (top) and 1, see Table V2-1. The rectangles indicate volumes where fractures are taken from the optimum realisation.*
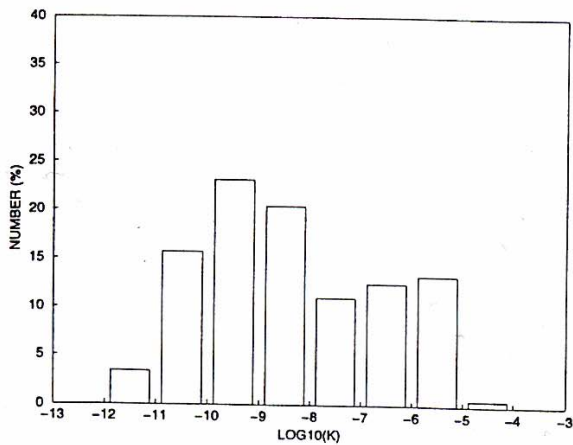
$$\text{Conductivity interval}: \begin{cases} \text{blue} > 10^{-8} \ \text{m/s} \\ 10^{-8} < \text{red} < 10^{-9} \ \text{m/s} \end{cases}$$
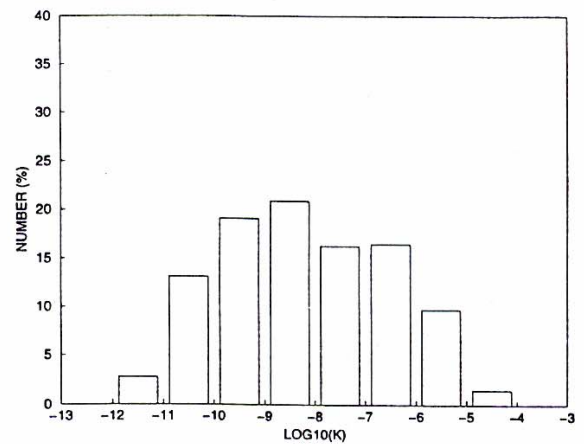
Measured
(Rhén et al., 1997)

Simulated
l_{min} = 2.5 m

Simulated
l_{min} = 2.5 m
Background
conductivity
added.

Simulated
l_{min} = 5.0 m
and Δ = 5.0 m
Background
conductivity
added.

Figure V2-3. Measured and simulated conductivity distributions on a 3 metres scale and simulated distribution for 5 metres scale.

influence the drawdown calculations, nor the frequency of high permeability features, presented above. It may however prove important to have also the "low conductivity connections" well described when transport simulations are attempted.

The field data are based on measurements in boreholes with a packer spacing of 3 metres. It may be questioned if it is relevant to compare these data with grid cell conductivities, with $\Delta = 3$ metres. If, as an example, we assume that the radius of influence is 3 metres in the field measurements we sample a cylinder with diameter 6 metres and length 3 metres. In order to see the influence of the cell size, the distribution for $\Delta = 5$ metres (using the main model domain) was also calculated. The result is shown in Figure V2-3. It is found that the conductivity distribution for $\Delta = 5$ metres is different and perhaps closer to the field data. Considering this uncertainty about the sampled volume, it is probably not worthwhile to strive for a closer agreement with the measured distribution. Further discussions about the field data can be found in La Pointe (1994) and Rhén at al. (1997).

Some further comparisons with data

In this section we will analyse the generated conductivity field and, when possible, compare with data. The results were not directly used in the calibration process but are anyway believed to illustrate the properties of, and add confidence to, the generated fields.

The first topic to be discussed is heterogeneity. As there is a large contrast in the hydraulic conductivity between fractures and intact rock, it is of interest to compare the heterogeneity of the generated conductivity field with field data. This can be done (Painter, 1999) by comparing the histograms of the increments in $\log K$, as shown in Figure V2-4. The basic idea is to determine the probability of finding a certain difference in $\log_{10} K$ when moving vertically a certain distance (the "lag" in Figure V2-4). Obviously, if we had a smoothly varying conductivity field the probability to find large increments for short lags would be low. The field data shown in Figure V2-4 are from 3 metres packer tests in eight boreholes on Äspö (see Rhén et al., 1997). These data were analysed, with respect to heterogeneity, by Painter (1999).

An illustration of the heterogeneity of the generated conductivity field is given in Figure V2-5. The cell conductivity, with $\Delta = 5$ metres, along a horizontal line is shown. The line is parallel to the final part of the tunnel (i.e. section 3400-3600 metres), at the same depth, but roughly 100 metres south of the Äspö tunnel. The reason for sampling this volume is that conductivity measurements, with 5 metres spacing, have recently been carried out in this volume. It is clear from Figure V2-5 that large variations in conductivity from cell to cell is a characteristic feature of the field generated. Qualitatively the distribution is in good agreement with the measurements.

An often used parameter to characterise a fracture network is the fracture area per unit volume, P_{32}. In Table V2-2, the contributions from different fracture sets are given. As can be seen, P_{32} is depending on the cut-off length in the fracture network. For the present cut-off length, 5 metres, the P_{32} parameter is 0.086. If however $l_{cut-off}$ was 2.5 metres P_{32} would increase to 0.117, and if $l_{cut-off}$ was 0.5 metres P_{32} would be 0.35; all calculated from the power-law distribution. Follin and Hermansson (1996) summarised reported estimates based on Äspö data. They found P_{32}-values in the range 0.0664 to 2.0 m^2/m^3. This is a wide range, which however includes the estimates from the present model.
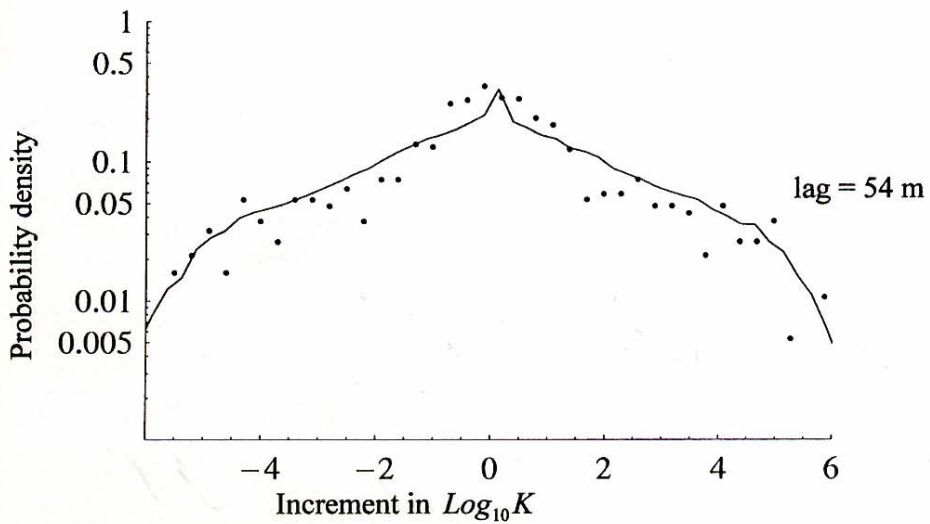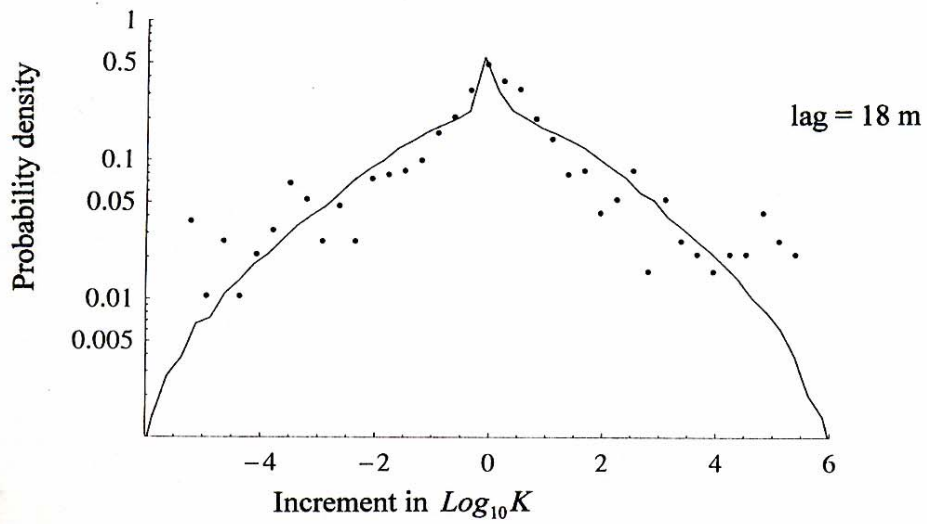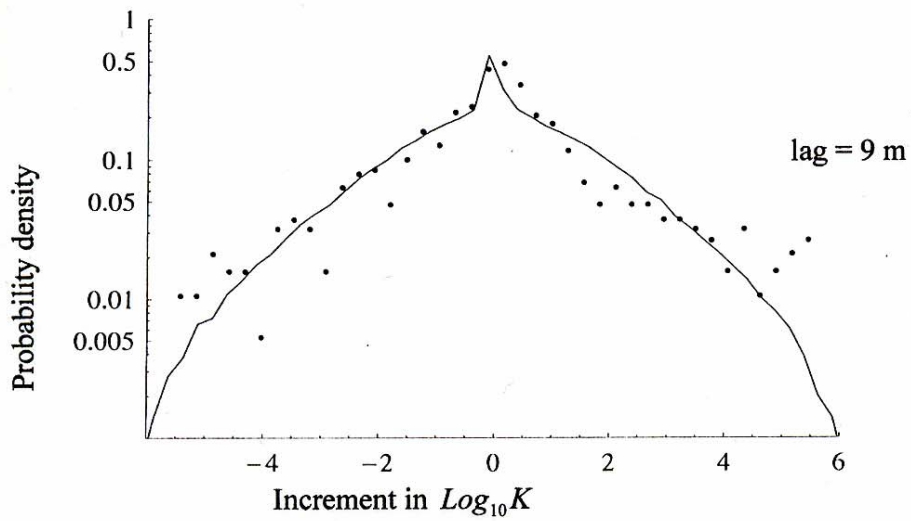
Figure V2-4. *Increment histograms. Measured (●) versus simulated (-) probability distribution for different lags.*
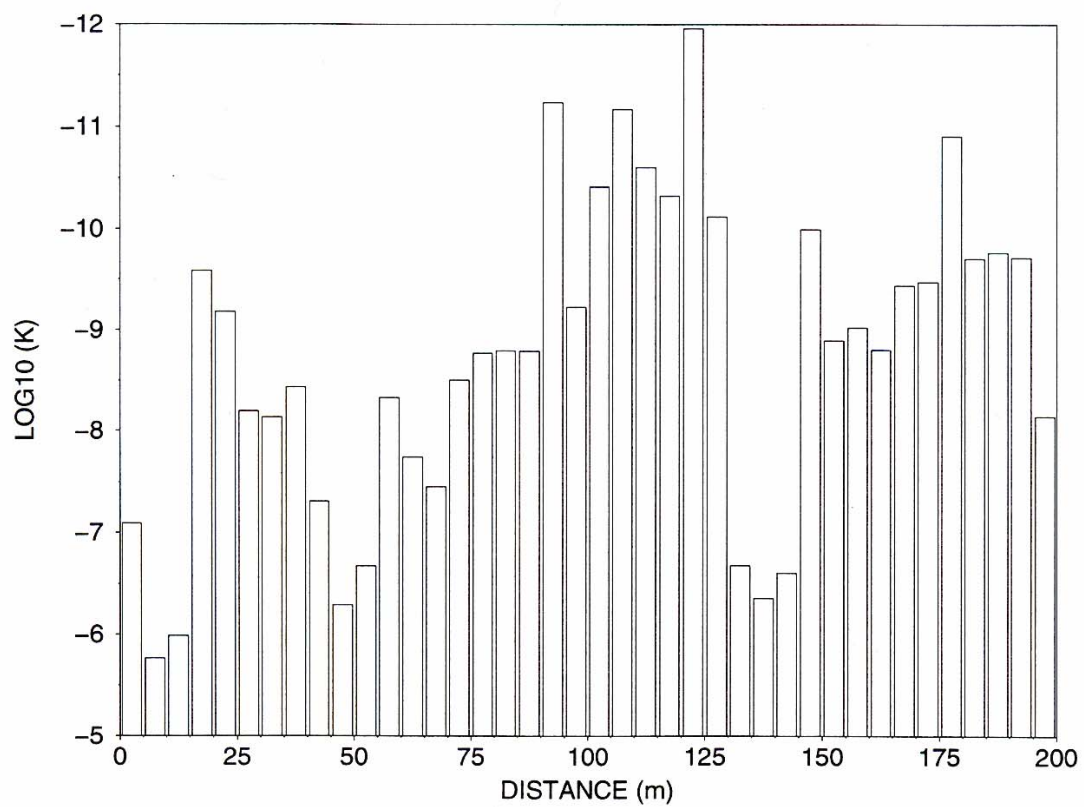
Figure V2-5. *Conductivity distribution along an east-west line south of the final part of the Äspö tunnel. The conductivity in the north-south direction is shown, but other directions are similar.*

Concluding remarks

The main conclusion from this calibration exercise is that the suggested method to generate conductivity fields can be calibrated to match Äspö data. This was achieved by the following actions:

- Retain the transmissivities for the major fracture zones, as used in the site scale model, without modification.

- Employ a background fracture network with a fracture transmissivity that decreases with fracture size, see Equation V2-1.

- Add a background cell conductivity, which has a lognormal distribution. Also apply a lower limit (=10^{-12} m/s) for the cell conductivity.

When comparisons with measured drawdowns in borehole sections were made, it was found advantageous to use different realisations of the background fracture network for different boreholes. This is a novel technique that seems to work well, but may require some further evaluation.

Table V2-2. The fracture intensity P_{32}, expressed as m^2/m^3, based on deterministic fractures and the background fracture network.

Fracture length interval	P_{32} [m^2/m^3]
Determ. fracture zones	0.014
160-320	0.008
80-160	0.007
40-80	0.008
20-40	0.011
10-20	0.016
5-10	0.022
	Σ 0.086

Case V3   A repository scale validation

Introduction

This validation study is taken from a recent report (Svensson, 2001), dealing with the Prototype Repository Project, which aims to test the components in SKB:s deep repository system; see Figure 1-1 (Report 1) for the location of the computational domain and Figure V3-1 for the layout of the Prototype Repository. The objective of the report mentioned was to "develop and establish an adequate model of the groundwater pressure and salinity distributions in the domain". More precisely five realisations that fulfilled some criteria were sought.

Calibration criteria

With the objective in mind, it was concluded that the following criteria ought to constrain the model in a useful way:

- Tunnel inflows. Measurements and estimates of the inflow to different tunnel parts are available, see Forsmark and Rhén (1999) and Stigsson et al. (2000). A recent re-evaluation (Rhén, 2001, pers.com.) of the inflow data has however revealed that the inflows are 2-3 times higher than given in the reports mentioned. Based on this information, the inflow to the tunnels has been divided into three parts, see Figure V3-2. The model should predict these inflows as closely as possible.

- Borehole pressures. Extensive data on borehole pressures, before, under and after the excavation of the deposition holes, are available, see Forsmark and Rhén (1999), Forsmark et al. (2001). The pressure measurements before the excavation will be compared with calculated pressures. Also the relation "Pressure-Distance from tunnel" will be studied as this is considered to be a well established relation from field data.

- Conductivity statistics. The conductivity distribution for the 1 metre scale has been estimated from borehole sections. This distribution will be compared with the cell conductivities in the Repository model (which has a cell size of 1 metre). It is however not obvious that field data from a packer spacing of 1 metre can be directly compared to the grid conductivities.
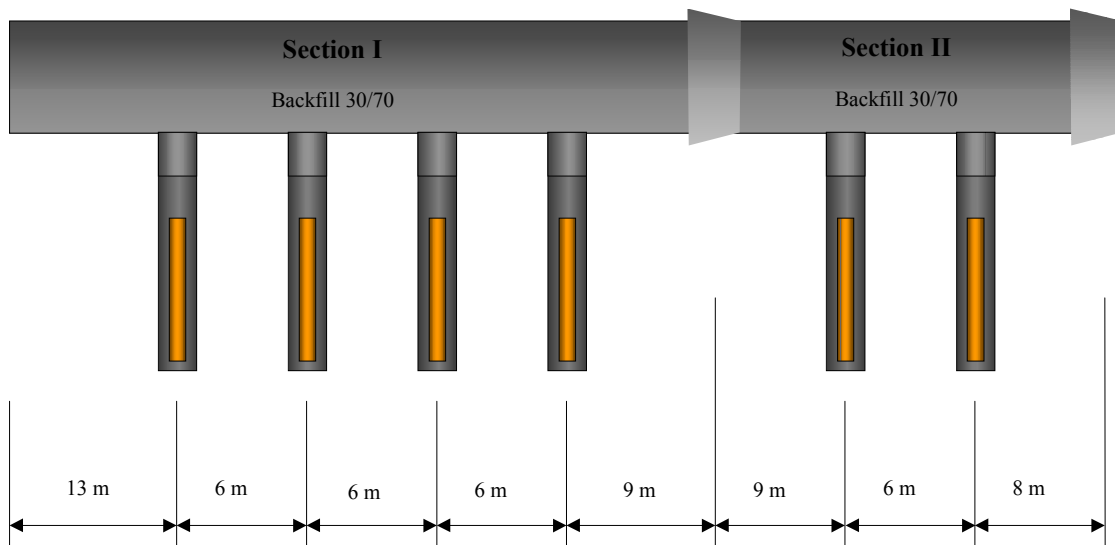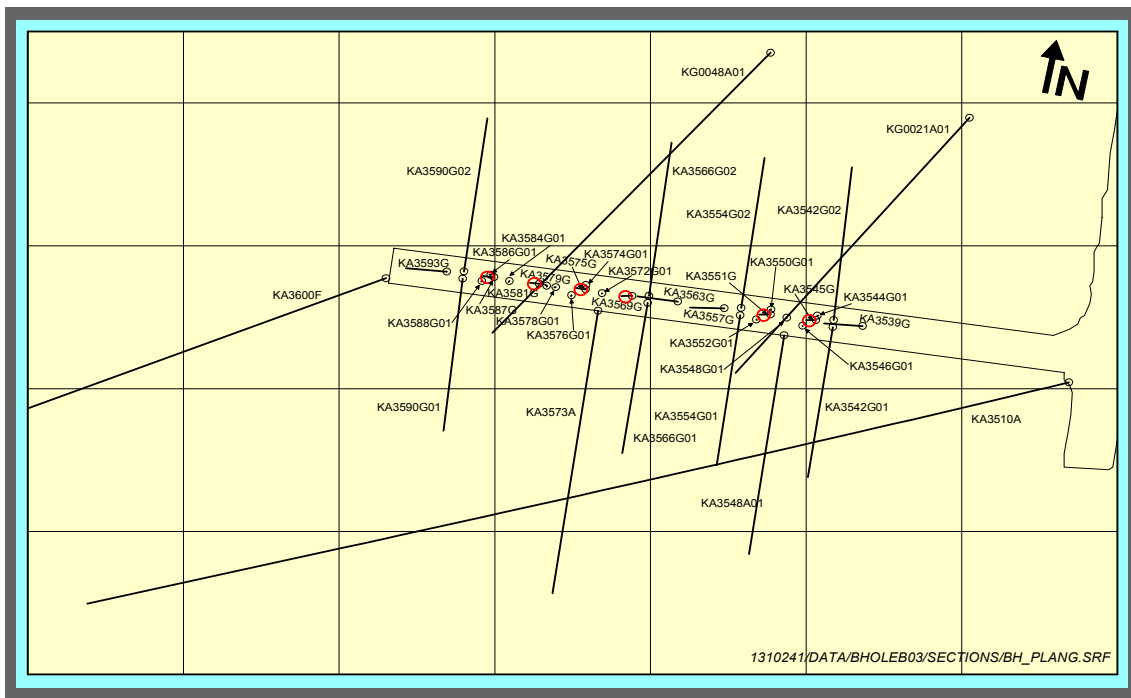
Figure V3-1. *The Prototype Repository area. Six deposition holes and boreholes used for pressure monitoring.*
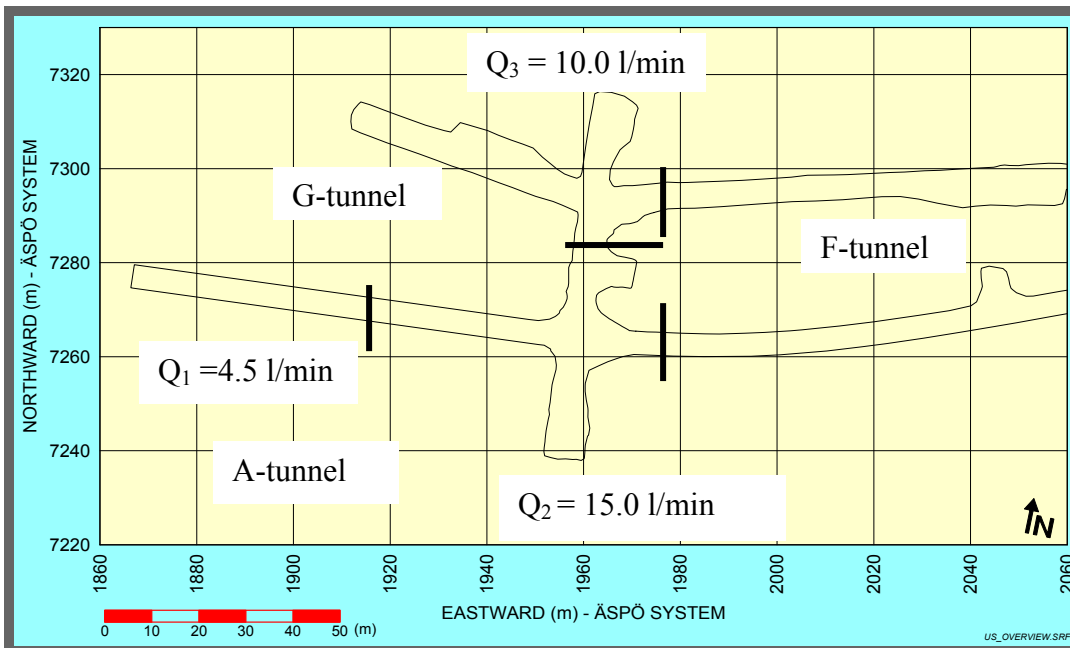
Figure V3-2. *Total inflow to the tunnels is partitioned into three inflows.*

Calibration process

The methods and concepts, embedded in DarcyTools, have earlier been applied to larger scale problems, i.e. the Laboratory and Site scale models. The pressure distribution around a tunnel is quite a different problem and it was not clear if, for example, the type of fracture network generated would be suitable also for this problem. However, it was decided to follow the procedures from the Laboratory model as a first test. Fracture properties, orientation, intensity, etc were thus determined from the formulae given in Svensson (1999), also for the Repository model. In the Laboratory model a background conductivity with a lognormal distribution was used as a tuning knob; the same approach will be used for the Repository model.

Preliminary tests showed that it ought to be possible to generate five realisations that fulfilled the criteria, simply by tuning the background conductivity. The following steps can thus describe the calibration process:

- Generate a large number of realisations of the conductivity field and select the five best based on the following criteria:

  - No large fracture, with its centre outside the Repository model, should be present close to the tunnels (Note that large fracture with centres inside the domain have been removed and replaced with deterministic fractures).

  - A "realistic" inflow (say $10 \rightarrow 50$ l/min, without skin) in each tunnel section shown in Figure V3-2. If a large fracture crossed a tunnel an inflow of perhaps several hundred l/min was generated, which means that the two conditions are partly linked. However, also a zero inflow case (or close to zero) has to be rejected, due to the first calibration criterion chosen.

- For the five realisations chosen, verify that the application of a skin around the tunnels can force the inflows to the desired values.

- Adjust the mean of the background conductivity, K_0, to get good agreement with the pressure data from boreholes. The standard deviation $\left(\text{for } \log_{10} K_0\right)$ of the added conductivity was fixed to 1.0.

- Check that the conductivity statistics for the 1 metre scale is in fair agreement with field data.

Results

Twenty realisations of the conductivity field were generated in order to select five acceptable. Some of these twenty realisations generated an inflow of several hundred l/min, others zero, in a tunnel section.

The five best could however be forced, by way of a skin factor, to give a correct inflow for all three tunnel sections shown in Figure V3-2. The skin factor multiplied all cell wall conductivities of the cells facing the tunnel. As can be seen in Table V3-1 the skin factors are in the range 0.02 →10. The upper limit for the skin factor was set to 10.0 and, as can be seen, this skin was applied for Q_2 in realisation 3. The inflow is still a little bit lower than desired.

In Table V3-1 also the mean values for the added background conductivity are given; these are in the range $3.0 \rightarrow 6.5 \times 10^{-10}$ m/s. The values were determined from a comparison with measured pressures in borehole sections, see Table V3-2. In this comparison we will intentionally call the difference between the measured and calculated pressures a "difference" and not an error, as an error is something that can be identified and corrected. Anyway, the objective of the calibration, using the added conductivity as a tuning knob, was to bring down the mean difference to a small value; as can be seen in Table V3-2 this was successful. If we like, one can consider the added conductivity as representing fractures smaller than the smallest fracture generated in the network, i.e. smaller than 1 metre. A conductivity value of around 10^{-10} m/s seems to be of the right magnitude to simulate such fractures. In Table V3-2 also the number of comparisons with an absolute difference in head, smaller than 100 metres is given; this gives an additional measure of the comparison. It should be added that more pressure recordings than given in Table V3-2 are available. The ones selected are those that were classified as "best quality" in Forsmark and Rhén (1999).

Another way of representing the comparison of pressures in Table V3-2, is shown in Figure V3-3. Now the pressures, measured and simulated, are shown as a function of the distance to the nearest tunnel centre. As we are interested in the nearfield around the tunnels, this way of plotting the information is of interest. The first diagram in Figure V3-3 shows the mean of all five realisations, as compared to the evaluated trend in the measured data. The trend in the measurements was estimated by fitting a straight line to the measured heads in Table V3-2. The rest of the diagrams show comparisons for each realisation. From Figure V3-3 one can conclude that the pressure head may vary with several hundred metres at a distance of, say, 10 metres from the tunnel centre. Further, the simulations show the same trend and spread as the measurements.

Finally, we will check the conductivity statistics. As mentioned above, it will be assumed that the 1 metre cell conductivities can be compared to the conductivities obtain from borehole measurements with a packer spacing of 1 metre. The distributions

from the five realisations are given in Table V3-3 and in Figure V3-4 the mean of the five realisations is compared to the measured distribution. It is found that the agreement is good for conductivities above 10^{-9} m/s, while a deviation is found below this value. The distribution is however sensitive to the value of the added background conductivity for small conductivities. This is illustrated in Figure V3-4, where the distribution for a background conductivity of 10^{-11} m/s is also shown. As can be seen this will result in a perfect agreement with the measured distribution. It was however regarded as more important to optimise the agreement with the pressure measurements, and the background conductivities given in Table V3-1 are thus kept.

Concluding remarks

It can be concluded that five realisations of the conductivity field, that fulfill the calibration criteria, have been found. The agreement with measurements is generally very good.

It is worth noting that this was achieved by adding a small background conductivity, while the basic methods and parameter estimates are kept from the Laboratory scale model.

Table V3-1. Inflows, skins and background conductivities for the Repository model. Skin factors are given with high accuracy in order to facilitate later comparisons.

Realisation	Q_1 l/min	Q_2 l/min	Q_3 l/min	Skin$_1$	Skin$_2$	Skin$_3$	Mean conductivity added m/s [x 10^{-10}]
1	4.5	15.0	10.0	0.0259	7.3655	0.1019	3.0
2	4.5	15.0	10.0	0.0715	0.0995	6.1238	5.0
3	4.5	13.6	10.0	0.0255	10.000	0.2430	6.5
4	4.5	15.0	10.0	0.0713	0.2595	0.0793	6.5
5	4.5	15.0	10.0	0.4360	0.0608	0.0352	3.0

Table V3-2. Comparison between measured pressures in borehole sections and simulated pressures from five realisations of the fracture network.

| Borehole	Measured Head [m]	Realisation									
		1		2		3		4		5	
		Head	Diff.	Head	Diff.	Head	Diff.	Head	Diff.	Head	Diff.
KA3510A:3	393.2	404.3	11.1	407.4	14.2	394.6	1.3	411.2	18.0	425.5	32.2
KA3539G:1	308.2	311.3	3.1	243.7	-64.5	289.9	-18.3	291.9	-16.3	338.4	30.0
KA3542G01:1	378.7	364.5	-14.1	323.3	-55.2	304.4	-74.1	319.6	-58.9	389.8	11.4
KA3542G02:1	321.9	154.2	-167.7	240.6	-81.3	134.1	-187.8	202.6	-119.3	235.1	-86.8
KA3550G01:1	18.1	220.5	202.4	256.7	238.5	174.4	156.2	198.6	180.5	230.5	212.4
KA3550G02:1	377.6	382.1	4.5	378.8	1.2	358.9	-18.7	376.9	-0.7	405.8	28.2
KA3563G01:1	327.8	261.8	-66.0	288.2	-39.6	269.1	-58.7	269.6	-58.2	302.8	-25.0
KA3563G01:2	142.0	389.7	247.6	347.3	205.2	336.5	194.5	341.9	199.9	292.2	150.2
KA3563G01:3	142.1	187.8	45.7	218.9	76.8	206.3	-64.2	169.9	27.8	267.6	125.5
KA3566G02:1	24.6	188.5	163.9	201.6	177.0	176.8	152.2	138.1	113.4	219.2	194.6
KA3566G02:2	349.2	354.6	5.4	296.6	-52.6	333.6	-15.6	323.2	-26.0	337.6	-11.6
KA3572G01:1	353.6	298.9	-54.7	298.3	-55.3	308.9	-44.7	300.6	-53.0	304.1	-49.5
KA3573A:1	191.5	359.3	167.8	303.2	111.7	316.8	125.3	286.3	94.9	280.1	88.7
KA3573A:2	404.9	366.7	-38.2	382.7	-22.2	371.8	-33.0	373.0	-31.8	324.5	-80.4
KA3579G01:1	391.5	280.3	-111.1	315.0	-76.4	316.0	-75.5	277.3	-114.2	289.4	-102.1
KA3584G01:1	204.1	416.7	212.6	322.6	118.5	348.3	144.2	323.7	119.6	280.0	75.9
KA3590G01:1	11.5	325.8	314.3	241.0	229.5	325.2	313.7	268.8	257.3	218.6	207.1
KA3590G01:2	395.6	425.1	29.5	382.1	-13.6	396.1	0.5	379.2	-16.4	326.7	-68.9
KA3590G02:1	389.8	340.5	-49.3	272.9	-116.9	332.9	-56.9	283.8	-106.1	227.8	-162.0
KA3590G02:2	368.0	350.5	-17.6	351.4	-16.7	382.2	14.1	360.7	-7.4	332.8	-35.3
KA3590G02:3	363.4	352.2	-11.2	339.8	-23.6	374.4	11.0	349.5	-14.0	315.4	-48.0
KA3590G02:4	276.8	339.1	62.3	320.3	43.4	362.0	85.2	332.1	55.3	285.8	8.9
KA3590G02:4	100.1	311.3	211.2	239.3	139.2	317.1	217.1	270.1	170.0	65.5	-34.6
KA3593G01:2	216.1	311.7	95.6	232.1	16.0	339.3	123.2	257.9	41.8	137.4	-78.6
KA3600F:2	409.7	404.9	-4.8	276.1	-133.6	372.5	-37.2	364.3	-45.4	315.2	-94.5
KG0021A01:2	349.5	114.0	-235.6	249.2	-100.3	197.6	-152.0	234.7	-114.9	271.3	-78.3
KG0021A01:3	349.6	68.7	-280.9	268.6	-81.0	163.9	-185.6	218.4	-131.2	255.8	-93.8
KG0021A01:4	331.7	88.5	-243.2	239.1	-92.6	159.2	-172.5	225.8	-105.9	263.8	-67.9
KG0021A01:5	231.1	149.2	-81.9	188.7	-42.4	111.3	-119.8	204.4	-26.6	261.5	30.5
KG0048A01:1	386.2	267.7	-118.5	277.2	-109.0	314.4	-71.8	268.1	-18.1	241.5	-144.7
KG0048A01:2	364.0	246.2	-117.8	278.1	-85.9	289.7	-74.3	267.1	-96.9	212.3	-151.7
KG0048A01:3	370.7	206.2	-164.5	272.2	-98.5	295.6	-75.1	276.5	-94.2	269.3	-101.5
KG0048A01:4	294.0	234.4	-59.5	132.3	-161.7	283.0	-11.0	254.6	-39.4	315.9	22.0
Mean Diff		-2		- 5		4		-3		-9	
Numbers with │Diff│ < 100		18		21		20		20		23	
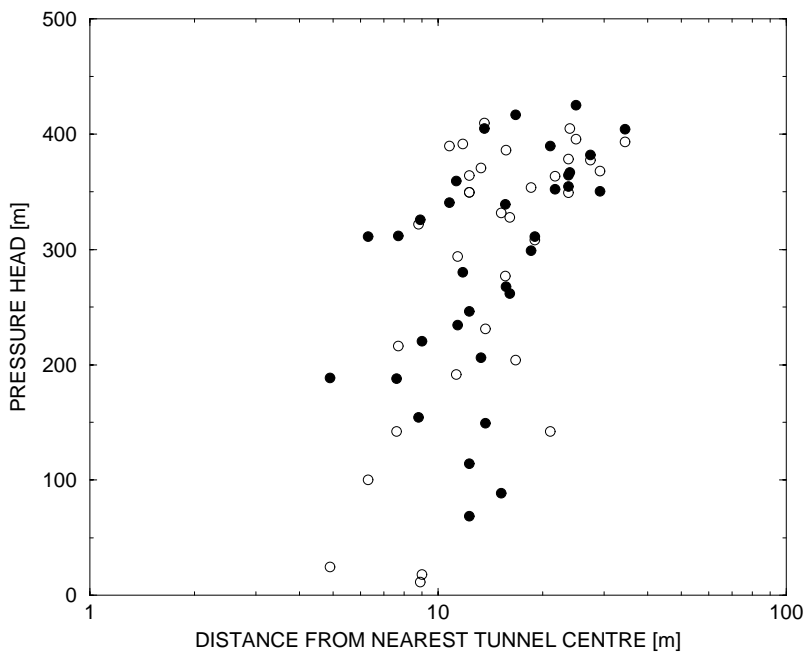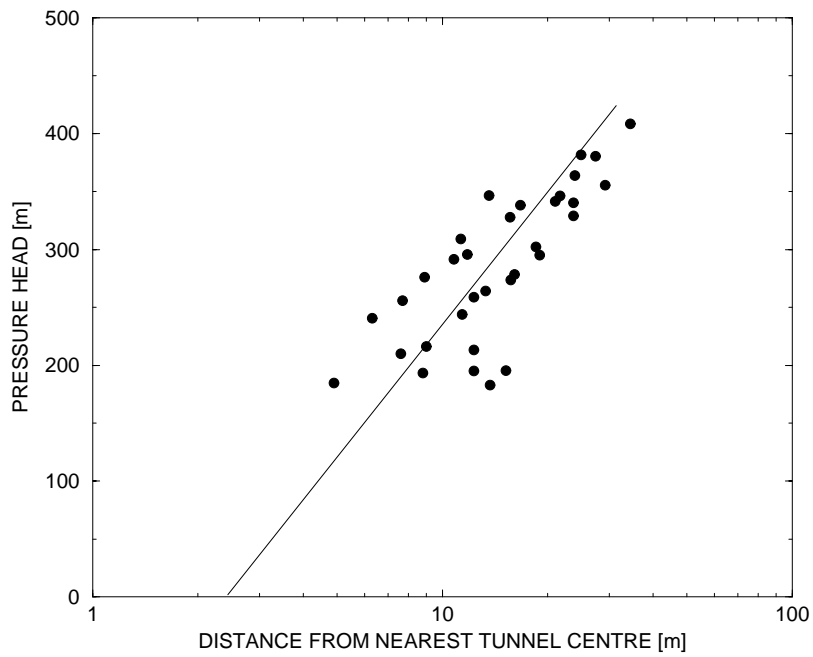
Figure V3-3. *Pressure head as a function of distance to nearest tunnel centre. Average of all five realisations compared to measured trend (top); straight line represents measurements. Bottom: Realisation 1 and measured data.*
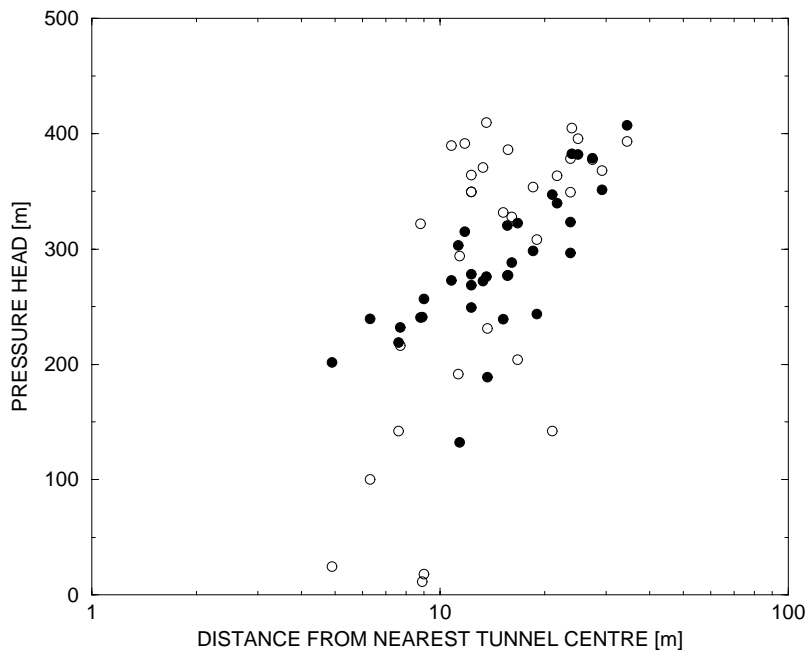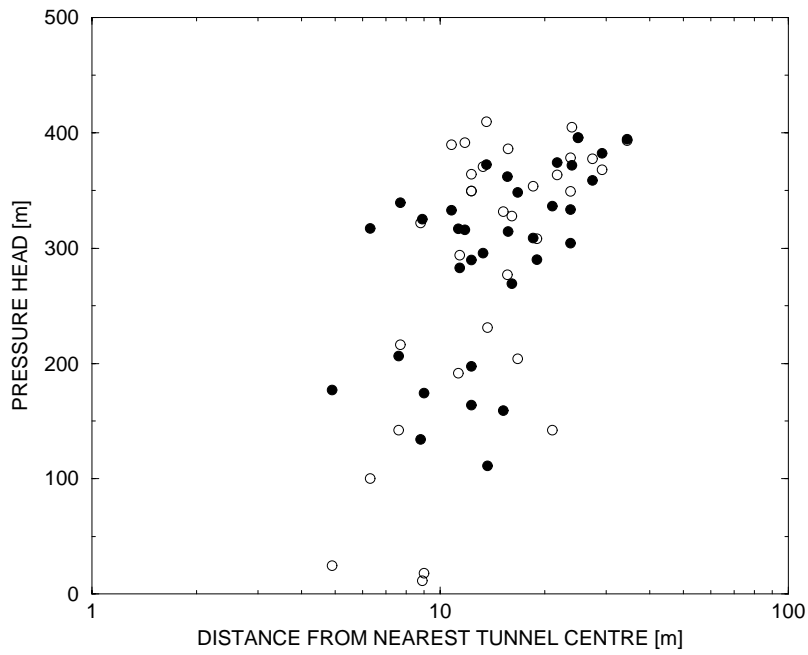○ *Measurements*
● *Simulations*

Figure V3-3, Cont. *Pressure head as a function of distance to nearest tunnel centre. Realisation 2 (top) and 3.*
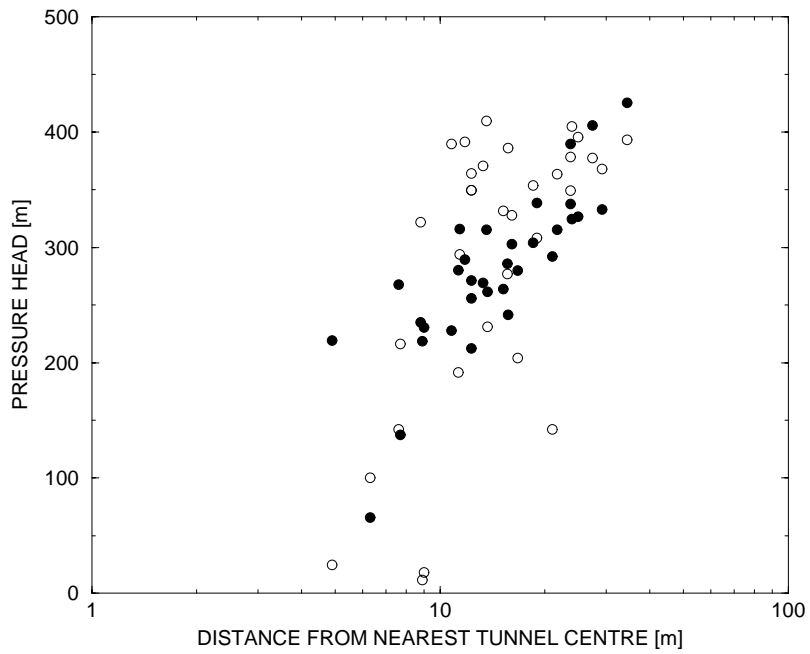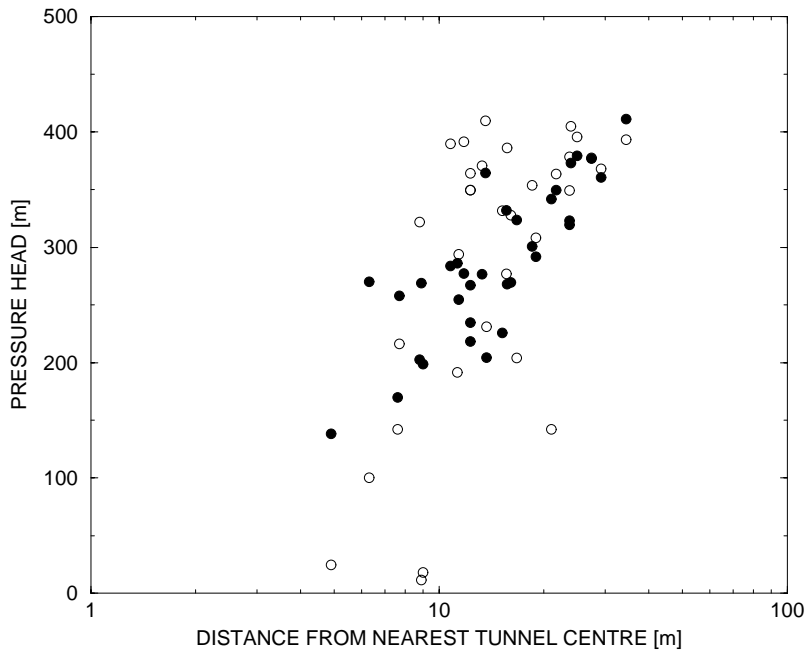○ *Measurements*
● *Simulations*

B38

Figure V3-3, Cont. *Pressure head as a function of distance to nearest tunnel centre*
Realisation 4 (top) and 5.
○ *Measurements*
● *Simulations*

Table V3-3. Simulated conductivity distributions. Five realisations and the average distribution.

Realisation	Cumulative conductivity distribution ($\log_{10} K$, in %), K [m/s]						
	<-11	<-10	<-9	<-8	<-7	<-6	<-5
1	5	25	58	81	92	96	100
2	3	21	55	83	96	99	100
3	3	18	50	80	95	99	100
4	3	17	50	80	94	99	100
5	5	26	60	84	95	99	100
Average	4	21	55	82	94	99	100
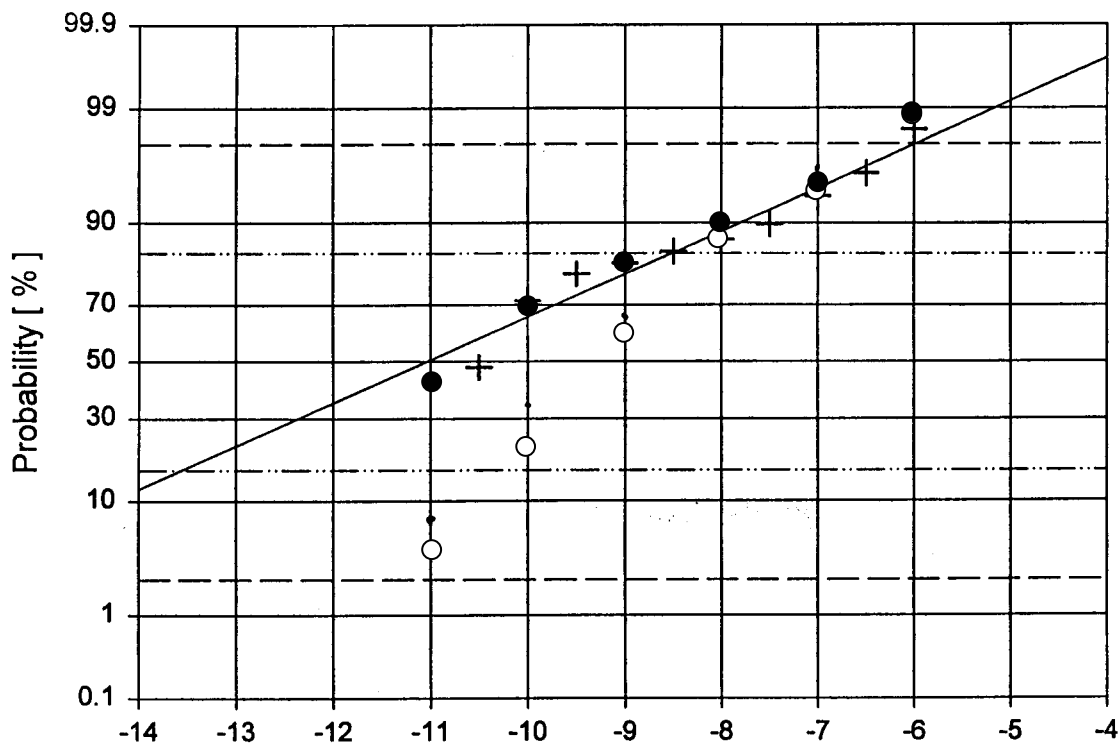
Figure V3-4. Comparison between measured (line and crosses) and simulated conductivity distribution for a scale of 1 metre. (Basic figure from Stigsson et al., 2000).
○ *Mean of five realisations.*
● *Realisation 4 with an added conductivity of 10^{-11} m/s.*

Case V4   An experimental scale validation

Introduction

Validation implies that the simulations should be compared with measurements. However, in this study a "somewhat derived form" of the field data will be used. The BTC:s measured in field have been deconvoluted to a unit response function, i.e. the BTC represents the expected result from a Dirac pulse input (see Elert and Svensson, 1999). For the present purpose we will however regard the deconvoluted BTC as field data.

The objective of the validation study is to show that the numerical model can be tuned to fit the experimental BTC:s. It is however not meaningful to use all model parameters in such a tuning or to use unrealistic values on parameters. A strategy is needed.

As this is the first comparison with field data (concerned with BTC:s) it is relevant to begin with a study that focuses on the most uncertain model parameters. We will call this study phase I. The real test of a tracer transport model is however to predict BTC:s. To do predictions, the model parameters should be known or possible to estimate without reference to the measured BTC. In phase II we will use fixed model parameters and only vary property data.

The problem specification is in most respects identical to the one given for Task 6A A general description of Task 6 and further details of this modelling exercise can be found in Svensson (2003). For a general description of the PARTRACK model, see Report 1.

Validation, phase I

If fracture and matrix properties, flow velocity, tracer properties, etc were all known the present model would still have two parameters that are undetermined:

- k, the late time slope. For a single rate diffusion problem we know that $k = 1.5$, but for more complex situations we can only say that $k > 1.5$. Haggerty et al. (2000) found, using a multi-rate model, that $k = 2.1 \rightarrow 2.2$ fits experimental data.

- α_{max} (rate for the smallest boxes) is uncertain because it is not clear if we should associate the fastest boxes with diffusion into stagnant water or diffusive exchange with the matrix. In the later case α_{max} should be estimated as $D_w / \left(l_{min}^2 R_{im} \right)$ while one may question if R_{im} should be involved (fully or not at all) for the stagnant water interpretation.

In phase I, k and α_{max} will hence be used as tuning knobs, with the objective to learn about sensitivity and limits. Some more conditions for the simulation:

- β_n (for non sorbing tracers) is first estimated. For sorbing tracers $\beta = R_{im} \times \beta_n / R_m$. R_{im} and R_m are estimated from the tracer data (see Table V4-1).

- $\alpha_{min} = 10^{-10}$ for HTO and $D_w / D_{w,HTO} \times 10^{-10} / R_{im}$ for other tracers.

B42

- The unit response BTC:s include the following tracers: HTO, Uranine, Na22, Sr85, Rb86 and Co58 (see Table V4-1).

Table V4-1. Tracer property data

Tracer	D_w $(\times 10^{-9})$	K_a	K_d	R_m	R_{im}
HTO/Uranine	2.4	0.	0.	1.	1.
Na22	1.33	7×10^{-7}	1.4×10^{-6}	1.0	1.95
Sr85	0.78	8×10^{-6}	4.7×10^{-6}	1.02	4.2
Rb86	2.0	5×10^{-4}	4×10^{-4}	2.0	271.
Co58	0.5	8×10^{-3}	8×10^{-4}	17.	542.

The first BTC discussed is for HTO, see Figure V4-1. As data are available also for Uranine (which should give a similar BTC) we include the data for Uranine as well. It is found that $\beta_n = 4$ and $k = 2.2$ give an excellent agreement with the measurements. Note that α_{max} is not uncertain for this case.

Next Na22 is considered. It is found from the measurements that "the peak is as high as for a non sorbing tracer, but delayed". It is not possible to obtain this effect, by the present model, without a $R_m > 1.0$. So, even if we set out to use the estimated values for R_m and R_{im}, we change R_m from 1.0 to 2.7, to get the peak arrival time right. α_{max} is estimated to be in the range $0.68 \rightarrow 1.33 \times 10^{-3}$. A $k = 2.05$ and $\alpha_{max} = 0.68 \times 10^{-3}$ give a fair agreement with measurements, as seen in Figure V4-2.

Strontium is the next, weakly sorbing, tracer to be studied. α_{max} should be in the interval $0.19 \rightarrow 0.78 \times 10^{-3}$. A somewhat larger value, 1.3×10^{-3}, and a $k = 2.05$ are needed to ensure good agreement, see Figure V4-3.

For Rubidium the α_{max} interval is $0.74 \times 10^{-5} \rightarrow 2.0 \times 10^{-3}$. A $\alpha_{max} = 1.1 \times 10^{-4}$ and a $k = 1.86$ give a fair agreement, see Figure V4-4, with the measured BTC.

Cobalt is the final tracer to be discussed. The α_{max} interval is now $0.92 \times 10^{-6} \rightarrow 0.5 \times 10^{-3}$. A $k = 2.0$ and $\alpha_{max} = 1.5 \times 10^{-5}$ is the best two-parameter tuning that could be found. The agreement with the measured BTC, see Figure V4-5, is however not very good.

Validation, phase II

The objective is now to evaluate how well we can tune the model to the experimental data by only changing tracer property data, as represented by R_m and R_{im}. We then need to conclude something about k and α_{max} from phase I. The k values range from $1.86 \rightarrow 2.2$. Let us put $k = 2.0$. α_{max} was found to be in the expected range, except for Sr85. It is however difficult to make further interpretations of the comparisons. In lack of further evidence, α_{max} will be based on the $\log_{10}$ average of the two limits (i.e. the average of 10^{-5} and 10^{-3} is 10^{-4}).

Again we start with HTO and estimate β_n. Now we only have one parameter to tune as HTO is non sorbing. A $\beta_n = 10.0$ gives a fair agreement as can be seen in Figure V4-6. One should however note that $k = 2.0$ is not the best value for the part after the peak (compare with Figure V4-1).

For Na22, see Figure V4-7, $R_m = 2.0$ and $R_{im} = 1.0$ give a good agreement, with the same arguments as in phase I. The estimated values, see Table V4-1, are $R_m = 1.0$ and $R_{im} = 1.95$.

For SR85 $R_m = 2.5$ and $R_{im} = 2.0$ produce a fair agreement, see Figure V4-8. These values are of the same magnitude as estimated.

In Figure V4-9, the comparison for Rubidium is shown. $R_m = 2.0$ and $R_{im} = 30.0$ were used in the simulation ($R_m = 2.0$ and $R_{im} = 271$ in Table V4-1). However, the "average rule" for α_{max} did not produce a good agreement for the early part of the BTC. A reduction, from $0.37 \rightarrow 0.07 \times 10^{-3}$, gives a significant improvement. Both curves are shown in Figure V4-9.

The same hold true for Cobalt, see Figure V4-10. The α_{max} based on the average is 2.1×10^{-5}, while the better BTC is based on $\alpha_{max} = 0.5 \times 10^{-5}$. For both curves the estimated $R_m \left(= 17 \right)$ and $R_{im} \left(= 542 \right)$ were used.

Concluding remarks

In the discussion section of the main Task 6 report (Svensson, 2003) some comments about the advantages and limitations of the present model can be found. These comments are to a large extent based on the simulations presented in this Appendix.
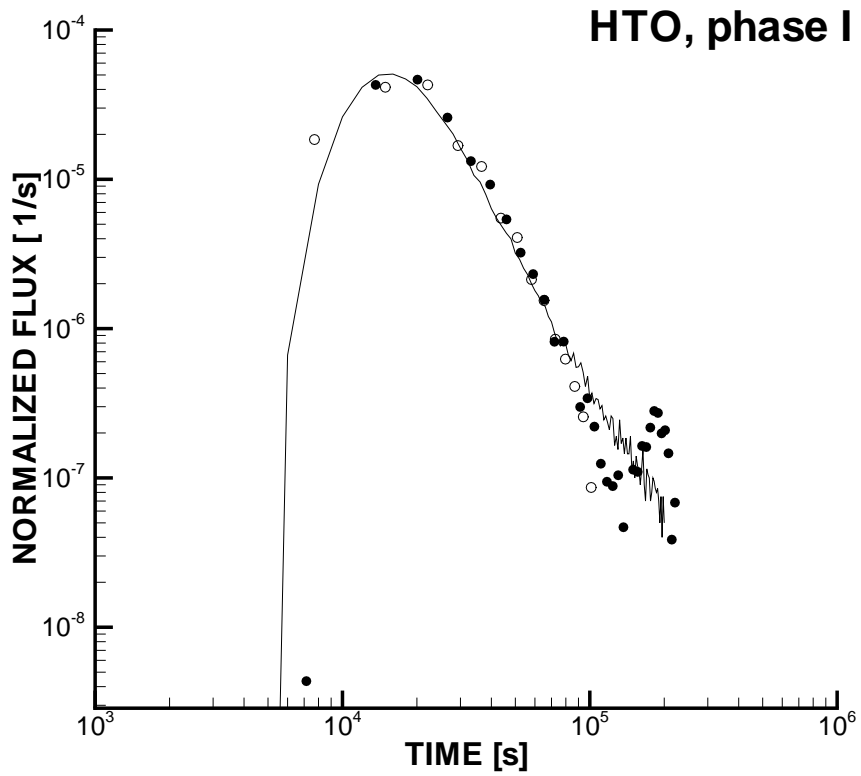
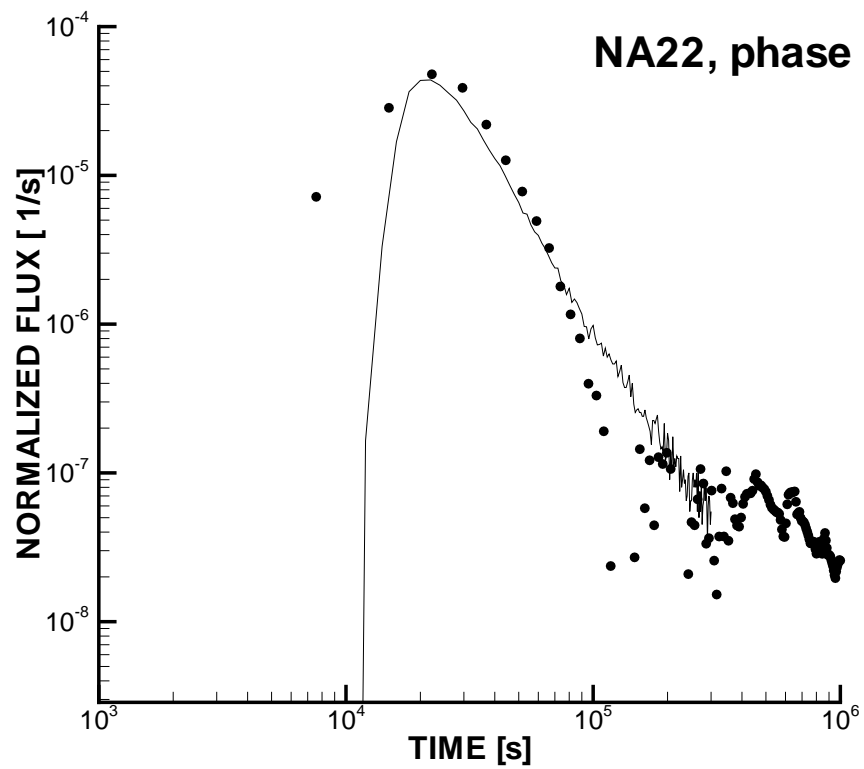***Figure V4-1.*** *Validation, phase I. Solid line gives simulation, open circles HTO and filled circles Uranine.*

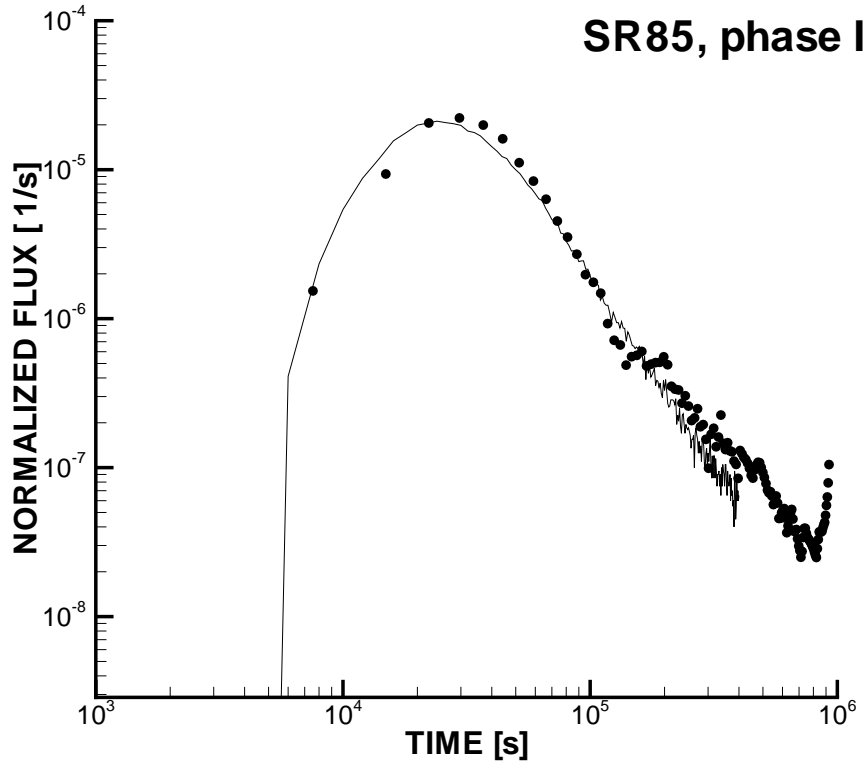***Figure V4-2.*** *Validation, phase I. Solid line gives simulation, circles measurements.*

B45

Figure V4-3 *Validation, phase I. Solid line gives simulation, circles measurements.*

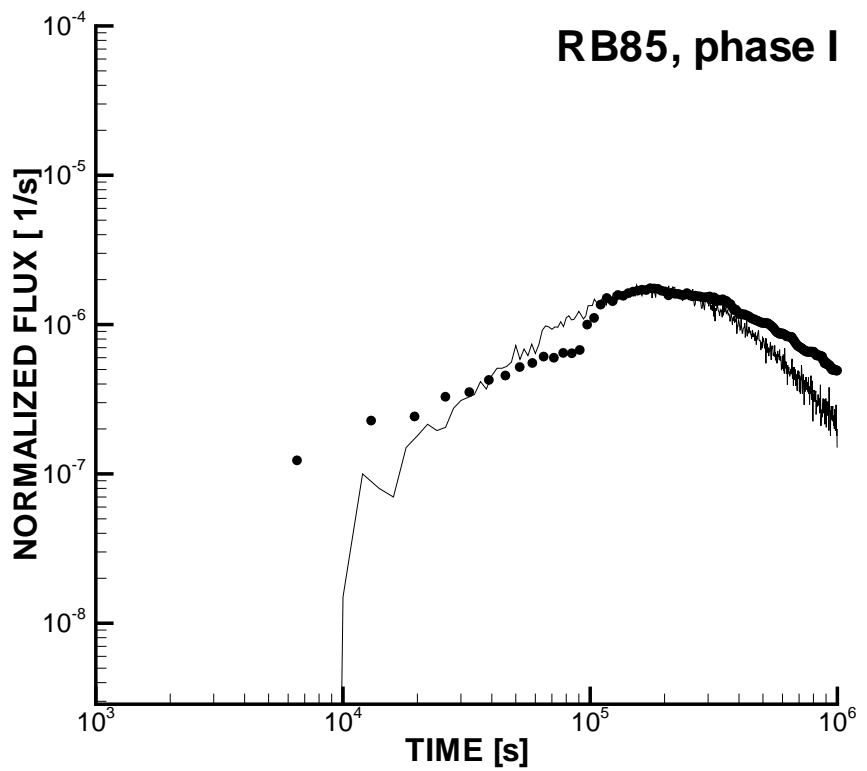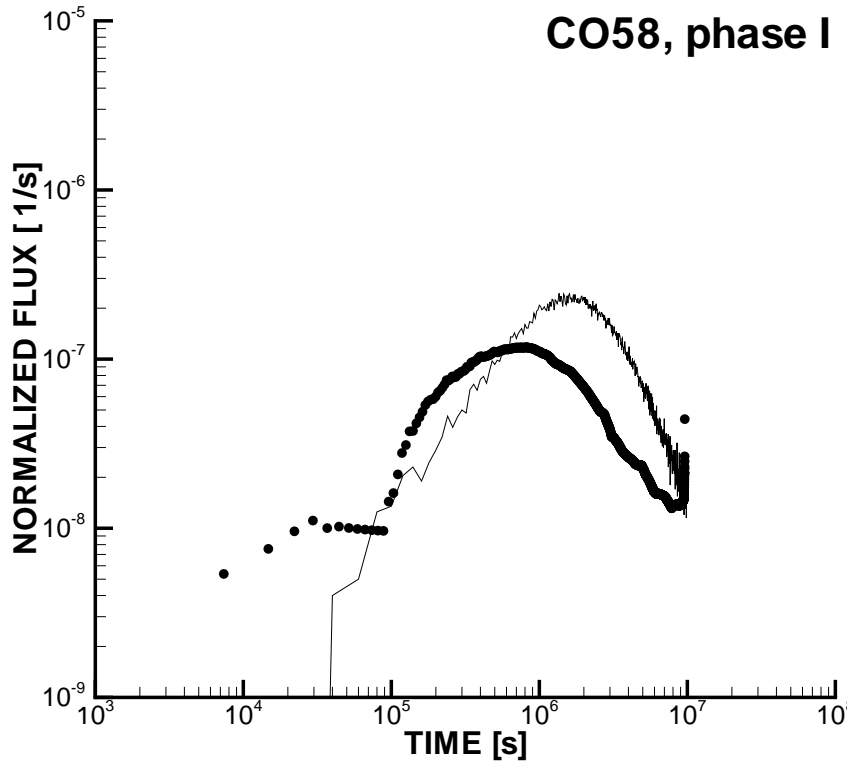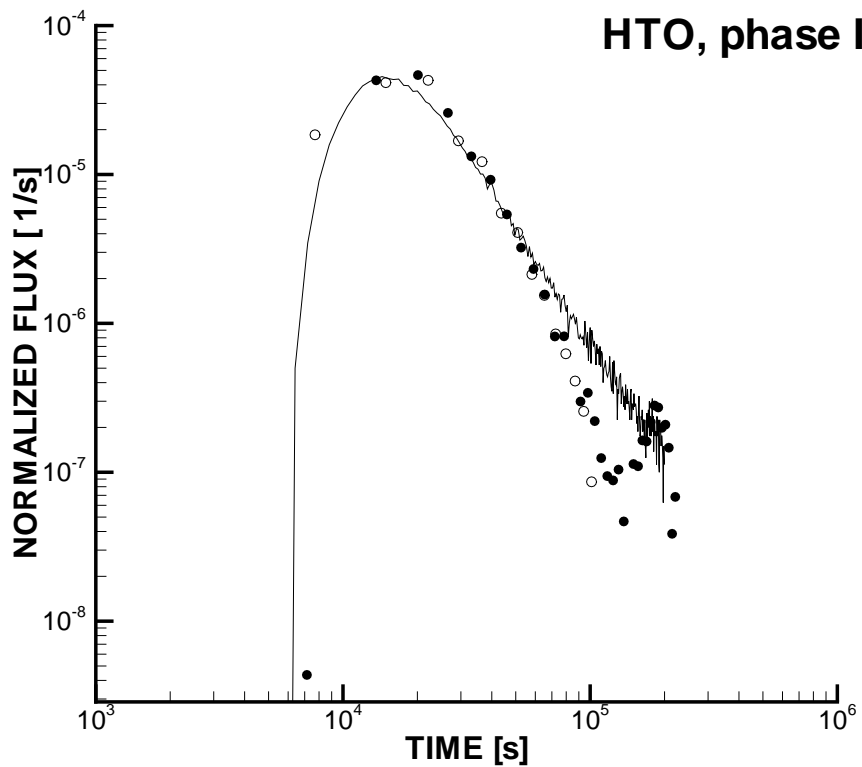***Figure V4-4.*** *Validation, phase I. Solid line gives simulation, circles measurements.*

B46

Figure V4-5. *Validation, phase I. Solid line gives simulation, circles measurements.*

Figure V4-6. *Validation, phase II. Solid line gives simulation, circles measurements.*
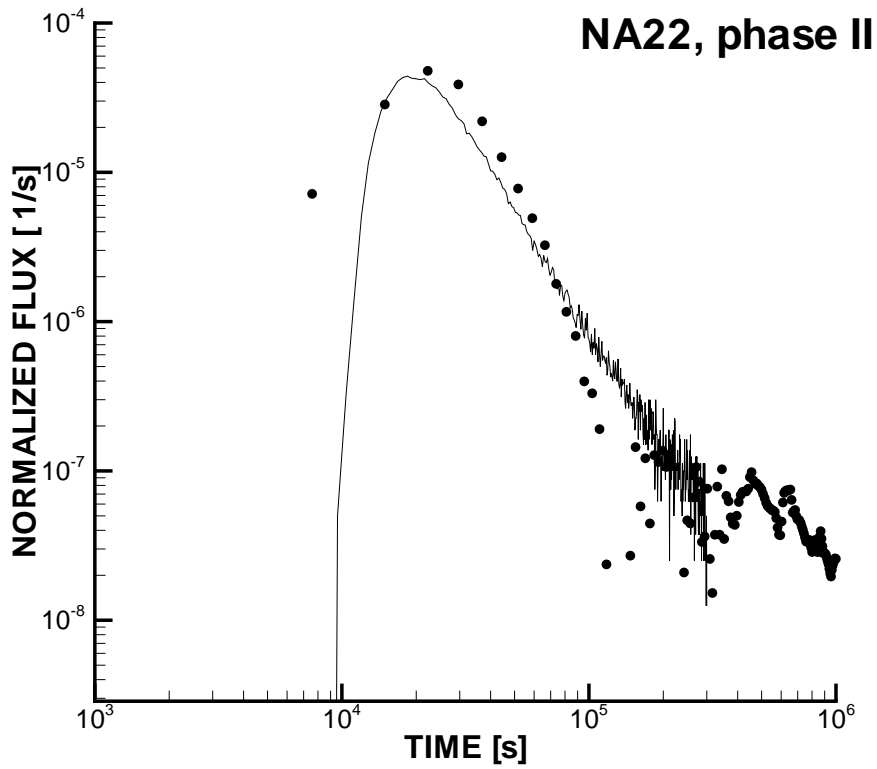*Solid line gives simulation, open circles HTO and filled circles Uranine.*

Figure V4-7. *Validation, phase II. Solid line gives simulation, circles measurements. Solid line gives simulation, circles measurements.*
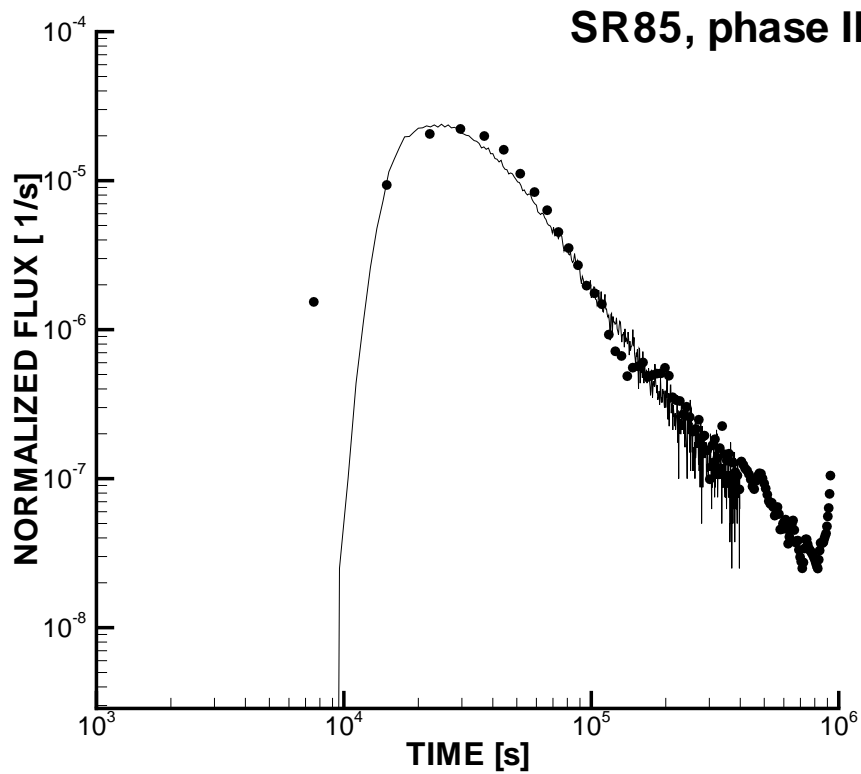

Figure V4-8. *Validation, phase II. Solid line gives simulation, circles measurements. Solid line gives simulation, circles measurements.*
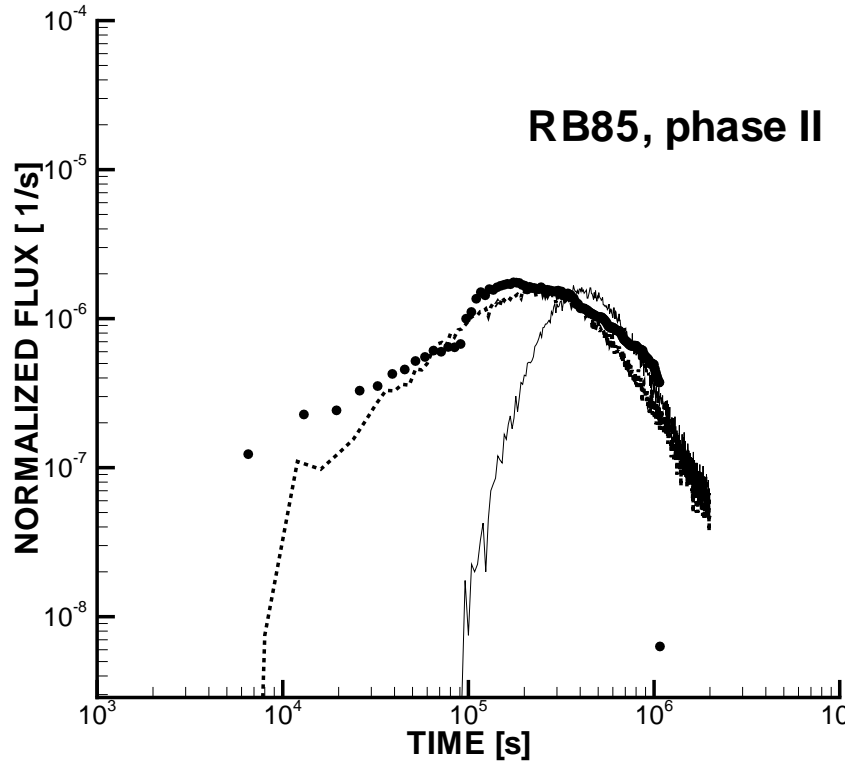
B48

Figure V4-9. *Validation, phase II. Solid line gives simulation, circles measurements.. Dashed line gives simulation with reduced* α_{max}.
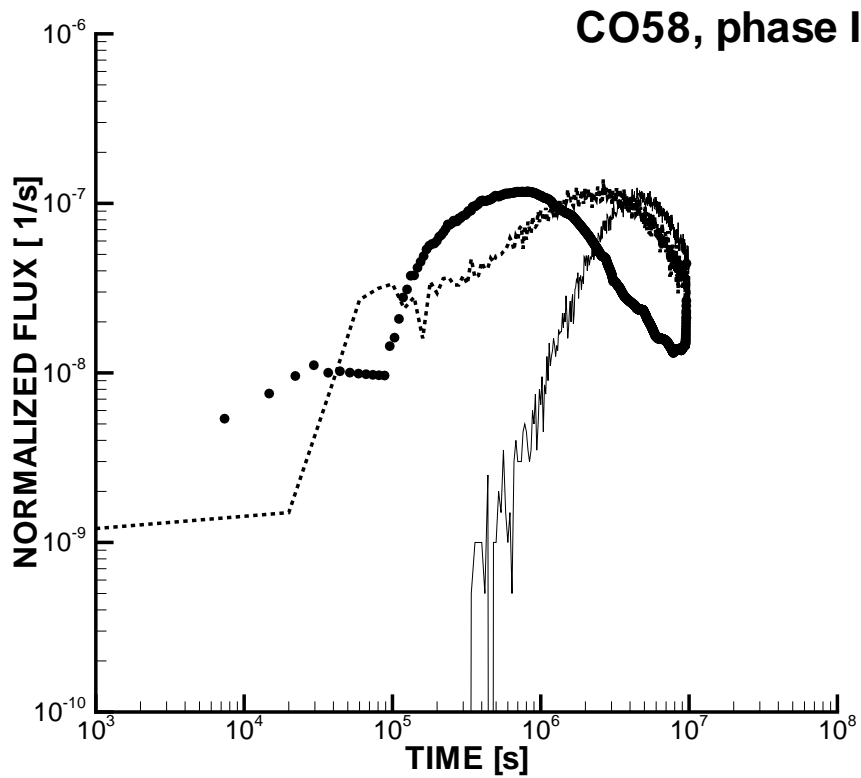

Figure V4-10. *Validation, phase II. Solid line gives simulation, circles measurements. Dashed line gives simulation with reduced* α_{max}.